ENZYMOLOGY OF LIPID METABOLISM BY CYP2J2 AS CONTROLLED BY MULTIPLE-LIGAND BINDING EVENTS

BY

WILLIAM RANDALL ARNOLD

DISSERTATION

Submitted in partial fulfillment of the requirements
for the degree of Doctor of Philosophy in Biochemistry
in the Graduate College of the
University of Illinois at Urbana-Champaign, 2019

Urbana, Illinois

Doctoral Committee

Assistant Professor Aditi Das, Chair and Research Director
Professor Robert Gennis
Assistant Professor Erik Procko
Associate Professor Rutilio Fratti

ABSTRACT

Lipid mediators are a recently discovered class of endogenous molecules that perform a variety of functions in the body. Specifically, polyunsaturated fatty acids (PUFAs) are transformed by three main pathways: the cyclooxygenase, lipoxygenase, and cytochrome P450 (CYP) epoxygenase pathways. Arachidonic acid is the canonical lipid mediator and it is transformed by the cyclooxygenase and lipoxygenase pathways into pro-inflammatory mediators at the onset of inflammation. For this reason, many drugs, particularly NSAIDs, have been developed to combat inflammation by inhibiting these enzymes. The CYP pathway, contrariwise, converts arachidonic acid into anti-inflammatory epoxide mediators known as epoxyeicosatrienoic acids (EETs). Additionally, these compounds regulate cardiovascular function, and importantly EETs are cardioprotective. The cyclooxygenase and lipoxygenase pathways were discovered first and have been extensively studied. There currently is not a lot known regarding the CYP pathway and how it is regulated. The CYPs responsible for producing EETs metabolize other PUFAs, lipids, and drugs. Complex substrate-substrate interactions have been observed with drug-metabolizing CYPs and is thought to mediate some of the known drug-drug interactions. Therefore, the aim of this work is to gain an enzymological understanding into lipid-drug interactions concerning the predominant CYP epoxygenase in the heart, CYP2J2. We aim to understand how multiple-ligand binding events effect the endogenous lipid metabolism by CYP2J2 in order to understand how they may effect cardiovascular and cerebrovascular function. We have developed a combined approach of kinetic and *in silico* molecular dynamic (MD) analysis in order to determine the nuances of multiple ligands binding to CYP2J2.

CYP2J2 is the most highly expressed CYP of the heart and has high levels of expression in the brain and endothelial tissues. All CYPs are membrane-bound proteins requiring the assistance of a membrane-bound redox partner, cytochrome P450 reductase (CPR). The hydrophobicity of CYP2J2, CPR, and the substrates have made studying this system challenging. We have been able to circumvent many of these challenges by recombinantly expressing CYP2J2 and CPR in *E. coli* and incorporating them into Nanodiscs. Nanodiscs are a membrane mimic composed of a lipid bilayer with two membrane scaffold proteins shielding the hydrophobic core. We then developed LC-MS/MS detection methods in order to quantify EETs and other lipid mediators. In Chapter 2, we study how arachidonic acid competes for metabolism by CYP2J2 within a pool of PUFA

substrates. In Chapter 3, we investigate how a cardiotoxic drug, doxorubicin, modulates arachidonic acid metabolism by CYP2J2.

PUFAs can be further transformed in the body into endocannabinoids, typically by conjugating the carboxylate headgroups with a variety of biological amines. These endocannabinoids modulate many of the functions associated with cannabinoids derived from marijuana (phytocannabinoids), including appetite, mood, and inflammation. Endocannabinoids are also substrates of CYP2J2, and the epoxide metabolites of these endocannabinoids have been shown to be anti-inflammatory. In Chapter 4, we determine that phytocannabinoids from cannabis plant are substrates of CYP2J2 and inhibit CYP2J2 mediated endocannabinoid metabolism. Particularly, Δ9-THC, the most psychoactive and often the most predominant cannabinoid in marijuana, potently shuts down endocannabinoid metabolism through a non-competitive model. In Chapter 5, we characterize a new class of endocannabinoids called endovanilloid epoxides. These molecules are derived from the conjugation of arachidonic acid with dopamine and serotonin and bind to the transient receptor potential vanilloid 1 (TRPV1). We determine that endovanilloids are also substrates of CYP2J2. The epoxides of these endovanilloids are potently anti-inflammatory and have distinct properties compared to the parent compounds. Particularly, an epoxide of N-arachidonoyl-serotonin is a potent TRPV1 antagonist and cannabinoid receptor 1 agonist, thereby making it a promising molecule to regulate pain and inflammation. Finally, we determine that the endocannabinoid, anandamide, potentiates endovanilloid metabolism in BV2 microglia and directly through substrate-substrate interactions in CYP2J2.

From these studies, we can build a map of substrates binding to CYP2J2 in the active and understand how multiple-ligand binding events modulate CYP2J2 activity. We are able to see how ligands compete, inhibit, or potentiate the binding of other ligands to CYP2J2 (Chapter 6).

ACKNOWLEDGEMENTS

I would first like to thank by thesis advisor, Prof. Aditi Das. She has taught me many of my biochemical techniques, especially since I studied as a chemist in undergrad. She has helped me greatly in developing my scientific technique, especially in how to plan and focus experiments. Additionally, she has given me a lot of advice and wisdom regarding my scientific career. She has also taught me, often through example, how to start a lab as an assistant professor and my career in general. I would also like to thank my committee, Profs. Rutty Fratti, Robert Gennis, Yi Lu, and Erik Procko. They have all provided with support and helped to develop my projects. I would next like to thank the Das Lab members, who have all been very helpful and amiable. Drs. Daryl Meling and Dan McDougle were instrumental in developing my early skills as a biochemist and in molecular biology, and in general for setting up many of the preliminary techniques in lab. I would like to thank Josephine Watson for helping set up cell culture and the PRESTO-TANGO assay in lab, and helpful discussions thereof. I would also like to thank Lauren Carnevale, Justin Kim, and Austin Weigle for listening to my ideas, for brainstorming, and for providing emotional support.

I also want to thank the Sligar Lab for providing materials and workspace at times, and especially to Dr. Ilia Denisov for teaching me about enzyme kinetics and analyzing complex enzyme systems. His discussions have been integral in being able to conduct experiments. I would next like to thank my collaborators. I thank Prof. Gang Logan Liu and colleagues for their work on the Lycurgus Cup Array project in the early stages of my career. I would like to thank Prof. Emad Tajkhorshid and his lab members Dr. Javier Lorenzo Baylon-Cardiel (former) and Andres Santiago Arango for their work on molecular dynamics simulations, which have provided much needed insight into the binding of different ligands to CYP2J2. They have been able to lend support to experimental observations that we could not fully explain. I also would like to thank Dr. (Lucas) Li Zhong from the Roy J. Carver Metabolomics Center for developing quantification methods to measure our metabolites, and for teaching me the basics of mass spectroscopy and analysis. I would also like to thank my undergraduate research advisor, Prof. Herlinger from Loyola University and Dr. Dan Kissel for staring me on my research career and providing advice regarding grad school.

I next want to thank my best friends, Dillon Cogan, Phil Olivares, and Susan Zelasko. They have not only provided scientific insight but importantly emotional support throughout my grad school career. They were especially there when I needed them the most.

I finally would like to thank my family: my mother and my sister. They have provided me with the strength and foundation for me to be able to complete my thesis work. I would not have been able to achieve all that I have without their support and without helping me to develop into the person that I am today. They have been true role models for strength, integrity, and discipline. I know that whatever obstacles I may face in the future that I will always have the loving support from them that I will need.

DEDICATION

This thesis is dedicated to my mother and sister. I could not have developed into the person that I am today and could not have gotten this far without them.

TABLE OF CONTENTS

Chapter 1: Overview of epoxy-PUFAs and their biosynthesis

1.1 The arachidonic acid cascade

Arachidonic acid (AA) is a C20:4 ω-6 polyunsaturated fatty acid (PUFA) that is converted by a series of oxidative enzymes into inflammatory and vascular lipid mediators[1-3]. These series of enzymes and metabolites comprise what is known as the arachidonic acid cascade (Figure 1.1). The arachidonic acid cascade contains three main branches that are named after the primary enzymes of each branch: the cyclooxygenase (COX), lipoxygenase (LOX), and epoxygenase (EPOX) pathways. The COX and LOX pathways are best known for converting AA into pro-inflammatory mediators at the onset of inflammation[2]. Various anti-inflammatory drugs have been developed to target COX and LOX enzymes. For example, NSAIDs (non-steroidal anti-inflammatory drugs) target COX[4], zileuton is an asthma medication that targets LOX[5], and dual COX/LOX inhibitors are currently being investigated[6]. The EPOX pathway, contrariwise, produces anti-inflammatory mediators from AA[3,7,8]. Drugs are being developed to help increase levels of the EPOX metabolites, but have not been established as therapeutics in humans[9]. To help increase the effectiveness and development of drugs for the EPOX pathway, a thorough understanding the EPOX pathway in the context of COX/LOX is needed.

COX is a family of hemoprotein dioxygenases that contains two isoforms: COX-1 and COX-2[10-12]. COX-1 is constitutively expressed and is mostly involved in maintaining vasculature tone, platelet aggregation, and thrombosis[13-15]. COX-2 is induced under inflammation to synthesize pro-inflammatory mediators[13-15]. Both COXs are responsible for converting AA into prostaglandin H_2 (PGH_2); however, their interactions with downstream enzymes determines how PGH_2 is further metabolized[15]. For instance, COX-1 couples with CYP5A1, which converts PGH_2 into thromboxane[16]. Thromboxane maintains vasoconstriction and platelet aggregation[17]. COX-2 couples with microsomal prostaglandin synthase E_2 to form E_2-series prostaglandins[15]. Additional control of prostaglandin synthesis occurs at the tissue expression level; for example, most cells express PGD_2 synthases, whereas pro-inflammatory macrophages express PGE_2 synthases[18]. The E_2-series prostaglandins (those derived from PGE_2) are the primary prostaglandins involved in the pro-inflammatory responses of the COX pathway[15,19,20], whereas D_2-series prostaglandins (those derived from PGD_2) are pro- and anti-inflammatory[15,21]. Eicosapentaenoic acid (EPA), a C20:5 ω-

3 counterpart to AA, is also a ligand for COX enzymes[22,23]. Whereas it is almost exclusively an inhibitor of COX-1, it is a substrate of COX-2, albeit poorer than AA[23,24]. COX-2 forms PGH_3 from EPA, which gets converted into E_3- and D_3- series of prostaglandins. Generally, the 3-series of prostaglandins are weaker than 2-series at their downstream receptors[23,25], though some researchers have reported equipotency between the 2- and 3-series[26]. Docosahexaenoic acid (DHA), a C22:6 ω-3 PUFA, is generally an inhibitor of COX enzymes[27,28]. The inhibition of COX enzymes by EPA and DHA is thought to partly mediate the anti-inflammatory benefits of ω-3 PUFAs[28,29].

LOX enzymes are a series of non-heme iron dioxygenases that produce various oxygenated products, including leukotrienes and hydroperoxy-PUFAs[30]. 5-LOX, 12-LOX, and 15-LOX are the best-known enzymes and are named for the position at which they oxidize AA. 5-LOX converts AA into leukotriene A4 (which is further metabolized to other leukotrienes) or into 5-hydroperoxyeicosatrienoic acid (which is further converted to 5-hydroxyeicosatetraenoic acid (5-HETE))[31]. 12-LOX produces 12-hydroperoxyeicosatetraenoic acid, which is further converted to 12-HETE[31,32]. These leukotrienes and HETE metabolites of 5-LOX and 12-LOX mediate various pro-inflammatory responses, notably immune cell chemotaxis[31-35]; further, 15-LOX can produce pro-inflammatory eoxins[36]. However, 5-LOX is also responsible for the synthesis of several specialized pro-resolving mediators (resolvins) derived from ω-3 PUFAs, such as EPA, DHA, and their metabolites[37]. 15-LOX is known for producing several lipoxins, resolvins, and protectins, all of which can help to remediate inflammation and associated inflammatory diseases[32,37-39]. Research into the biosynthesis of resolvins and protectins is ongoing; however, the LOX pathway is generally considered to be a pro-inflammatory pathway.

1.2 The EPOX pathway and epoxy-PUFAs

The third pathway of the arachidonic acid cascade is unique insofar as it makes almost exclusively anti-inflammatory and vasodilatory epoxy-PUFAs[8] (Figure 1.1). The primary enzymes of this pathway are the cytochromes P450 (CYPs), which are discussed in detail in Section 1.4. CYPs are monooxygenases that add an epoxide moiety at the alkenes of PUFAs and hydroxides at the terminal carbons[1,3,7,40,41]. The AA-derived metabolites of these enzymes, epoxyeicosatrienoic acids (EETs) and 19- and 20-HETEs, are among the oldest and most studied.

Four regioisomers of EETs are made from AA: 5,6-EET; 8,9-EET; 11,12-EET; and 14,15-EET[1,42-44]. EETs are mostly anti-inflammatory and vasodilatory[8], though there are some key differences discussed in Section 4. As a result, they have received the most attention for the purpose of combatting inflammation and cardiovascular diseases. Their degradation occurs mainly through soluble epoxide hydrolase (sEH), which makes dihydroxyeicosatrienoic acids. 19-HETE and 20-HETE are vasodilatory[45] and vasoconstrictive[46], respectively, and 20-HETE is pro-inflammatory[47]. The functions of these HETEs are partly due to their metabolism by downstream enzymes such as COX-2[48-50].

1.2.1 Epoxides and inflammation

EETs have been shown to be promising anti-inflammatory mediators. As such, there is an interest in exploiting the EET pathway for inflammation therapies[9,51]. The mechanisms by which EETs exert these effects are still being elucidated. EETs are known to inhibit TNFα/NFκB signaling in a regioisomer-specific manner, resulting in the downregulation of key pro-inflammatory mediators such as V-CAM[42,52-54]. They have also been shown to activate STAT3, which was shown to mediate the anti-inflammatory effects of IL-10[54-56]. Further, they are agonists of PPARs, leading to the reduction of COX-2 expression and NFκB signaling[54]. Through yet unknown mechanisms, EETs and epoxygenases have been implicated in mediating analgesia of nociceptive/neuropathic pain. Inhibition of sEH and knockdown/inhibition of epoxygenases indicated the mechanism may be indirect: via the reduction of inflammation or modulation of downstream pain receptors and not due to the direct binding of EETs to a receptor[57,58]. Similarly, epoxides of ω-3 PUFAs have been shown to be anti-inflammatory. The corresponding epoxides of EPA—EEQs—have shown to reduce TNFα, COX-2, and p38-MAPK phosphorylation[59]. EEQs and epoxides of DHA—EDPs—have also been shown to reduce pain in a similar mechanism as EETs[57,58]. The function of EETs and likely other epoxides is thought to partially be mediated by an unknown EET receptor[57,58]. This receptor is postulated to be located in endothelial cells and especially vascular endothelial cells, and is discussed in Chapter 1.2.2.

1.2.2 Epoxides and cardiovascular health

EETs additionally have a variety of beneficial effects on the cardiovascular system. They are therefore considered to be cardioprotective[8]. EETs have been identified as hyperpolarization

factors leading to the activation of K_{Ca} channels, which results in vasorelaxation[60,61]. They further contribute to vascular tone through interacting with other channels: they have been shown to inhibit Cl^- channels[62], effect transient receptor potential (TRP) channels by promoting their translocation to the cell surface[63], and 5,6-EET has been shown to bind TRPV4 directly[64,65]. Further, they have been shown to promote endothelial nitric oxidase synthase expression and phosphorylation, which leads to an increase in NO production and resulting in vasodilation[66,67]. EETs are also pro-proliferative, anti-apoptotic, and mitobiogenic and therefore promote angiogenesis[68-73]. Because of these functions, EETs have been shown to reduce and improve many cardiovascular diseases. EETs and CYPs have been implicated in mediating blood pressure and hypotension due to their vasodilatory properties. Administration of EETs has shown to reduce ischemia-reperfusion injury and improve the outcome of myocardial infarction[37]. Additionally, EETs and the overexpression of CYP epoxygenases have been shown to reduce chemical-induced toxicity, such as doxorubicin-[74] and alcohol-induced cardiotoxicity[61].

The unknown EET receptor is conjectured to mediate many of the vascular effects of EETs. This receptor is postulated to be a Gαs GPCR ~45 KDa in mass and expressed in vascular endothelial cells. Upon activation, the receptor stimulates PKA signaling, leading to the activation of VEGF and the P38/MAPK/ERK pathways to promote angiogenesis and proliferation[75-83]. Further, the effects of EETs on ion channels have been shown to be partly mediated by this receptor[60-63]. K_{Ca}-mediate vasorelaxation was blocked by addition of the G-protein inhibitor GDP-β-S or by anti-Gαs antibody, and further G-protein-dependent effects were observed for the inhibition of Cl^- channels[60-62]. PKA activation was also shown to mediate TRP channel translocation[63]. Therefore, finding the identity of this unknown is crucial in being able to exploit the EET pathway to promote cardiovascular health and therapies.

1.3 The endocannabinoid system

The functions of PUFAs are partly mediated by their conversion to endocannabinoids (eCBs). The search for the receptors mediating the known effects of cannabinoids from marijuana lead to the discovery of the endocannabinoid system in the early 1990s[84-86]. It was found that the body synthesizes cannabinoids, known as eCBs, that are PUFA derivatives with functionalized headgroups[87-90]. Anandamide (AEA) and 2-arachidonoyl-glycerol (2-AG) were the first

discovered and are the best-characterized[87-89]. Anandamide is an AA conjugated to an *N*-linked ethanolamine and 2-AG is AA conjugated to glycerol at the second position. Ethanolamide and glycerol derivatives of other PUFAs such as EPA and DHA have been discovered, though are not as well-characterized[91,92]. Further eCB-like modifications include amide-linked derivations with amino acids and taurine[90,93]. The endocannabinoid system comprises many receptors mediating the typical responses of cannabinoids. Together, eCBs and cannabinoids mediate such physiological responses as mood, appetite, nociceptive pain, inflammation, and the vascular system. These responses are mediated canonically by cannabinoid receptors 1 and 2 (CB1 and CB2), and more receptors for eCBs are being discovered[84-86]. Understanding how these molecules activate receptors, as well as their downstream metabolites, is crucial for understanding how the endocannabinoid system functions. This is especially true considering the high amount of ligand bias that has been observed with these receptors. Ligand bias occurs when different ligands induce unique conformational changes in proteins, which affect interactions with downstream receptors and pathways: for example, switching binding preference from $G\alpha_{i/0}$ to $G\alpha_s$[94-96].

1.3.1 Cannabinoid receptors 1 and 2

CB1 is expressed in the central nervous system, particularly the presynaptic terminals of neurons, and is also present in the heart, intestine, and reproductive tissues[84,97-101]. CB1 is best known for mediating the psychotropic effects of cannabinoids. These include nociceptive pain signaling, motor function, mood such as relaxation vs. anxiety, and is the receptor that is most responsible for mediating the "high" effects of Δ9-THC from marijuana[102-104]. These effects are explained by the high expression of CB1 in the hippocampus, amygdala, prefrontal cortex, hypothalamus, and basal ganglia[105]. Ultimately, CB1-mediated psychotropic effects function by leading to suppression of neurotransmitter release, such as glutamate and γ-aminobutyric acid (GABA), from the presynapse[106,107]. Apart from neurological functions, CB1 regulates cardiovascular and inflammatory functions[108,109]. CB2 has high levels of expression in immune cells[86] and is most responsible for the anti-inflammatory effects of cannabinoids[108,110]. These anti-inflammatory effects are partly due to CB2-mediated inhibition of adenyl cyclase[111] and activation of MAPK[112] pathways, as well as modulating ion channel activity[113,114].

CB1 and CB2 are promiscuous in the number of ligands that bind them, which include several endocannabinoids and several hundred drugs. Many drugs have been discovered or synthesized have different binding preferences for CB1 and CB2. For example, Δ9-THC binds almost equally to CB1 and CB2[115]; rimonabant[116], arachidonoyl-2'-chloroethylamine[117], and AM 281[118] bind CB1 selectively; and HU-308[119] and β-caryophyllene[120] bind CB2 selectively. The eCBs also have cannabinoid receptor selectivity. AEA binds almost exclusively to CB1 over CB2 and 2-AG binds to both receptors equally[114,121-125]. The promiscuity of these receptors also contributes to a high degree of ligand bias[94-96]. For example, HU-210 and CP-55940 are CB1 $G\alpha_{i/0}$ agonists and showed different potencies and efficacies for activating CREB- vs. AP-1-dependent transcription. This led to a rise in tyrosine hydroxylase expression by HU-210 and a decrease in expression by CP-55940[126-131]. Additionally, CP-55940 has been shown to induce cAMP accumulation and thus activate $G\alpha_s$ in addition to $G\alpha_{i/0}$[132,133]. Two stereoisomers of α-pinene derivatives of Δ9-THC were developed as potential drugs binding to CB2, named HU-308 and HU-433, and these drugs demonstrate that binding affinity alone does not determine the potency of activation[134]. Interestingly, whereas HU-308 binds to CB2 more tightly than HU433, HU-433 activated CB2 and produced biological activity more potently than HU-308. *In silico* docking studies showed that HU-433 binds in a position that facilitates a better active confirmation of CB2 than HU-308; therefore, even though HU-308 binds tighter HU-433 is more effective[134]. Combined, the promiscuity and ligand bias associated with CB1 and CB2 make endocannabinoid signaling complex, which necessitates a thorough understanding of the endocannabinoid system in order to be exploited medicinally.

1.3.2 Other receptors

In addition to CB1 and CB2, other receptors are being discovered that bind eCBs. These are often the orphan GPCRs. Two GPCRs gaining recognition as cannabinoid receptors are GPR18[135] and GPR55[136]. GPR18 activation by eCBs was shown to enhance migration and apoptosis[137]. GPR55 is activated by cannabinoids; is expressed in neurons, immune cells, and vascular endothelial cells; and is responsible for anti-inflammatory, hypotensive, and anti-nociceptive actions[138]. Notably, other cannabinoid receptors include an unknown endothelial cannabinoid receptor, often referred to as the abnormal-CBD receptor due to the putative responses of abnormal-CBD by this receptor[139-141]. This receptor has been postulated to be expressed in

neurons, vascular endothelial cells, and immune cells, thus mediating some of the anti-inflammatory and vasodilatory properties of cannabinoids[139-141]. Although showing similar properties as GPR55, this receptor is postulated to be $G\alpha_{i/0}$-coupled, whereas GPR55 is $G\alpha_{13,}$ thereby making these two receptors likely unique[139-141].

The non-selective cation TRP channels have also been shown be activated by eCBs, notably TRP vanilloid 1 (TRPV1)[142-146]. TRPV1 is mainly located in sensory neurons and endothelial cells and is primarily responsible for the nociceptive pain associated with noxious heat and, partly, inflammation[147-150]. TRPV1 binds many endogenous lipid-like molecules, many of which are inflammatory mediators; however, it is most famously activated by capsaicin, which is responsible for the burning sensation of *chili* peppers[150]. TRPV1 activation leads to an influx of cations, importantly Ca^{2+} ions, that mediate most of its function. This influx of Ca^{2+} leads to downstream activation of Ca^{2+}-sensitive receptors such as calmodulin protein kinase II[151]. TRPV1 activation is also associated with many responses apart from modulating pain, such as mediating pro- or anti-inflammatory responses[152-155]. TRPV1 has been shown to play many, often conflicting roles in cardiovascular health[156]. The activation of eNOS enzymes leads to NO-induced vasorelaxation[157,158] and can therefore control the flow of blood and, along with releasing calcitonin gene-related peptide (CGRP), prevent ischemia-reperfusion injury[159]. However, the Ca^{2+} influx can lead to calcium overload in heart cells and promote apoptosis and mitochondrial dysfunction, leading to cardiotoxicity[160]. The context in which TRPV1 is activated needs to be further studied in order to understand its role in functions other than nociceptive pain.

1.3.3 Metabolism of endocannabinoids

Enzymes of the arachidonic acid cascade also metabolize eCBs, notably the CYP epoxygenases[161,162]. The metabolites of eCBs are not as well-characterized as their parent molecules. Regardless, some important distinctions can be made. The epoxides of eCBs are postulated to mediate similar functions as their eCB and epoxy-PUFA counterparts[162]. For example, epoxides of ω-3 eCBs were shown to be potently anti-inflammatory and anti-cancer[163,164]. Furthermore, 5,6-EET-EA and many of the ω-3 eCB epoxides show a greater selectivity for CB2 binding than their parent molecules, suggesting that the epoxidation of eCBs switches CB1/CB2 preference[163-165].

1.4 Cytochromes P450 (CYPs)

The primary epoxygenases of PUFAs and eCBs are the CYPs. CYPs comprise a superfamily of membrane-bound hemoproteins located in either the endoplasmic reticulum or the mitochondria[166]. They were first isolated in liver microsomes (membrane preparations of the endoplasmic reticulum) and were named for the characteristic absorbance at 450 nm when CO is bound to the heme. In humans, there are 57 CYPs performing various functions[167]. The heme cofactor binds molecular oxygen to produce a highly reactive ferryl-oxygen (most likely) or perferryl-oxygen species through a process known as the CYP Cycle[168]. CYPs then utilize this strongly oxidizing agent to oxidize organic molecules. Particularly, they insert an oxygen atom at C-H, C=C, or N- bonds, and sometimes perform degradative functions such as *N*- or *O*-dealkylation[169]. However, many other types of "atypical" CYP reactions are possible[169]. All CYPs, excluding CYP5A1 and CYP8A1, require redox partners to perform their catalysis. Cytochrome P450 reductase (CPR) is the primary redox partner of CYPs[170], though other reductases such as adrenodoxin reductase can perform these functions for mitochondrial CYPs[171]. Additionally, cytochrome b5 can act as an electron mediator between CPR and CYPs and subsequently modulate CYP substrate metabolism, as seen with CYP17A1[172-175].

1.4.1 Biosynthetic CYPs

CYPs have been evolved to perform important endogenous functions. Many CYPs are involved in steroidogenesis. These include CYP11A1 (converting cholesterol to pregnenolone)[171], CYP17A1 (hydroxylating or lysing pregnenolone and progesterone)[176], CYP19A1 (converting testosterone to estrogen)[177], and CYP11B1 (converting 11-deoxycortisol and 11-deoxycorticosterone to cortisol and corticosterone, respectively)[178]. Additionally, CYP2R1 hydroxylates vitamin D to calcifediol[179] and CYP27B1 hydroxylates calcifediol to calcitriol[180]. CYP5A1 and CYP8A1 are atypical CYPs insofar as they are isomerases as opposed to oxidases. CYP5A1 isomerizes PGH_2 to thromboxane[181] and CYP8A1 isomerizes PGH_2 to PGI_2[182]. Many drugs have been developed to target the steroidogenic varieties of CYPs. Particularly, CYP19A1 is targeted to reduce estrogen production, which combats breast cancers and increases testosterone levels in men for testosterone replacement therapy[177,183,184]. Importantly, these biosynthetic CYPs have been evolved to perform a particular function in the body. As a result, they are selective for

their substrate recognition and generally do not metabolize extraneous substrates. In contrast, xenobiotic CYPs are highly promiscuous with complicated substrate metabolism kinetics.

1.4.2 Xenobiotic CYPs

CYPs are better known in pharmacology for their role in first-pass drug metabolism[185,186]. These CYPs metabolize drugs or other xenobiotics by functionalizing them with an oxygen atom (producing a hydroxide or epoxide) or through dealkylation resulting in a free N or O moiety[169]. These transformations of the xenobiotics help to increase their solubility in aqueous media and to provide a molecular handle for further transformations by second-pass enzymes. Second-pass enzymes will conjugate the xenobiotic to molecules such as glucuronide and glutathione, which further helps to increase their solubility and elimination from the body[187]. CYP3A4 is the primary xenobiotic-metabolizing CYP in humans, responsible for the metabolism of over half the drugs on the market[188-190]. Contrary to biosynthetic CYPs, xenobiotic CYPs have been evolved to be highly promiscuous in order to effectively metabolize any foreign substance that enters the body. As a result, their active sites are not as restrictive as the prototypical enzyme that specifically binds one substrate. Xenobiotic CYPs have shown to have complex substrate-substrate interactions due to the concurrent binding of multiple drugs at allosteric sites or even in the active site[191-193]. Substrates can also alter the positioning of other substrates in the active site of CYPs, as seen with the modulation of midazolam binding by carbamazepine in CYP3A4, leading from 1'-hydroxylation of midazolam to 4-hydroxylation[194].

1.4.3 CYP2J2 and other epoxygenases

The 2C and 2J families are the primary CYP epoxygenases that produce EETs, epoxy-PUFAs, and epoxy-endocannabinoids[8,161,163]. In humans, these enzymes include CYP2J2 (the only 2J enzyme in humans), CYP2C8, CYP2C9, and to a lesser extent CYP2C19[8]. The 2C enzymes, much like their other xenobiotic counterparts, have the highest levels of expression in the liver[186,195]. Contrariwise, CYP2J2 is the most expressed CYP in the heart and other endothelial tissue, and has lower expression in the liver[196]. CYP2J2 mRNA levels were found to be almost 20,000-fold higher than CYP2C8 or CYP2C9 in the myocardium and also has high levels of expression in the vascular endothelium[197-199]. Importantly, it was found that the EET profile observed in the heart matches the EET profile produced by CYP2J2, thus demonstrating that CYP2J2 is the primary

epoxygenase[196]. Owing to its importance in synthesizing cardioprotective EETs, CYP2J2 expression has been shown or been implicated to reverse several adverse toxicities in the heart, such as the cardiotoxicity induced by doxorubicin[74], diabetes[200,201], and ischemia-reperfusion injury[202]. CYP2J2 is also one of the most expressed CYPs found in many regions of the brain including the hippocampus, cerebellum, and astrocytes (www.proteinatlas.org and[203-205]). Rodents such as mice and rats have multiple CYP2J enzymes, and these have been shown to also be expressed in various brain regions and astrocytes[206-208]. Likewise to the heart, CYP2J in the brain has been shown to provide a protective role for various brain diseases, such as Parkinson's[209].

An important feature of the epoxygenases is that unlike other biosynthetic CYPs, these CYPs are promiscuous and are known to metabolize several drugs in addition to various PUFAs[8]. These CYPs can also display complicated substrate metabolism kinetics due to substrate-substrate interactions. For instance, 6-hydroxyflavone was shown to noncompetitively inhibit CYP2C9 by binding to a site just outside the heme pocket and preventing substrate ingression[210]. The impact of substrate-substrate interactions on the metabolism of PUFAs by these CYPs is an area that is not fully explored. Particularly, CYP2J2 was discovered relatively recently in 1996[196] and much of its mechanisms of substrate metabolism is poorly understood, especially concerning the kinetics of substrate metabolism. This is partly due to a lack of recombinant data on CYP2J2 in an isolated reconstituted system.

1.5 Enzyme kinetics

In order to understand how substrates are recognized by an enzyme, and further how multiple-ligand binding can affect enzymatic activity, careful enzyme kinetics need to be studied. The foundations for modelling enzyme kinetics was conducted at the early half of the 20th Century. The prototypical and most basic model for enzyme kinetics is the Michaelis-Menten model. However, since CYPs bind multiple substrates/ligands, their kinetics can stray away from the Michaelis-Menten model. Sections 1.5.1 and 1.5.2 will give a brief overview on Michaelis-Menten kinetics, the basis of all enzyme reactions. Section 1.5.3 will then provide a brief overview on the non-Michaelis-Menten kinetics seen by CYPs due to multiple-ligand binding events.

1.5.1 Michaelis-Menten kinetics

The Michaelis-Menten kinetic model is a model for one-site reversible kinetics that has become the standard for enzymology. The details of Michaelis-Menten kinetics, as well as other considerations, can be found in many textbooks. Sections 1.5.1-1.5.3 will summarize the key aspects as stated by Segel[211]. Before exploring enzyme kinetics, it is important to understand basic kinetics and equilibria in chemistry. These sections will be presented assuming a basic knowledge of these areas.

1.5.1.1 The rapid equilibrium approach

Henri proposed the groundwork for enzyme kinetics, which Michaelis and Menten expanded upon into the final form that we know today as the Michaelis-Menten kinetic model. The model is built upon a rapid equilibrium approach with the given assumptions:

1. The enzyme is a catalyst.
2. Enzyme (E) and substrate (S) react rapidly to form the enzyme-substrate complex (ES). *Hereafter, complexes will be designated as EX (e.g., enzyme-substrate ≡ ES), and concentrations of species that are multiplied will be designated as $E \cdot X$ (e.g., $E \cdot S$).*
3. Only a single E and a single S are involved in the reaction, and ES breaks down to form product (P). That is, P is formed exclusively from the reaction of S by binding to E in ES.
4. E and S are in a rapid equilibrium with ES, i.e. the rate of formation and dissociation of ES is much greater than the rate of product formation.
5. $[S] \gg [E]$ so that a negligible amount of [S] is consumed in the formation of ES and $S_{total} \approx S_{free}$.
6. The overall reaction is dependent on the breakdown of ES.
7. The reaction is monitored at the very early stages of the reaction so an insignificant amount of P is formed and the reverse reaction (P → ES → S) does not occur significantly. *It is important to note that, concerning CYPs, the oxidation of S to P is rarely reversible, and so this assumption is especially appropriate. However, P may itself be a substrate of the CYP. While the conversion of P to P' can easily be assessed as its own reaction, the enzymologist ought to still perform experiments where minimal P is converted to P'.*

Under these conditions, we can derive a kinetic model based on this rapid equilibrium approach, which is shown below.

$$\mathbf{E + S} \underset{\mathbf{k_{-1}}}{\overset{\mathbf{k_1}}{\rightleftharpoons}} \mathbf{ES} \xrightarrow{\mathbf{k_p}} \mathbf{E + P}$$

Using this model, we can derive a kinetic equation. First, we write the velocity equation for the formation of P.

$$v = k_p ES$$

As we do not know the concentration of ES outright, we need to write the equation in terms of E and S. We can achieve this by first dividing the velocity equation by the mass balance equation $E_t = E + ES$.

$$\frac{v}{E_t} = \frac{k_p ES}{E + ES}$$

We can then use the equilibrium equation to substitute ES.

$$K_{eq} = \frac{ES}{E \cdot S} = \frac{1}{K_D}$$

$$ES = \frac{E \cdot S}{K_D}$$

$$\frac{v}{E_t} = \frac{k_p \frac{S}{K_D} E}{E + \frac{S}{K_D} E}$$

$$\frac{v}{E_t} = \frac{\cancel{E}\left(k_p \frac{S}{K_D}\right)}{\cancel{E}\left(1 + \frac{S}{K_D}\right)}$$

We can then define $k_p E_t \equiv V_{max}$, which is the rate if all of the enzyme were bound in ES and were metabolizing S to P. This is of course an impossibility given that ES is in equilibrium with E + S, and so V_{max} represents an asymptote for the rate of formation of P. This equation is therefore a hyperbolic function. The terms “hyperbolic”, “one-site”, and “Michaelis-Menten” are often used

(interchangeably) to describe these types of kinetics. Substituting V_{max} arrives at the familiar Michaelis-Menten equation.

$$v = \frac{V_{max}\frac{S}{K_D}}{1 + \frac{S}{K_D}} = \frac{V_{max}S}{K_D + S}$$

In this model, we assumed that the rate limiting step is the product formation (k_p is very small compared to K_D). It became apparent that this is not the only case when it comes to enzyme kinetics. Soon after the development of the rapid equilibrium model by Henri-Michaelis-Menten, Briggs-Haldane developed a more generalizable, steady-state approach to enzyme kinetics. It is still useful to understand the basics of the rapid equilibrium approach because it is the simplest model. As such, complex multi-ligand kinetic models (Section 1.5.3) are more easily derived from the rapid equilibrium approach. Note that the K_D (or any enzyme binding constant) is in units of M (or nM, µM, etc.) and v (or Vmax) is in units of mol/s (or nmol/min, etc.). CYP kinetics are often presented with v and V_{max} in units of $mol_{product}$/min/$mol_{enzyme,}$ which is actually the unit for turnover. This does not nominally change the fit of the equation but the meaning of the ordinal axis.

1.5.1.2 The Briggs-Haldane steady-state approach

Briggs-Haldane reconsidered Michaelis-Menten kinetics by introducing the idea that ES does not need to be in a rapid equilibrium with E + S. Instead, a very short time after the start of the reaction ES will approach a constant concentration (a steady-state). This is especially true when the value of k_p approaches k_{-1}. The period in which product formation is linear over time is the indication that ES is in a steady-state. A hypothetical plot for this type of reaction is given below.

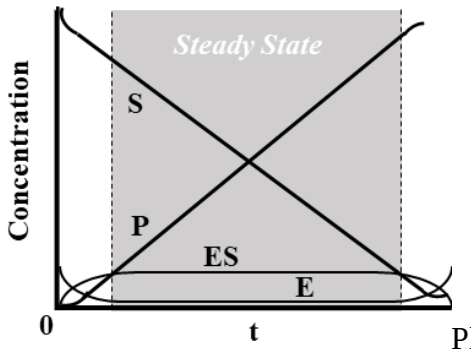

Plot 1.1

Knowing, this, we can derive a steady-state model based on a constant [ES]. The model begins with the same reaction scheme as the Michaelis-Menten model.

$$\mathbf{E + S} \underset{\mathbf{k_{-1}}}{\overset{\mathbf{k_1}}{\rightleftharpoons}} \mathbf{ES} \xrightarrow{\mathbf{k_p}} \mathbf{E + P}$$

We will now consider the reaction in terms of the formation and decomposition of ES. ES forms by one process:

$$\mathbf{E + S} \xrightarrow{\mathbf{k_1}} \mathbf{ES}$$

but decomposes by two processes:

$$\mathbf{1.}\quad \mathbf{ES} \xrightarrow{\mathbf{k_p}} \mathbf{E + P}$$

$$\mathbf{2.}\quad \mathbf{ES} \xrightarrow{\mathbf{k_{-1}}} \mathbf{E + S}$$

Therefore:

$$r_{+ES} = +\frac{dES}{dt} = k_1 E \cdot S$$

$$r_{-ES} = -\frac{dES}{dt} = k_{-1} ES + k_p ES$$

We are assuming that ES is at a constant concentration, i.e. $\frac{dES}{dt} = 0$. Therefore:

$$+\frac{dES}{dt} = -\frac{dES}{dt}$$

$$k_1 E \cdot S = (k_{-1} + k_p) ES$$

$$\frac{k_1 E \cdot S}{k_{-1} + k_p} = ES$$

We then start with the velocity-dependence equation as we had done for the rapid-equilibrium derivation. However, instead of substituting ES using the equilibrium equation, we substitute ES using the formula we derived above.

$$v = \frac{V_{max}\frac{k_1}{k_{-1}+k_p}S}{1+\frac{k_1}{k_{-1}+k_p}S}$$

We can then define $K_m \equiv \frac{k_{-1}+k_p}{k_1}$, which is referred to as the Michaelis-Menten constant (although it was derived by Briggs-Haldane). This produces the more familiar Michaelis-Menten equation.

$$v = \frac{V_{max}\frac{S}{K_m}}{1+\frac{S}{K_m}} = \frac{V_{max}S}{K_m+S}$$

This equation is nominally the same as the equation we derived from the rapid-equilibrium approach. The difference is in the meaning of the equilibrium constants. In the rapid-equilibrium approach, the equilibrium constant is the K_D, which only considers the binding of the substrate to the enzyme. In the steady-state approach, the equilibrium constant is K_m, which includes k_p. The steady-state is a general model, and by this model enzyme reactions in which the rate-limiting step is the product formation will approach a rapid-equilibrium. Both one-site kinetic (measuring product turnover) and one-site thermodynamic (measuring substrate binding without product turnover) data will fit to the general formula $B = \frac{B_{max}S}{K+S}$. It is the nature of the experiment that determines if the measured K is a K_D or K_m.

The steady-state assumption will become truer the higher the S_0:E_{total} ratio becomes. That is, when S is substantially higher than E, the ES will form faster and will reach a steady-state sooner. A final note is that there are 4 differential rate equations, one each for E, S, ES, and P. Including the mass balance equation, we have 5 equations to solve 4 variables, which naïvely would be enough equations to solve for 4 variables. However, it is impossible to write differential equations for S and P without ES. Therefore, unless we define ES to be constant, S and P will be dependent on ES and the rate equation can only be derived using calculus.

Both the rapid-equilibrium and steady-state approaches rely on the condition that E is significantly smaller than S. This way, an insignificant amount of S is bound to ES, and $S_{total} \approx S_{free}$. When E is not significantly lower than S, or when the K_m (or K_D) is near [E], then a significant amount of S is bound to ES and $S_{total} \neq S_{free}$. In these situations, we need the substrate mass balance

equation (S_t = S + ES) as well as the enzyme mass balance equation (E_t = E + ES). Using these equations as substitutes for ES, we arrive at the Morrison (tight-binding) equation given below.

$$v = V_{max}\frac{(E_t + S_t + K) - \sqrt{(E_t + S_t + K)^2 - 4E_tS_t}}{2E_t}$$

1.5.2 Reversible (Michaelis-Menten) inhibition kinetics

Now that we have derived models for a one-site, single substrate case, we can complicate the model by considering the effects of inhibitors. A reversible inhibitor may bind to the enzyme in two distinct ways given below.

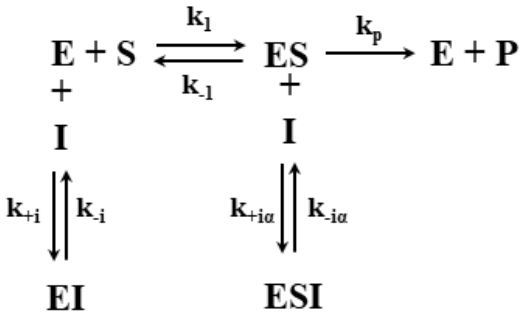

The inhibitor, I, may bind to the substrate-free enzyme or to ES. The affinity for the inhibitor to E is defined as K_i, and the affinity of I to E when substrate is bound (ES) is defined as $K_{i\alpha}$. A general inhibition equation derived from this model as given below.

$$v = \frac{V_{max}[S]}{K_m\left(1 + \frac{[I]}{K_i}\right) + [S]\left(1 + \frac{[I]}{K_{i\alpha}}\right)}$$

The inhibitor alters the apparent K_m (or K_D) or apparent V_{max} of the substrate. It is apparent insofar as the inhibitor does not change the intrinsic value of these parameters but alters their apparent value by a factor *b*. The inhibitor works by artificially lowering the concentrations of certain species by diverting the species to an off-pathway. Le Châtlier's Principle will then drive the equilibrium towards the formation of the species made lower in concentration by the inhibitor. There are 4 main types of reversible inhibition models, which are given below. Although the inhibitor in these cases is a non-substrate inhibitor (i.e., the inhibitor is not catalyzed by the enzyme), these inhibition models may still be used in cases in which both ligands are substrates.

If each substrate is considered in separate reference frames, then the other substrate is considered to be I in these models and the catalysis of "I" to P_2 can be largely ignored, much like the loss of [S] to the conversion of P can be ignored.

Competitive inhibition. I only binds the free enzyme (E). This drives the equilibrium towards the dissociation of ES to E + S. This results in a higher apparent K_m (i.e., a lower apparent affinity for the substrate). Importantly, since the state of ES is unaltered, there is no apparent change to V_{max}. Inhibitors of this sort are termed as competitive as the inhibitor and substrate are competing for binding to the active site: there is only one site and it binds both the substrate and inhibitor. Competitive inhibition can be overridden by the addition of more substrate, since S will drive the equilibrium towards the formation of ES. For competitive inhibition, the $1 + \frac{[I]}{K_{i\alpha}}$ term becomes 1 (i.e., it drops out).

Uncompetitive inhibition. If I binds only ES, then I reduces [ES]. This drives the equilibrium towards forming ES, resulting in a lower apparent K_m (i.e. greater apparent affinity for substrate). However, E is always partitioned between the ES (productive) and ESI (unproductive) states; therefore, the apparent V_{max} is lowered. This type of inhibition is known as uncompetitive and results typically from a conformational change to the enzyme upon substrate binding that opens an allosteric site for the inhibitor to bind. In this case, the $1 + \frac{[I]}{K_i}$ term becomes 1 (i.e., it drops out).

Mixed inhibition. If I binds to both E and ES, then the inhibition is considered mixed and will apparently affect K_m and V_{max} depending on the relative affinities of I for E or ES.

Noncompetitive inhibition. If I has equal affinity for E and ES, then I equally lowers [E] and [ES] (i.e., does not alter the ratio of [E] to [ES]), and the K_m is unaffected. However, the V_{max} is apparently lower due to the partitioning of E between ES and ESI. This is a special case of mixed inhibition that is termed noncompetitive inhibition.

Many text books will give classic examples of how these models manifest (e.g., by the inhibitor binding to the active site, to an allosteric site, etc.). It is best, however, not to concern oneself with specific examples of how a certain inhibition model occurs but instead on what effect the inhibitor has on the reaction scheme. Especially concerning CYPs, inhibitors may not behave in a "textbook" manner. For example, noncompetitive inhibition is often portrayed as the inhibitor

binding to an allosteric site, which changes the conformation of the enzyme into an inactive form. However, noncompetitive inhibition has been observed with CYP2C9 in which the inhibitor binds near the active site and directly prevents substrate access, without allosterically altering the conformation[210]. Furthermore, irreversible inhibition or enzyme degradation (due to experimental instability) can also manifest as noncompetitive inhibition, as E_{total} is irreversibly lowered and E and ES are concomitantly lower. Therefore, considering what happens to the reaction scheme in each model (e.g., noncompetitive means that E + S and ES are equally being lowered) will allow the enzymologist to develop a better mechanism by which the inhibition manifests without the influence of "textbook" examples.

1.5.3 CYPs and non-Michaelis-Menten kinetics (Multi-ligand binding)

CYP substrates typically follow Michaelis-Menten kinetics and inhibitors follow the 4 basic models given in Section 1.5.2. However, due to the complicated and sometimes multifaceted binding of ligands to CYPs, many non-Michaelis-Menten interactions are observed[191-193]. Some inhibitors, particularly those containing an activated or free N group, can ligate the heme. These can function as pseudo-irreversible inhibitors, as the ligand can form a stable complex with the heme and appear irreversible but may be removed upon dialysis or dilution. Imidazole is a common pseudo-irreversible CYP inhibitor of this sort. If irreversible inhibition is suspected, a common assay to determine pseudo-irreversible inhibition is to dialyze the inhibitor off of the enzyme and see if activity is recovered compared to a control. If inhibition is still occurring, then the inhibitor is a true irreversible inhibitor. Many irreversible inhibitors covalently modify either the heme or the CYP directly, and usually results from a mechanism-based formation of a reactive intermediate during the catalysis of a substrate[212,213]. The hallmark of an irreversible inhibitor is that exposure of E to I over time results in greater inhibition that cannot be reversed. Therefore, irreversible kinetics are determined by time-based kinetics exposing E to I during a reaction for different periods of time. A portion of the reaction is then aliquoted into a secondary "readout" reaction with a secondary ligand, S. If irreversible inhibition is present, then the E that has been exposed to I the longest will have the most inactivation; if it is reversible, then there is no time-dependence upon exposure to I. From these experiments, one can determine the k_{obs} and k_{inact} to determine the kinetics of the irreversible inhibitor (since it is irreversible, there is no true K_i as there is no k_{-i}).

The concurrent binding of multiple ligands can result in a variety of outcomes[214]. In the cases of multiple-binding events, the other ligands apart from the substrate are considered effectors. When an effector alters the binding affinity of another ligand, it is referred to as cooperativity. If the effector binds to a pocket apart from the active site it is called allostery. The ligand itself may function as an effector if it binds to multiple sites (homotropic cooperativity) or another ligand can function as the effector (heterotropic cooperativity). The effector alters the affinity of the enzyme for the substrate usually by altering the confirmation of the enzyme. Negative cooperativity is the reduction of the binding affinity for the substrate, whereas positive cooperativity is an enhanced affinity. The canonical example of positive cooperativity is oxygen binding to hemoglobin, which was the system from which Hill derived his famous formula for cooperativity, $v = \frac{V_{\max}[S]}{K^n + [S]^n}$, where n is nominally the number of binding sites. Though the Hill formula is often used, it is an oversimplified model that does not provide insight into how the ligand binds the enzyme, and therefore is the least useful in determining the binding of effectors to enzymes[215]. The best way to determine cooperativity is to derive velocity formulae from rapid equilibrium schemes in a similar fashion as with the derivation of the Michaelis-Menten equation. Deriving cooperative models from a rapid equilibrium approach is much easier than a steady-state approach, as the complexity increases exponentially with each additional ligand. An example of a multi-ligand reaction scheme is given below.

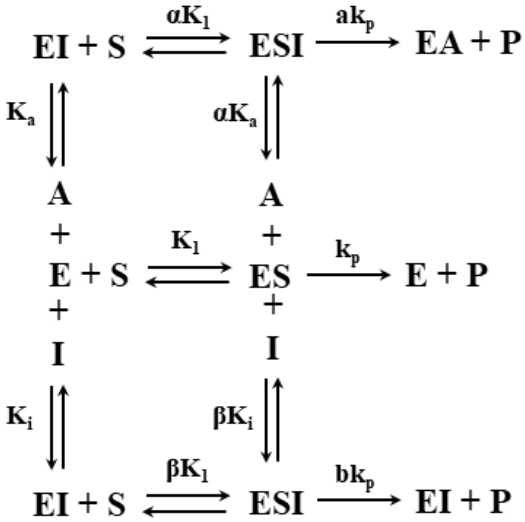

This example includes two effectors, an activator A and an inhibitor I. The cooperative effect that A has on the enzyme is designated as α (binding) and a (metabolism), and for I is defined as β

(binding) and b (metabolism). To derive a formula, we start by writing the rapid-equilibrium equation, which in general is given below.

$$v = k_p ES + \alpha k_p ESA + \beta k_p ESI + \cdots$$

We can then divide by the mass balance equation.

$$\frac{v}{E_t} = \frac{k_p ES + \alpha k_p ESA + \beta k_p ESI + \cdots}{E + ES + EA + EI + ESA + ESI + \cdots}$$

We then need to express all species in terms of E. To do this, we can use a shortcut by considering each species as:

$$\frac{\prod ligands\ in\ the\ complex}{\prod disociation\ contants\ between\ E\ and\ the\ complex}$$

Therefore:

$$\frac{v}{E_t} = \frac{k_p \frac{S}{K_D} + ak_p \frac{S \cdot A}{\alpha K_D K_A} + bk_p \frac{S \cdot I}{\beta K_D K_i} + \cdots}{1 + \frac{S}{K_D} + \frac{A}{K_A} + \frac{I}{K_i} + \frac{S * A}{\alpha K_D K_A} + \frac{S * I}{\beta K_D K_i} + \cdots}$$

Multiplying both sides by E_t will convert all k_p constants into V_{maxima}. There is no *one* equation or reaction scheme that can describe all multi-ligand binding cases. For instance, the activator may only bind ES, or the same ligand may be an inhibitor of the free E but an activator of ES. Three or more ligands may also bind the enzyme, which will complicate the models greatly. How the cooperative effect manifests is also highly dependent on each individual case. The effector can cause a conformational change to induce the effect, or the effector may directly interact with the ligand to promote or inhibit the binding of the ligand. Kinetic plots that deviate from hyperbolic models are indications of complicated allostery/cooperativity. Commonly encountered are sigmoidal plots, as is seen with oxygen binding to hemoglobin. Additionally, the appearance of several V_{maxima} is possible. Therefore, deriving a binding model is largely dependent on the situation and cannot be determined by fitting to one equation. Whichever model can best (and by Occam's razor most simply) describe the data is the one to use. Determining multi-ligand binding is easier to accomplish the more the binding constants are dissimilar, usually being fairly apparent when they are different by orders of magnitude. If the binding constants are similar, such as the example below, then the model may still appear to be hyperbolic and therefore will appear to be a

one-site model. Determining multi-ligand kinetics with two similar binding constants will also be convoluted by the inherent experimental error. Often the details needed to determine these very similar binding affinities will be buried the error. In these situations, unless there is evidence to support the existence of another binding site, the simplest model is a one-site model.

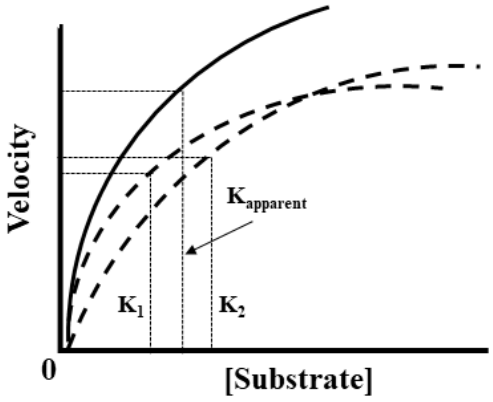

Plot 1.2

Multiple experiments may need to be conducted to determine the multiple binding constants of ligands binding to CYPs, such as substrate metabolism, Soret binding, and NADPH oxidation kinetics[191,216,217]. These data may then be analyzed globally to achieve a complete model of the binding events[217,218]. CYPs have been observed to bind up to 3 or 4 ligands simultaneously depending on the size of the ligands[216-218]. As a result, each ligand can affect the binding of the other ligands either by inducing a conformational change in the CYP or directly influencing the binding of the other ligand(s). For example, progesterone was demonstrated to increase the active site volume of CYP3A4 by almost twofold, which better accommodates the binding of carbamazepine[218]. Combined experimental, NMR, and *in silico* modelling studies demonstrated that carbamazepine directly alters the binding of midazolam in CYP3A4 to change its orientation to the heme and thus the site of metabolism[194]. The modulation of enzyme activity is often specific not only to the enzyme but to the substrate analyte. For example, Effector A may be a positive regulator of Substrate X binding to an enzyme, but may be a negative regulator of Substrate Y binding. In the same system Effector B may not affect Substrate X binding but potentiates Substrate Y. Therefore, the modulation of substrate metabolism by effectors must be considered within their own substrate/effector(s) reference frame and cannot be translated universally. In order to understand how epoxygenase metabolism is altered by effectors, it is important to study the ligands in question directly, for example the modulation of AA metabolism by Drug X.

1.6 Conclusions and thesis aims

The epoxidation of PUFA (epoxy-PUFA) to form epoxides is a recently discovered pathway. This epoxy-PUFA system drives the inflammation and cardiovascular function. There remains a lot to be known regarding how epoxy-PUFA metabolism is regulated in addition to the biological activities of epoxy-PUFAs. Complicated substrate-substrate interactions have been observed for the metabolism of drugs by CYPs. However, the biophysical investigations into substrate-substrate interactions among PUFAs has not been fully investigated. These include PUFA-PUFA interactions, which can provide insight into how endogenous lipids can regulate epoxy-PUFA biosynthesis. Additionally, PUFA-drug interactions can also affect the biosynthesis of epoxy-PUFAs and have implications regarding inflammatory and cardiovascular health with these drugs. The lack of data regarding PUFA metabolism is partly due to the difficulties of investigating membrane proteins and the ephemeral nature of epoxides. Further, the metabolism of PUFAs by CYPs is known to be generally slower than other drugs, meaning there is less signal to measure. PUFAs are also less amenable to quantification by common spectroscopic techniques, which combined with their lower abundance frustrates direct analysis of their metabolism.

Therefore, the aim of this thesis is to provide a biophysical investigation into epoxy-PUFA biosynthesis, with an emphasis on the primary epoxygenase in humans, CYP2J2. Chapter 2 investigates how PUFAs bind to CYP2J2 and how they compete for metabolism. Chapter 3 determines that AA binding to CYP2J2 is altered by doxorubicin, which results in a change in the site of metabolism for AA. Chapter 4 explores phytocannabinoids as substrates of CYP2J2 and determines their inhibition of endocannabinoid metabolism. Finally, Chapter 5 elucidates the recently discovered endovanilloid pathway and the potentiation of endovanilloid metabolism by anandamide through CYP2J2. The kinetics of PUFA-PUFA and PUFA-drug interactions is investigated to provide molecular models. These data may then provide molecular insight into the structure-function relationship of substrate recognition by CYP2J2 and aid in the development of therapeutics exploiting the benefits of epoxy-PUFAs and remediating some of the negative consequences of cardiotoxic drugs.

1.7 Introduction figure

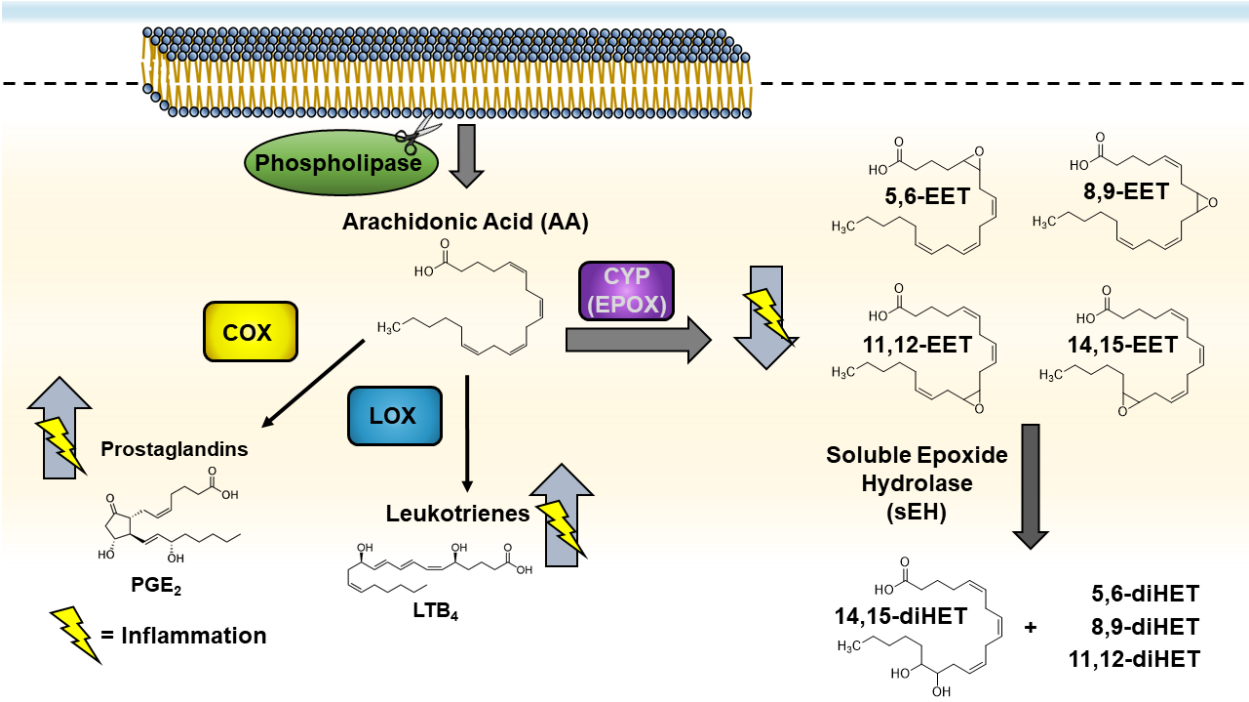

Figure 1.1 *The arachidonic acid cascade*. During an inflammatory response, arachidonic acid (AA) is cleaved from the lipid bilayer by phospholipases. AA can then be transformed by three main pathways: the cyclooxygenase (COX), lipoxygenase (LOX), and cytochrome P450 (CYP) epoxygenase pathways. COX and LOX produce pro-inflammatory prostaglandins and leukotrienes, respectively, at the onset of inflammation. The CYP pathway produces mostly anti-inflammatory epoxyeicosatrienoic acids (EETs). EETs are degraded into dihydroxyeicosatrienoic acids (diHETs) by soluble epoxide hydrolase.

Chapter 2: Structural determinants for PUFAs binding to CYP2J2[1]

2.1 Introduction

The ω-3 and ω-6 polyunsaturated fatty acids (PUFAs) are converted to lipid metabolites by three classes of eicosanoid-synthesizing enzymes: cyclooxygenase (COX), lipoxygenase (LOX), and cytochrome P450 (CYP) epoxygenase. Collectively, these eicosanoids are responsible for producing several physiological responses related to inflammation, and their imbalance has been observed in several diseases and cancer.[1,7,219-225]

CYP epoxygenases belong to the hemoprotein superfamily of CYPs that are primarily involved in xenobiotic metabolism and steroid biosynthesis. The CYP-mediated metabolism of ω-3 and ω-6 PUFAs has gained scientific interest due to their implications in cardiovascular health.[219,226-231] It was demonstrated that dietary ω-3 and ω-6 PUFAs are metabolized by the enzymes in the CYP-epoxygenase pathway into predominantly epoxide metabolites[8,40,42,43,232-234] (Figure 1) that are biologically active and are generally anti-inflammatory. The primary CYP epoxygenase in human cardiomyocytes is CYP2J2.[196] CYP2J2 epoxidizes AA into four anti-inflammatory epoxyeicosatrienoic acids (EETs)[42,196,232] and hydroxylates it into two hydroxyeicosatetraenoic acids (HETEs)[1,44,232] (Figure 2.1).

CYP2J2 has also been shown to epoxidize another ω-6 PUFA, linoleic acid (LA), into two epoxyoctadecenoic acids (EpOMEs).[235] It also metabolizes the ω-3 PUFA eicosapentaenoic acid (EPA) into epoxyeicosatetraenoic acids (EEQs) and hydroxyeicosapentaenoic acids (HEPEs).[17, 26] Additionally, it metabolizes the ω-3 PUFA docosahexaenoic acid (DHA) into epoxydocosapentaenoic acids (EDPs) and hydroxydocosahexaenoic acids (HDHEs).[232,236] The ω-3 epoxide metabolites have been shown to elicit more potent anti-inflammatory and cardioprotective responses as compared to their AA-derived counterparts, EETs.[40,237,238]

It is important to study how these different PUFAs compete for metabolism by eicosanoid-synthesizing enzymes. For instance, the metabolism of ω-6 PUFAs by COX and LOX is often inhibited by the presence of ω-3 PUFAs,[23,24,239] owing to the structural similarity of these two

[1] This work has been published as: Arnold, W. R.; Baylon, J. L.; Tajkhorshid, E.; and Das, Aditi. "Asymmetric binding and metabolism of polyunsaturated fatty acids (PUFAs) by CYP2J2 epoxygenase," Biochemistry, 2016 (55) 6969−6980. The work is allowed to be republished under the Creative Commons Attribution license (https://creativecommons.org/licenses/by/4.0/)

classes of PUFAs.[22,240] However, the biochemistry of CYP-epoxygenase interactions with both ω-3 and ω-6 PUFAs remains largely unknown. CYPs generally possess a large and promiscuous active site leading to drug-drug interactions.[69,191,241,242] Therefore, it becomes imperative to establish the complex kinetics of PUFA-PUFA interactions at the CYP2J2 active site.

Herein we have performed detailed kinetic analyses to determine the effect various PUFAs have on AA metabolism by CYP2J2. We use the Nanodisc (ND) system to stabilize CYP2J2 and its redox partner cytochrome P450 reductase (CPR).[243] Nanodiscs are nanoscale lipid bilayers that have been used extensively to stabilize various types of membrane proteins in aqueous solutions.[244-250] Using CYP2J2-NDs, we first determined the metabolism of AA in the presence of DHA, LA, and EPA. We find that these PUFAs competitively inhibit each other with different potencies. Using competitive binding and inhibition studies, we determined that the binding affinities of these PUFAs to the active site of CYP2J2 are different from each other. Notably, it was found that DHA binds the tightest compared to AA, LA, or EPA. Furthermore, we utilize a combined approach of molecular dynamic (MD) simulations and molecular docking to predict key residues that mediate the binding of the PUFAs to the active site of CYP2J2.[251-253] The studies revealed three key residues in the CYP2J2 active site that govern the binding strength of these PUFAs. Our mutational analyses confirmed the importance of these residues in directing the binding of these PUFA to the active site of CYP2J2. Taken together, our studies show that the binding and metabolism of PUFAs by CYP2J2 is asymmetric due to differential binding affinities of the PUFAs, despite their strong structural similarity to each other.

2.2 Experimental Procedures

Materials. Human CYP2J2 cDNA was obtained from OriGene (Catalog No. SC321730) and modified as published before.[250] Ampicillin, arabinose, chloramphenicol, isopropyl β-D-1-thiogalactopyranoside (IPTG), and Ni-NTA resin were obtained from Gold Biotechnology. δ-aminolevulinic acid was obtained from Frontier Scientific. NADPH and $NADP^+$ were obtained from P212121.com. 1-palmitoyl-2-oleoyl-sn-glycero-3-phosphocholine (POPC) and 1-hexadecanoyl-2-(9Z-octadecenoyl)-sn-glycero-3-phospho-L serine (POPS) were purchased from Avanti Polar Lipids, Inc. EPA; DHA; AA; 9,10-EpOMe; 12,13-EpOME; 14,15-EEQ; 17,18-EEQ; 16,17-EDP; and 19,20-EDP were obtained from Cayman Chemical. Restriction enzymes and

molecular biology materials were purchased from New England Biolabs. All other materials and reagents used were purchased from Sigma-Aldrich and Fisher Scientific.

Recombinant expression of CYP102A1 (BM3) in E. coli. The plasmid for expressing BM3 was a generous gift from Dr. Stephen G. Sligar. It was transformed into BL21 Gold cells and the expression of the protein was executed using a published protocol.[254] Cells were flash frozen and stored at -80^{o}C for less than a month.

Expression and purification of recombinant CYP2J2 in E. coli. Recombinant D34-CYP2J2 containing a His_5 tag was expressed and purified as previously performed.[243,250] The D34-CYP2J2 is a 34-residue N-terminal truncation (residues 3-37) of CYP2J2 with a substitution of Leu2 for an Ala residue. These modifications have been previously shown to increase protein yield without affecting activity.[38, 45] CYP2J2-T318V and CYP2J2-T318V/S493A mutant variants of the D34-CYP2J2 construct were expressed and purified using the same WT protocol. WT and mutants were characterized using a previously published CO-binding assay[245,246,250,255] based on a modified version of Omura and Sato's method.[256]

Expression and purification of cytochrome P450 reductase. Expression of cytochrome P450 reductase (CPR) was performed as described previously.[250]

CYP2J2-T318V and T318V/S493A-double-mutant mutagenesis. CYP2J2 mutant variants CYP2J2-T318V (T318V) and a T318V/S493A double variant (Double) were generated using overlap-extension PCR. Residue numbers refer to the WT sequence. Mutagenesis primers also contained silent mutations to introduce restriction enzyme sites for screening purposes (Supplementary Table 2.3). For T318V an *AleI* site was introduced and for S493A a *BsiEI* site.

Incorporation of CYP2J2 into Nanodiscs. Nanodiscs containing CYP2J2 and CYP2J2 mutants were prepared as previously described.[250] MSP1E3D1 and a 20:80 POPS:POPC lipid composition were used for making the Nanodiscs.

CYP102A1 (BM3) NADPH kinetics. The rate of NADPH consumption by BM3 in the presence of AA or EPA was determined using UV-Vis spectroscopy as previously described.[257] Briefly, 0.01 μM BM3 was incubated for 1 min in 50 mM MOPS buffer with 100 μM of AA or EPA (5 mM in ethanol stocks). 200 μM of NADPH was added to initiate the reaction. Rates of NADPH consumption were determined by measuring the decrease in the NADPH absorption at 340 nm.

CYP2J2-ND ebastine (EBS) kinetics. CYP2J2 metabolism of ebastine (EBS)[258] was studied as previously mentioned with a modified LC-MS/MS technique as described below.[250] The rates of ebastine hydroxylation were fitted to the Michaelis-Menten equation and agree with previously published data.[258] All fittings were done using OriginPro 9.1 (Origin Labs Inc., Northhampton, MA).

CYP2J2-ND and BM3 PUFA metabolisms. PUFA metabolism incubations were conducted using the following procedure. PUFAs (5-100 μM from a 5 mM stock in ethanol) were solubilized in a 0.1 M KPi buffer for 30 minutes at 37ºC. 0.2 μM CYP2J2-ND and 0.6 μM CPR were added in a separate 0.1 M KPi mixture and allowed to incubate at 37ºC for 10 min. The PUFAs and protein were mixed and were further incubated for additional 10 min. The reaction was initiated with the addition of 0.5 mM NADPH and allowed to proceed at 37ºC for 30 minutes based upon our linearity measurements (reaction is linear up to 35 min). The reaction was terminated with the addition of 100 μL of glacial acetic acid (pH<4) and the metabolites were extracted thrice with equivolume ethyl acetate. The organic layer was dried under a flow of N_2 gas and then reconstituted in ethanol for LC-MS/MS analysis. All single kinetic studies were fitted to the Michaelis-Menten equation using OriginPro 9.1. A standard of 14,15-EET was used to determine the extraction efficiency by treating 14,15-EET to the same conditions. The extraction efficiency was determined to be ~70-80%.

Reactions with BM3 were performed similarly, but with the following modifications. AA or EPA was solubilized for 30 min at 30º C in 50 mM MOPS buffer before adding 0.01 μM BM3 for 1 min. The reaction was started using 0.5 mM NADPH, and terminated with acetic acid (pH<4) after 30 s. AA and EPA metabolites were extracted and analyzed as described above.

Co-kinetic assays measuring the products of AA with DHA, LA, or EPA metabolism by CYP2J2 were performed similarly. 15 μM and 50 μM of DHA, LA, or EPA were concurrently solubilized in separate mixtures alongside AA. CYP2J2 and CPR were added to the DHA, LA, or EPA mixtures and allowed to incubate for 10 min before the AA and PUFA/protein mixtures were combined and incubated for an additional 10 min. The rest of the reaction and extraction procedure was followed as stated above. The metabolites of AA and DHA, LA, or EPA (terminal two epoxides) were simultaneously measured using the methods described below. Mixed-substrate kinetic data fit to a competitive inhibition model (Equation 2.1) using OriginPro 9.1.

Liquid chromatography- tandem mass spectrometry for quantitation of fatty acid metabolites. Analyses were performed at the Metabolomics Lab of Roy J. Carver Biotechnology Center, University of Illinois at Urbana-Champaign, as previously described.[245,246] Metabolites were separated using mobile phase A (0.1% formic acid in water) and mobile phase B (0.1% formic acid in acetonitrile) at a flow rate was 0.4 mL/min. The linear gradient was as follows: 0-2min, 90%A; 8min, 55%A; 13-25min, 40%A; 30min, 30%A; 35min, 25%A; 40min, 20%A; 45-47min, 15%A; 48-54min, 90%A. The autosampler was set at 5°C. The injection volume was 10 µL. Negative mass spectra were acquired with the ion spray voltage of -4500 V under electrospray ionization (ESI). The source temperature was 450 °C. The curtain gas, ion source gas 1, and ion source gas 2 were 32 psi, 50 psi, and 55 psi, respectively. Multiple reaction monitoring (MRM) was used for quantitation: : 5,6-EET m/z 319.2 → m/z 191.0; 8,9-EET m/z 319.2 → m/z 155.1; 11,12-EET m/z 319.2 → m/z 167.0; 14,15-EET m/z 319.2 → m/z 219.1; 17,18-EEQ m/z 317.0 → m/z 299.0; 14,15-EEQ m/z 317.0 → m/z 207.0; 12,13-EpOME m/z 295.0 → m/z 195.0; 9,10-EpOME m/z 295.0 → m/z 277.0; 16,17-EDP m/z 343.0 → m/z 274.0; 19,20-EDP m/z 343.0 → m/z 299.0. Four methods were developed to analyze the different combinations of metabolites. 1.) EETs and HETEs alone were quantified using 16,17-EDP (m/z 343.0.0 → m/z 274.0) as the Internal standard. 2.) EETS, HETEs, and EEQs were quantified using 16,17-EDP as the internal standard. 3.) EETs, HETEs, and EDPs were quantified using 17,18-EEQ (m/z 317.0.0 → m/z 299.0) as the Internal standard. 4.) EETs, HETEs, and EpOMEs were quantified using 17,18-EEQ as the internal standard.

Liquid chromatography- tandem mass spectrometry for quantitation of ebastine (EBS) metabolites. Metabolites were separated using mobile phase A (0.1% formic acid in water) and mobile phase B (0.1% formic acid in acetonitrile). The flow rate was 0.4 mL/min. The linear gradient was as follows: 0-2 min, 90% A; 8 min, 55% A; 13-25 min, 40% A; 30 min, 30% A; 35 min, 25% A; 40 min, 20% A; 45-47min, 15%A; 48-54min, 90%A. The autosampler was set at 15ºC. The injection volume was 1 µL. Mass spectra were acquired under positive electrospray ionization (ESI) with ion spray voltage at 5500 V. The source temperature was 450 ºC. The curtain gas, ion source gas 1, and ion source gas 2 were 32, 50, and 65 psi, respectively. Multiple reaction monitoring (MRM) was used for quantitation: Ebastine m/z 470.4 → m/z 302.3; Hydroxyebastine m/z 486.4 → m/z 318.3; internal standard terfenadine m/z 472.4 → m/z 262.1.

Ebastine competitive binding. Ebastine binding near the heme was determined via monitoring the Soret shift from ~420 nm to ~390 nm. Absorbance spectra were taken using a Cary Bio 300 UV-Vis spectrophotometer (Agilent Technologies, Santa Clara, CA). Substrates were dissolved in DMSO as 10 mM, 1 mM, and 0.1 mM stocks, as DMSO had been previously shown to not affect the CYP2J2 heme absorption.[40, 41] Titrated volumes remained < 2.5% the initial volume. 3 μM of CYP2J2 was incubated at 37°C during the experiments and titrations were incubated for 5 min before taking the spectra. Concentrations of ebastine ranged from 0 to 155 μM in the presence or absence of 30 μM of AA, DHA, EPA, or LA pre-incubated with CYP2J2. The data was processed using Matlab R2014a (MathWorks Inc., Natick MA) by subtracting the titration spectra from the substrate-free spectrum. Difference spectra in the mixed systems were determined by subtracting the PUFA-bound spectrum from each ebastine spectrum. Ebastine binding was fitted to the Michaelis-Menten equation and the binding affinity of each PUFA inhibition was determined via the competitive binding equation (Equation 2.1) using OriginPro 9.1.

Competitive inhibition equation used in studies. All inhibition studies are best described by a competitive inhibition model (Equation 2.1)

$$B = \frac{B_{max}[S]}{K\left(1+\frac{[I]}{K_i}\right)+[S]} \quad \text{(Equation 2.1)}$$

where B_{max} and K are the Michaelis-Menten kinetic parameters of the substrate $[S]$ without inhibitor, $[I]$ is the concentration of inhibitor, and K_i is the inhibition constant. For kinetic experiments, B and K represent velocity and K_m, respectively; for Soret binding experiments, B and K represent ΔA and K_D, respectively.

MD simulations of AA, EPA, and DHA binding to CYP2J2. Molecular docking of AA, DHA and EPA using AutoDock Vina,[259] was employed to probe its binding to CYP2J2. We employed our previously obtained 100 ns MD simulation of POPC membrane-bound CYP2J2[245] to include a large number of snapshots in the docking. This allows taking into the account the dynamics of the protein in the presence of the membrane and probing putative binding sites that are only transiently present during the simulation. Snapshots of membrane-bound CYP2J2 were taken from the MD trajectory at 100 ps intervals, resulting in 1000 different snapshots used for AA, EPA and DHA docking. A grid box with dimensions 22.5 Å in the *x*, *y* and *z* directions and with center in the

active site of CYP2J2 was employed. For each ligand (AA, EPA or DHA), the top 10 docking poses for each snapshot were collected for further analysis, resulting in 10000 docked poses for each fatty acid. The resulting docked structures were then clustered by RMSD of the heavy atoms, with a maximal value distance between two poses of 4.0 Å. This approach identified four main conformations of the fatty acids in the active site (Figure 2.4). For each cluster, further filtering was performed on the basis of the distance of the carbons involved in the in the formation of the major epoxide experimentally observed (i.e., carbons 14,15 in AA; 17,18 in EPA and 19,20 in DHA) and the heme iron, with a cutoff distance of 6 Å, as well as docking score. For each cluster, the docked pose within the cutoff distance with the best docking score was selected as the initial structure for simulations, resulting in four initial conformations for each ligand (Figure 2.5). The resulting membrane-bound protein-ligand systems were minimized for 1000 steps and equilibrated for 100 ps while the heavy atoms of the protein backbone and the ligand were harmonically restrained ($k = 1$ kcal mol^{-1} Å^{-2}), then followed by unrestrained, production simulations for 100 ns for clusters 1,2 and 3, and 200 ns for cluster 4 for each fatty acid.

Simulation protocol. MD simulations were performed using NAMD2,[260] with the CHARMM36 force field for protein[261] and lipids.[262] Parameters for AA, EPA and DHA were obtained by analogy from the CHARMM General Force Field,[263] employing DHA force field parameters previously derived.[264] The TIP3P model was used for water.[265] Simulations were performed as an NPT ensemble at 1.0 atm and 310 K, with a time step of 2 fs. Constant pressure was maintained using the Nose–́ Hoover Langevin piston method.[266] Constant temperature was maintained by Langevin dynamics with a damping coefficient of 0.5 ps^{-1} applied to all atoms.[267] Nonbonded interactions were cut off after 12 Å with a smoothing function applied after 10 Å. Bond distances involving hydrogen atoms were constrained using the SHAKE algorithm.[268] The particle mesh Ewald (PME) method was used for long-range electrostatic calculations with a grid density of >1 Å^{-3}.[269]

Simulation analysis. To identify key CYP2J2 residues interacting with the fatty acids (AA, EPA or DHA), interaction energies were calculated for each simulation employing a generalized implicit solvation approach.[270]

2.3 Results

CYP2J2 epoxygenase was expressed in *E. coli* as described before[243,250] and was assembled into the nanoscale lipid bilayers of nanodiscs (NDs).[244-247,250] All the studies reported here are done with the CYP2J2-ND-CPR system (Figure 2.1).

Initial characterizations of PUFA metabolism analysis and CYP2J2 activity. We characterized the CYP102A1- (BM3)-mediated metabolism of AA and EPA to confirm the accuracy of our PUFA metabolism measurements. BM3 is a bacterial CYP that is known to metabolize AA and EPA with high turnover rates.[254,257,271] Firstly, NADPH consumption rates as BM3 metabolizes AA and EPA were determined. We measured the k_{cat} of NADPH consumption to be 7.12 $\pm$ 0.05 μmol/min/nmol$_{BM3}$ for AA and 5.49 $\pm$ 0.18 μmol/min/nmol$_{BM3}$ for EPA. These values agree with previous measurements.[257,271] Subsequently, we measured the rate of 14,15-EET formation from AA and 17,18-EEQ formation from EPA. The rate of formation of 14,15-EET was determined to be 1.10 $\pm$ 0.21 μmol/min/nmol$_{BM3}$, and for 17,18-EEQ to be 2.57 $\pm$ 0.09 μmol/min/nmol$_{BM3}$, which correlates well to previous data.[257,271]

We then demonstrated functional CYP2J2 by measuring ebastine (EBS) metabolism kinetics (Figure 2.2A) (Table 2.1) and compared the results to previously published data.[250,258] The results agree with previously reported data for CYP2J2-mediated EBS metabolism.[258]

Metabolism of AA, DHA, EPA and LA by CYP2J2-ND-CPR. DHA, EPA, and LA have been previously shown to be metabolized by CYP2J2 [232,235,236]. We developed quantitative LC-MS/MS methods to monitor the terminal two epoxides (the major metabolites) of these PUFAs (Figure 2.1). These metabolites correspond to 16,17- and 19,20-EDPs; 14,15- and 17,18-EEQs; and 9,10- and 12,13-EpOMEs for DHA, EPA, and LA, respectively. CYP2J2-ND-CPR were incubated with AA, DHA, EPA and LA separately. The rate of formation of the products is reported as a function of substrate concentration (Figure 2.2B-E) and is described by Michaelis-Menten kinetics (Table 2.1) with a constant ratio of metabolites. Due to the inherent insolubility of these substrates, these studies were performed below the critical micelle concentration (CMC) of each lipid substrate.

AA and LA have kinetic properties that are most similar to each other and therefore display similar catalytic efficiencies. The kinetic parameter values of DHA and EPA are most similar and have more similar catalytic efficiencies. As the soluble range of the PUFAs remained below the

calculated K_m for each, in order to corroborate the calculated catalytic efficiencies from these steady-state experiments, an estimate of the catalytic efficiency was obtained from the linear time measurements and fitting the data to Equation 2.2

$$[S] = [S_0]e^{-kt} \quad \text{(Equation 2.2)}$$

where $[S_0]$ is the initial concentration of the substrate and $k = \frac{k_{cat}}{K_m}[E]$.[272] Analyzing the time-based kinetics data of the PUFA metabolism, we were able to obtain values for the catalytic efficiencies of theses PUFAs (Supplementary Table 2.1) that agree well with the catalytic efficiencies determined from our steady-state experiments (Table 2.1).

Co-substrate metabolism kinetics of AA in the presence of DHA, EPA, and LA by CYP2J2-ND-CPR. In order to determine PUFA-PUFA interactions, mixed-substrate kinetics were performed where the metabolism of AA was measured in the presence of low concentrations (15 μM) and high concentrations (50 μM) of DHA, LA, or EPA. In order to accomplish this, dual LC-MS/MS methods were developed for the concurrent analysis of the AA and the DHA, LA, or EPA metabolites within the same samples. Three different methods were developed to analyze the different combinations of metabolites. (1) An EPA epoxide method [EETS, HETEs, and EEQs]. (2) A DHA epoxide method [EETs, HETEs, and EDPs]. (3) An LA epoxide method [EETs, HETEs, and EpOMEs]. Experiments were conducted with the total fatty acid concentrations kept below CMC in order to avoid co-micellar formation between the PUFAs.

Co-metabolism of the PUFAs is best described using a competitive inhibition model (Equation 2.1, Table 2.2). The inhibition constant is given as $K_i^{Inhib \rightarrow Sub}$ in order to identify the inhibitor and substrate for each analysis. Treating AA as a substrate in the analysis reveals that DHA has the strongest inhibition of AA metabolism (Figure 2.3), with a $K_i^{DHA \rightarrow AA}$ of 16.5 $\pm$ 2.2 μM (Table 2.2). This is about four-fold stronger than the inhibition of DHA metabolism by AA ($K_i^{AA \rightarrow DHA}$ = 65.2 $\pm$ 15.8 μM). In comparison, LA and AA inhibit each other with similar potencies (Supplementary Figure 2.1), with a $K_i^{LA \rightarrow AA}$ value that is similar to the value of $K_i^{AA \rightarrow LA}$ (Table 2.2). Inhibition between AA and EPA (Supplementary Figure 2.2) was the weakest and can be considered negligible. This may be due to the fact that out of all these pairings, these two substrates are the most similar structurally. To determine the mechanism behind these asymmetric inhibition strengths, we next sought to determine how these substrates bind to CYP2J2.

Spectral competitive binding studies of CYP2J2 with DHA, EPA, AA and LA to determine the origin of inhibition. Substrate binding to CYPs displaces a water molecule from the iron of the heme, producing a high-spin iron that concomitantly shifts the UV-Vis absorbance from ~417 nm to ~390 nm. The magnitude of this change is then used to determine substrate binding to CYPs, and the spin-state equilibrium constant, K_S, is taken to approximate K_D. We performed binding studies using UV-Vis spectral titrations of the PUFAs directly; however due to weak spin-state shift, an accurate binding constant could not be determined (Supplementary Figure 2.3). Therefore, we determined the relative binding of the PUFAs by measuring their inhibition of EBS binding. EBS binds to CYP2J2 and produces ~90% spin-state shift, which is at least an order of magnitude greater spectral change as compared to the binding of PUFAs.[246,250] The binding of EBS (Supplementary Figure 2.4) can be described by a Michaelis-Menten binding model with values for A_{max} and K_S of 0.218 ± 0.007 and 8.16 ± 0.29 μM, respectively. These titrations were then repeated by incubating the CYP2J2-ND system with 30 μM of each fatty acid substrate followed by titrations with EBS. At this concentration all PUFAs were soluble, bound tight enough to produce a measurable inhibition of EBS binding, and produced a relatively insignificant spin-state change compared to EBS.

The PUFA data were fitted to competitive binding equation (Equation 2.1) and the values are tabulated in Table 2.3. DHA had a K_i that is 53.4% ($p = 0.01$) the value of AA, which shows that DHA binds about two-fold more tightly to CYP2J2. For LA, the value of K_i was 160% the value for AA, but due to error is not significant. For EPA, the value was 168% ($p = 0.01$) of AA, signifying that EPA binds significantly weaker compared to AA. These data indicate that, similar to the metabolism data, DHA binds and inhibits CYP2J2 more strongly than AA. In comparison, LA binds similarly as AA and EPA binds weaker.

Molecular Dynamic Simulations of PUFA Binding to CYP2J2. To understand the atomistic details of fatty acid binding to CYP2J2, we employed a combined approach of molecular docking and MD simulations, as described in Experimental Procedures. We used the same CYP2J2 model that we had previously used to successfully predict key residues within the F-G loop that mediate CYP2J2 binding to the membrane.[245] Since the bound form of the fatty acids is not known, we employed different initial conformations of AA, EPA, and DHA in the active site of CYP2J2 in POPC membranes, obtained from molecular docking, as initial seeds to perform MD simulations.

The initial conformations were selected from four identified clusters of conformations of docked poses resulting from ensemble molecular docking (Figure 2.4). For each cluster, a starting conformation was selected based on the minimum distance of the carbons involved in the formation of the major epoxidation product as shown in Figure 2.1 (carbons 14,15 in AA; 17,18 in EPA and 19,20 in DHA) to the heme and the best docking score.

Cluster analysis of the resulting docking poses revealed that AA, EPA, and DHA similarly adopt two major orientations in the active site of CYP2J2 (Figure 2.4A). The main difference between the two orientations is the location of the fatty acid carboxyl group within the active site. For clusters 1, 2, and 3, the fatty acids are extended along the active site cavity and the carboxyl group is pointing towards the F-G loop of the protein, formed by residues 224 to 240. In the simulations that started from these positions, the fatty acids adopt similar conformations, maintaining their overall orientation during the simulations. In contrast, in cluster 4 the carboxyl group is located close to helix I, composed of residues 297 to 330 (Figure 2.4A), adopting a significantly different orientation and position compared to the three other clusters during simulation.

For DHA and EPA, the MD simulations showed that the alkene moieties of the fatty acid are close to heme for all starting conformations (i.e., carbon-to-heme distance < 6Å in Figure 2.4B and Supplementary Figure 2.4), suggesting that either of the simulated orientations could lead to formation of metabolites shown in Figure 2.1. For AA, the carbon-to-heme distance distributions show an increase of about 4 Å compared to DHA and EPA, suggesting that this fatty acid is less restrained in active site than the other two. CYP2J2-substrate interaction energies revealed that fatty acids are stabilized mostly by establishing contacts with residues located in the active site of CYP2J2, mainly Ile-127, Phe-310, and Ile-489 (Figure 2.4A). In addition to these contacts, some important electrostatic interactions were identified for cluster 4.

DHA binding is stabilized by helix I interactions. For the three tested fatty acids, the conformation adopted in cluster 4 (Figure 2.4A) positions the carboxyl group close to Arg-321 located in helix I. Simulations revealed that fatty acids establish favorable interactions with the Arg-321 side-chain (Figure 2.5), and these interactions in turn facilitate formation of additional electrostatic interactions. AA, DHA, and EPA can transiently form hydrogen bonds with Thr-318 and Ser-493. As shown in Figure 2.4B, these interactions facilitate the accommodation of the

epoxidation sites close to the heme (with a carbon-to-heme distance < 6 Å) for DHA and EPA, and < 8 Å for AA. Of the three fatty acids, DHA showed the highest degree of interactions during the simulations, suggesting a tighter binding mode when compared to AA or EPA for this particular orientation of the fatty acid in the active site (Figure 2.5B). An additional transient interaction can be also formed with Arg-484 (Supplementary Figure 2.5A), located in the vicinity of the other three side-chains; however when this interaction dominates, the distance of the epoxidation sites to the heme is significantly increased (> 10 Å), as observed for EPA after 150 ns of simulation (Supplementary Figure 2.5B).

Characterizations of CYP2J2-T318V (T318V) and CYP2J2-T318V/S493A (Double) mutations. In order to verify the significance of residues Thr-318 and Ser-493 in mediating DHA binding, we made a single mutant (T318V) and a T318V/S493A double mutant (Double) of CYP2J2. These mutations are expected to disrupt the preferable interactions of DHA with the hydroxyl groups of Thr-318 and Ser-493. We did CO-binding measurements to confirm that these mutants were properly folded (Supplementary Figure 2.6).

We determined the binding affinity of AA and DHA binding to these mutants using the EBS competitive binding assay (Table 2.4). The K_S of EBS binding to these mutants decreases as compared to the WT. Contrariwise, AA and DHA show weaker binding to T318V mutant and to the double mutant compared to WT as assessed by their K_i values. However, whereas the value of K_i for DHA is ~ 50% that of the value for AA with the WT or T318V variants, for the Double variant it is ~80% of AA (Table 2.4). This demonstrates that when the Thr-318 and Ser-493 residues are mutated to Val and Ala, DHA binds to CYP2J2 with a similar affinity as AA. This suggests that these residues are important in selectively directing the tighter binding of DHA to the active site of CYP2J2.

We next determined if the weaker binding of DHA to CYP2J2 active site will result in a weaker inhibition of AA metabolism by CYP2J2. The metabolism of AA in the presence of an equal amount of DHA for the mutants showed poor inhibition (95.6% for T318V and 88.6% for Double) as compared to the inhibition of AA by DHA that was observed for the WT (31%) (Table 2.4). Likewise, the presence of AA has only a minor effect on the DHA metabolism by the CYP2J2 mutants (Supplementary Table 2.2). Therefore, these binding and metabolism studies with the

mutants indicate that the residues Thr-318V and Ser-493A are important in directing the selective inhibition of CYP2J2 mediated AA metabolism by DHA.

2.4 Discussion

The enzyme pathways involved in PUFA metabolism are complex due to the multitude of PUFAs present in the cell. Herein, we report kinetic and thermodynamic analyses of the metabolism of PUFAs by the major cardiac enzyme, CYP2J2. *Ab initio*, we accurately measure the metabolism of AA and EPA by BM3, which confirms our accuracy in measuring the PUFA kinetics using LC-MS/MS. We next confirm the viability of the CYP2J2-ND-CPR system by measuring the metabolism of EBS that shows similar kinetics as previously reported.[250,258]

Sequentially, we further describe what happens to the rate of AA metabolism in the presence of other dietary lipids that are commonly present in the cardiovascular system, i.e. LA, EPA, and DHA. We perform global metabolism inhibition analyses at varying concentrations of AA and DHA that reveal a value of $K_i^{DHA \rightarrow AA}$ that is four-fold smaller than the $K_i^{AA \rightarrow DHA}$. This indicates that DHA is a stronger inhibitor of AA than AA is as an inhibitor of DHA. The EBS competitive binding assay shows that DHA binds almost two-fold more strongly to CYP2J2 than AA. Together, these data indicate that DHA exhibits preferential binding to CYP2J2 as compared to AA and the tighter binding of DHA likely contributes to its inhibitory properties.

LA shows a weaker competitive inhibition of AA metabolism by CYP2J2, i.e. the $K_i^{LA \rightarrow AA}$ is similar to the $K_i^{AA \rightarrow LA}$ value. Furthermore, the EBS binding inhibition reveals similar binding affinities of LA and AA. These data are supported by the fact that these two substrates also have similar values of V_{max} and K_m. Overall, the inhibitions of AA and LA against each other appear to be the result of similar binding and kinetic properties.

EPA and AA inhibition of each other is not significant, showing $K_i^{Inhib \rightarrow Sub}$ values for each other's metabolism that are high. This contradicts previously published data,[232] which looked at a 1:1:1 ratio of AA:DHA:EPA metabolism with CYP2J2. EPA was shown to be preferentially metabolized by CYP2J2, with a four-fold greater metabolite formation. However, the previous experiments were conducted using supersomes, which are a different system compared to the to the homogenous CYP2J2-ND-CPR system. The discrepancies could arise from the different protein and lipid composition of the supersomes. EBS competitive binding shows that EPA binds

with a K_i value that is 168% that of AA. Of all the substrates tested, EPA and AA are the most similar in structure with respect to the length of the carbon chain, different only in one extra double bond in EPA. Taken together, the kinetics and thermodynamics data reveal that DHA inhibits the most strongly compared to AA, LA, or EPA.

In order to understand how these lipid substrates with similar structures can have differential interactions with the active site of CYP2J2, we use MD simulations to investigate key residues that are involved in binding to the PUFAs. It was determined that PUFA binding is mainly governed by hydrophobic interactions with non-polar side chains including Ile-127, Phe-310, and Ile-489, located in the active site. In addition to these contacts, some additional electrostatic interactions appear to stabilize the binding of these PUFAs. We identified that the fatty acids in the binding site adopt two main orientations (Figure 2.4). In the main orientation (cluster 1, 2 and 3), the fatty acids are extended along the cavity connecting the active site and surface of the protein. In the second orientation (cluster 4), the carboxyl head of the molecule is located in the vicinity of Arg-321 of the I-helix. The three PUFAs can interact with Arg-321, but only DHA can form multiple additional electrostatic interactions with Thr-318 and Ser-493 at the same time, as observed in the calculated interaction energies. This can be due to the presence of one additional alkene moiety closer to carboxyl head in DHA (between carbons 4 and 5), not present in either AA or EPA. It has been shown that the polyunsaturation in DHA increases its flexibility, particularly by lowering rotational barriers about methylene bridges.[264] Therefore, DHA has increased flexibility closer to carboxyl group due to the additional double bond, which can facilitate interactions with surrounding residues, such as Thr-318 and Ser-493, in addition to Arg-321. In contrast, AA and EPA are less flexible around their carboxyl head due to the close saturated carbons. The interaction energy for AA and EPA with Arg-321 and Thr-318 in this conformation is similar (Figure 2.5), suggesting a similar binding mode for the two molecules, which can explain why there is no significant difference seen in our inhibition studies and subsequent binding analyses. Contrariwise, DHA binding establishes a key residue triad that could explain why the binding of DHA is stronger than AA or EPA. Interestingly, MD simulations of arachidonic acid binding to CYP2E1 also revealed its own unique triad of interacting residues separate from the triad seen in our simulations of CYP2J2 (His 107, Ala 108, and His 109 of CYP2E1).[252] This shows that the residues mediating fatty acid binding to CYPs may not be necessarily conserved, although it may involve a similar triadic theme. Further, since CYP2E1 mainly forms ω-1 and ω-

2 hydroxylations, this could explain the differences in the preferred metabolism between CYP2J2 and CYP2E1.

In absence of a crystal structure, we have been able to use the homology model used in this study to successfully predict key membrane-interacting residues for CYP2J2.[245] Using homology models in MD simulations may not be as reliable as using crystal structures to predict protein-substrate interactions, which need to be verified experimentally. Therefore, to corroborate the MD data, mutants CYP2J2-T318V (T318V) and CYP2J2 T318V/S493A (Double) were made. Binding of EBS to these mutants was tighter than the WT; however, the binding of AA and DHA (as determined by EBS competitive binding assay) was weaker compared to WT. This demonstrates the importance of these residues in mediating PUFA binding specifically. The order of binding strength for both AA and DHA is WT > T318V > Double. However, the binding affinity of DHA with the Double mutant is more similar to AA when compared to WT or T318V. This supports the fact that without the preferential interactions offered by the hydroxyl groups of Thr-318 and Ser-493, AA and DHA bind similarly to the active site of CYP2J2.

Our kinetic data agrees well with kinetic values obtained with similar PUFA systems determined by other researchers. CYP4F11 hydroxylation of PUFAs showed V_{max} values between 1-2 nmol/min/mg and K_m values at ~50 μM; and CYP2C enzymes showed PUFA metabolic rates between 100 and 1000 pmol/min/nmol.[273,274] Further, estimates of the catalytic efficiency based upon linear time measurements corroborates the catalytic efficiencies from our steady-state metabolism experiments. Therefore, we observe that PUFA kinetics with CYP2J2 and similar membrane-bound CYP systems are slow compared to soluble CYPs such as BM3.[232,273,274] It is highly likely that CYP2J2 was evolutionarily selected to metabolize AA and other PUFAs into epoxide metabolites in order to selectively regulate cardiovascular physiology.

Our data also indicates that PUFA metabolism and inhibition by CYP2J2 is governed by the restricted conformation and length of the bound lipid substrate. For instance, EPA and AA showed similar flexibilities and adopt similar conformation when interacting the Arg-321, Thr-318 and Ser-493 triad. DHA, however, is an ω-3 PUFA which two extra carbons in the fatty acid chain length as compared to AA that adopts the conformation to favorably interact with this triad and therefore bind tighter to CYP2J2.

2.5 Figures and tables

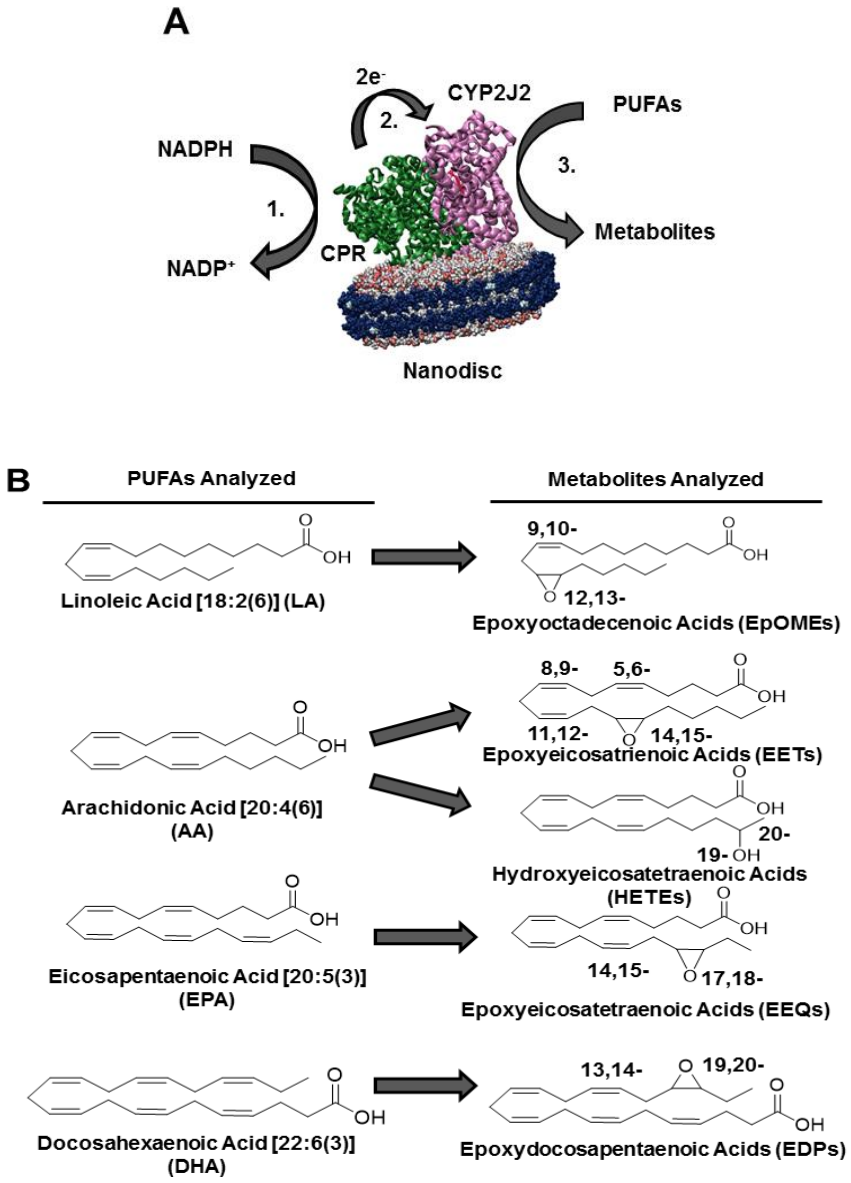

Figure 2.1. (A) Metabolism of arachidonic acid (AA) by CYP2J2. Reaction schematic showing CYP2J2 and its redox partner CPR incorporated into Nanodiscs metabolizing PUFAs into products. Reaction steps are indicated: (1) CPR is reduced by two electrons from NADPH. (2) CPR transfers the electrons to CYP2J2 sequentially. (3) CYP2J2 utilizes the electrons in order to oxidize substrates (AA) into EETs and HETEs. (B) Structures and names of fatty acids used in study. [carbon length : degree of unsaturation (omega 3 or 6)]. Abbreviations given at the end. Metabolite structures and names also given. Numbering refers to the positions of the other regioisomers of epoxides and hydroxides, with the only the major metabolites shown for clarity.

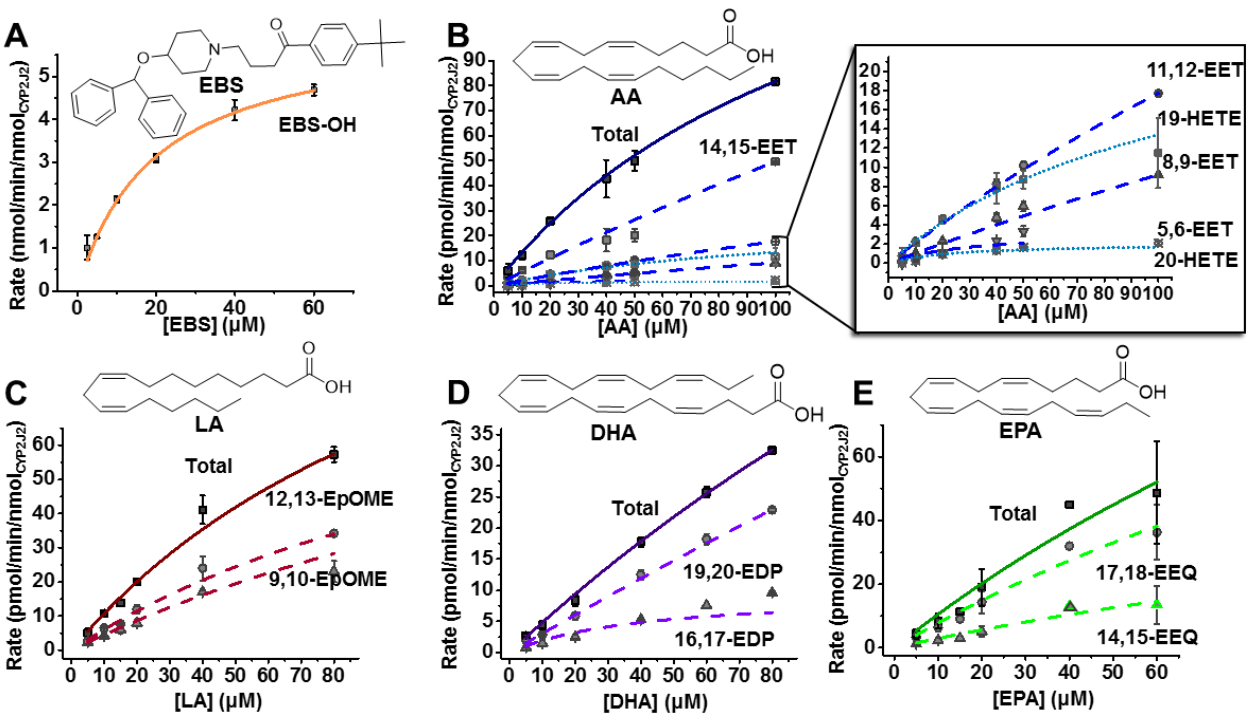

Figure 2.2. CYP2J2-mediated metabolism of (A) ebastine (EBS), (B) arachidonic acid (AA), (C) docosahexaenoic acid (DHA), (D) eicosapentaenoic acid (EPA), and (E) linoleic acid (LA) forming the indicated metabolites. Structures of parent compounds shown. "Total" refers to total metabolites plotted. Total = black, filled squares and solid lines; epoxides = grey shapes and dashed lines; hydroxides = light grey shapes and dotted lines. Data fit to the Michaelis-Menten model for all substrates. Error bars represent ± SEM.

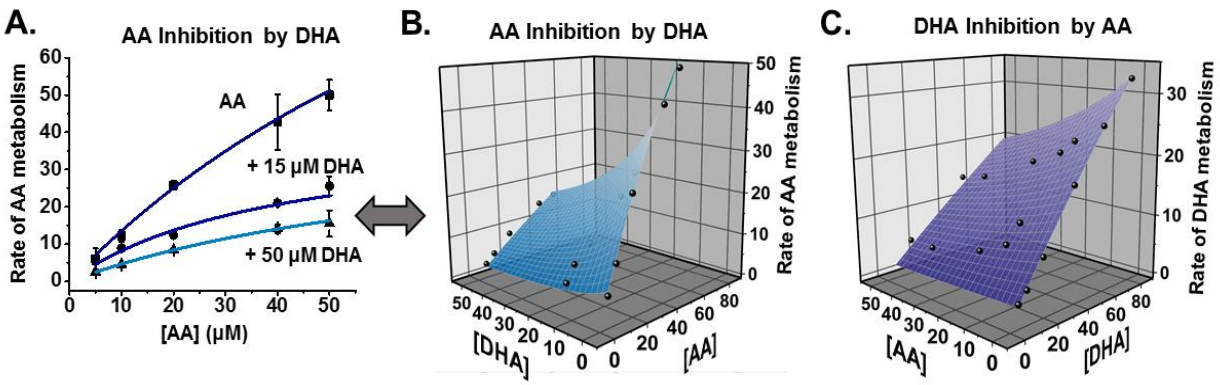

Figure 2.3. AA and DHA mixed kinetics. (A) 2D plot of AA metabolism in the presence of indicated amounts of DHA. (B) 3D plot of AA metabolism in the presence of DHA. Here, DHA is treated as the inhibitor and its effects on AA calculated. (C) 3D plot of DHA metabolism in the presence of AA. Here, AA is treated as the inhibitor in the calculations. Total metabolite formation best fit to a competitive inhibition model. Rates are in units of $pmol_{products}/min/nmol_{CYP2J2}$. Error bars represent $\pm$ SEM.

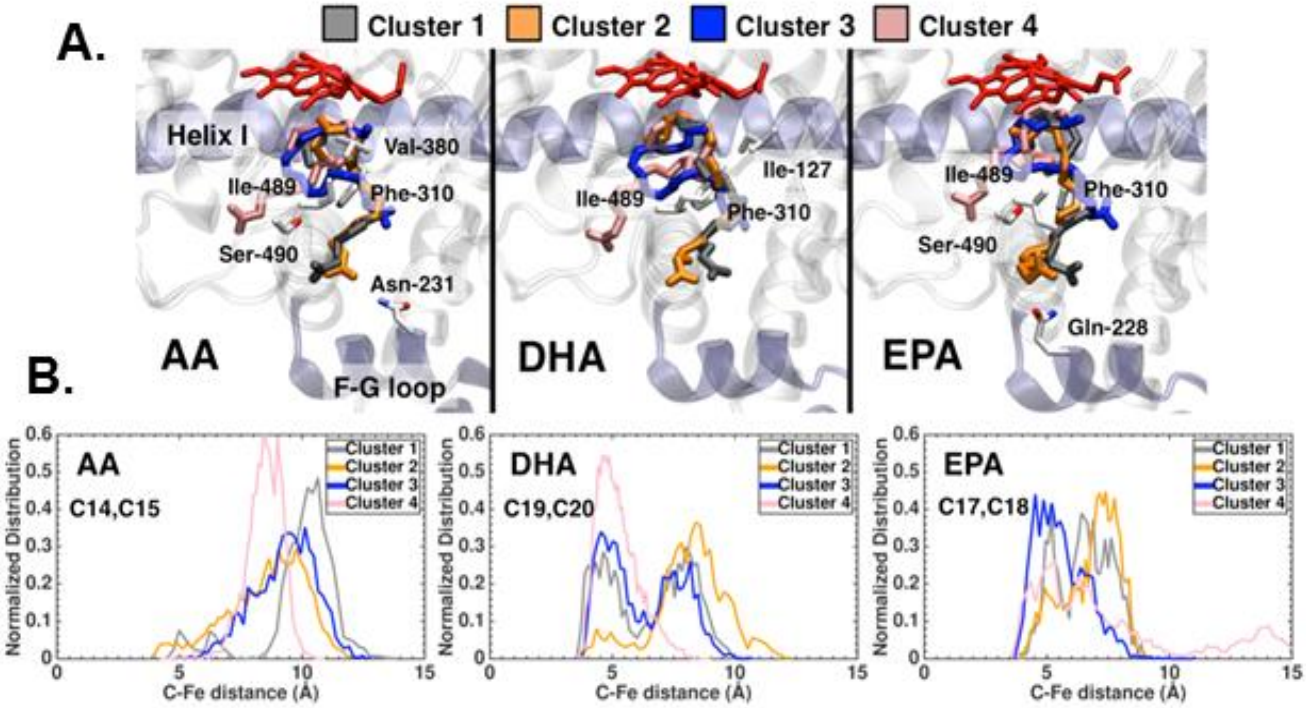

Figure 2.4. Conformation of AA, EPA, and DHA in the active site of CYP2J2. (A) Representative conformations of the four identified clusters identified from molecular docking of AA, DHA, and EPA. These conformations were employed as starting points for subsequent MD simulations. In each case, the ligand and the heme are shown in stick representation. The side-chain of residues interacting with the fatty acid during the simulations are also shown in stick representation. (B) Distribution of distances between epoxidation sites of AA, DHA and EPA to the iron atom of the heme, obtained from MD simulations. For each fatty acid, data were obtained from 100 ns simulations for cluster 1,2 and 3, and 200 ns simulations for cluster 4.

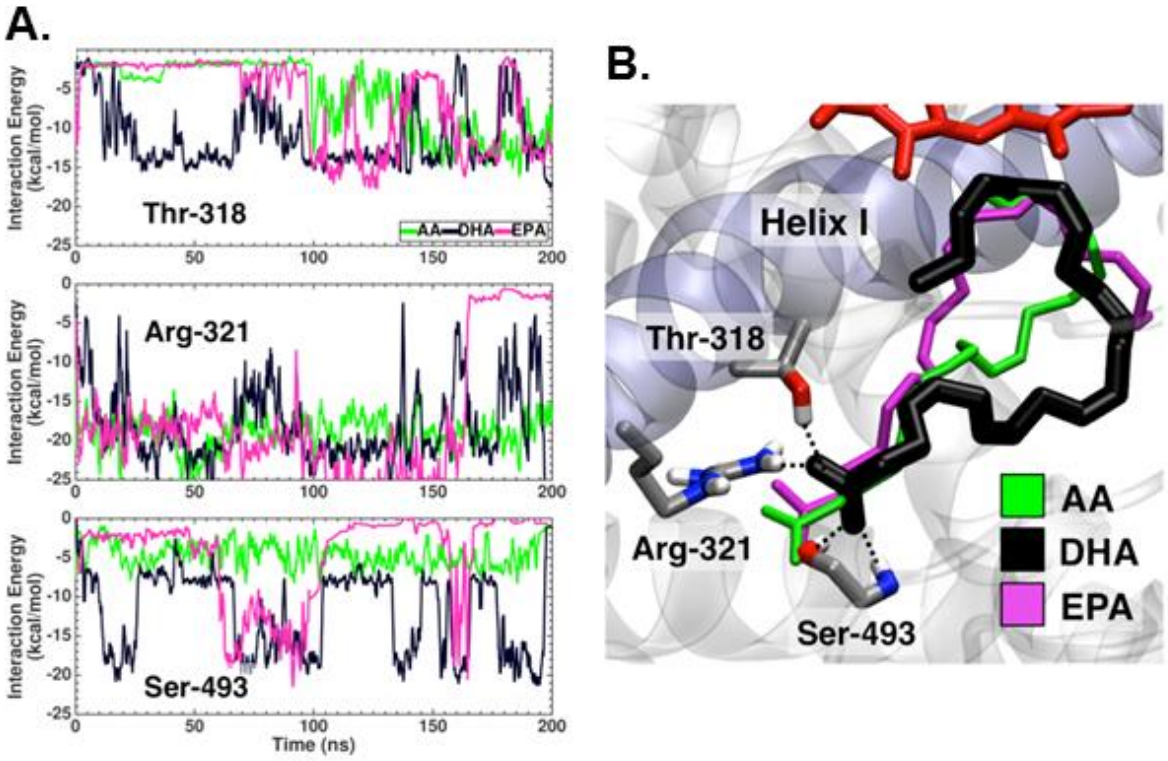

Figure 2.5. Interaction of fatty acids with helix I of CYP2J2. (A) Time series of the interaction energy of AA, DHA, and EPA with residues Thr-318, Arg-321, and Ser-493 (B) Representative conformations of AA, DHA, and EPA in the active site, observed in the simulations. Residues Thr-318 and Arg-321 are located in helix I, shown in cartoon representation with purple color. The fatty acids are shown in stick representation, AA in green, DHA in black, and EPA in magenta. Side chains and heme are also shown in stick representation.

Table 2.1. Kinetic parameters of single-substrate studies. Each substrate fit to the Michaelis-Menten model. Error represents the SEM.

Substrate	V_{max} (pmol/min/nmol)	K_m (μM)	k_{cat}/K_m (min^{-1} nM^{-1})
EBS	6,170 ± 150	19.4 ± 0.8	318
AA	189 ± 9	131 ± 11	1.44
LA	146 ± 17	118 ± 20	1.24
EPA	259 ± 77	251 ± 19	1.03
DHA	254 ± 11	542 ± 34	0.469

Table 2.2. 3D mixed-inhibition fits of AA/DHA, AA/EPA, and AA/LA. Kinetic metabolism measurements of CYP2J2 with AA and either LA, EPA, or DHA were performed at varying concentrations of each substrate. Each analyte was treated as either a substrate or inhibitor for each fit. Data fit best to a competitive inhibition model with a measured inhibition constant $K_i^{Inhib \rightarrow Sub}$. Error represents the error of the fits.

AA as a Substrate

Inhibitor	$K_i^{PUFA \rightarrow AA}$ (μM)
DHA	16.5 ± 2.2
EPA	260 ± 157
LA	46.4 ± 9.9

AA as an Inhibitor

Substrate	$K_i^{AA \rightarrow PUFA}$ (μM)
DHA	65.2 ± 15.8
EPA	∞
LA	78.4 ± 31.9

Table 2.3. Ebastine binding inhibition by FAs. Ebastine inhibition by these FAs was determined by Soret spectral titrations. The data fit best to a competitive model (Equation 2.1) The binding affinity of the inhibitors (PUFAs) are then compared to AA as a percentage of the AA value. Error represents the SEM.

	EBS Competitive Inhibition	
	K_i (μM)	**% K_i (AA)**
AA	66.4 ± 1.8	100%
DHA	35.5 ± 2.4	53.4%
LA	106 ± 26	160%
EPA	111 ± 5	168%

Table 2.4. Effects of CYP2J2-T318V (T318V) and CYP2J2-T318V/S493A (Double) on AA and DHA binding and inhibition. Binding of AA and DHA to T318V and Double were determined by using competitive ebastine (EBS) binding assay. %K_i (AA) compares the K_i of DHA as a percentage of the value of AA for each construct. The inhibition of AA by DHA was also determined for each construct using 50 μM of AA or 50 μM of AA + 50 μM of DHA. Rates are in pmol/min/nmolCYP and the inhibition by DHA (DHA Inhib) is shown as the percent of the AA metabolism rate. Error represents ± SEM.

	EBS competitive binding				AA inhibition		
	EBS	AA	DHA		AA	AA + DHA	DHA Inhib
	K_S (μM)	K_i (μM)	K_i (μM)	% K_i (AA)	Rate (AA)	Rate (AA)	% (AA)
WT	8.16 ± 0.29	66.4 ± 1.8	35.5 ± 2.4	53.4%	50.0 ± 4.1	15.5 ± 3.6	31.0%
T318V	3.72 ± 0.06	115 ± 8	60.5 ± 3.9	52.6%	42.8 ± 1.3	40.9 ± 0.7	95.6%
Double	5.60 ± 0.76	230 ± 126	180 ± 80	78.3%	46.3 ± 1.5	41.0 ± 0.9	88.6%

2.6 Supplementary Information

Methods

Titration binding of PUFAs. Substrate binding near the heme was determined via monitoring the Soret Shift from ~420nm to ~390nm. Absorbance spectra were taken using a Cary Bio 300 UV-Vis spectrophotometer (Agilent Technologies, Santa Clara, CA). Substrates in DMSO were titrated from 0 μM to saturating amounts into 0.1M KPi (pH 7.4) containing 3 μM CYP2J2 in Nanodiscs at 37ºC. Substrates were incubated with protein for 5 minutes before each spectrum was taken. Total volumes of titrated substrates remained <2% of the initial volume. Titrations using the same concentrations of substrates at 37ºC into 0.1 M KPi containing empty Nanodiscs were used as blanks. The data was processed using Matlab R2014a (MathWorks Inc., Natick MA) by subtracting the titration spectra from the substrate-free spectrum.

Figures

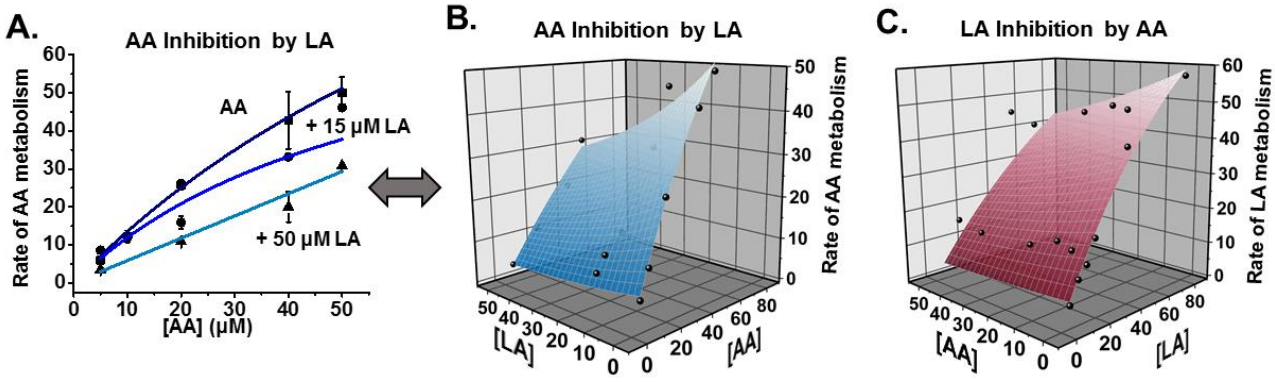

Supplementary Figure 2.1. AA and LA mixed kinetics. (A) 2D plot of AA metabolism in the presence of indicated amounts of LA. (B) 3D plot of AA metabolism in the presence of LA. Here, LA is treated as the inhibitor and its effects on AA calculated. (C) 3D plot of LA metabolism in the presence of AA. Here, AA is treated as the inhibitor in the calculations. Total metabolite formation was fitted to the competitive inhibition equation (Equation S2.1) taken as a concentration of all species. Rates are in units of $pmol_{products}/min/nmol_{CYP2J2}$. Error bars represent $\pm$ SEM.

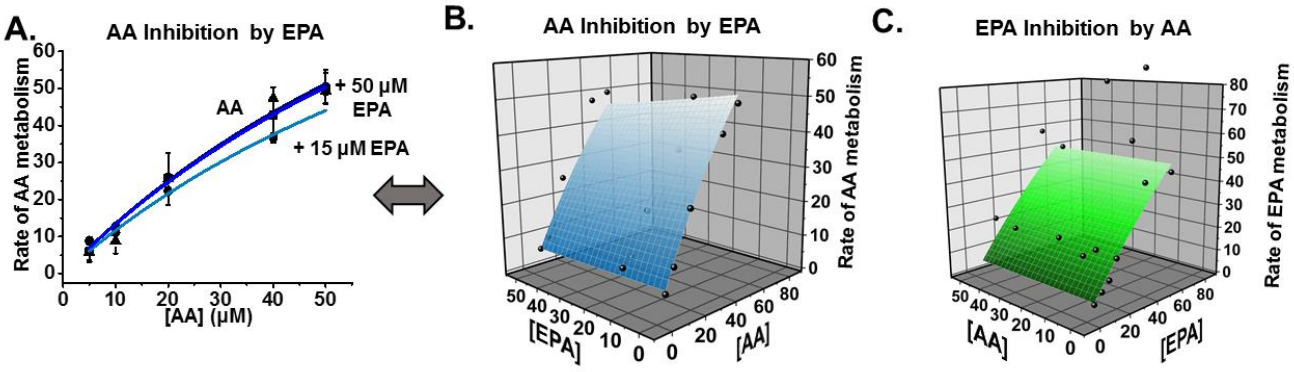

Supplementary Figure 2.2. AA and EPA mixed kinetics. (A) 2D plot of AA metabolism in the presence of indicated amounts of EPA. (B) 3D plot of AA metabolism in the presence of EPA. Here, EPA is treated as the inhibitor and its effects on AA calculated. (C) 3D plot of EPA metabolism in the presence of AA. Here, AA is treated as the inhibitor in the calculations. Total metabolite formation was fitted to the competitive inhibition equation (Equation S1) taken as a concentration of all species. Rates are in units of $pmol_{products}/min/nmol_{CYP2J2}$. Error bars represent $\pm$ SEM.

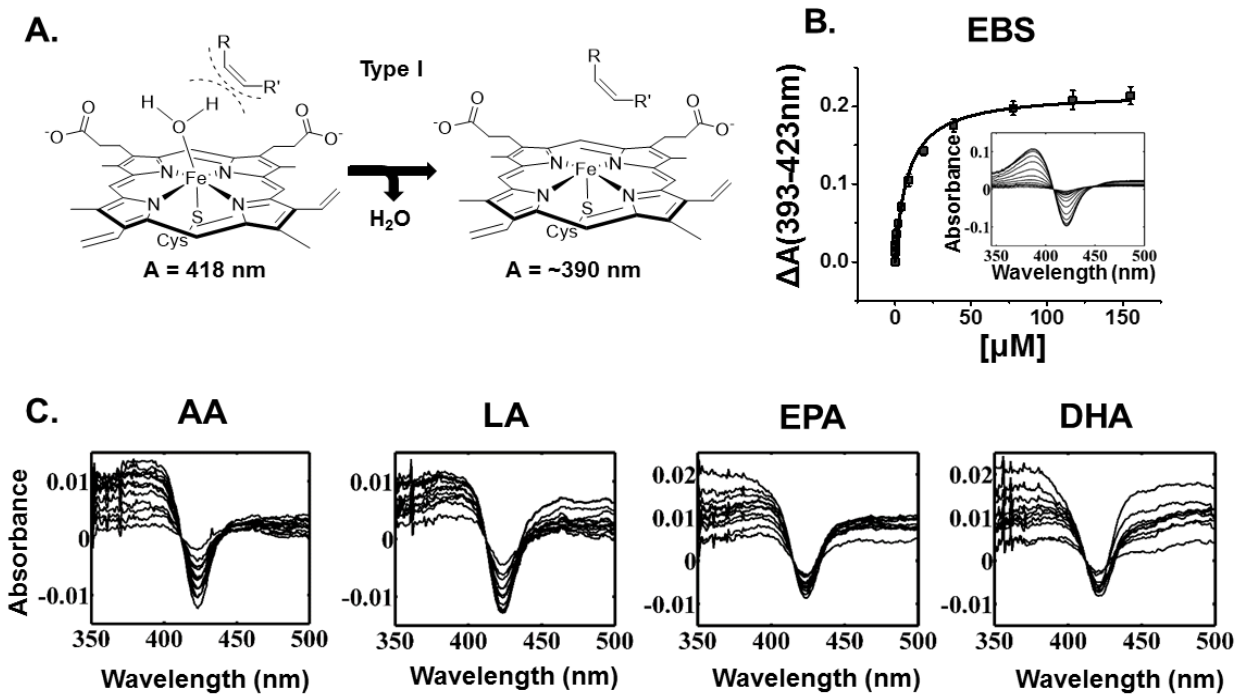

Supplementary Figure 2.3. Soret Binding Titrations of Substrates. (A) Schematic of substrate binding to the heme and perturbing a bound water molecule to produce a high-spin (type I) Soret shift. (B) Ebastine (EBS) binding plot with Soret difference spectra shown in the insert. Data fit to the Michaelis-Menten binding model. Error represents ± SEM. (C) Soret difference spectra of AA, LA, EPA, and DHA.

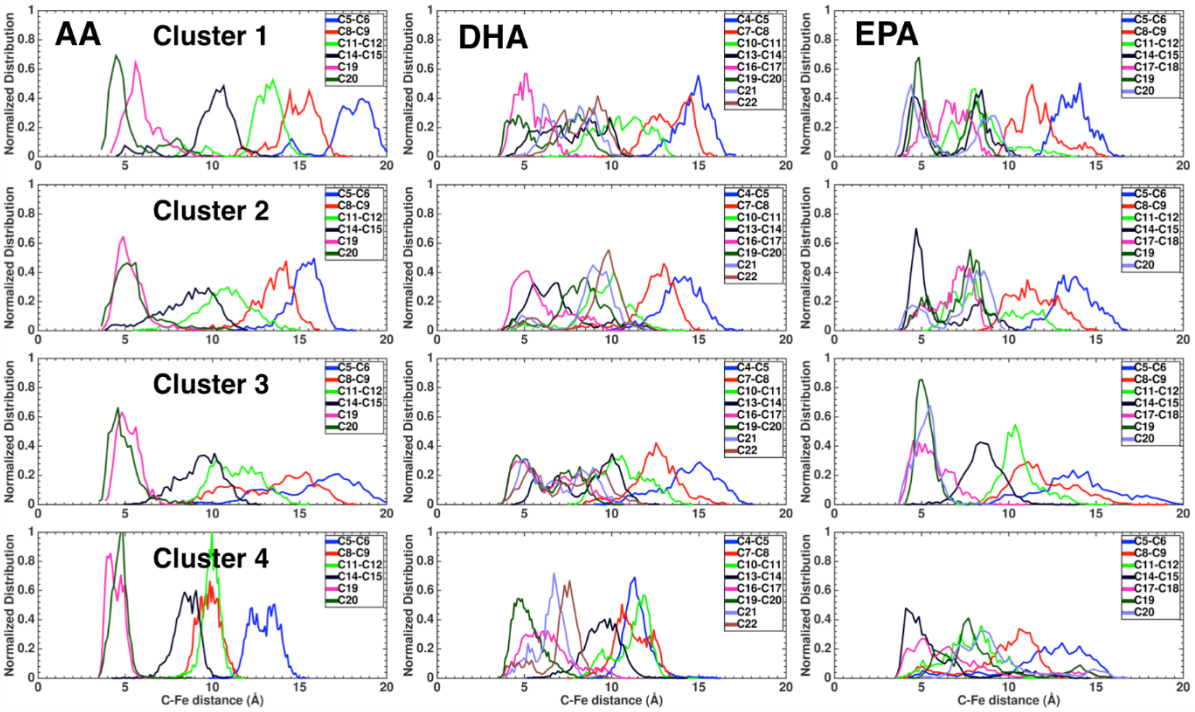

Supplementary Figure 2.4. Positioning of fatty acids in the active site of CYP2J2. Distribution of carbon-to-heme distances between epoxidation/hydroxylation sites of AA, DHA and EPA to the iron atom of the heme, obtained from MD simulations. For each fatty acid, data was obtained from 100 ns simulations for cluster 1, 2 and 3, and 200 ns simulations for cluster 4.

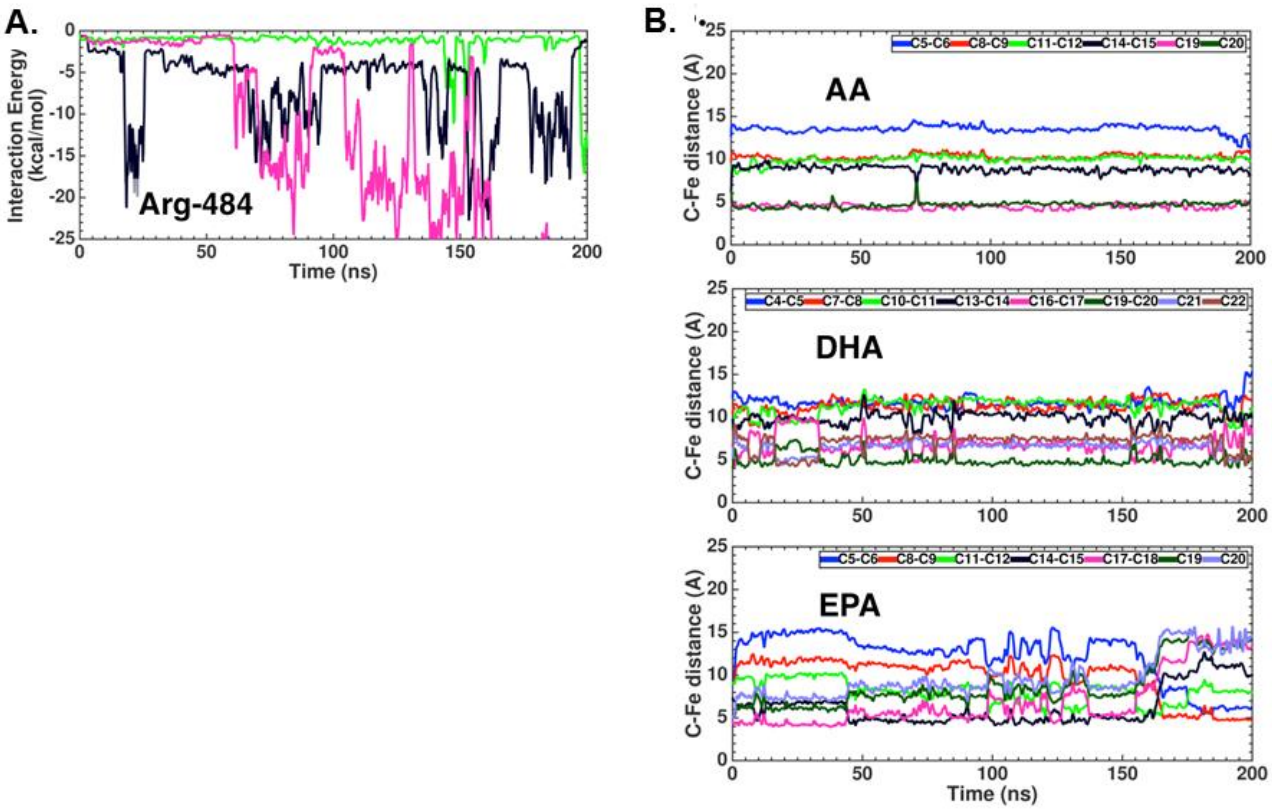

Supplementary Figure 2.5. Interaction of fatty acids with Arg-484. (A) Time series of the interaction energy of AA, DHA, and EPA with Arg-484 (B) Time series of carbon-to-heme distances of AA, DHA, and EPA for cluster 4. For EPA, as the interaction with Arg-484 increases (t > 100 ns), carbons 17 and 18 are moved away from the heme (distance ~ 15Å after 150 ns).

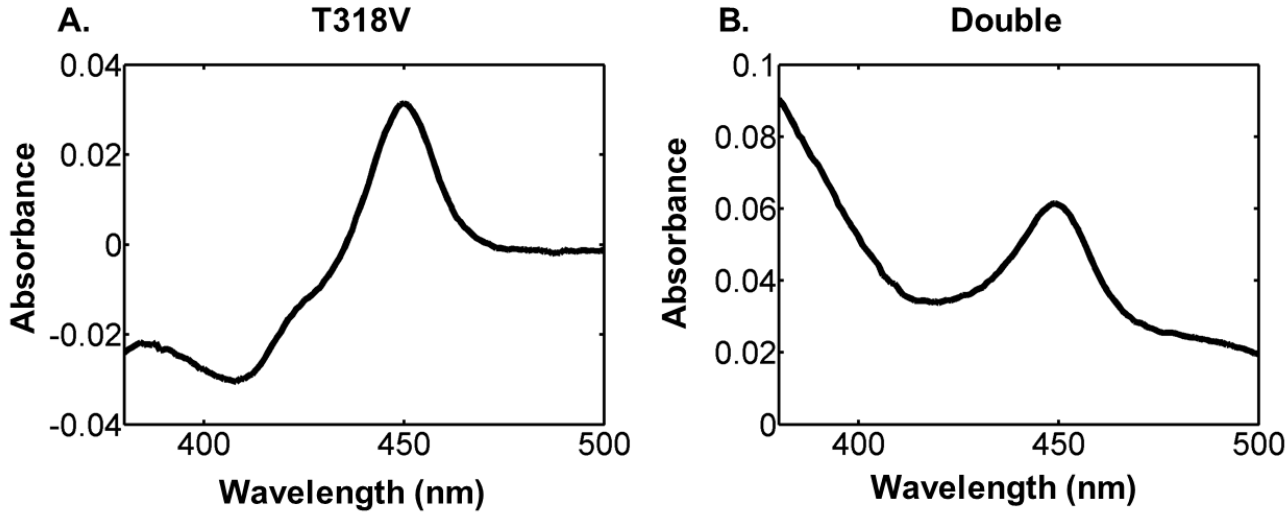

Supplementary Figure 2.6. CO difference spectra of mutants CYP2J2-T318V (T318V) and CYP2J2-T318V/S493A (Double). Both mutant constructs effectively bind CO and demonstrate properly ligated and functional heme.

Tables

Supplementary Table 2.1. PUFA catalytic efficiency estimates based on linear time kinetics. Catalytic efficiencies for each PUFA substrate were calculated from linear time kinetics using Equation 1 as discussed in the text.

Substrate	k_{cat}/K_m **(min^{-1} nM^{-1})**
AA	0.863 ± 0.064
LA	0.710 ± 0.092
EPA	0.823 ± 0.027
DHA	0.421 ± 0.037

Supplementary Table 2.2. DHA inhibition by AA with CYP2J2-T318V (T318V) and CYP2J2-T318V/S493A (Double) mutant variants. The inhibition of DHA by AA was also determined for each construct using 50 μM of AA + 50 μM of DHA. Rates are in pmol/min/nmolCYP and the inhibition by DHA (DHA Inhib) is shown as the percent of the calculated WT metabolism rate. Error represents ± SEM.

	Inhibition of DHA	
	Rate	**%WT**
WT	21.5	100
T318V	19.3 ± 0.0	90.0
Double	27.0 ± 0.4	125

Supplementary Table 2.3. Mutagenesis primer design. Mutagenesis primers were created for overlap-extension PCR as described in Materials and Methods. Forward primers (For) and reverse primers (Rev) were designed based upon the wild-type sequences shown (WT). Restriction enzyme sites for AleI and BsiEI were introduced as silent mutations for the purpose of screening the T318V and S493A mutations, respectively. Restriction enzyme recognition sequences are shown with blue lettering and mutations are bolded and underlined. Sequences are shown 5'→3'.

	T318V	S493A
WT	E T T S T T L R W A CCGAGACAACTTCCACAACTCTGCGATGGGC	I S P V S H R L C A CCATTTCCCCAGTCAGTCACCGCCTCTGCG
For	E T T S **V** T L R W A CCGAGAC**C**ACTTCC**GTG**ACTCTGCGATGGGC	I S P V **A** H R L C A CCATTTCCCC**G**GTC**G****C**TCACCGCCTCTGCG
Rev	GCCCATCGCAGAGT**CAC**GGAAGT**G**GTCTCGG	CGCAGAGGCGGTGA**GC**GAC**C**GGGGAAATGG

Chapter 3: Modulation of arachidonic acid metabolism by doxorubicin[2]

3.1 Introduction

Anthracyclines are one of the major classes of chemotherapeutics that are used in the treatment of a wide variety of cancers.[275,276] The prototypical anthracyclines are daunorubicin, which was naturally discovered in *Streptomyoces peucetius*, and the 14-OH derivative, doxorubicin (DOX).[277,278] Their anticancer mechanisms involve DNA intercalation and topoisomerase II inhibition.[276,279] DOX produces reactive oxygen species (ROS) leading to nonspecific cytotoxicity. DOX is especially cardiotoxic and causes arrhythmia as a result of QT interval prolongation.[280,281] Though ROS-related injury, including mitochondrial damage and lipid peroxidation, has been suggested to cause cardiotoxicity, there remain unknown mechanisms.[282-284] For instance, zorubicin (ZRN) and 5-iminodaunorubicin (5-IDN) are daunorubicin analogues that have reduced cardiotoxicity; however, whereas the former produces ROS, the latter does not,[275,285] indicating there are other potential mechanisms of DOX cardiotoxicity. It is also known that DOX cardiotoxicity is dependent on the cumulative dose, indicating that in addition to DOX, the DOX metabolites are highly likely to be involved in long-term cardiotoxicity.

Cytochromes P450 (CYPs) are involved in first-pass drug metabolism.[167] After metabolism by liver, the drug metabolites are delivered to the heart. Therefore, it is important to understand the interaction of drugs and their metabolites with cardiovascular CYPs such as CYP2J2. Similar to other CYPs such CYP3A4, [69,191,216,241,242] our hypothesis is that CYP2J2 should be capable of binding several substrates at once, which might explain the potential cardiotoxicity of certain drugs.

There is an absence of any direct metabolism study of DOX with CYPs. In one study it was shown that CYP2B1 was able to reduce DOX to a semiquinone using EPR measurements.[286] However, DOX is typically reduced by the CYP redox partner, cytochrome P450 reductase (CPR),[247] to a semiquinone, producing ROS and leading to reductive aglycosylation, producing mostly 7-deoxydoxorubicin aglycone (7-de-aDOX) (Figure 3.1).[286-288] Since CPR reduces DOX

[2] This work has been published as: Arnold, W. R.; Baylon, J. L.; Tajkhorshid, E.; and Das, A. "Arachidonic Acid Metabolism by Human Cardiovascular CYP2J2 Is Modulated by Doxorubicin." Biochemistry, 2017, 56 (51), 6700-6712. The work is allowed to be republished under the Creative Commons Attribution license (https://creativecommons.org/licenses/by/4.0/)

directly and CYPs require CPR to do catalysis, delineating the role of CYPs in DOX metabolism has been challenging. Herein, we carefully delineate the role of heart CYP2J2 in the metabolism of DOX, and the modulation of CYP2J2 activity by DOX and its primary metabolite 7-de-aDOX.

CYP2J2 is highly expressed in human cardiomyocytes[196] and is responsible for the endogenous oxidation of arachidonic acid (AA) into four regioisomers of epoxyeicosatrienoic acids (EETs)[42,196,232,246,289] (Figure 3.1) and two hydroxyeicosatetraenoic acids (HETEs).[1,44,232,289] Together, these metabolites are responsible for mediating several cardiac physiologies, including anti-inflammation, vasodilation, and cellular proliferation.[8,68,290] They also protect against post-ischemia reperfusion injury and reduce myocardium infarct size.[8,70,291] Therefore, these CYP2J2-derived metabolites are cardioprotective.[71] However, the efficacy of these EET regioisomers are not similar to each other.[290] For instance, 5,6-EET and 8,9-EET have been shown to be both vasoconstrictory and vasodilatory depending on the tissue,[292,293] and 8,9-EET did not reduce myocardial infarct size.[68] Overexpression of CYP2J2 was found to protect against DOX-induced injury in human-CYP2J2-overexpressed mice with an unknown mechanism.[74] In this study, a decrease in mitochondrial damage was observed when 11,12-EET was administered to H9c2 cells. This effectively demonstrates the importance of different regioisomers of EETs (e.g.11,12-EET) in mediating cardioprotection.

CYP2J2 has also been found to metabolize several cardiotoxic drugs, such as terfenadine, astemizole, amiodarone, and dronedarone.[294-297] Our hypothesis is if cardiotoxic drugs inhibit CYP2J2-mediated drug metabolism, they should also inhibit CYP2J2-mediated AA metabolism. The inhibition of endogenous AA metabolism by CYP2J2 can have deleterious cardiovascular effects as EETs play an important role in cardiovascular function.

Herein, we use fluorescence polarization (FP) measurements, molecular dynamics (MD) simulations, and substrate kinetics to delineate the mechanism of the DOX/CYP2J2/AA interactions. We demonstrate that DOX inhibits CYP2J2-mediated AA metabolism. Additionally, it alters the site of AA metabolism indirectly through its metabolite 7-de-aDOX. 7-de-aDOX modulates the binding of AA in the active site of CYP2J2 leading to significant change in the regioselectivity of AA epoxidation. We further show that DOX analogues, 5-IDN and ZRN, inhibit CYP2J2 with different potencies, but neither of them alter the regioselectivity of AA metabolism. FP binding measurements and kinetics studies indicate that 7-de-aDOX can bind at a separate site from AA. These studies are supported by MD simulations, which demonstrate that 7-de-aDOX

binds into a binding site we had previously determined to be crucial for PUFA binding. [289] This positions AA into a conformation to support our observed changes in the site of metabolism.

3.2 Experimental procedures

Materials expression and purification of CYP2J2, CPR, and CYPB5; EBS kinetics and quantification; EET LC-MS/MS quantification; and IC_{50} calculations. See Supplementary information, methods section.

Use of reactive oxygen species (ROS) scavengers in in vitro kinetic experiments. To account for ROS-mediated effects, kinetic experiments were performed with and without ROS scavengers (10 U/mL of catalase and 10 U/mL of superoxide dismutase final, each an order of magnitude larger than required). Scavenger stocks were made in 0.1 M KPi buffer, pH 7.4, and handled and stored according to manufacturer's recommendations. There were no significant differences in the data with and without the scavengers, and all the data presented is in the presence of scavengers.

Arachidonic Acid (AA) metabolism kinetics. The kinetics of AA metabolism by CYP2J2 with and without DOX were determined as follows. CYP2J2 and CPR (0.6 μM each) were incubated in a 20% POPS lipid reconstituted system (see Supplementary Methods) in 0.5 mL of potassium phosphate buffer (pH 7.4). This mixture was then preincubated with 100 μM AA with varying concentrations of DOX or 7-de-aDOX (0-50 μM from 1 mM and 10 mM stocks in DMSO) for 10 min. Reactions were started with 6 mM NADPH and terminated after 5 min with 100 μL acetic acid. Metabolites were extracted and quantified as previously described[289]. AA epoxidation by CYP2J2 was determined to be linear up to 8 min under these conditions. IC_{50} and K_i values were determined as stated in the Supplementary Methods. To investigate the effects of ROS-mediated epoxidation of AA from the reduction of DOX, the same procedure was repeated with CPR and without CYP2J2 and without ROS scavengers.

Fluorescence polarization binding of DOX and 7-de-aDOX. Steady-state fluorescence measurements were conducted with a K2 multi-frequency phase and modulation fluorimeter (ISS, Urbana, IL). Spectra were recorded using Vinci 2 software (Urbana, IL). Measurements were taken with a 1 nm slit width filter. Fluorescence emission spectra between 500 nm and 650 nm of DOX and 7-de-aDOX were determined using an excitation wavelength of 480 nm, with both showing optimal absorbance between 590 and 595 nm. Experiments were conducted at 37°C using a circulating water bath and monomeric protein stocks were solubilized in 0.1% cholate. The

presence of CYPs or CYB5 did not alter the fluorescence of DOX or 7-de-aDOX. Polarization measurements were taken using a 594-nm cut-off filter, and the initial G and polarization (r_0) values were determined. For all measurements, G ≈ 1.000 and r_0 ≈ 0.900 and did not significantly change between experiments. 0-40 μM of CYP2J2 and CYB5 were titrated into 1 μM DOX or 7-de-aDOX in 0.1% cholate and 0.1 M potassium phosphate (KPi) buffer (pH 7.4) at 37°C and incubated for 2 min before each measurement. For concentrations of protein greater than 10 μM, 1 μM of DOX or 7-de-aDOX were titrated into diluted protein stocks. The polarization values were plotted and fitted to either linear (CYB5) or one-binding site (Equation 3.1) (CYP2J2) equations

$$r = r_o + \frac{r_1\left(\frac{[S]}{K}\right)}{1+\left(\frac{[S]}{K}\right)} \quad \text{(Equation 3.1)}$$

where r_0 = the intrinsic (initial) polarization value and r_1 = the maximum polarization value.

Competitive FP binding. EBS and AA competitive binding experiments to probe where DOX and 7-de-aDOX bind to CYP2J2 were performed as above with the following modifications. CYP2J2 protein stocks were preincubated with 60 μM EBS or 100 μM AA prior to the titration. Initial fluorescence measurements using 1 μM compound were also determined in the presence of 60 μM EBS and 100 μM. The CYP2J2 and substrate mixture was then titrated into the solution and the FP determined as above. Data fit to a competitive binding equation whenever inhibition was present.

Doxorubicin (DOX) Metabolism Kinetics. In vitro DOX metabolism was determined by pre-incubating CPR and CYP2J2 (0.6 μM each) with DOX (10 mM and 1 mM stocks in DMSO) and a 20% POPS lipid reconstituted system for 10 min at 37°C in 0.1 M KPi buffer (pH 7.4). Reactions were initiated upon the addition of 6 mM NADPH based upon our initial NADPH kinetic rates. Reactions were terminated with 100 μL acetic acid and were extracted thrice with equal volumes of ethyl acetate to purify doxorubicin aglycone (aDOX) metabolites. Undigested DOX remained in the aqueous layer with no noticeable accumulation of aDOX metabolites. The organic extracts were then dried under a stream of N_2 gas and resuspended in 100 μL acetonitrile for HPLC quantification. Samples were heated with warm water to facilitate solubilization.

HPLC separation and quantification of DOX metabolites. A high-performance liquid chromatography (HPLC) system consisting of an Alliance 2695 analytical separation module (Waters, Milford, MA) and a Waters 996 photodiode diode array detector (Waters) was used for the separation and quantification of DOX metabolites. Metabolites were separated using a

Phenomenex Prodigy® 5µm ODS-2, 150 x 4.60 mm column (Phenomenex, PN 00F-3300-E0, Torrance, CA) and a linear-gradient reverse-phase method at a flow rate of 0.5 mL/min. The mobile phase consisted of Mobile Phase A (filtered ultrapure water titrated with formic acid to pH = 3.0) and Mobile Phase B (acetonitrile). The gradient consisted of 95% Mobile Phase A to 100% Mobile Phase B over a 35-min period and held at 100% Solvent B for 5 more min (40 min total) to wash the column. DOX eluted at 15 min and aDOX metabolites (DOX metabolites without the daunosamine sugar) eluted between 17 and 24 min, with a major peak at 21.7 min. Incubations with CPR produced a major 21.7 min peak and a minor peak at 23 min. The major peak was identified as 7-deoxy-doxorubicin aglycone (7-de-aDOX) by comparing elution time and mass spectroscopy fragmentation against an authentic standard. DOX metabolism was quantified at λ = 484 nm using an authentic standard curve.

High-resolution LC-MS/MS identification of Anthracycline metabolites. For high resolution LC/MS, the samples were analyzed by using the Q-Exactive MS system (Thermo. Bremen, Germany) in the Metabolomics Laboratory of Roy J. Carver Biotechnology Center, University of Illinois at Urbana-Champaign. Software Xcalibur 3.0.63 was used for data acquisition and analysis. The Dionex Ultimate 3000 series HPLC system (Thermo, Germering, Germany) used includes a degasser, an autosampler, and a binary pump. The LC separation was performed using the same Phenomenex Prodigy® 5µm ODS-2 column as for HPLC. The autosampler was set to 10°C. The injection volume was 10 µL. Mass spectra were acquired under positive electrospray ionization (sheath gas flow rate, 49; aux gas flow rate: 12; sweep gas flow rate, 2; spray voltage, 3.5 kV; capillary temp, 259 °C; Aux gas heater temp, 419 °C). Mass scan range is 70 - 1,000. For full scan, the resolution was set to 70,000, and the AGC target was 1E6 with a maximum injection time of 50 ms. For MS/MS scan, the resolution was set to 17,500 and the AGC target was 5E4 with a maximum injection time of 50 ms. NCE was 25 and 30.

NADPH kinetics. The rate of NADPH consumption in the presence of anthracyclines (0-50 µM from 1 mM and 10 mM stocks in DMSO) was determined using UV-Vis spectroscopy as previously described [257]. Experiments were performed using 0.6 µM CPR with or without 0.6 µM CYP2J2 and a 20% POPS lipid reconstituted system. 200 µM of NADPH was added to initiate the reaction to keep the absorbance values below 1. Rates were determined based on the initial linear rate of three experiments.

Statistical Analysis. All data were produced from the means of 3 repeats. Statistical significance was based on a two-tailed student's t-test confidence level of $P < 0.05$. All data curve fittings were determined using OriginPro 9.1 software (Origin Labs Inc., Northhampton, MA).

Modeling and simulation of membrane-bound CYP2J2 with AA and 7-de-aDOX. Initial structural models of membrane-bound CYP2J2 bound to AA and 7-de-aDOX were generated with molecular docking performed with AutoDock Vina.[259] We started by docking 7-de-aDOX to our previously derived models of CYP2J2 bound to AA based upon the homology model of Lafite, P. et al.[289,298] For this docking step, we employed configurations of AA in which sites involved in the regioselectivity shift (i.e., carbons C5,C6 and C8,C9) were close to the heme (with distance < 5 ˚A), resulting in about 20 initial structures used for docking. A grid box of dimension 22 ˚A in x, y and z and centered in the active site of CYP2J2 was employed. The resulting docked poses of 7-deaDOX were then clustered based on the RMSD of its heavy atoms, resulting in four clusters. Finally, for each cluster, the configurations of CYP2J2 with both AA and 7-de-aDOX bound with the best docking score were selected as a starting point for MD simulations. Each system was then minimized for 2,000 steps, and equilibrated for 1 ns with the Cα of CYP2J2 and the heavy atoms of AA and 7-de-aDOX harmonically restrained (with force constant k=1 kcal/mol/˚A2). Following this preparation step, the four systems were simulated for a short time (20 ns) to assess the stability of 7-de-aDOX binding. After this step, only one system showed stable binding of 7-de-aDOX to CYP2J2, and this system was further extended to 200 ns of simulation without restraints. As a control, an additional simulation in which 7-de-aDOX was removed from this initial model was also performed following the same preparation protocol, with 200 ns of production simulation.

As a control, we also performed docking of DOX both to apo membrane-bound CYP2J2 and to the CYP2J2-AA complex, following the similar protocol as for 7-de-aDOX. Snapshots of apo membrane-bound CYP2J2 were obtained from our simulations previously reported.[245] From DOX docking to CYP2J2, two main configurations of DOX in the active site were identified through clustering and employed starting points for MD simulations (see Supplementary Movies). For DOX docking to the CYP2J2-AA complex, only one main configuration of DOX was identified (Figure 3.7). In this configuration, DOX was located ~17 Å from the heme (center of mass distance) and not within the active site, and thus this configuration was not simulated.

Docking of EBS to the CYP2J2/7-de-aDOX complex. We generated a model of EBS-bound CYP2J2 by employing the last snapshot of the CYP2J2-7-de-aDOX/AA simulation for molecular

docking. For this, we removed AA from the structure, while 7-de-aDOX was preserved. A grid box with same dimensions as previously described and centered in the active site of CYP2J2 was employed for EBS docking. From this step, 10 different docked poses of EBS with the CYP2J2/7-de-aDOX complex were generated, and sorted based on docking score.

Simulation protocol. The simulations were performed using NAMD2.[260] The CHARMM27 force field with cMAP[299,300] corrections was used for the protein and the CHARMM36[262,301] force field was used for lipids. Parameters for AA and 7-de-aDOX were obtained by analogy from the CHARMM General Force Field.[263] The TIP3P model was used for water.[265] Simulations were performed with the NPT ensemble with a time step of 2 fs. A constant pressure of 1 atm was maintained using the Nos´e-Hoover Langevin piston method.[266,267] Temperature was maintained at 310 K using Langevin dynamics with a damping coefficient γ of 0.5 ps-1applied to all atoms. Nonbonded interactions were cut off at 12 ˚A, with smoothing applied at 10 ˚A. The particle mesh Ewald (PME) method[269] was used for long-range electrostatic calculations with a grid density of > 1 ˚A-3 .

3.3 Results

CYP2J2-mediated AA metabolism in the presence of DOX and 7-de-aDOX. We firstly investigated the effect of DOX on CYP2J2-mediated arachidonic acid (AA) metabolism. We used AA at a concentration near the previously determined K_m.[289] The concentration ranges for DOX covers plasma levels upon immediate exposure (~1-10 μM) to the toxic cumulative dose (~50 μM).[302,303] We see that DOX inhibits the total AA metabolism with an IC_{50} of 5.48 $\pm$ 0.04 μM and a K_i of 3.11 $\pm$ 0.02 μM.

DOX is converted to 7-de-aDOX by cytochrome P450 reductase. In order to do the studies, we synthesized 7-de-aDOX from DOX through reduction (Supplementary Methods and Supplementary Figure 3.1). We next determined the effect of 7-de-aDOX on AA metabolism. 7-de-aDOX also inhibits AA metabolism, with an IC_{50} of 10.2 $\pm$ 0.1 μM and a K_i of 5.78 $\pm$ 0.03 μM. However, the maximum inhibition by 7-de-aDOX appears to be almost half as effective compared to DOX, with a y_0 of 42.9 $\pm$ 5.6 pmol $(min)^{-1}$ $(nmol_{CYP2J2})^{-1}$ for 7-de-aDOX and a y_0 of 19.8 $\pm$ 3.8 pmol $(min)^{-1}$ $(nmol_{CYP2J2})^{-1}$ for DOX (Figure 3.2B). This implies that 51% of the enzyme activity is retained in the presence of saturating amounts of 7-de-aDOX, compared to 23% in the presence of DOX. In theory, competitive inhibition of an enzyme would result in a $y_0 = 0$

due to the inhibitor completely outcompeting the substrate. Since the y_0 of the 7-de-aDOX data does not approach 0, this demonstrates that the inhibition is not competitive and suggests a possible second binding site for binding 7-de-aDOX.

To confirm these observations, we proceeded to measure the AA metabolism with a 50:50 mixture of DOX and 7-de-aDOX, maintaining the total anthracycline concentration (Figure 3.2B). If the incomplete inhibition of 7-de-aDOX is due to 7-de-aDOX and AA concurrently binding, then the data would be a linear combination of the individual DOX and 7-de-aDOX data. The theoretical values for this mixture based on the DOX and 7-de-aDOX data are as follows: IC_{50} = 6.68 $\pm$ 0.05 μM (K_i = 3.79 $\pm$ 0.03 μM) and y_0 = 32.1 $\pm$ 4.2. Our experimental values were: IC_{50} = 10.1 $\pm$ 0.03 μM (K_i = 5.73 $\pm$ 0.02 μM) and y_0 = 24.8 $\pm$ 5.5. These values agree well to the theoretical values and support that DOX competitively inhibits AA metabolism, and that 7-de-aDOX allows for the concurrent metabolism of AA and an incomplete inhibition.

DOX and 7-de-aDOX changes the regioselectivity of the AA epoxidation. AA metabolism by *Formation of different EET regioisomers by CYP2J2-mediated AA metabolism in the presence of DOX or 7-de-aDOX*. CYP2J2 leads to the formation of four different EET regioisomers. We further observed that DOX had a concentration-dependent change on the regioselectivity of AA epoxidation (Figure 3.3B and Figure 3.3D). With increasing concentrations of DOX, the ratio of 5,6-EET significantly increases (1.41-fold with 50 μM DOX) (Figure 3.3D) and 14,15-EET significantly decreases (0.78-fold with 50 μM DOX), with less-pronounced albeit significant changes in 8,9-EET and 11,12-EET (Figure 3.3B and D).

As a control, incubating AA with CPR and 50 μM DOX, without ROS scavengers produces a negligible epoxidation of AA (Figure 3.3E) with a different distribution of EETs compared to that produced by CYP2J2 (Figure 3.3F). Furthermore, since all these experiments with CYP2J2 were conducted in the presence of ROS scavengers, this EET regioselective change is CYP2J2-mediated and not ROS-mediated.

The experiments with 7-de-aDOX also resulted in a similar regioselectivity change of the AA epoxidation (1.41-fold for 5,6-EET and 0.86-fold for 14,15-EET with 50 μM 7-de-aDOX) (Figure 3.3B and D). Similar changes were observed in the 50:50 mixture (Figure 3.3B). Since DOX displays competitive inhibition and 7-de-aDOX displays incomplete inhibition, 7-de-aDOX appears to be the modulator of the EET regioselectivity. The regioselective change with DOX is likely due to its rapid conversion to 7-de-aDOX. Coincidentally, 11,12-EET and 14,15-EET have

been shown to be the most effective at reducing ischemic injury, whereas 5,6-EET and 8,9-EET have not.[68]

CYP2J2-mediated AA metabolism in the presence of non-cardiotoxic DOX analogues, ZRN and 5-IDN. DOX and 7-de-aDOX inhibited AA metabolism and altered the site of metabolism. In order to determine if these observations are unique to DOX and 7-de-aDOX, we repeated the study using two DOX analogues. The rationale for choosing the analogues is that both ZRN and 5-IDN are chemotherapeutic DOX analogues with lowered cardiotoxicity compared to DOX. ZRN redox cycles and produces ROS as effectively as DOX, while 5-IDN has a lowered rate of redox cycling.[275,285,304] The structural differences are shown in Figure 3.2A. ZRN contains a large benzohydrazide modification, and the presence of an imino group in place of a keto makes 5-IDN inhibit redox cycling. ZRN inhibits AA metabolism as effectively as DOX, with inhibition parameters of: IC_{50} = 6.46 $\pm$ 0.03 μM (K_i = 3.67 $\pm$ 0.02 μM) and y_0 = 18.7 $\pm$ 3.5 (Figure 3.2C). 5-IDN displayed a lower inhibition affinity compared to ZRN or DOX, with an IC_{50} = 27.4 $\pm$ 0.03 μM (K_i = 15.6 $\pm$ 0.02 μM) (Figure 3.2C).

However, there is not a significant change in the epoxide regioselectivity for either 5-IDN or ZRN compared to DOX or 7-de-aDOX (Figure 3.3C and D). The minor changes in the regioselectivity (Figure 3.3D) are likely due to the conversion of 5-IDN and ZRN to their respective aglycones, which do not modulate AA metabolism as effectively as 7-de-aDOX (Supplementary Figures 3.2-3.3). For ZRN, the bulky benzohydrazide would significantly change the binding of the ZRN-aglycone. In summary, ZRN and IDN differ in their inhibition potential towards CYP2J2-mediated AA metabolism and do not produce a significant concentration-dependent regioselectivity change (Figure 3.3C and D).

Fluorescence polarization (FP) binding of DOX and 7-de-aDOX to CYP2J2. To further investigate the mechanistic details of the AA metabolism modulation by DOX and 7-de-aDOX, we measured their binding to CYP2J2 using FP measurements. Heme Soret titration could not be used to measure the binding, as DOX and its derivatives have a high absorbance between 400-500 nm. Cytochrome b5 (CYB5) was used as a nonspecific binding control, as it does not interact with DOX. None of these hemoproteins altered the fluorescent properties of DOX (Supplementary Figure 3.4). CPR, however, has an intrinsic fluorescence in the same region as DOX fluorescence and could not be used in this assay (Supplementary Figure 3.4D).

The binding parameters are shown in Table 3.1. CYB5 showed polarization values, *r*, that are linear as a function of protein concentration indicating nonspecific binding (Supplementary Figure 3.5). CYP2J2 demonstrated one-site binding with a K_D of 5.32 $\pm$ 0.89 μM (Figure 3.4A), agreeing well with the IC_{50}/K_i of DOX for the AA inhibition. AA, however, weakly inhibits DOX binding.

To determine if DOX is binding to the active site of CYP2J2, we performed these studies with CYP2J2 and DOX in the presence of 60 μM ebastine (EBS) to saturate the active site (Figure 3.4A). EBS is a substrate of CYP2J2 with a similar K_D as DOX (8.16 μM) and demonstrates one-site binding to the active site.[250,289] EBS competitively inhibited DOX binding to CYP2J2, with a K_i of 13.8 $\pm$ 1.6 μM that agrees well with the K_D and K_m values for EBS.[289] These data conclude that DOX and EBS are competing for binding to the active site of CYP2J2 and that AA weakly inhibits DOX binding (Figure 3.4A).

CYP2J2 had a larger amplitude of change on the 7-de-aDOX polarization compared to DOX and demonstrated one-site binding with a K_D of 13.1 $\pm$ 1.1 μM (Figure 3.4B). AA showed little inhibition of 7-de-aDOX binding (K_i > 200 μM). Despite EBS having a tighter K_D than 7-de-aDOX (8.16 μM[289] vs. 13.1 μM), EBS did not inhibit 7-de-aDOX binding to CYP2J2 (Figure 3.4B). The inability of EBS to inhibit 7-de-aDOX binding suggests that these two molecules do not compete for binding to the same site. Since EBS binds the active site, this proposes a peripheral binding site for 7-de-aDOX. The presence of peripheral binding sites is common in CYPs.[69,191,216,241,242]

FP also measures the "rigidity" of binding, where an FP value of *r* = 0.4 represents the theoretical maximum value and the most restriction to rotational mobility. Therefore, the *r* maximum (r_1) value of the one-site model can be used as a semi-quantitative measurement of the rotational flexibility of the molecule in the active site of the protein [305]. The binding of DOX to CYP2J2 produced an r_1 value of 0.219 $\pm$ 0.010 and thus DOX maintains some rotational freedom while bound to the active site. Contrariwise, CYP2J2 binding of 7-de-aDOX showed an r_1 value of 0.351 $\pm$ 0.022. This indicates that 7-de-aDOX has more rotational restriction when bound to CYP2J2.

Effects of DOX on CYP2J2-mediated EBS metabolism. In order to further probe the inhibitory characteristics of DOX and 7-de-aDOX, we investigated their effects on EBS metabolism by CYP2J2. The binding and kinetics of EBS metabolism are closer to the parameters of DOX and therefore provides clearer insights into the interactions. We determined the K_m of EBS metabolism

by CYP2J2 to be 19.4 μM.[289] Therefore, we looked at the effect that DOX has on the CYP2J2-mediated metabolism with 20 μM of EBS. DOX inhibited EBS metabolism with an IC_{50} of 17.9 ± 0.0 μM and a K_i of 8.97 ± 0.01 μM (Figure 3.4C). Incubations with 7-de-aDOX, however, did not result in an inhibition of EBS metabolism (Figure 3.4C). This is similar to the observations from the FP binding experiments, in which 7-de-aDOX binding to CYP2J2 was not inhibited by EBS. Therefore, EBS and 7-de-aDOX likely bind to different sites in CYP2J2. To confirm, we measured the EBS metabolism in the presence of a 50:50 mixture of DOX and 7-de-aDOX. The theoretical combination of the DOX (y_0 = 5.87 ± 2.84) and 7-de-aDOX (b = 22.5 ± 1.2) data results in a y_0 = 13.2. The 50:50 DOX:7-de-aDOX data match the theoretical model as a linear combination of the 7-de-aDOX and DOX data quite well, resulting in an IC_{50} of 9.07 ± 0.08 μM (K_i = 4.53 ± 0.04 μM) and a y_0 of 14.2 ± 2.1. This confirms our observations that DOX competes with EBS for binding to the active site of CYP2J2, whereas 7-de-aDOX binds in a site that allows for the binding of a second ligand such as EBS or AA. Furthermore, this demonstrates that the effects of 7-de-aDOX are not universal for all CYP2J2 substrates, since 7-de-aDOX alters the metabolism of AA but not the metabolism of EBS.

Metabolism of DOX, ZRN, and 5-IDN by CPR. We next investigated if CYP2J2 is capable of metabolizing DOX. This is difficult to delineate as CPR, the obligate redox partner of CYPs, can reduce DOX to produce a DOX semiquinone (DOX-sQ) via NADPH oxidation (Figure 3.1B). DOX-sQ can then produce reactive oxygen species or reductively aglycosylate the daunosamine sugar moiety to produce doxorubicin aglycone (aDOX) metabolites.[286-288] Previously, the steady-state kinetics of these reactions have not been measured. We determined the kinetics of DOX metabolism by CPR. HPLC analysis (Supplementary Figure 3.6) of the reaction products showed a major 7-de-aDOX peak (20.5 min) that was confirmed using authentic standards (Supplementary Figure 3.7), and a minor peak (22.4 min) (Supplementary Figure 3.6). The minor peak had MS/MS fragments that were +14 m/z values of the 7-de-aDOX fragments (Supplementary Figure 3.8), which may be due to the oxidation of the 7-OH of doxorubicin aglycone to a ketone. The product was not analyzed further due to poor yields.

A similar metabolism was observed for the reduction of ZRN and 5-IDN by CPR (Figures S3.2 and S3.3). ZRN elutes at 17.2 min, and masses corresponding to 7-deoxyzorbucin aglycone were identified at 22.2 and 25.7 min (Supplementary Figure 3.2). 5-IDN elutes at 16.4 min and a mass

corresponding to the 7-deoxy aglycone analogue was identified at 22.7 min (Supplementary Figure 3.3).

Kinetics of DOX, 7-de-aDOX, ZRN, and 5-IDN metabolism by CPR. The rate of NADPH oxidation in the presence of DOX or 7-de-aDOX was negligible in the absence of any enzyme. The rate of NADPH oxidation was linear when CPR is reducing DOX or 7-de-aDOX, indicating that the reduction proceeds without a discernable binding event (Figure 3.5A-B and Supplementary Table 3.1). The rate with 7-de-aDOX (Figure 3.5B) was approximately tenfold lower than with DOX (Figure 3.5A) and implies that 7-de-aDOX is not readily reduced by CPR to form ROS. Comparatively, NADPH oxidation in the presence of ZRN is similar to DOX, and with 5-IDN is significantly slower (Supplementary Figure 3.9 and Supplementary Table 3.1). This confirms the observation that ZRN redox cycles as effectively as DOX and 5-IDN has a much lower rate of redox cycling. The metabolism of DOX to 7-de-aDOX by CPR is also linear, confirming the metabolism of DOX by CPR proceeds without a binding event (Figure 3.5C and Supplementary Table 3.1).

NADPH oxidation and Kinetics of DOX metabolism by CYP2J2-CPR. With the addition of CYP2J2, the NADPH oxidation with DOX follows a hyperbolic curve, with an apparent K_m of 10.4 ± 1.6 μM (Figure 3.5A). This implies that CYP2J2 reduces DOX. The NADPH oxidation does not increase when 7-de-aDOX binds CYP2J2 and implies that 7-de-aDOX is not reduced by CYP2J2 (Figure 3.5B).

The conversion of DOX to 7-de-aDOX remained linear and is inhibited in the presence of CYP2J2 (Figure 3.5C and Supplementary Table 3.1). Therefore, we conclude that CYP2J2 does not contribute towards the reductive aglycosylation of DOX (Figure 3.5C). Overall, this shows that CYP2J2 does not metabolize DOX or 7-de-aDOX to form new products (none detected by LC-MS/MS analysis), but it reduces DOX (Figure 3.5A).

Molecular dynamic (MD) simulations to investigate the effect of 7-de-aDOX on AA orientation in the active site of CYP2J2. To gain insight into how 7-de-aDOX may be modulating the AA metabolism by CYP2J2, we employed a combined approach of molecular docking and MD simulations, as described in Experimental Procedures. We have successfully used these techniques to identify key residues that differentially moderate PUFA binding to the CYP2J2 active site.[289] To investigate how the presence of 7-de-aDOX modulates AA regioselectivity by CYP2J2, we performed MD simulations starting from structures of membrane-bound CYP2J2 in complex with

AA and 7-de-aDOX obtained with molecular docking (see Methods). The initial model included both 7-de-aDOX and AA molecules in the active site of CYP2J2. The initial orientation of AA was selected so that sites involved in the regioselectivity shift (i.e., carbons C5,C6 and C8,C9) were initially close to the heme (with distance < 5 ˚A) (Figure 3.6). As a control, a simulation where 7-de-aDOX was removed from the initial model was also performed to assess the stability of AA in its initial orientation.

The simulations suggest that the regioselectivity shift is in part due to how 7-de-aDOX sits in the active site of CYP2J2 (Figure 3.6A). A specific orientation of 7-de-aDOX located near the active site interacts with key residues that have been shown to be important for AA binding to CYP2J2 (i.e., R321 and S493) [289]. In this configuration, 7-de-aDOX prevents AA from fully extending to place its main epoxidation

sites (i.e., carbons C11,C12 and C14,C15) close to the heme, and instead favors positioning of other sites (carbons C8,C9 and to a lesser extent C5,C6) at potentially productive distances from the heme (< 5 ˚A for C8,C9) during the majority of the simulation (Figure 3.6B).

In contrast, by removing 7-de-aDOX from the starting model, AA quickly adopts the orientation that we have previously reported,[289] interacting with residues near the active site (including T318, R321 and S493) and placing its main epoxidation sites (carbons C11,C12 and C14,C15) close to the heme (distance < 5 ˚A) during the simulation (Figure 3.6B).

Furthermore, docking 7-de-aDOX and EBS together in the active site shows that there is minimal perturbation by 7-de-aDOX on the binding of EBS near the heme, which supports the experimental data (Figure 3.6C). Simulations of membrane-bound CYP2J2 with DOX revealed that this drug occupies a majority of the active site volume of CYP2J2, suggesting that AA and DOX cannot concurrently bind. Indeed, docking of DOX to the CYP2J2-AA structures employed for 7-de-aDOX docking revealed that DOX cannot bind within the active site of CYP2J2 once AA is present (Figure 3.7), in contrast to the simulated 7-de-aDOX configuration where both AA and 7-de-aDOX are accommodated within the active site volume (Figure 3.6A). Interestingly, the binding of both AA and 7-de-aDOX does not require a significant conformational change of the active site relative to the apo- (without substrate) or a single-ligand-bound CYP2J2, and relies more on finding the right orientation for both ligands within the active site volume.

3.4 Discussion

CYP2J2 metabolizes AA and other PUFAs to produce epoxides, such as EETs, that are cardioprotective. In addition to metabolism of endogenous PUFAs, CYP2J2 is also involved in the metabolism of several drugs that show cardiotoxicity. It is our hypothesis that the cardiotoxicity of these drugs is in part due to modulation of CYP2J2-mediated AA metabolism. Herein, we show that the metabolism of AA by CYP2J2 is inhibited by DOX, a cardiotoxic drug (Figure 3.2 and Figure 3.7). This is the first direct measurement of AA inhibition by a cardiotoxic drug for any mammalian CYP epoxygenase. We have determined that DOX potently inhibits AA metabolism by CYP2J2. The mode of inhibition by DOX is competitive, as at saturating concentrations it almost completely inhibits CYP2J2's AA metabolism. The residual AA metabolism at saturating concentrations is most likely due to the conversion of DOX to 7-de-aDOX during the experiment. Furthermore, FP binding demonstrates that DOX binds CYP2J2 in a one-site model and is competitively inhibited by EBS and weakly by AA (Figure 3.4, Table 3.1).

7-de-aDOX, however, shows an incomplete inhibition at saturating concentrations (Figure 3.2) indicating a second binding site. As determined by FP measurements, AA very weakly inhibits 7-de-aDOX binding to CYP2J2 and EBS does not inhibit 7-de-aDOX binding, despite EBS inhibiting DOX binding (Figure 3.4, Table 3.1). These data demonstrate that 7-de-aDOX concurrently binds with EBS and AA. While the inhibition of AA metabolism by DOX and 7-de-aDOX is the most pronounced effect, there is a significant change in the regioselectivity of AA epoxidation by CYP2J2 in the presence of DOX and 7-de-aDOX (Figure 3.3). The ratio of 5,6-EET and 8,9-EET increases with a concomitant decrease of 11,12-EET and 14,15-EET. The regioselective changes are likely due to 7-de-aDOX. As DOX demonstrates one-site, competitive binding, the regioselective change observed with DOX may be consequence of its conversion to 7-de-aDOX during the CYP2J2-mediated AA metabolism studies.

Although AA and EBS are structurally dissimilar substrates, the effects of DOX and 7-de-aDOX on EBS metabolism parallel those to AA (Figure 3.4). DOX inhibits EBS metabolism similarly as the inhibition of AA, and demonstrates competitive inhibition. Interestingly, 7-de-aDOX does not inhibit EBS metabolism, and therefore these two molecules are capable of concurrently binding CYP2J2 as supported by kinetics and FP measurements. These studies highlight the importance of determining the effects of cardiotoxic drugs directly on AA metabolism by CYP2J2 instead of using probe substrates such as EBS. The partial inhibition and

regioselective changes to AA in the presence of 7-de-aDOX did not manifest with EBS and therefore the effects of 7-de-aDOX on AA metabolism would have been overlooked if EBS was used as the probe substrate.

We further determined that CPR metabolizes DOX to 7-de-aDOX while CYP2J2 does not directly metabolize DOX or 7-de-aDOX. This might be explained by the lack of available sites for metabolism. The NADPH oxidation rate increases on DOX binding to CYP2J2 which indicates that CYP2J2 assists in reduction of DOX similar to CYP2B1.[286]

These experimental observations are further supported by MD simulations. DOX occludes most of the active site volume and does not allow for AA to bind (Figure 3.7). 7-de-aDOX, however, binds rather rigidly at the PUFA binding pocket we had previously determined (Figure 3.6).[289] This rigidity in binding is confirmed by our FP measurements (Figure 3.4), which show that 7-de-aDOX has greater restriction to rotation in the active site compared to DOX. When bound at the active site, 7-de-aDOX positions the binding of AA to favor the formation of 5,6-EET and 8,9-EET. However, since EBS does not bind near this PUFA binding pocket, it is not perturbed by the binding of 7-de-aDOX (Figure 3.6C). Taken together, DOX and 7-de-aDOX modulate CYP2J2-mediated AA metabolism by inhibiting AA metabolism and by altering the binding of AA to make epoxidation towards the carboxyl head of AA more favorable.

The MD data suggests that the A ring, especially carbons C13 and C14 in 7-de-aDOX is instrumental in perturbing the binding of AA, which produces the regioselective change in the AA epoxidation. It is important to note that the DOX analogues that are least cardiotoxic all have major modifications to carbons C13 and C14, whereas modifications to other parts of the molecule retained cardiotoxicity.[1]

DOX has been shown to reduce EET levels in acute doses in both liver and heart of rats.[306-308] Herein, we present a different mechanism (Figure 3.8) based on our data by which DOX may alter AA metabolism in humans, namely, through direct inhibition of CYP2J2 and the binding of 7-de-aDOX that concurrently changes the EET regioselectivity. DOX generates ROS that initiates an assault on cardiac cells. Additionally, DOX also inhibits CYP2J2-mediated AA metabolism leading to a decrease in cardioprotective EETs. DOX is converted to 7-de-aDOX by CPR and other reductases. 7-de-aDOX continues to inhibit CYP2J2-mediated AA metabolism and also concurrently binds CYP2J2 to alter the EET ratio, promoting 5,6-EET production. Compared to less cardiotoxic analogues of DOX, 5-IDN weakly inhibits CYP2J2 and ZRN inhibits CYP2J2 as

strongly as DOX. Both 5-IDN and ZRN do not change the EET regioisomers ratio significantly. 5-IDN is known to produce less ROS than DOX. ZRN produces ROS, although is not cardiotoxic.

Currently, the impact that altering the EET ratios has on the cardiovascular system is not well-understood. The four EET regioisomers have differing affinities for their downstream targets and can also uniquely activate other pathways.[54,290,309] For instance, 11,12-EET was found to most potently decrease TNF-α levels in human endothelial cells, with 5,6-EET being the weakest; 14,15-EET had no effect.[42] 5,6-EET and 8,9-EET have been shown to be both vasoconstrictory and vasodilatory depending on tissue, which has been hypothesized to be mediated by their conversion to pro-inflammatory lipid mediators by COX-2.[292,293] 8,9-EET and 11,12-EET signal proliferation through the p38 MAPK pathway, whereas 5,6-EET and 14,15-EET signal proliferation through the PI3K pathway.[310] Finally, as aforementioned, 8,9-EET was found to not reduce myocardial infarct size.[68] It is possible that the modulation of the EET ratio alters the homeostasis in the vasculature. This may then further exacerbate the toxicity of DOX in conjunction to the overall inhibition of EET production. If this is true, then this can also help to explain the reduced cardiotoxicity with ZRN and 5-IDN, insofar as they do not produce a significant EET regioselectivity change.

Therefore, while the overall inhibition of AA metabolism by DOX and 7-de-aDOX would prevent the cells from recovering from DOX-induced cardiotoxicity, the alteration of the EET ratios may be a novel pathway of cardiotoxicity that needs to be tested further. Moreover, the differential effects of the DOX/7-de-aDOX on CYP2J2-mediated metabolism of AA and EBS demonstrates a need for screening of cardiotoxicity using endogenous probe substrates. These data provide valuable insight into drug design and investigating cardiotoxic drug interactions through CYP2J2.

3.5 Figures and table

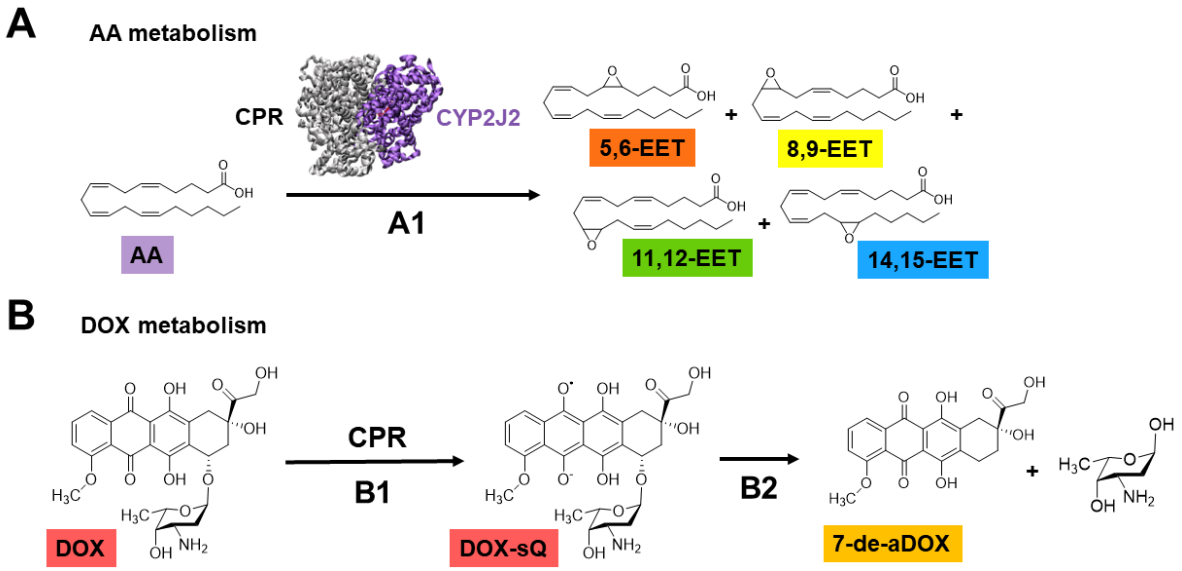

Figure 3.1. Schematic of DOX and AA metabolism by CYP2J2 and CPR. (A) CYP2J2-CPR metabolizes arachidonic acid (AA) into four regioisomers of epoxyeicosatrienoic acids (EETs) (A1). (B) CPR reduces doxorubicin (DOX) to a semiquinone (DOX-sQ) (B1) that leads to the formation of ROS and the reductive aglycosylation of DOX to form 7-deoxydoxorubicin aglycone (7-de-aDOX) (B2).

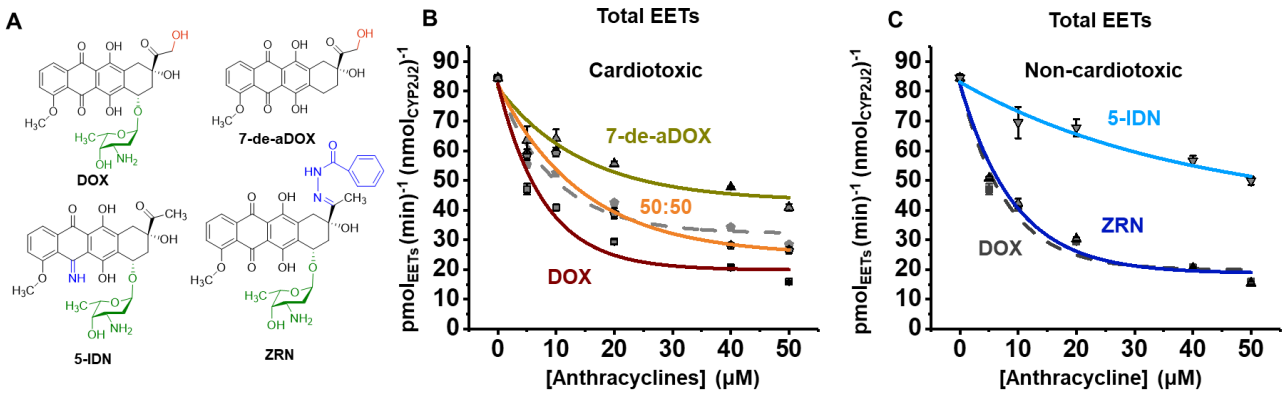

Figure 3.2. AA Inhibition by DOX, 7-de-aDOX, and the non-toxic analogues ZRN and 5-IDN. (A) Structures of the anthracyclines doxorubicin (DOX), 7-deoxydoxorubicin aglycone (7-de-aDOX), 5-iminodaunorubicin (5-IDN), and zorubicin (ZRN). (B) Rate of epoxidation of 100 μM AA to EETs by CYP2J2-CPr in the presence of increasing concentrations of cardiotoxic DOX, 7-de-aDOX, or a 50:50 mixture of DOX:7-de-aDOX. The theoretical fit based on the linear combination of DOX and 7-de-aDOX is shown as a grey, dashed line to demonstrate the overlap of the theoretical fit to the experimental (see Results for details). (C) Rate of epoxidation in the presence of non-cardiotoxic analogues, zorubicin (ZRN) and 5-iminodaunorubicin (5-IDN) with the DOX data from panel (B) shown in grey for comparison. 100 μM of AA was used in all experiments. Concentrations of anthracyclines represent the total amount of anthracyclines present. All inhibition data fit to eq S1. Error represents the SEM of 3 experiments.

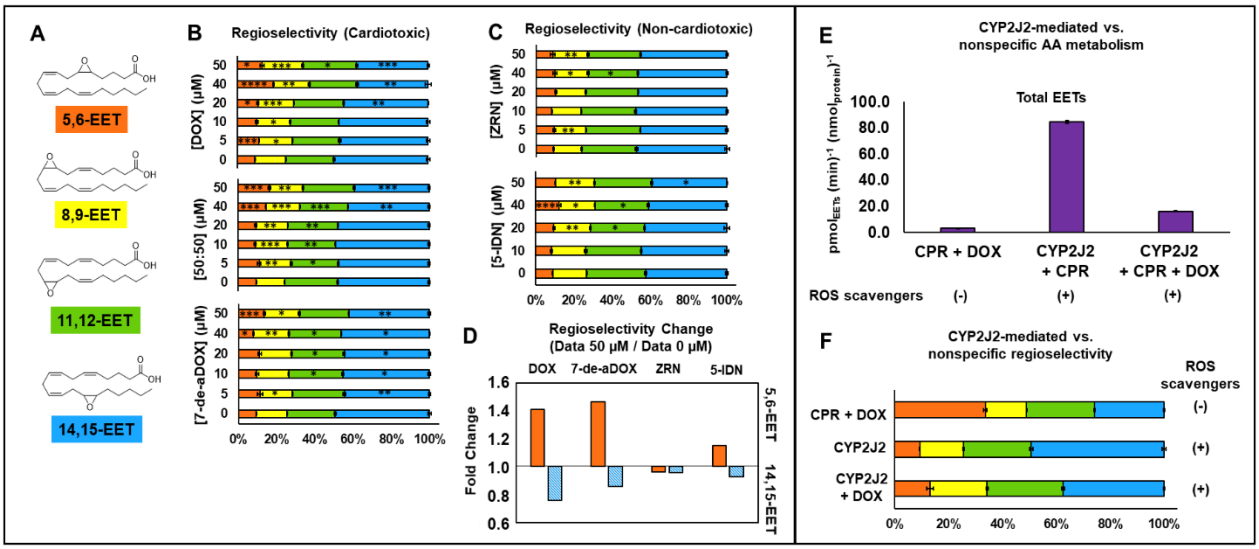

Figure 3.3. Regioselectivity of the epoxidation of AA by CYP2J2 in the presence of anthracyclines. (A) EET regioisomers. (B) Regioselectivity of EETs in the presence of DOX, 7-de-aDOX, and the 50:50 mixture of DOX:7-de-aDOX. Each EET is shown as a percentage of the total EETs. The colors of the bars represent the colors associated with EETs in panel (A). (C) Regioselectivity of epoxidation in the presence of ZRN and 5-IDN. (D) Fold-change of the regioselectivity for 5,6-EET and 14,15-EET of the data in Panels (B) and (C). Fold change = (Percent of regioisomer in the presence of 50 μM anthracycline) / (Percent of regioisomer in the presence of 0 μM anthracycline). Data presented in (A-D) is obtained from the same dataset as presented in Figure 3.2. (E) Rate of epoxidation of AA by CYP2J2 and/or CPR in presence and absence of ROS scavengers. Rates are normalized to the amount of CPR (0.3 nmol) or CYP2J2 (0.3 nmol). (F) Regioselectivity of epoxidation by CYP2J2 vs. nonspecific epoxidation. In all these experiments 50 μM DOX and 100 μM of AA was used. Concentrations of anthracyclines represent the total amount of anthracyclines present. Error represents the SEM of 3 experiments. P values: * < 0.05; ** < 0.01; *** < 0.001; **** < 0.0001.

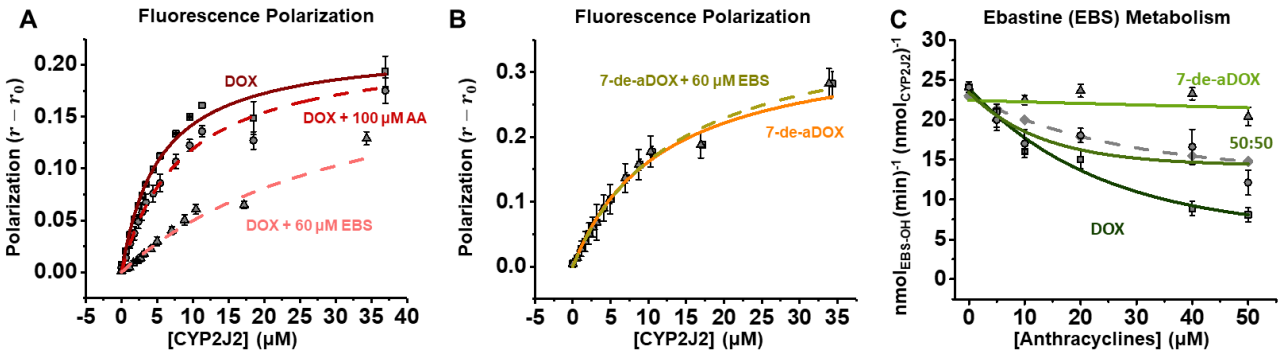

Figure 3.4. Binding and metabolism studies of DOX and 7-de-aDOX. (A-B) Fluorescence polarization measurements of DOX (A) and 7-de-aDOX (B) binding to CYP2J2. Both DOX and 7-de-aDOX demonstrate one-site binding (eq 1). Binding was repeated in the presence of 60 µM ebastine (EBS) or 100 µM AA. DOX data in the presence of EBS or AA fit to a competitive binding model and 7-de-aDOX is fitted to eq 1 (no inhibition). For all experiments, [DOX] and [7-de-aDOX] = 1 µM. (C) EBS metabolism in the presence of DOX, 7-de-aDOX, and a 50:50 mixture of DOX:7-de-aDOX. DOX data fit to eq S1 and 7-de-aDOX data is linear. The theoretical fit based on the linear combination of DOX and 7-de-aDOX is shown as a grey, dashed line to demonstrate the closeness of the theoretical fit to the experimental fit. Concentrations of anthracyclines represent the total amount of anthracyclines present. Error represents ± SEM of 3 experiments.

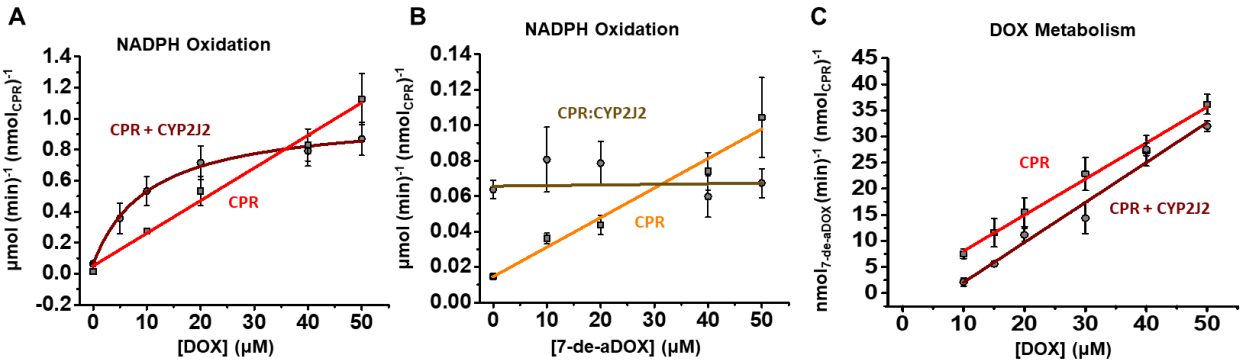

Figure 3.5. *Dox metabolism kinetics.* (A) Rate of NADPH oxidation by CPR (red, squares) and by CPR with CYP2J2 (dark red, circles) to reduce DOX. CPR displayed linear kinetics towards the reduction of DOX (equation shown on plot) and the presence of CYP2J2 displayed one-binding-site kinetics. (B) Rate of NADPH oxidation by CPR (orange, squares) and by CPR with CYP2J2 (gold, circles) to reduce 7-de-aDOX. (C) DOX metabolism to 7-de-aDOX by CPR and in the presence of CPR + CYP2J2. Concentrations of anthracyclines represent the total amount of anthracyclines present. Error represents ± SEM of 3 experiments.

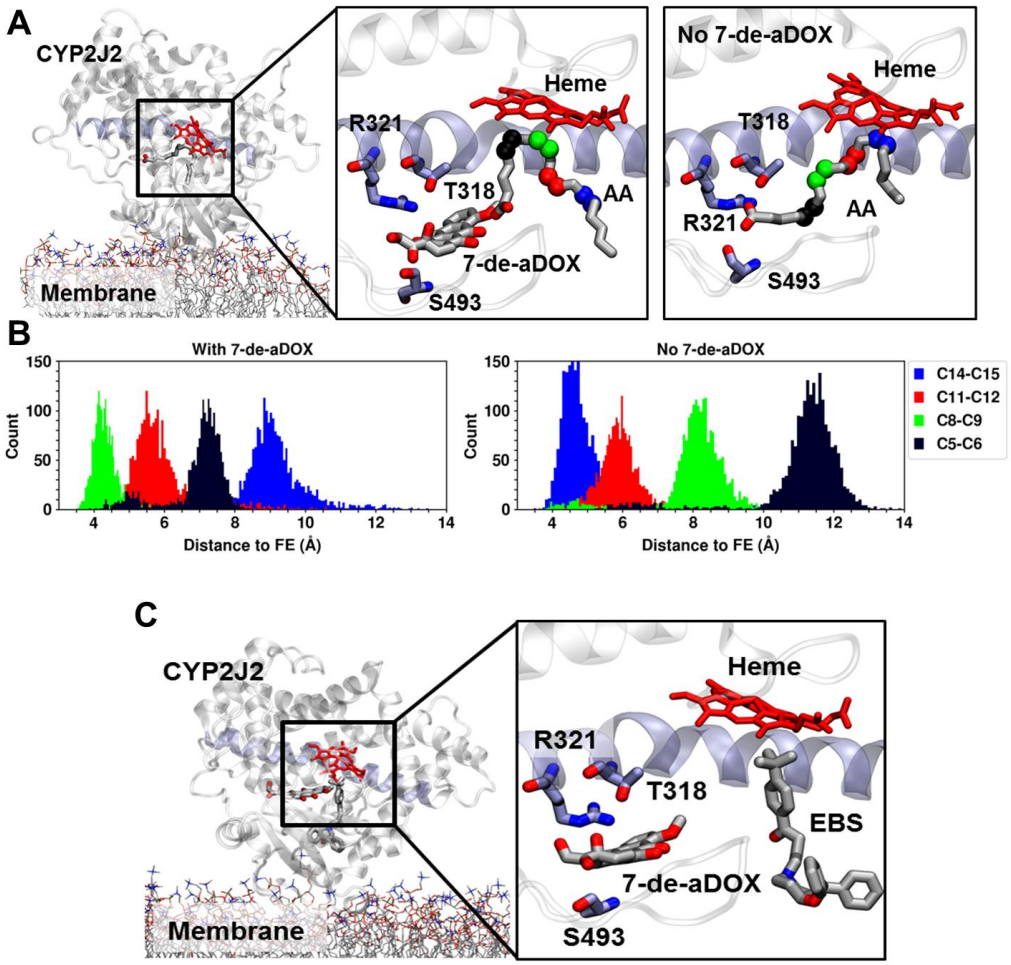

Figure 3.6. Effect of 7-de-aDOX on AA orientation in CYP2J2 simulations. (A) Representative snapshots (i.e., most often observed configuration) of the active site of membrane-bound CYP2J2 in complex with AA/7-de-aDOX in with AA only. Membrane Lipids are shown in stick representation. CYP2J2 in cartoon representation, with helix I (longest helix in CYP2J2) in purple cartoon. AA and 7-de-aDOX molecules are shown as sticks. Residues involved in AA interactions as previously reported are also shown as sticks. Carbons involved in epoxidation are highlighted as spheres, with colors corresponding to the distributions shown in the next panel. (B) Distribution of carbon-to-heme distances obtained from 200 ns MD simulations for the main epoxidation sites of AA. Colors correspond to the spheres shown in (A). (C) Representative snapshot obtained from molecular docking of EBS to the CYP2J2/7-de-aDOX structure obtained from MD simulations. Docking shows that EBS can be accommodated in a productive orientation (i.e., with its methyl groups close to the heme) with 7-de-aDOX bound to CYP2J2 without hindrance.

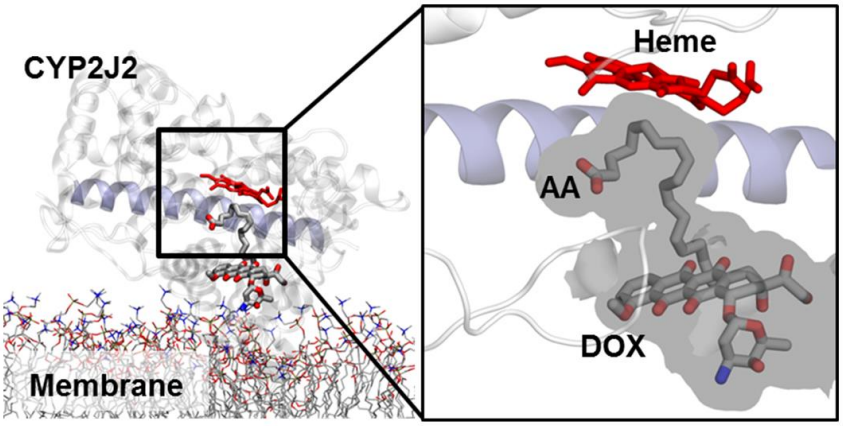

Figure 3.7. Representative snapshot (i.e., most often observed configuration) of DOX docked pose obtained from docking to membrane-bound CYP2J2-AA structures, with AA located close to the heme (see Methods). The volume available is shown as a grey surface, surrounding the two ligands. The docked poses reveal that DOX cannot be accommodated within the active site when AA is present, and is located away from the heme and at the entrance of the substrate access channel (with center of mass distance ~17 Å).

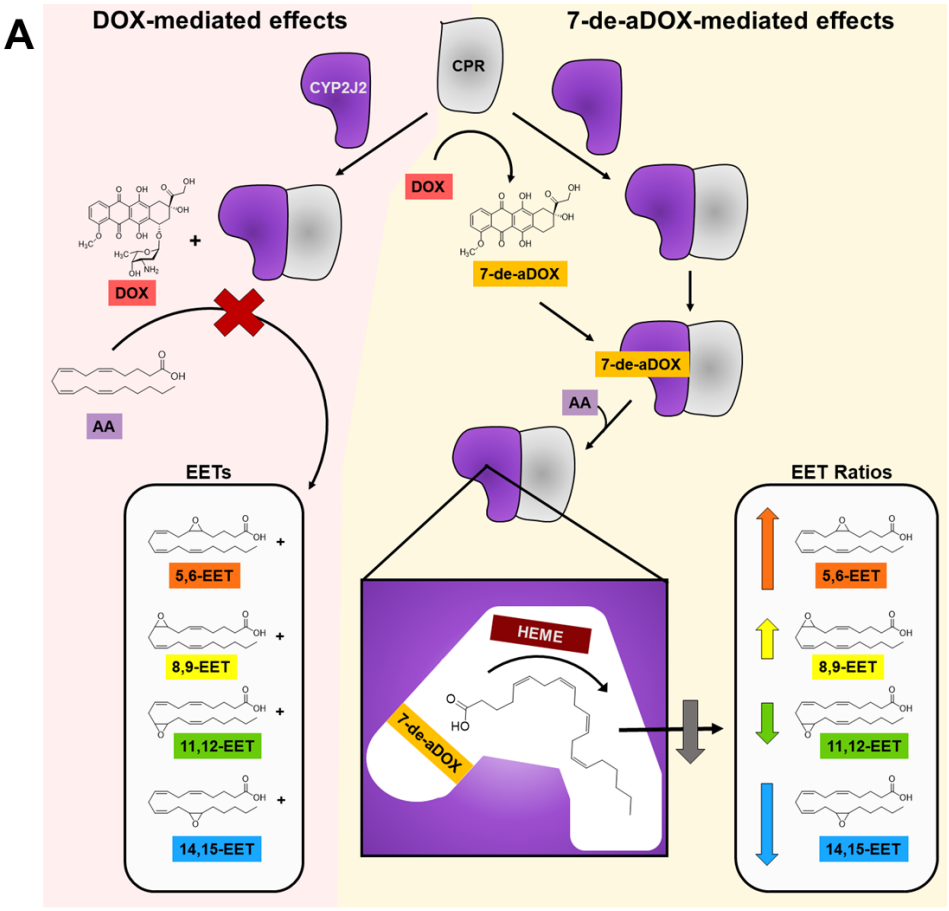

B

	Inhibition of AA	Conversion to aglycone	Altered EET regioselectivity
DOX	Strong	Fast	Yes
5-IDN	Weak	Slow	No
ZRN	Strong	Fast	No

Figure 3.8. Summary DOX-mediated and 7-de-aDOX-mediated effects on AA metabolism by CYP2J2. (A) DOX-mediated effects. DOX binding from all data displays one-site, competitive inhibition of AA metabolism. When bound to the active site of CYP2J2, DOX occupies a majority of the volume and prevents AA from binding and being converted to EETs. 7-de-aDOX-mediated effects. DOX is reduced to 7-de-aDOX by CPR. 7-de-aDOX then binds into the active site of CYP2J2 into a pocket that directs AA binding. This positions AA with Carbons C5, C6, C8, and C9 closest to the heme. The result is an incomplete inhibition of AA metabolism with a larger percentage of 5,6-EET and a lower percentage of 14,15-EET in the total EETs present. (B) Summary of CYP2J2-mediated AA metabolism by all anthracyclines studied.

Table 3.1. Calculated fitting parameters of the fluorescence polarization data of DOX and 7-de-aDOX binding (Figure 3.4). K_i refers to the inhibition of DOX or 7-de-aDOX by either AA or EBS as indicated. Error represents the SEM of 3 experiments.

	Summary of Binding Parameters			
	r_0	r_1	K_D (μM)	K_i (μM)
DOX				
DOX	0.083 ± 0.007	0.219 ± 0.010	5.32 ± 0.89	---
DOX + AA	0.094 ± 0.005	---	---	176 ± 64
DOX + EBS	0.101 ± 0.003	---	---	13.8 ± 1.6
7-de-aDOX				
7-de-aDOX	0.055 ± 0.006	0.351 ± 0.022	13.1 ± 1.1	---
7-de-aDOX + AA	0.084 ± 0.002	---	---	210 ± 26
7-de-aDOX + EBS	0.159 ± 0.006	0.383 ± 0.021 (*app*)	13.4 ± 1.4 (*app*)	∞

3.6 Supplementary information

Methods

Materials. Human CYP2J2 cDNA was obtained from OriGene (Catalog No. SC321730) and modified.[250] Ampicillin, arabinose, chloramphenicol, isopropyl β-D-1-thiogalactopyranoside (IPTG), and Ni-NTA resin were obtained from Gold Biotechnology and Sigma. δ-aminolevulinic acid was obtained from Frontier Scientific. NADPH and $NADP^+$ were obtained from P212121.com. 1-palmitoyl-2-oleoyl-sn-glycero-3-phosphocholine (POPC) and 1-hexadecanoyl-2-(9Z-octadecenoyl)-sn-glycero-3-phospho-L serine (POPS) were purchased from Avanti Polar Lipids, Inc. AA; 5,6-EET; 8,9-EET; 11,12-EET; 14,15-EET; 19-HETE; and 20 HETE were obtained from Cayman Chemical. Doxorubicin was obtained from Santa Cruz Biotech (experimental purposes) and Cayman Chemical (synthetic purposes). 7-deoxy-doxorubicin aglycone was purchased from Toronto Research Chemicals and was spectroscopically pure (as determined by LC-MS/MS). Zorubicin was obtained from the National Cancer Institute. All other materials and reagents used were purchased from Sigma and Fisher Scientific.

Recombinant expression of CYP2J2 in E. coli. Expression of recombinant D34-CYP2J2, a 34-residue N-terminal deletion modification (residues 3-37) with a L2A residue mutation and a His_5 tag that which does not show significant activity changes compared to WT, was prepared as previously described.[243,250,289] CYP2J2 *in vitro* experiments were performed in a 50 μM 20% POPS (20mol:80mol POPS:POPC) reconstituted system as previously described.[311]

Expression and purification of cytochrome P450 reductase. Expression of cytochrome P450 reductase (CPR) was described previously.[250]

Expression and purification of cytochrome b5 (CYB5). E. coli expressing CYB5 were a gift from Dr. Sligar and the expression and purification of CYB5 was performed as previously described.[312]

LC-MS/MS quantification of EETs. EETs were quantified using a 5500 QTRAP LC/MS/MS system (Sciex, Framingham, MA) in Metabolomics Lab of Roy J. Carver Biotechnology Center, University of Illinois at Urbana-Champaign, as previously described.[3]

Reductive synthesis of 7-deoxy-doxorucibicin aglycone (7-de-aDOX) from DOX. 7-de-aDOX was synthesized from the parent compound (DOX) by reductive aglycosylation of the daunosamine sugar moiety. Dithonite was aliquoted anaerobically in a Coy glove box and used as the reducing agent. 100 μM DOX was reacted outside the glove box for 10 min at 37°C with $FeCl_3$ and dithionite in a 1:1:10 molar ratio in 0.1 M KPi buffer (pH 7.4) to optimize dithionite reactivity. The products were extracted thrice with equivolume ethyl acetate, dried under N_2, and resuspended in acetonitrile for HPLC purification. Purification was achieved using the HPLC method (see main text) The reaction produced 4 minor products (19.2, 20.2, 23.7 and 25.7 min elution times) and the major product (21.7 min) was identified as 7-de-aDOX by comparing elution time and MS/MS fragmentation pattern against an authentic standard (see above). Yield = 72%.

Ebastine (EBS) metabolism kinetics. The kinetics of EBS metabolism by CYP2J2 with and without DOX were determined using our previously reported method[289] with the following modifications. CYP2J2 and CPR (0.6 μM each) were incubated in a 20% POPS lipid reconstituted system in 0.5 mL of potassium phosphate buffer (pH 7.4). The entire system was preincubated with 20 μM EBS with varying concentrations of DOX or 7-de-aDOX (0-50 μM from 1 mM and 10 mM stocks in DMSO) for 10 min. Reactions were started with 6 mM NADPH and terminated after 0.75 min with 100 μL acetic acid. Metabolites were extracted as previously described[289] and resuspended in 100 μL of Mobile Phase A (see below) for HPLC quantification. EBS metabolism under these conditions was determined to be linear up to 1 min, after which CYP2J2 began to significantly oxidize the mono-oxygenated product, hydroxyebastine, to carebastine.

EBS metabolism quantification. EBS metabolism to hydroxyebastine and carebastine was determined using a modification of a previously published method.[313] An HPLC system consisting of an Alliance 2695 analytical separation module (Waters, Milford, MA) and a Waters 996 photodiode diode array detector (Waters) was used for the separation and quantification of EBS metabolites. Samples were separated and quantified using reverse-phase HPLC with an Alltech 5μm 250 x 4.6 mm CN column (Cat. No. 605CN). Mobile Phase A consisted of a 20:30:48 V:V:V solution of acetonitrile:methanol:ammonium acetate buffer. Mobile Phase B consisted of 100% acetonitrile. Metabolites were separated using a linear-gradient of 100% A to 50% A over a 30-

minute period with a 1 mL/min flow rate and a column temperature of 40° C. Carebastine, hydroxyebastine, and ebastine elute at 14.5, 17.5, and 21.5 min, respectively. Metabolites were quantified using an EBS authentic standard curve at the UV wavelength of 254 nm.

IC_{50} value determinations. IC_{50} values were determined by fitting the data to equation (S3.1) and were calculated from the fits using equation S3.2

$$y = e^{(a-b)} + y_0 \qquad \text{(Equation S3.1)}$$

$$IC_{50} = \frac{\ln(2)}{b} \qquad \text{(Equation S3.2)}$$

K_i values were calculated from the IC_{50} values using the Cheng-Prusoff equation[314] (eq S3.3).

$$K_i = \frac{IC_{50}}{1+\frac{[S]}{K_m}} \qquad \text{(Equation S3.3)}$$

REFERENCES

(1) McDougle, D. R.; Palaria, A.; Magnetta, E.; Meling, D. D.; Das, A. *Protein Sci* **2013**, *22*, 964.

(2) Zelasko, S.; Palaria, A.; Das, A. *Protein Expres Purif* **2013**, *92*, 77.

(3) Arnold, W. R.; Baylon, J. L.; Tajkhorshid, E.; Das, A. *Biochemistry* **2016**, *55*, 6969.

(4) McDougle, D. R., Palaria, A., Magnetta, E., Meling, D.D, and Das, A. *Protein Science* **2013**.

(5) Mulrooney, S. B.; Waskell, L. *Protein Expr Purif* **2000**, *19*, 173.

(6) Matsuda, M.; Mizuki, Y.; Terauchi, Y. *J Chromatogr B* **2001**, *765*, 205.

(7) Cheng, Y.; Prusoff, W. H. *Biochem Pharmacol* **1973**, *22*, 3099.

Figures

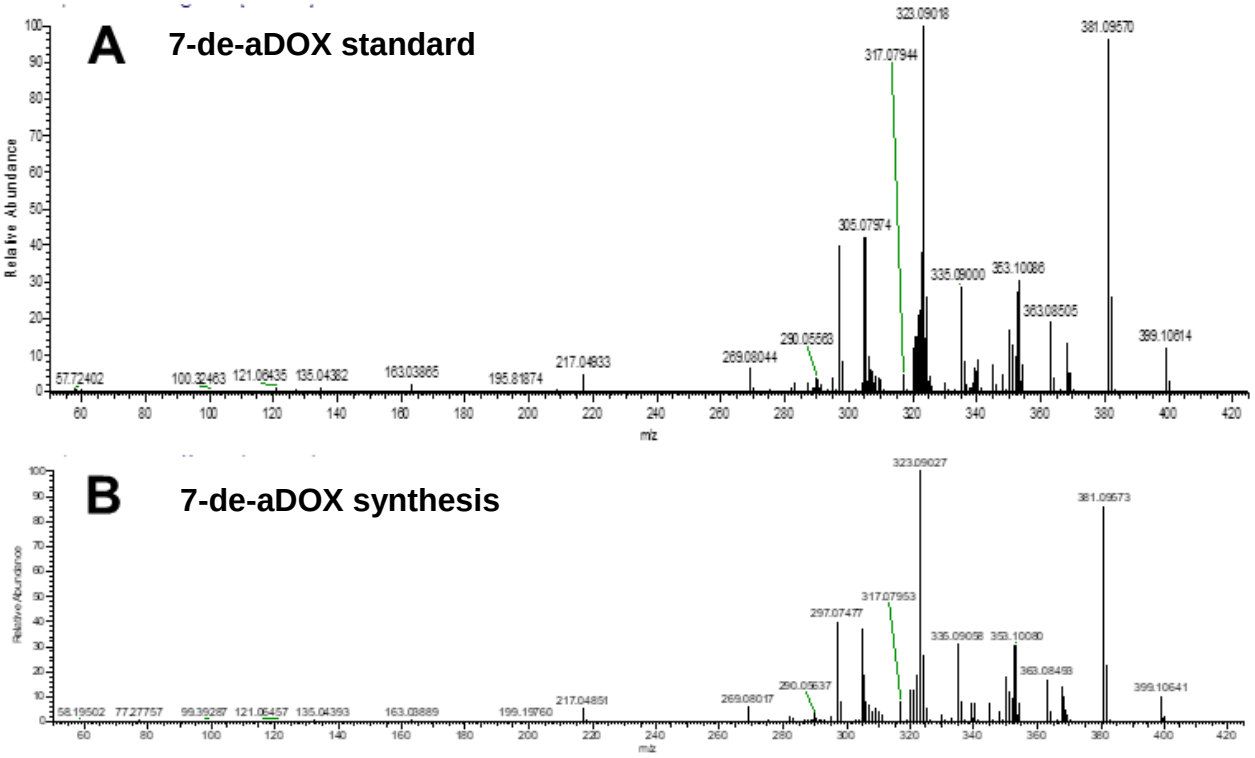

Supplementary Figure 3.1. *MS/MS analysis of reductive 7-de-aDOX synthesis*. (A) MS/MS chromatogram of 7-de-aDOX standard. (B) MS/MS chromatogram of 7-de-aDOX synthesis product. Products were separated by HPLC chromatography as stated in the Methods section.

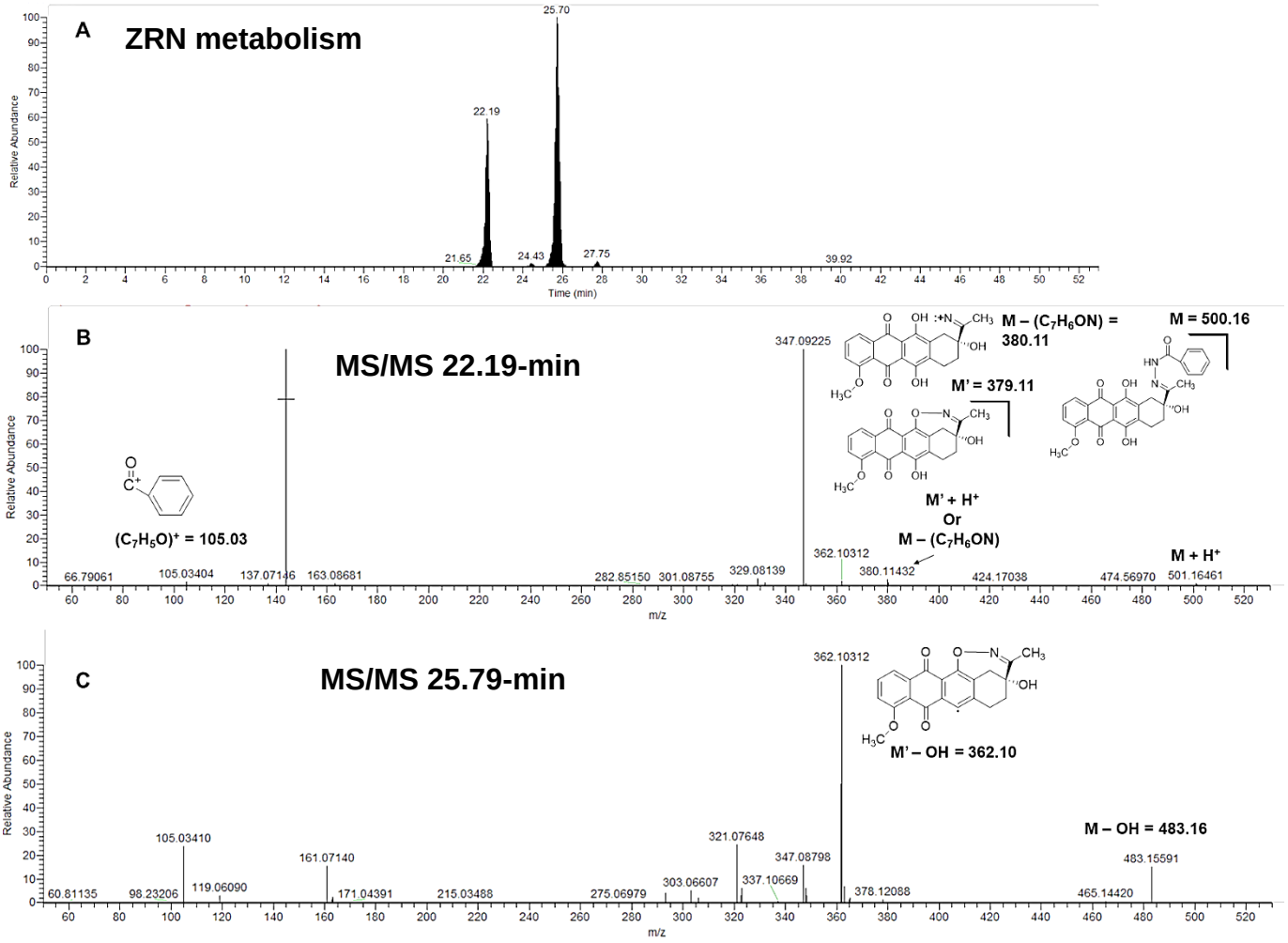

Supplementary Figure 3.2. *LC-MS/MS analysis of ZRN aglycone formation*. (A) Chromatogram of ZRN metabolism showing masses corresponding to the 7-deoxy aglycone analogue of ZRN in positive ion mode (501.16563 m/z $\pm$ 5 ppm). (B) MS/MS fragmentation of 22.19-min peak. (C) MS/MS fragmentation of 25.79-min peak. Corresponding fragmentation m/z for selected ions given.

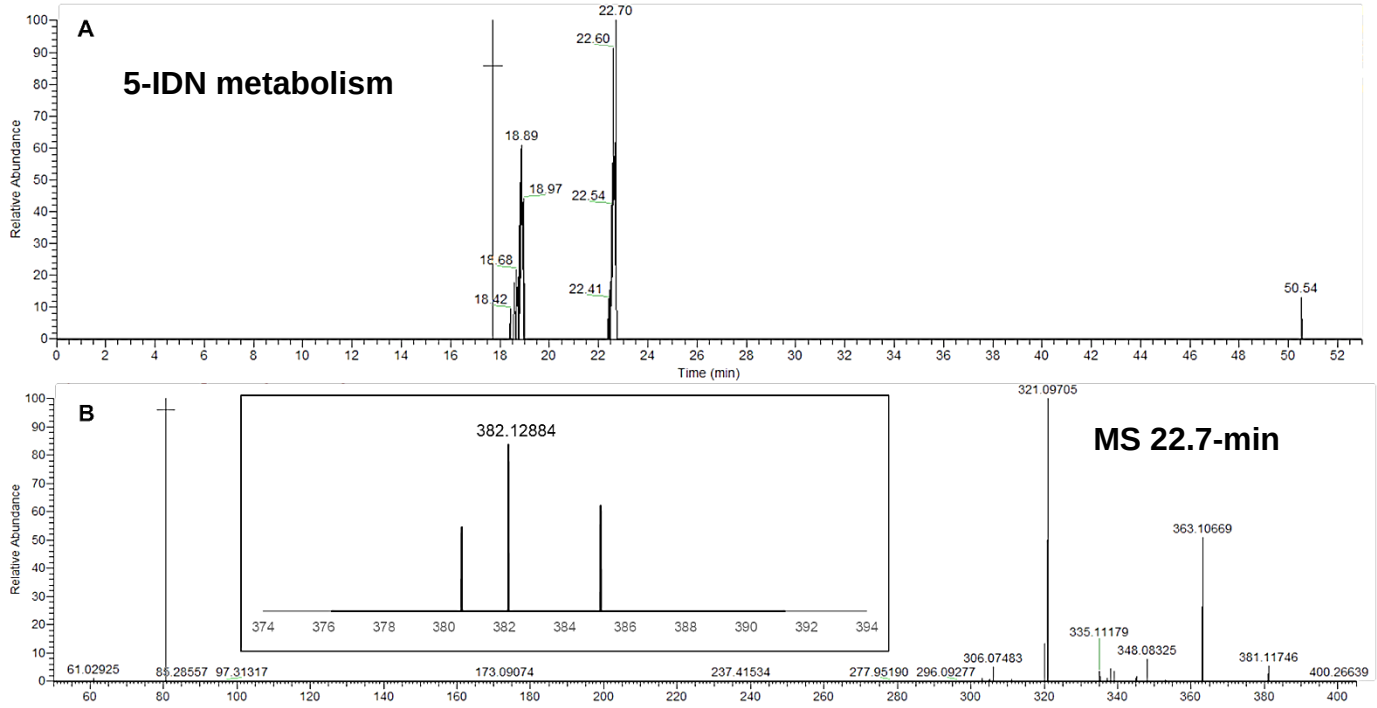

Supplementary Figure 3.3. *LC-MS/MS analysis of 5-IDN aglycone formation*. (A) Chromatogram of 5-IDN metabolism showing masses corresponding to the 7-deoxy aglycone analogue of 5-IDN in positive ion mode (382.12851 m/z $\pm$ 5 ppm). The peak at 18.89 min was determined to be the fragmentation of 5-IDN to the aglycone. (B) MS spectrum of 22.70-min peak. Insert is a magnification of the mass range corresponding to the aglycone. This ion was too low of abundance for MS/MS analysis.

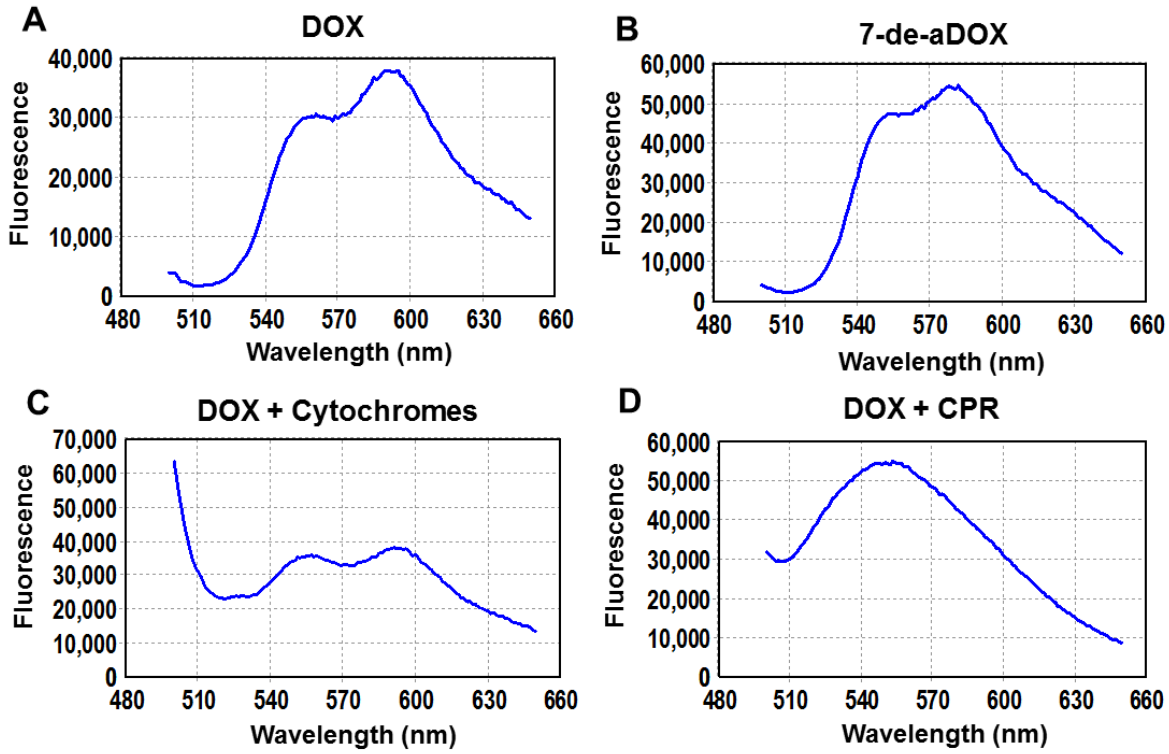

Supplementary Figure 3.4. *DOX fluorescence spectra.* Fluorescence of (A) DOX and (B) 7-de-aDOX is similar. (C) Representative fluorescence of DOX after a CYP2J2 titration. All other hemoproteins showed similar spectra. The presence of the heme (proteins) does not significantly alter DOX or 7-de-aDOX fluorescence. (D) DOX fluorescence in the presence of CPR is occluded by the intrinsic fluorescence of CPR. All spectra were obtained with 1 μM of analyte and were excited at 480 nm wavelength.

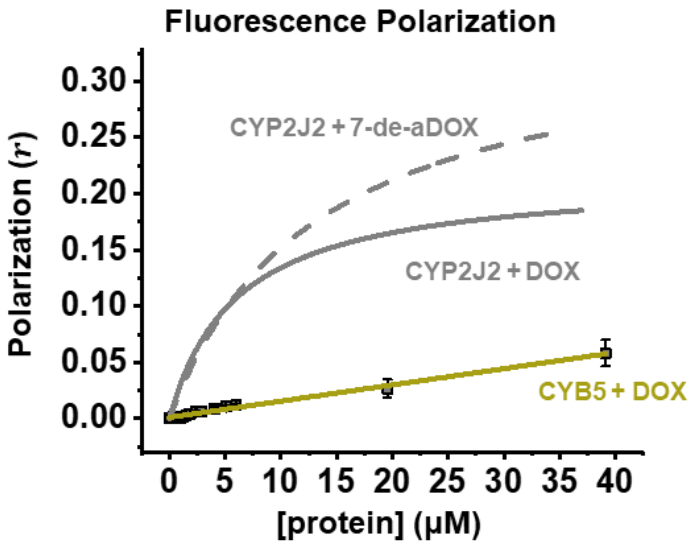

Supplementary Figure 3.5. *Fluorescence polarization data for cytochrome b5 (CYB5).* DOX polarization in the presence of CYB5 is compared to DOX and 7-de-aDOX polarization (Figure 3.4) in the presence of CYP2J2. CYB5 data fits to a linear model and demonstrates nonspecific binding. Data represents the SEM of 3 experiments.

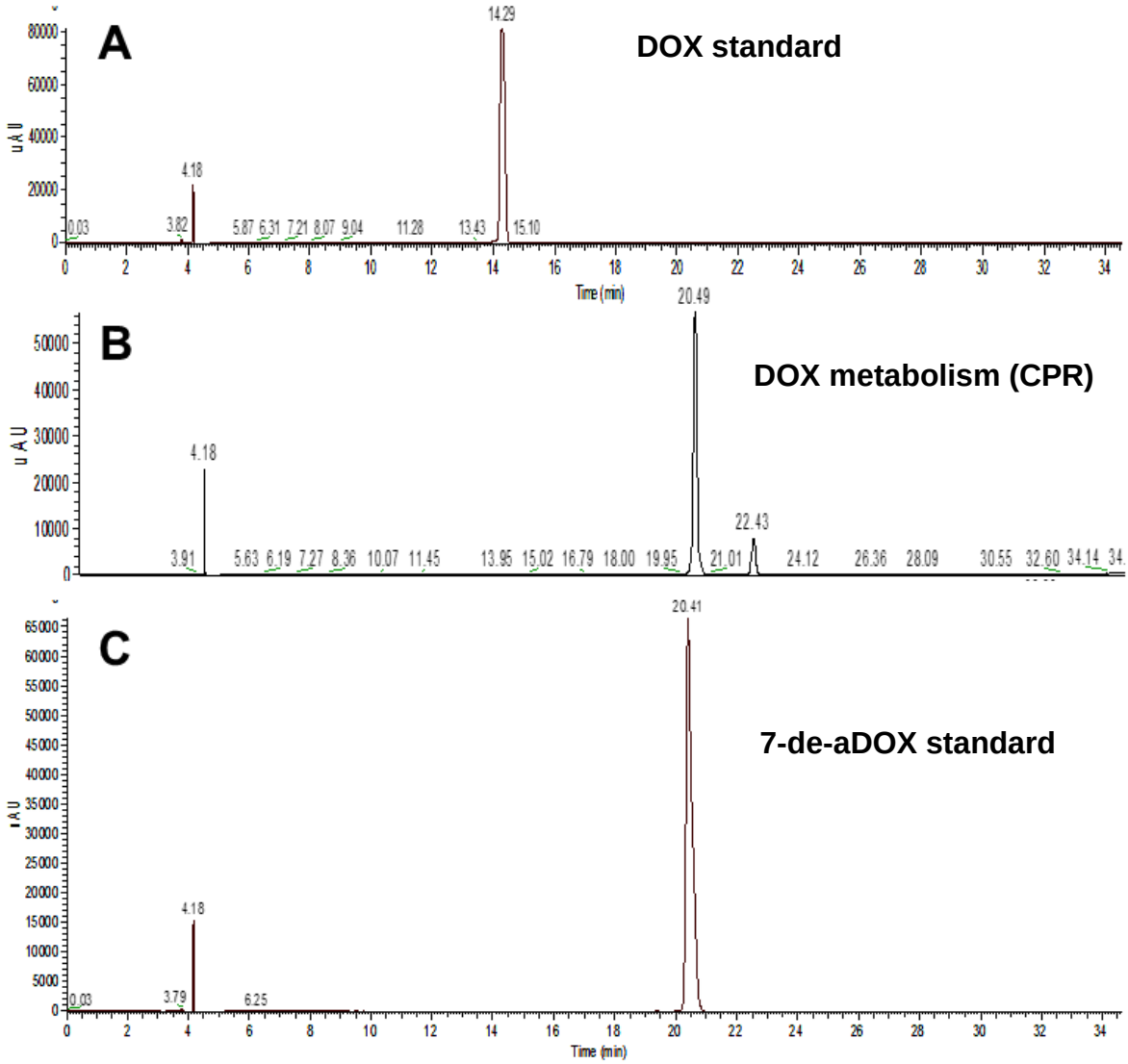

Supplementary Figure 3.6. *HPLC chromatograms of doxorubicin and 7-deoxydoxorubicin aglycone*. (A) Doxorubicin standard. (B) CPR-mediated metabolism of doxorubicin after full conversion. The major peak (20.5 min) and minor peak (22.4 min) are representative of digests with CPR and CPR + CYP2J2. (C) 7-deoxydoxorubicin aglycone standard.

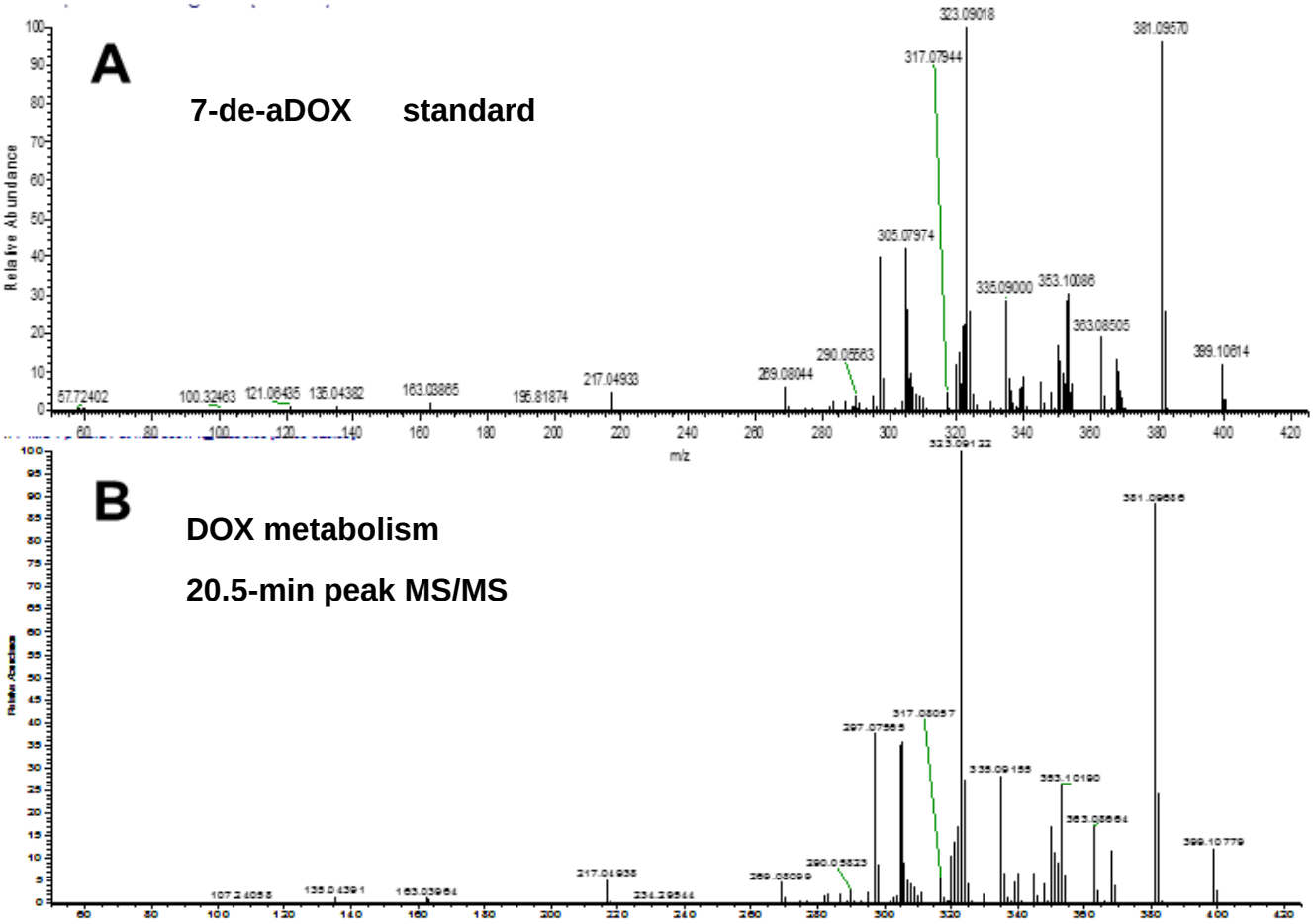

Supplementary Figure 3.7. *MS/MS chromatograms of 7-deoxydoxorubicin aglycone.* (A) 7-deoxydoxorubicin standard. (B) CPR-mediated metabolism fragmentation of major (20.5 min) peak.

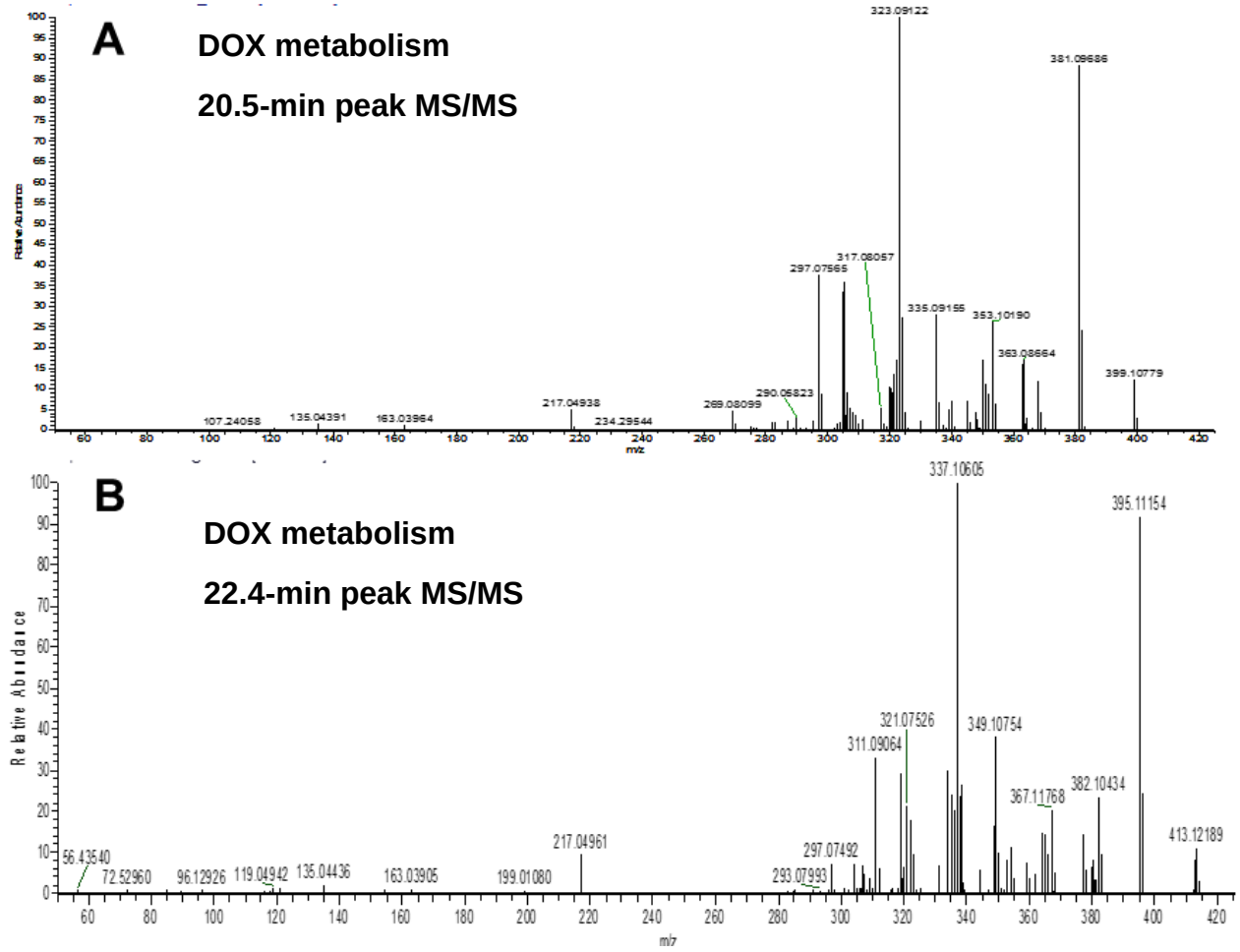

Supplementary Figure 3.8. *MS/MS chromatograms of CPR-mediated doxorubicin metabolism.* (A) Major (20.5 min) peak from Supplementary Figure 3.6B. (B) Minor (22.4 min) peak.

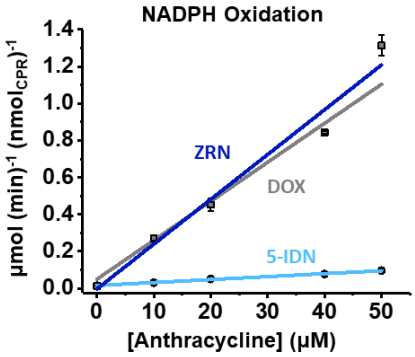

Supplementary Figure 3.9. Rate of NADPH oxidation with ZRN or 5-IDN and CPR. The DOX data from Figure 3.5A is shown as grey for comparison. Error represents the SEM of 3 experiments.

Table

Supplementary Table 3.1. Table of kinetic parameters for the NADPH oxidation data (Supplementary Figure 3.7) and DOX metabolism (Figure 3.3C). Parameters for linear fits are given in parenthesis, and values for the one-binding site (Michaelis-Menten) are without parentheses. Error represent the SEM of 3 experiments. Rates for NADPH data are μmol_{NADPH} $(min)^{-1}$ $(nmol_{CPR})^{-1}$ and for DOX metabolism rates are $nmol_{7\text{-}de\text{-}aDOX}$ $(min)^{-1}$ $(nmol_{CPR})^{-1}$

		Summary of Kinetic Parameters		
	Fit	v_0 **(*b*)**	v_1 **(*m*)**	K_M **(μM)**
NADPH (DOX)				
CPR	Linear	(0.0499 ± 0.0416)	(0.0211 ± 0.0014)	---
CPR:CYP2J2	One-site	0.0599 ± 0.0249	0.961 ± 0.042	10.4 ± 1.6
NADPH (7-de-aDOX)				
CPR	Linear	(0.0148 ± 0.0007)	$(0.00166 \pm 0.\ 0002)$	---
CPR:CYP2J2	Linear	(0.0656 ± 0.0042)	$[(3.08 \pm 1.37) \times 10^{-5}]$	---
NADPH (ZRN)				
CPR	Linear	$-(0.00256 \pm 0.071)$	(0.0242 ± 0.0024)	---
NADPH (5-IDN)				
CPR	Linear	(0.0158 ± 0.001)	(0.0016 ± 0.0001)	---
DOX Metabolism				
CPR	Linear	(1.17 ± 0.89)	(0.690 ± 0.029)	---
CPR:CYP2J2	Linear	$-(5.57 \pm 1.90)$	(0.765 ± 0.062)	---

Chapter 4: Phytocannabinoid and endocannabinoid metabolism by CYP2J2[3]

4.1 Introduction

Cannabis sativa has been used for centuries throughout human history for both its psychoactive effects and medicinal properties. Increasingly, legalization of cannabis for medical and recreational use is gaining worldwide support, in conjunction with trends of increased cannabinoid potency. Therefore, studying the effects of cannabinoids derived from cannabis on human health is of medical and scientific interest.

Cannabinoids are broadly classified into three categories depending on their source: (1) endocannabinoids (eCB) that are endogenously produced derivatives of polyunsaturated fatty acids (PUFAs) in animals; (2) phytocannabinoids (pCBs) that are derived from plants; and (3) synthetic cannabinoids. Psychoactive pCBs include Δ9-tetrahydrocannabinol (Δ9-THC), the primary psychoactive component of the plant, Δ8-tetrahydrocannabinol (Δ8-THC), and cannabinol (CBN). Some of the most abundant non-psychoactive pCBs in cannabis include cannabichromene (CBC), cannabidiol (CBD), and cannabigerol (CBG) (Figure 4.1).

Phytocannabinoids have well-known cardiovascular implications that have been difficult to interpret due to variations regarding their effects in different species. For instance, the cardiovascular effects of THC in animals versus humans are contradictory [315,316]. Δ9-THC induces tachycardia in humans, and only reproduces similar results in conscious monkeys; and prolonged exposure resulted in a reduction in elevated heart rate, as is seen in humans with developed tolerance [317]. In other animal models, Δ9-THC induces bradycardia [318-320]. Interpreting animal model data is further complicated using anesthesia. Experiments using anaesthetized [319] versus non-anaesthetized [318] rats did and did not exhibit tolerance to bradycardia symptoms, respectively, despite increased Δ9-THC administration. This lack of consensus in cross-species studies, changing variables in experimental design, and the psychoactivity of pCBs have obfuscated focus on discerning the exact cardiovascular implications of cannabis. Therefore, in order to understand

[3] This work has been published as: Arnold, W. R.; Weigle, A. T.; and Das, A.; "Cross-talk of Cannabinoid and Endocannabinoid Metabolism is Mediated via Human Cardiac CYP2J2." J. Inorg. Biochem, 2018, 184, 88-99. The work is allowed to be republished under the Creative Commons Attribution license (https://creativecommons.org/licenses/by/4.0/)

the impact of pCBs on human cardiovascular health, there is a need to study the metabolism of pCBs by human cardiac enzymes. Of interest are the cytochromes P450 (CYPs), the primary enzymes that are involved in drug metabolism in the human body.

CYPs are known for their ability to metabolize diverse xenobiotics, synthesize steroids, and be involved in fatty acid metabolism [167]. CYPs generally require electrons donated by cytochrome P450 reductase (CPR) in order to oxidize their substrates. Previously, it was demonstrated that pCBs inhibit the metabolism of drugs by microsomal CYPs (1A1 [321,322], 1A2 [321], 1B1 [323], 2A6 [324], 2B6 [323-325], 2C8 [325], 2C9 [326-328], 2C11 [329], 2C19 [330], 2D6 [331], 3A4 [325,332], 3A5 [325,332], and 3A11 [333]). Currently, there is absence of any mechanistic study on the metabolism of pCBs by CYP2J2, the most abundant CYP expressed in the cardiomyocytes of the heart [321,322].

CYP2J2 is involved in the metabolism of both ω-3 and ω-6 eCBs leading to the formation of eCB epoxides that are vasodilatory, anti-platelet aggregatory, anti-inflammatory, and overall cardioprotective [8]. Anandamide (AEA) was the first eCB discovered. It is derived from the ω-6 fatty acid, arachidonic acid (AA) (Figure 4.1A) [334]. AEA was shown to be metabolized by several CYPs, including CYP2J2, forming different regioisomers of epoxyeicosatrienoyl ethanolamides (EET-EAs) (Figure 4.1A) [161,246]. CYP2J2 has also been shown to metabolize several drugs, and many of which are known to be cardiotoxic [294-297].

Despite structural differences between eCBs and pCBs, both of these classes of cannabinoids interact with the endocannabinoid system (ECS) in the body. The ECS system consists of an ensemble of eCBs and eCB-like mediators, their corresponding receptors, and metabolic enzymes involved in ligand formation and degradation [335]. The ECS is involved in homeostatic functions dynamically regulating the functionality of the immune, reproductive, gastrointestinal, and central nervous systems, in addition to that of the brain, liver, and heart [336]. Physiological modulation by the ECS is largely dependent upon the nature and location of the diseased state [337].

The activity of the ECS is primarily elicited via molecular recognition of both pCBs and eCBs by cannabinoid receptors 1 and 2 (CB1 and CB2). ECS regulatory roles in the cardiovascular system are complex as the two receptors elicit varied responses [338,339]. Activation of CB1 translates to cardiovascular complications by decreasing blood flow and inducing vasoconstriction [340-344]; while CB2 activity suppresses inflammatory responses of endothelial cells and monocytes [342,345-347] and is also suggested to provide a protective role against cardiovascular diseases through

induced vasodilation [346]. Thus, conflicting natures of CB1 and CB2 activation make the ECS a contributor to the generation, as well as amelioration, of cardiovascular disease.

Previously, we showed that CYP2J2 converts AEA into EET-EAs and similar epoxides from ω-3 fatty acid ethanolamides that are derived from DHA and EPA [163]. During inflammation, the levels of these epoxides are comparable to AEA [163]. Inasmuch as CYP2J2 generates cardioprotective epoxides from eCBs and also metabolizes several drugs, CYP2J2 is a prime enzyme for studying the potential effects of pCBs on eCB metabolism. It has been hypothesized that AEA metabolism by unknown CYPs is inhibited by pCBs [348]. Herein, we determine the direct metabolism of selected pCBs by CYP2J2 and evaluate their effects on AEA metabolism. We have determined that the 6 pCBs tested (Δ9-THC, Δ8-THC, CBC, CBD, CBG, and CBN) are all metabolized by CYP2J2 to form new hydroxyl products of the pCBs, with various di-oxygenated products as well. The catalytic efficiencies of the pCB turnovers are similar to or greater than that of AEA. Using CYP2J2-nanodiscs, we measured the kinetics of AEA metabolism by CYP2J2. Further, we have determined that the pCBs are potent inhibitors of AEA metabolism. We determined that CBG is a competitive inhibitor of AEA, whereas Δ9-THC, Δ8-THC, CBD, CBN, and CBC are noncompetitive inhibitors. Of these, Δ9-THC is the strongest inhibitor of AEA metabolism and reduces CYP2J2-mediated AEA metabolism to 20% of the uninhibited activity. Our study demonstrates that the pCBs, especially Δ9-THC, inhibits CYP2J2 and prevent the metabolism of endogenous substrates such as AEA.

4.2 Experimental procedures

Materials, CYP2J2 and CPR expression, nanodiscs and Soret titrations can be found in the Supplementary Materials.

Metabolism of pCBs by CYP2J2. Initial metabolism identification of pCB products were determined using a lipid-reconstituted system as previously described [349]. Briefly, CYP2J2 was reconstituted in 20% POPS using 0.6 μM CYP and 0.6 μM CPR. 60 μM of each pCB was pre-incubated with CYP2J2 and μM CPR for 10 min at 37ºC in 0.5 mL of 0.1 M potassium phosphate buffer (pH 7.4). Reactions were initiated upon the addition of 1 mM NADPH and allowed to react for 60 min. Reactions were terminated with 0.1 mL glacial acetic acid and extracted thrice with 0.5 mL ethyl acetate. The samples were centrifuged at 3K RPM and 4ºC for 5 min to separate the layers, and the organic layers were combined and dried down under a stream of N_2 gas. Metabolites

were resuspended in 0.1 mL acetonitrile and were identified using LC-MS/MS analysis as described below.

Kinetics of pCB metabolism. Kinetics of pCB metabolism were determined using a lipid-reconstituted system as previously described [349]. Metabolites were quantified using an HPLC method (see below). 0.2 μM of CYP2J2 and 0.6 μM of CPR were incubated with varying concentrations of pCBs individually (5-60 μM) for 10 min at 37°C in 0.5 mL of 0.1 M potassium phosphate buffer (pH 7.4). Reactions were initiated with 0.5 mM NADPH and allowed to react for 30 min. Reactions were terminated and extracted using ethyl acetate as stated above. Metabolism of the pCBs was determined to be linear for up to 45 min for each pCB.

Kinetics of AEA metabolism. AEA metabolism by CYP2J2 was determined in Nanodiscs using 0.2 μM of CYP2J2-NDs and 0.6 μM CPR. AEA was pre-incubated with CYP2J2-ND/CPR for 10 min at 37°C in 0.5 mL of 0.1 M potassium phosphate buffer (pH 7.4). For inhibition experiments, AEA was pre-incubated with the CYP2J2-ND/CPR system along with 30 μM of the tested pCB. Reactions were initiated with 0.5 mM NADPH and allowed to react for 30 min. EET-EAs were extracted using ethyl acetate as stated above, but were resuspended in 180-proof ethanol for LC-MS/MS quantification.

HPLC quantification of pCB metabolism. Metabolism products were analyzed via high-performance liquid chromatography (HPLC) consisting of an Alliance 2695 analytical separation module (Waters, Milford, MA) and a Waters 996 photodiode diode array detector (Waters). Metabolites were separated in reverse phase using a Phenomenex Prodigy® 5μm ODS-2, 150 x 4.60 mm column (Phenomenex, PN 00F-3300-E0, Torrance, CA). Mobile Phase A consisted of H_2O + 0.1% formic acid and Mobile Phase B consisted of acetonitrile + 0.1% formic acid. Metabolites were separated using a linear gradient of 25% Mobile Phase B to 100% Mobile Phase B over 20 min, and then held at 100% Mobile Phase B for an additional 10 min. Δ9-THC, Δ8-THC, and CBD hydroxyl metabolites were monitored at $\lambda = 281$ nm; CBG hydroxyl products were monitored at $\lambda = 278$ nm; and CBN and CBC at $\lambda = 283$ nm. Standard curves for quantification were made using a Δ9-THC-11-OH standard for Δ9-THC-OH, Δ8-THC-OH, and CBD-OH; CBG standard for CBG-OH; CBN standard for CBN-OH; and CBC standard for CBC-OH. There was no significant variation in the absorbance intensities among Δ9-THC, Δ8-THC, and CBD. Elution times are reported in the Section 4.3 (Figure 4.2).

High-resolution LC-MS and LC-MS/MS analysis of metabolites. Masses of products were determined using the Q-Exactive MS system (Thermo. Bremen, Germany) in the Metabolomics Laboratory of Roy J. Carver Biotechnology Center, University of Illinois at Urbana-Champaign as previously described [349]. Metabolites were separated using the above HPLC method and the Phenomenex Prodigy® 5µm ODS-2, 150 x 4.60 mm column. Negative and positive electrospray ionization was employed. Masses were considered significant if $\pm$ 5 ppm of the calculated exact mass.

LC-MS/MS quantitation of EET-EAs. Samples were analyzed with the 5500 QTRAP LC/MS/MS system (Sciex, Framingham, MA) in Metabolomics Lab of Roy J. Carver Biotechnology Center, University of Illinois at Urbana-Champaign. Software Analyst 1.6.2 was used for data acquisition and analysis. The 1200 series HPLC system (Agilent Technologies, Santa Clara, CA) includes a degasser, an autosampler, and a binary pump. The LC separation was performed on an Agilent Eclipse XDB-C18 (4.6 x 150mm, 5µm) with mobile phase A (0.1% formic acid in water) and mobile phase B (0.1% formic acid in acetontrile). The flow rate was 0.4 mL/min. The linear gradient was as follows: 0-2min, 90%A; 8min, 55%A; 13-25min, 40%A; 30min, 30%A; 35min, 25%A; 36-43min, 90%A. The autosampler was set at 10°C. The injection volume was 10 µL. Mass spectra were acquired under positive electrospray ionization (ESI) with the ion spray voltage of +5500 V. The source temperature was 450 °C. The curtain gas, ion source gas 1, and ion source gas 2 were 32, 65, and 50, respectively. Multiple reaction monitoring (MRM) was used for quantitation: m/z 364.2 → m/z 62.0. Internal standard 14,15-EET-EA-d8 was monitored at m/z 372.1 → m/z 63.1.

Competitive and noncompetitive inhibition equations used in studies. All inhibition studies are best described by a competitive inhibition model (Equation 4.1) or a noncompetitive inhibition model (Equation 4.2)

$$B = \frac{B_{max}[S]}{K\left(1+\frac{[I]}{K_i}\right)+[S]} \qquad \text{(Equation 4.1)}$$

$$B = \frac{B_{max}[S]}{(K+[S])\left(1+\frac{[I]}{K_i}\right)} \qquad \text{(Equation 4.2)}$$

where B_{max} and K are the Michaelis-Menten kinetic parameters of the substrate $[S]$ without inhibitor, $[I]$ is the concentration of inhibitor, and K_i is the inhibition constant. For kinetic

experiments, B and K represent the velocity and K_m, respectively; for Soret binding experiments, B and K represent ΔA and K_S, respectively.

4.3 Results

CYP2J2 metabolizes pCBs primarily to 1'/1"-OH metabolites. We first tested the direct endpoint metabolism of the pCBs by CYP2J2-CPR. We determined that the pCBs—Δ9-THC, Δ8-THC, CBD, CBG, CBN, and CBC—are all substrates of CYP2J2 (Figures 4.2-4.4). LC-MS/MS analysis indicates that the following classes of oxidation products were produced for each pCB: mono-oxygenation, carboxylation, and di-oxygenation (masses of the products are within 5 ppm of the predicted masses). Chromatograms for the mono-oxygenated products are shown in Figure 4.2. MS/MS spectra of the major mono-oxygenated products are shown in Figures 4.3 and 4.4. A detailed analysis of the MS/MS data is provided in the Supplementary Material.

A resorcinolic ion (193.12 m/z) is produced upon the fragmentation of the Δ9-THC and Δ9-THC-11-OH standards (Figure 4.3A-B) [350]. The major Δ9-THC-OH product of the CYP2J2 metabolism shows a mass corresponding to mono-oxygenation of the resorcinolic ion followed by the elimination of a water molecule (209.12 m/z → 191.11 m/z) (Figure 4.3A-B). The Δ9-THC standard additionally fragments between Carbons 1' and 2' to produce an ion of 259.17 m/z. The CYP2J2 product shows a mass indicating mono-oxygenation (275.16 m/z) of this ion, which is not present in the Δ9-THC-11-OH standard, followed by the elimination of a water molecule (257.16 m/z). This identifies the CYP2J2 product as Δ9-THC-1'-OH. Furthermore, the 257.16 m/z peak is the largest peak in the CYP2J2 product spectrum, but not the Δ9-THC-11-OH standard. Fragmentation between Carbons 1' and 2' is likely facilitated by the elimination of the 1'-OH as a water molecule, thereby making it the most abundant ion.

The Δ8-THC, CBD, CBG, and CBC (Figures 4.3C-F) standards show similar fragmentation patterns as the Δ9-THC standard (Figure 4.3B). Likewise, the major mono-oxygenated products for these compounds show similar fragmentation patterns as the CYP2J2 product for Δ9-THC, as mentioned above (Figures 4.3C-F). Therefore, the metabolites for these compounds can be identified as Δ8-THC-1'-OH, CBD-1"-OH, CBG-1"-OH, and CBC-1"-OH. However, there are additional ions in the CBD sample that are reminiscent of ions in the Δ9-THC-11-OH standard, notably the resorcinolic 193.12 m/z ion (Figures 4.3A and 4.3D). Therefore, it is likely that

CYP2J2 additionally produces CBD-7-OH, the analogous product compared to Δ9-THC-11-OH. The CBD-7-OH and CBD-1"-OH co-elute and could not be separated further.

CBN fragments differently when compared to the other pCBs due to the extended conjugation of the dibenzene moiety (Figure 4.4A). As a result, no ion corresponding to the separation of the resorcinol and terpenoid halves is observed in either the CBN standard or the product (Figure 4.4). There are two important ions of the product that are mono-oxygenated fragments of the parent compound (237.13 m/z → 253.12 m/z and 195.12 m/z → 211.11 m/z) (Figure 4.4B). These two fragments share the dibenzene moiety and Carbons 11 and 1' (Figure 4.4). There are no other fragments of either the standard or the product that could distinguish between Carbons 11 and 1'. Therefore, the product is CBN-11-OH, CBN-1'-OH, or a combination of the two. The pentyl tail of CBN fragments to produce an ion of 71.09 m/z in the CBN standard, which is 69.07 m/z in the product (Figure 4.4B). This could be the result of a hydroxyl cleavage at the 1' position and subsequent olefination of this fragment, which supports CBN-1'-OH as the identity of the product.

Formation of other pCB metabolites by CYP2J2. All pCBs were metabolized by CYP2J2 to produce ions suggestive of pCB carboxylation by CYP2J2. Δ9-THC-11-COOH was identified and compared to a standard, which is verified by a fragment resembling the carboxylated species without the pentyl side chain (Supplementary Figure 4.1, Δ9-THC, Ion **9**). Other carboxylated metabolites for each of the pCBs follow similar fragmentation, where an ion lacking an aliphatic carbon chain can be detected. Some pCBs (CBC, CBG, CBN) possess fragmentation suggestive of multiple carboxylation sites, due to the presence of representative ions being restricted to either positive or negative ion modes.

Each pCB was also metabolized by CYP2J2 into di-hydroxylated products in addition to the 1'/1" hydroxylation. Although MS analysis suggests their presence, the identities of these di-hydroxylated metabolites could not be determined from their MS/MS spectra due to lack of standards.

Overall, the relative abundances of these ions are much lower compared to the major hydroxylated products. Findings related to the formation of other metabolites are summarized in Figure 4.5 but are presented in greater detail in the Supplementary Material.

Kinetics of pCB metabolism by CYP2J2. We next determined the kinetics of metabolism for the pCBs. To do this, we developed an ultraviolet/visible wavelength (UV-Vis) HPLC quantification method based on the absorbance of the resorcinol moiety (λ = 278-283 nm) as

described in the Materials and Methods section. The initial mono-oxygenated products were analyzed to determine the steady-state kinetics (Figure 4.6, Table 4.1). These correspond to Δ9-THC-1'-OH; Δ8-THC-1'-OH; CBN-1'-OH or CBN-11-OH; CBD-1"-OH and CBD-7-OH; CBG-1"-OH; and CBC-1"-OH. The other metabolites were below the detection limit.

The pCBs were effectively metabolized with differing kinetic characteristics. The V_{max} values ranged from 80.9 to 710 pmol · min^{-1} · $nmol_{CYP2J2}^{-1}$ and the K_m values ranged from 8.27 to 84.2 μM. Δ9-THC displayed the greatest catalytic efficiency (18.9 min^{-1} · nM^{-1}). This value is twice that of the other dibenzopyran cannabinoids, Δ8-THC and CBN, which had catalytic efficiencies of 9.50 and 9.13 min^{-1} · nM^{-1}, respectively. CBC, CBD, and CBG varied in their efficiencies from 4.41 to 14.9 min^{-1} · nM^{-1}. Compared to the kinetics we had previously determined for AA, the canonical endogenous substrate of CYP2J2, these pCBs are metabolized more efficiently [289].

Binding of pCBs to CYP2J2-Nanodiscs (CYP2J2-NDs). We next determined the binding of the pCBs and AEA to CYP2J2 using UV-Vis Soret titration binding. To produce accurate binding spectra, we used CYP2J2-NDs, which solubilize CYP2J2 in a membrane mimic (Figure 4.7A). Substrates binding to CYPs typically displace a water molecule from the 6th coordination position of the iron-heme, producing a high-spin iron. This results in a characteristic shift in the Soret absorbance from ~417 nm to ~390 nm. The pCBs were titrated into CYP2J2-NDs and the spin-state equilibrium constants (K_S) were determined, which is used as an approximation of the K_D for CYPs. CBD, CBG, and CBN produced a measurable Soret shift upon binding (Figure 4.7B-E). At saturating concentrations, CBD, CBG, and CBN produced 32%, 48%, and 38% high-spin shift, respectively. Among these, CBD and CBG showed the tightest binding (K_S of 11.5 $\pm$ 3.0 μM and 11.1 $\pm$ 1.2 μM for CBD and CBG, respectively). The binding of Δ9-THC, Δ8-THC, CBC, and AEA did not produce a significant change in the high-spin content. Therefore, to measure their relative binding affinity, we measured their inhibition of ebastine binding to CYP2J2, a technique we had previously used to determine the binding constant of AA [289]. All the pCBs displayed binding affinities that are greater than AEA, with most between 10 and 20 μM, and Δ9-THC being the weakest (Figure 4.7E).

Inhibition of AEA metabolism by pCBs. Having established that the pCBs are substrates of CYP2J2, we next determined the inhibition of the CYP2J2-mediated AEA metabolism by the pCBs using a CYP2J2-ND/CPR system (Figure 4.8A). AEA is metabolized by CYP2J2 with a V_{max} of 135 $\pm$ 14.0 $pmol_{EET\text{-}EAs}$ · min^{-1} · $nmol_{CYP2J2}^{-1}$ and a K_m of 30.9 $\pm$ 7.3 μM (Figure 4.8A,

Table 4.1), which is a greater catalytic efficiency compared to AA,[289] but less than that of most of the pCBs. The predominant metabolite is 14,15-EET-EA (51.7% of the total) with 5,6-EET-EA being the least (0.4%) (Figure 4.8A). The metabolism of AEA was repeated in the presence of 30 μM of each pCB in separate experiments (Figure 4.8B-G, Table 4.1). CBG inhibited AEA metabolism competitively with a K_i of 10.8 $\pm$ 1.4 μM. The rest of the pCBs noncompetitively inhibited AEA metabolism. The apparent V_{max} of the AEA metabolism was reduced to 20-45% of the uninhibited enzyme in the presence of Δ9-THC, Δ8-THC, CBN, CBD, and CBC (Figure 4.8B-G). Of these, Δ9-THC inhibited most strongly with a K_i of 9.86 $\pm$ 0.45 μM. The next strongest was CBD with a K_i that is almost double that of Δ9-THC (16.9 $\pm$ 1.1 μM for CBD). CBN, CBC, and Δ8-THC inhibited with K_i values around 20 μM. For all these pCBs, the K_i values are in close approximation to their determined binding affinities, except for Δ9-THC, which is comparatively stronger (Table 4.1).

4.4 Discussion

Phytocannabinoids are known for their psychotropic effects. However, their role in overall human physiology remains to be elucidated. For instance, pCBs have strong effect on the human cardiovascular physiology, including inflammation; additionally, the principal component of cannabis, Δ9-THC, induces tachycardia in humans. Previous studies have produced variable results regarding their effects on cardiovascular health, which is partly due to the dearth of information regarding most of the pCBs, their metabolites, and their modulation of the endocannabinoid system.

Herein, we have performed direct *in vitro* assays to determine the effects of pCBs on a human cardioprotective enzyme, CYP2J2. Given that CYP2J2 is known to metabolize drugs and convert eCBs, such as AEA, to cardioprotective epoxides makes this enzyme a prime target for investigating the impact of pCBs on the metabolism of AEA. We have determined that the 6 most common pCBs, Δ9-THC, Δ8-THC, CBN, CBD, CBG, and CBC, are mostly converted to 1'/1"-OH metabolites by CYP2J2. We further determine that these pCBs demonstrate greater catalytic efficiencies compared to typical endogenous CYP2J2 substrates. Finally, we determined that these pCBs potently inhibit AEA metabolism. While CBG inhibits competitively, the other 5 pCBs inhibit via a noncompetitive model, thereby shutting down AEA metabolism through CYP2J2. Of these pCBs, Δ9-THC is the strongest inhibitor of AEA metabolism.

Δ8/Δ 9-THC-11-OH are the best studied metabolites of the THCs as these metabolites are psychotropic and are the most abundant metabolite formed by CYPs in liver microsomes.[351-353] Other CYP-mediated oxidations of THCs the liver involve C-ring oxidations and acyl hydroxylation, namely 3'-OH (CYP1A1) and 4'-OH (CYP2C11) [354-356]. Other organs, such as the brain and lung, produce primarily hydroxylated metabolites on the acyl chain, notably -4'-OH and -5'-OH [357,358]. However, despite being found as a metabolite of pCBs, the 1'/1" hydroxylation was found to be a minor metabolite of other CYPs that have been tested, such as CYP1A1/2 [48]. Likewise, CBD is hydroxylated on both the C ring and pentyl side chain, and CBD-1"-OH has been primarily shown to be produced by CYP1A1/2, albeit it is still not the major metabolite of these CYP enzymes [8]. The primarily 1'/1" hydroxylation is therefore unique to CYP2J2 and may be used as a probe regarding its activity. In smaller quantities, we also propose that CYP2J2 generates Δ8/Δ9-THC-11-COOH, CBN-11/5"-COOH, CBD-7-COOH, CBG-8'/9'/10'-COOH, and CBC-9'/5"-COOH. Throughout the literature, THC and CBD are the best studied cannabinoids with respect to CYP metabolism. Herein, we measure the CYP2J2-mediated metabolism of CBC, CBG, and CBN that are not extensively studied but nonetheless very important constituents of cannabis.

All the pCBs inhibited CYP2J2-mediated AEA metabolism. Interestingly, two modes of AEA inhibition by the pCBs were observed. CBG inhibited AEA metabolism competitively. Compared to the other pCBs, CBG has a structure that is the most linear and most resembles the structure of AEA. We have previously determined that the competitive nature of PUFAs arises from their flexibility, which allows them to occupy most of the active site volume [289]. Likewise, CBG and AEA may be competitive for similar reasons.

The other pCBs inhibit AEA metabolism in a noncompetitive manner. Classically, noncompetitive inhibition arises from the binding of the inhibitor to an allosteric site, preventing the metabolism of a substrate when both are bound. CYP2C9's metabolism of diclofenac was shown to be noncompetitively inhibited by 6-hydroxyflavone in an atypical manner. 6-hydroxyflavone was shown to bind into a site that prevents full access of diclofenac to the heme [210]. Since these pCBs are also substrates of CYP2J2, they must bind near the heme. Therefore, in addition to the classical mode of noncompetitive inhibition, the pCBs may be binding the active site along with AEA and preventing AEA from being metabolized. We had previously demonstrated that 7-deoxydoxorubicin aglycone concurrently binds the active site with AA and

alters AA metabolism by changing the binding conformation of AA [349]. This is mediated in part to the polycyclic and planar structure of 7-deoxydoxorubicin aglycone. The rest of the pCBs other than CBG likewise have polycyclic structures, giving them less flexibility.

Another intriguing characteristic of the AEA inhibition by these pCBs is the differences in the inhibitory strength concerning the dibenzopyran varieties, Δ9-THC, Δ8-THC, and CBN. Among these, Δ9-THC has a K_i value for the inhibition of AEA that is twofold tighter than Δ8-THC or CBN. Coincidentally, the catalytic efficiency of the Δ9-THC metabolism was determined to be twice that of the metabolism of Δ8-THC or CBN. These data demonstrate that the positioning and frequency of double bonds in the C-ring of the dibenzopyran pCBs governs the metabolism of these pCBs and the inhibition of AEA metabolism, with the Δ9 position being crucial.

All the pCBs tested herein potently inhibit AEA metabolism by CYP2J2. These data have intriguing physiological implications, particularly in relation to trafficking and molecular recognition of cannabinoid-like ligands within the ECS. The pCBs have been shown to stall the catabolism of AEA by inhibiting fatty-acid-binding proteins that aid in the delivery of AEA to fatty acid amide hydrolase (FAAH) [359], and FAAH has been shown to be weakly inhibited by CBD [360]. As a result, the extended lifetime of AEA [360] results in greater targeting of CB1, which is further amplified by the activation of CB1 by select pCBs themselves. Through noncompetitive inhibition, our data shows that in addition to pCB signaling through CB1 receptors, they also prevent CYP2J2-mediated AEA metabolism. As EET-EAs are CB2-preferring agonists [163,336,361], pCBs prevent the formation of CB2-preferring ligands in addition to increasing actions at CB1. Interestingly, a study performed on Rhesus monkeys shows that Δ8-THC-1'-OH is the least effective at inducing behavioral changes associated with cannabis use [362]. As CB1 is responsible for the psychotropic effects of cannabinoids, this presumes that Δ8-THC-1'-OH is the weakest agonist of CB1. Such crosstalk is not only mediated by CYP metabolism, but also by CB signaling. It has been shown previously that selective blockade of CB1 receptor and activation of CB2 is ideal for the treatment and management of cardiovascular disease [363]. Therefore, the inhibited formation of CB2-preferring EET-EAs and stronger CB1 activation by select pCBs may explain the increase risk of myocardial infarction after the first hour of cannabis use. CYP2J2 then clears the pCBs by converting them to weaker CB1 agonists and resumes normal EET-EA metabolism after the first hour and the cardiotoxic risk is lowered. Taken together, this study indicates that

pCBs will elicit complex cardiovascular physiology that will be partially mediated through inhibition of human cardiac CYP2J2.

4.5 Figures and table

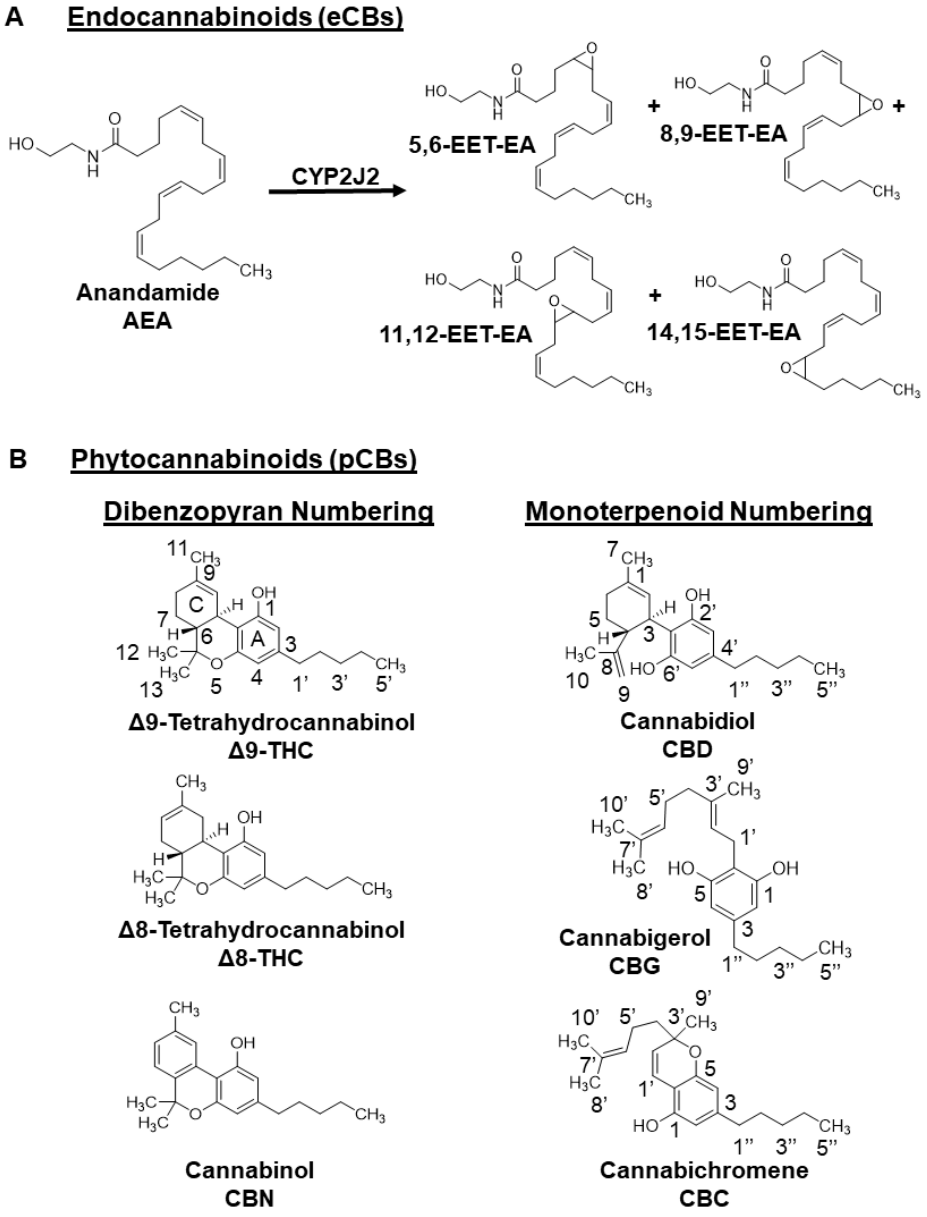

Figure 4.1. *Chemical structures.* (A) Endocannabinoids (eCBs): anandamide (AEA) and epoxyeicosatrienoyl ethanolamides (EET-EEAs). (B) Phytocannabinoids (pCBs). The numbering for each pCB is given, and Δ8-tetrahydrocannbionol (Δ8-THC) and cannabinol (CBN) follow analogous numbering as Δ9-tetrahydrocannabinol (Δ9-THC). These psychoactive pCBs follow the dibenzopyran numbering system. The non-psychoactive pCBs in cannabis include cannabidiol (CBD), cannabigerol (CBG), and cannabichromene (CBC). They follow a monoterpenoid numbering scheme. The resorcinol ring for each pCB is designated as the A-ring.

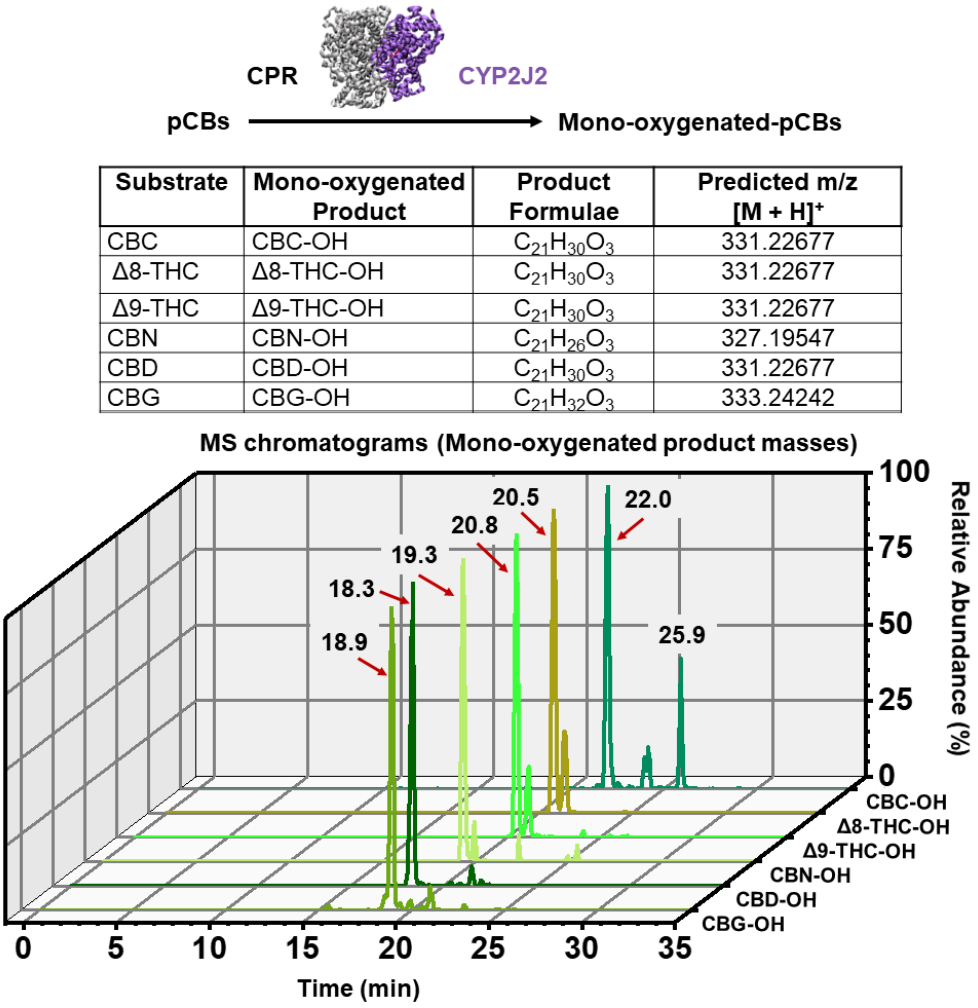

Substrate	Mono-oxygenated Product	Product Formulae	Predicted m/z $[M + H]^+$
CBC	CBC-OH	$C_{21}H_{30}O_3$	331.22677
Δ8-THC	Δ8-THC-OH	$C_{21}H_{30}O_3$	331.22677
Δ9-THC	Δ9-THC-OH	$C_{21}H_{30}O_3$	331.22677
CBN	CBN-OH	$C_{21}H_{26}O_3$	327.19547
CBD	CBD-OH	$C_{21}H_{30}O_3$	331.22677
CBG	CBG-OH	$C_{21}H_{32}O_3$	333.24242

Figure 4.2. *Targeted LC-MS analysis of CYP2J2-mediated pCB metabolism.* The indicated pCBs were incubated with CYP2J2/CPR and the products were extracted with ethyl acetate and analyzed via LC-MS/MS as described in the Section 2.5. Mass peaks corresponding to the predicted mono-oxygenated m/z values ± 5 ppm are shown. Peaks are labelled according to their elution time.

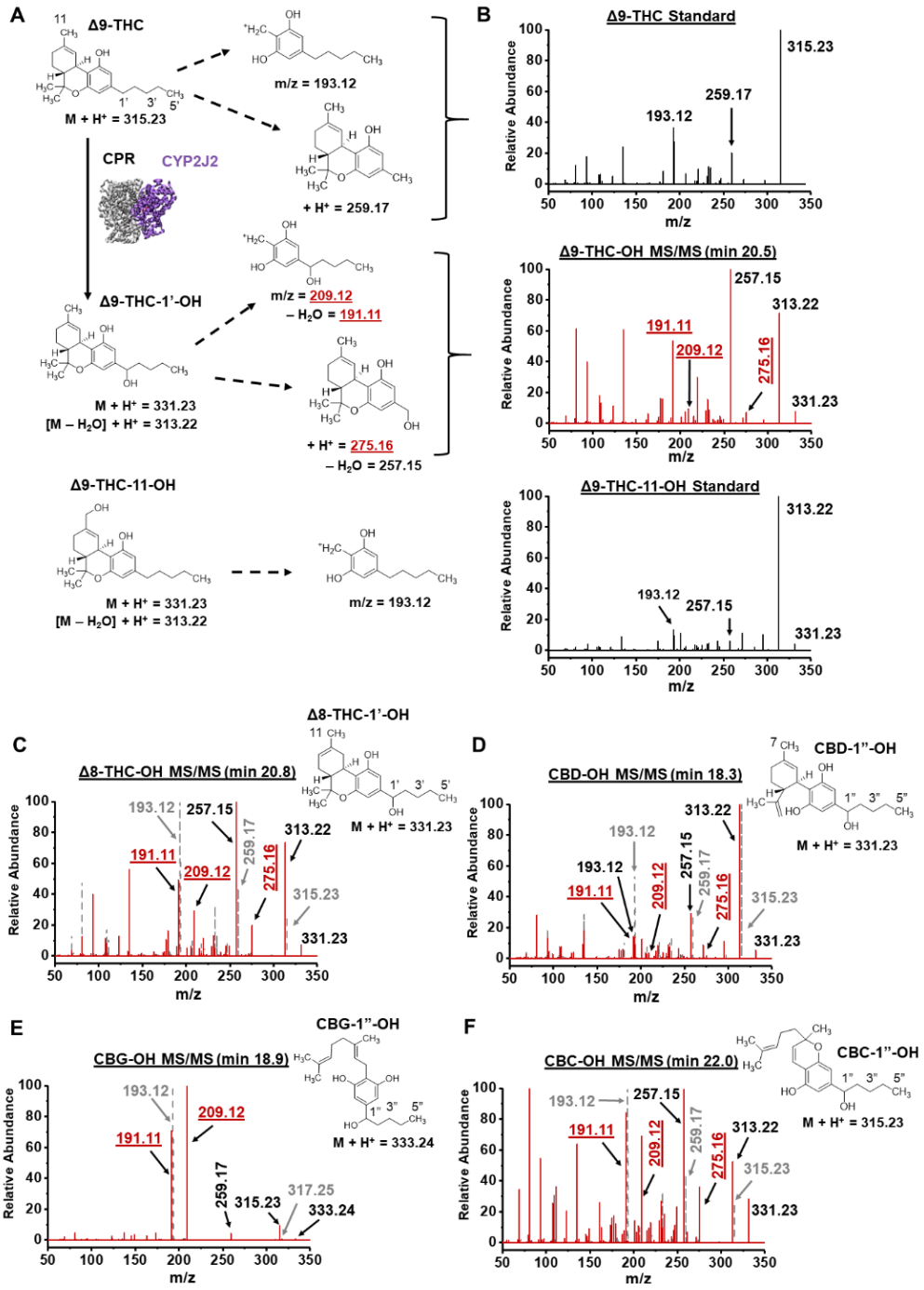

Figure 4.3. *MS/MS spectra of the major mono-oxygenated products of Δ9-THC, Δ8-THC, CBD, CBG and CBC.* (A) Schematic of Δ9-THC fragmentation pathways for the Δ9-THC and Δ9-THC-11-OH standards and the CYP2J2-mediated Δ9-THC-OH product. Analogous ions are identified for the other pCBs. (B) Spectra of the Δ9-THC standard, Δ9-THC-11-OH standard, and the major CYP2J2 product of Δ9-THC. (C-F) Spectra of the (C) Δ8-THC-OH product, (D) CBD-OH product, (E) CBG-OH product, and (F) CBC-OH product. Corresponding standard spectra for (C-F) are shown as grey dashes and grey font. Elution times of products are given. Masses that indicate 1'/1"-OH as the product are labelled in red and underlined. Masses were considered significant if within 5 ppm of the predicted masses.

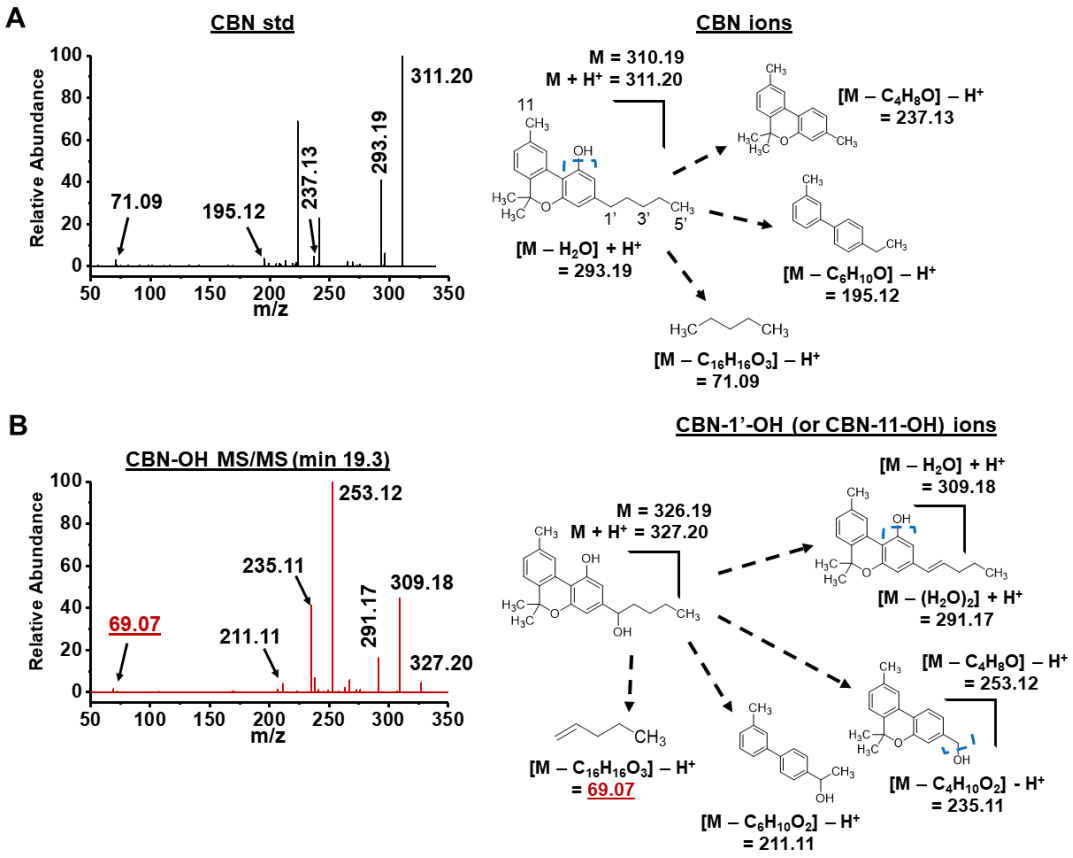

Figure 4.4. *MS/MS spectra of the CBN standard (std) and the major mono-oxygenated CYP2J2 product (CBN-OH).* (A) Spectra of the CBC standard and scheme of major fragmentations. (B) The major CYP2J2 product of CBC and major fragmentations. Elution times of products are given. Blue, dashed brackets indicate sites of fragmentation. Masses that indicate 1'-OH are labelled in red and underlined. Masses were considered significant if within 5 ppm of the predicted masses.

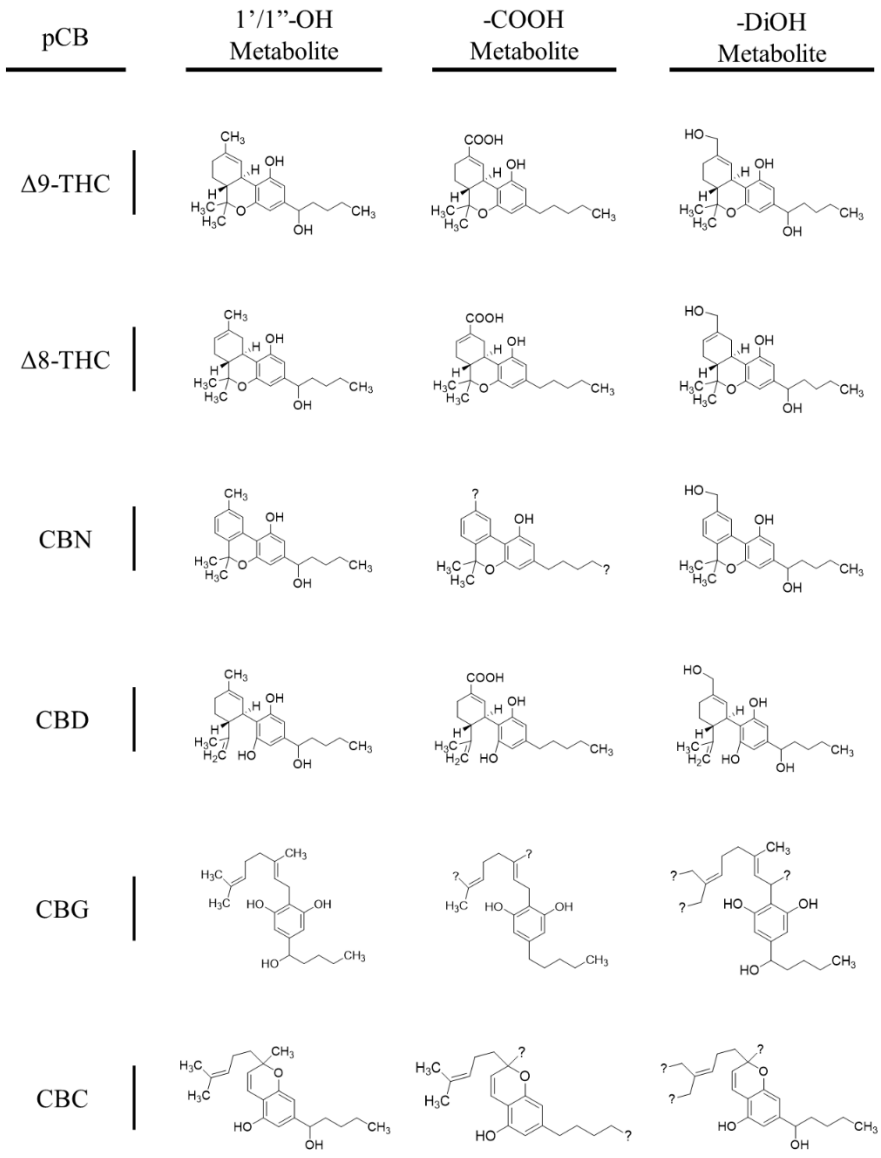

Figure 4.5. *Major products of CYP2J2-pCB metabolism.* Question marks (?) are positioned to suggest multiple species derived from the fragmentation pathways for each metabolite (reference Supplementary Materials). Metabolites are as follows (left to right, row by row): Δ9-THC-1'-OH, Δ9-THC-11-COOH, Δ9-THC-DiOH; Δ8-THC-1'-OH, Δ8-THC-11-COOH, Δ8-THC-DiOH; CBN-1'-OH, CBN-5"/11-COOH, CBN-DiOH; CBD-1'-OH, CBD-7-COOH, CBD-DiOH; CBG-1'-OH, CBG-8'/9'/10'-COOH, CBG-DiOH; CBC-1'-OH, CBC-5"/9'-COOH, CBC-DiOH. Structures of -DiOH products are representative as the position of the second OH could not be determined.

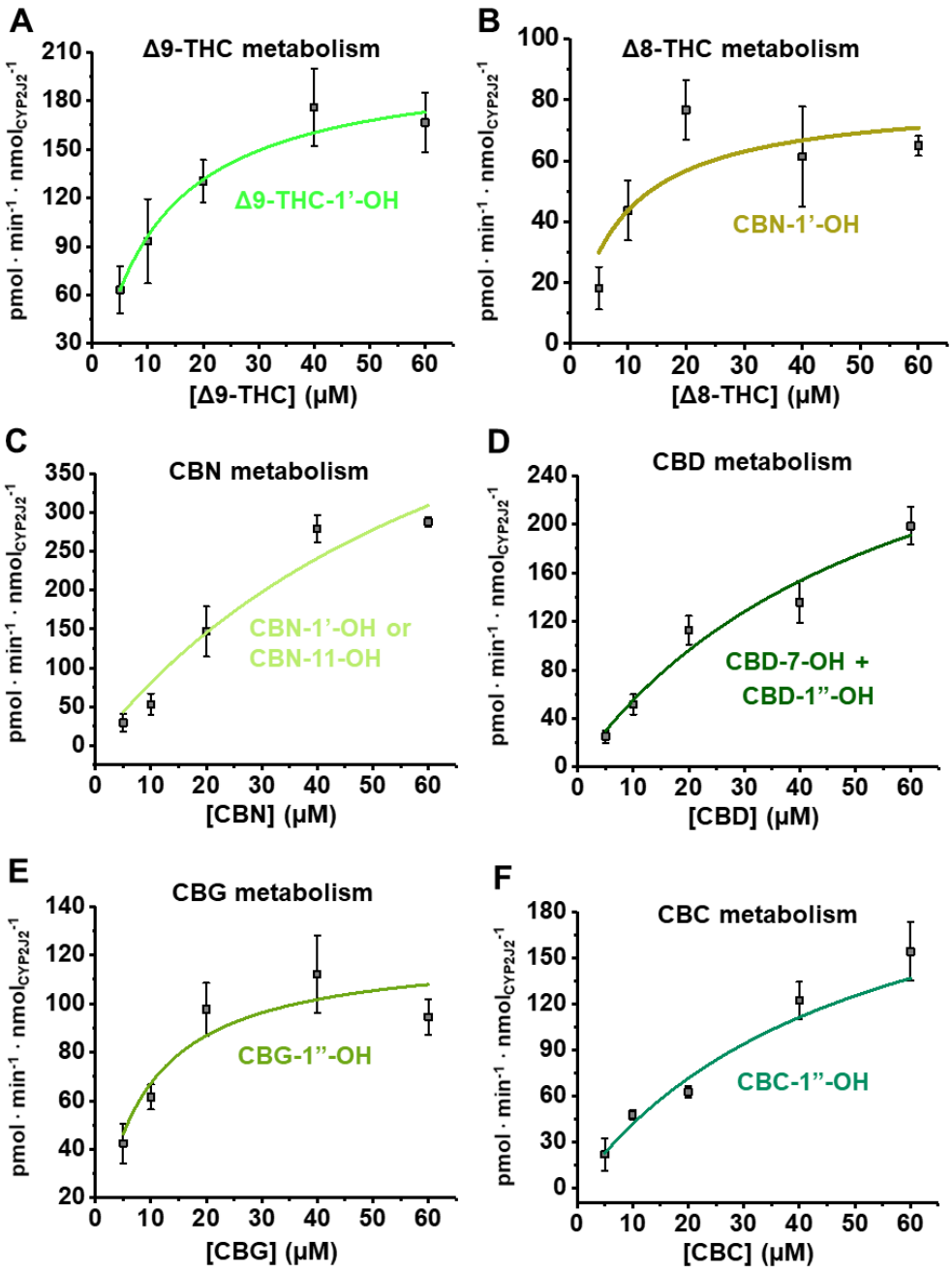

Figure 4.6. *Kinetics of pCB metabolism*. Mono-oxygenated products identified by LC-MS/MS analysis for the metabolism of (A) Δ9-THC, (B) Δ8-THC, (C) CBN, (D), CBD, (E) CBG, and (F) CBC were quantified using UV-HPLC as stated in the Materials and Methods section. Data fit to the Michaelis-Menten equation. Error represents the SEM of 3 experiments.

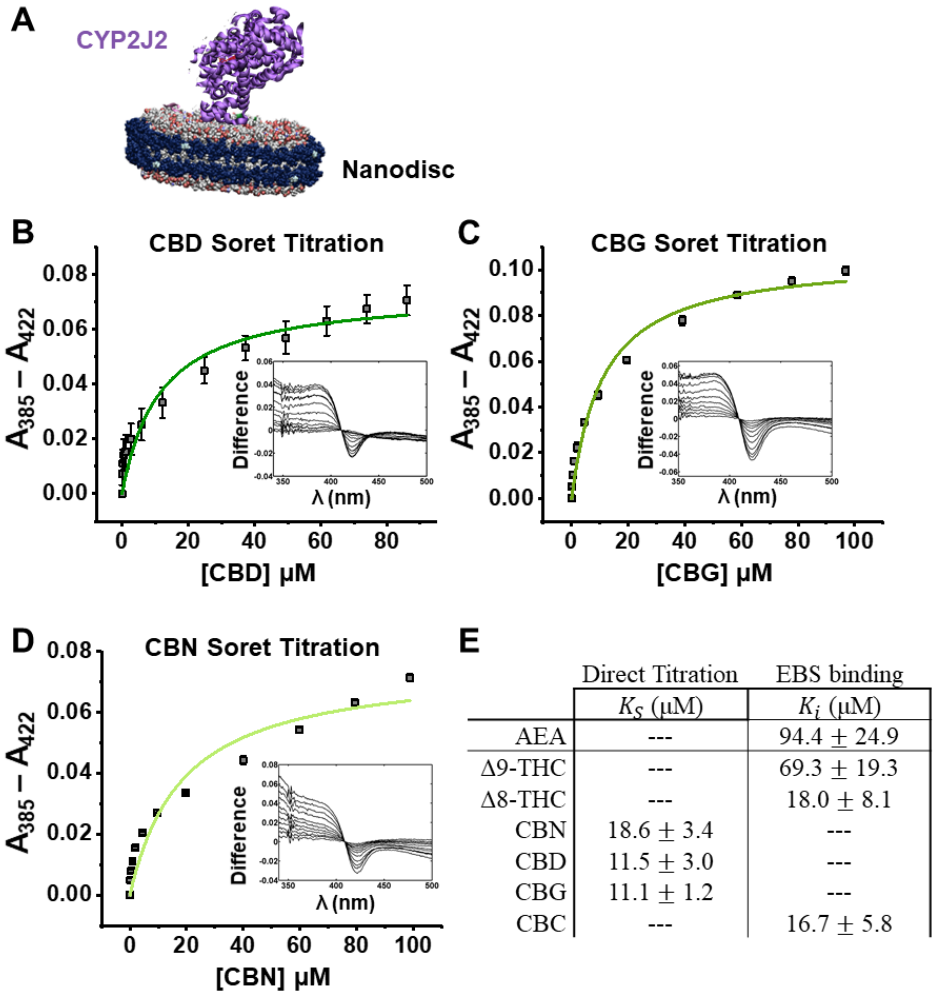

E

	Direct Titration	EBS binding
	K_S (μM)	K_i (μM)
AEA	---	94.4 ± 24.9
Δ9-THC	---	69.3 ± 19.3
Δ8-THC	---	18.0 ± 8.1
CBN	18.6 ± 3.4	---
CBD	11.5 ± 3.0	---
CBG	11.1 ± 1.2	---
CBC	---	16.7 ± 5.8

Figure 4.7. *Soret binding titration*. (A) CYP2J2 in Nanodiscs. (B) CBD, (C) CBG, and (D) CBN produced a measurable Soret shift with 32%, 48%, and 38% high-spin shift, respectively. (E) Binding parameters as determined directly from the Soret titration or through inhibition of ebastine (EBS) binding. Data displayed one-site binding and data shown are the mean ± SEM of 3 titrations.

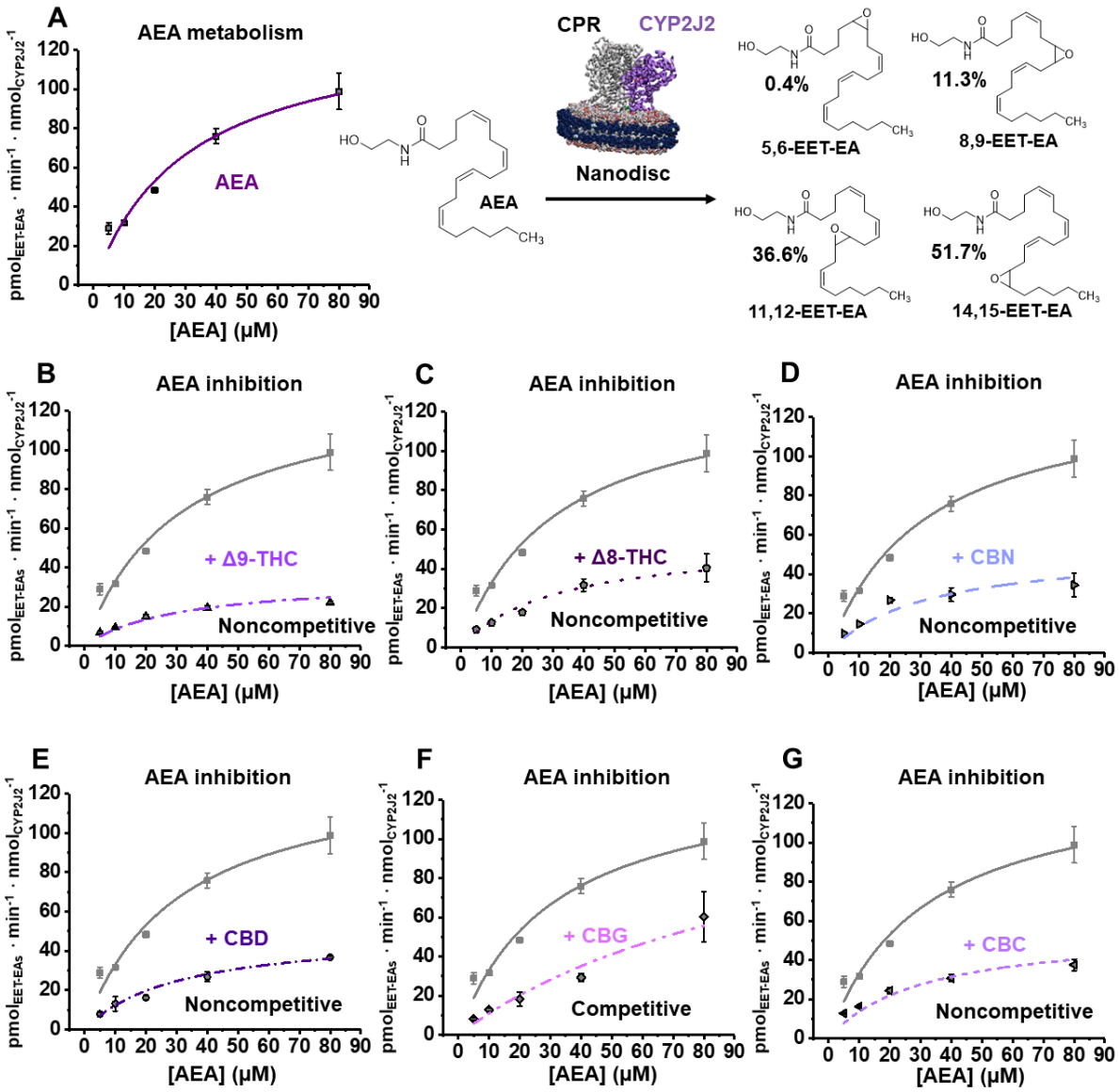

Figure 4.8. *Anandamide (AEA) metabolism inhibition by pCBs.* (A) Kinetics of AEA metabolism. A schematic of CYP2J2-Nanodiscs and CPR metabolizing AEA is given. The total amount of EET-EAs are plotted. The percent of each regioisomer to the total amount of EET-EAs is given to the right. (B-G) Inhibition of AEA metabolism by the indicated pCB. AEA data from Panel A is shown as grey for comparison and the model of inhibition is given. 30 μM of each pCB was used to determine inhibition. Error represents the SEM of 3 experiments.

Table 4.1. Kinetic parameters of experiments.

	Metabolism				AEA Metabolism Inhibition	
	Metabolite(s)	V_{max}[a]	K_m (μM)	$k_{cat} \cdot {K_m}^{-1}$[b]	K_i (μM)	Type
AEA	EET-EAs	135 ± 14	30.9 ± 7.3	4.47	---	---
Δ9-THC	-1'-OH	211 ± 28	11.9 ± 4.8	18.7	9.86 ± 0.45	Noncompetitive
Δ8-THC	-1'-OH	80.9 ± 14.3	8.52 ± 5.30	9.50	20.2 ± 1.9	Noncompetitive
CBN	-1'-OH or -11-OH	710 ± 248	77.8 ± 42.2	9.13	19.4 ± 2.0	Noncompetitive
CBD	-7-OH + -1"-OH	372 ± 100	57.2 ± 26.5	6.50	16.9 ± 1.1	Noncompetitive
CBG	-1"-OH	123 ± 14	8.27 ± 3.24	14.9	10.8 ± 1.4	Competitive
CBC	-1"-OH	371 ± 134	84.2 ± 46.2	4.41	21.1 ± 1.4	Noncompetitive

[a] ($pmol \cdot min^{-1} \cdot nmol_{CYP2J2}^{-1}$)
[b] ($nM^{-1} \cdot min^{-1}$)

4.6 Supplementary information

Methods

Materials. Human CYP2J2 cDNA was obtained from OriGene (Catalog No. SC321730) and modified as published before.[250] Ampicillin, arabinose, chloramphenicol, isopropyl β-D-1-thiogalactopyranoside (IPTG), and Ni-NTA resin were obtained from Gold Biotechnology. δ-aminolevulinic acid was obtained from Frontier Scientific. NADPH was obtained from P212121.com. 1-palmitoyl-2-oleoyl-sn-glycero-3-phosphocholine (POPC) and 1-hexadecanoyl-2-(9Z-octadecenoyl)-sn-glycero-3-phospho-L serine (POPS) were purchased from Avanti Polar Lipids, Inc. AEA and EET-EAs were obtained from Cayman Chemical. pCBs were purchased as DEA-exempt preparations of each pCB dissolved in methanol to 1.0 mg/mL from Cayman Chemical. All other materials and reagents used were purchased from Sigma-Aldrich and Fisher Scientific.

Expression and purification of recombinant CYP2J2 in E. coli. Recombinant D34-CYP2J2 containing a His_5 tag was expressed and purified as previously performed.[243,250] The D34-CYP2J2 is a 34-residue N-terminal truncation (residues 3-37) of CYP2J2 with a substitution of Leu2 for an Ala residue. These modifications have been previously shown to increase protein yield without affecting activity. [243,250]

Expression and purification of cytochrome P450 reductase. Expression of cytochrome P450 reductase (CPR) was performed as described previously.[250]

Incorporation of CYP2J2 into Nanodiscs. Nanodiscs (NDs) containing CYP2J2 were prepared in 20% POPS discs as previously described.[289] NDs were used for all experiments except for pCB metabolism experiments.

Soret titration binding. Soret titration binding experiments were performed as previously described.[289] The pCBs were dried with N_2 gas and re-dissolved in DMSO. CBD, CBG, and CBN produced a Soret shift upon binding and their direct binding was measured. AEA, Δ9-THC, Δ8-THC, and CBC did not produce a significant Soret shift, and so an ebastine (EBS) competitive binding was utilized to measure the binding as previously described for AA.[289]

REFERENCES

[1] McDougle, D. R., Palaria, A., Magnetta, E., Meling, D. D., and Das, A. (2013) Functional studies of N-terminally modified CYP2J2 epoxygenase in model lipid bilayers, *Protein Sci 22*, 964-979.

[2] Zelasko, S., Palaria, A., and Das, A. (2013) Optimizations to achieve high-level expression of cytochrome P450 proteins using Escherichia coli expression systems, *Protein Expres Purif 92*, 77-87.

[3] Arnold, W. R., Baylon, J. L., Tajkhorshid, E., and Das, A. (2016) Asymmetric Binding and Metabolism of Polyunsaturated Fatty Acids (PUFAs) by CYP2J2 Epoxygenase, *Biochemistry 55*, 6969-6980.

Guide for reading Supplementary Tables

In each of the Supplementary Tables, **Ions** are classified by the chemical species from which they were fragmented. The unmetabolized phytocannabinoid is referred to as **Parent**, while each respective metabolite is named after its **Modification** (e.g. **1'/1''-OH** for monohydroxylation observed along the pentyl chain). **DiOH** is listed as is, for the exact position for second hydroxylation performed by CYP2J2 could not be determined from the spectral data for every phytocannabinoid tested. In most dehydroxylated species, the 1'/1''-OH is suggested.

Within each listed **Modification**, the number of **Ions**, representing fragments of the chemical species, are listed by row. Relative abundance is given for each species and is calculated as a percentage of the highest intensity **Ion** signal, given the same retention time for the **Ions** considered. Relative abundance values are calculated from MS/MS data unless indicated otherwise.

For example, in **Supplementary Table 4.1**, **Ion 2**, representing a fragment 1'-OH-Δ9-THC, elutes at 20.42 and 21.05 minutes. The intensities for each of these reported peaks are 3504953.25 and 556748.44, respectively. When calculating each peak's relative abundance, compared to other fragments eluting at the same time, one would compare these intensities to those of the most abundant **Ion**, which would be **Ion 4**, for both retention times. Dividing the reported intensities for **Ion 2** by that of **Ion 4**, at each respective retention time, yields the displayed relative abundance.

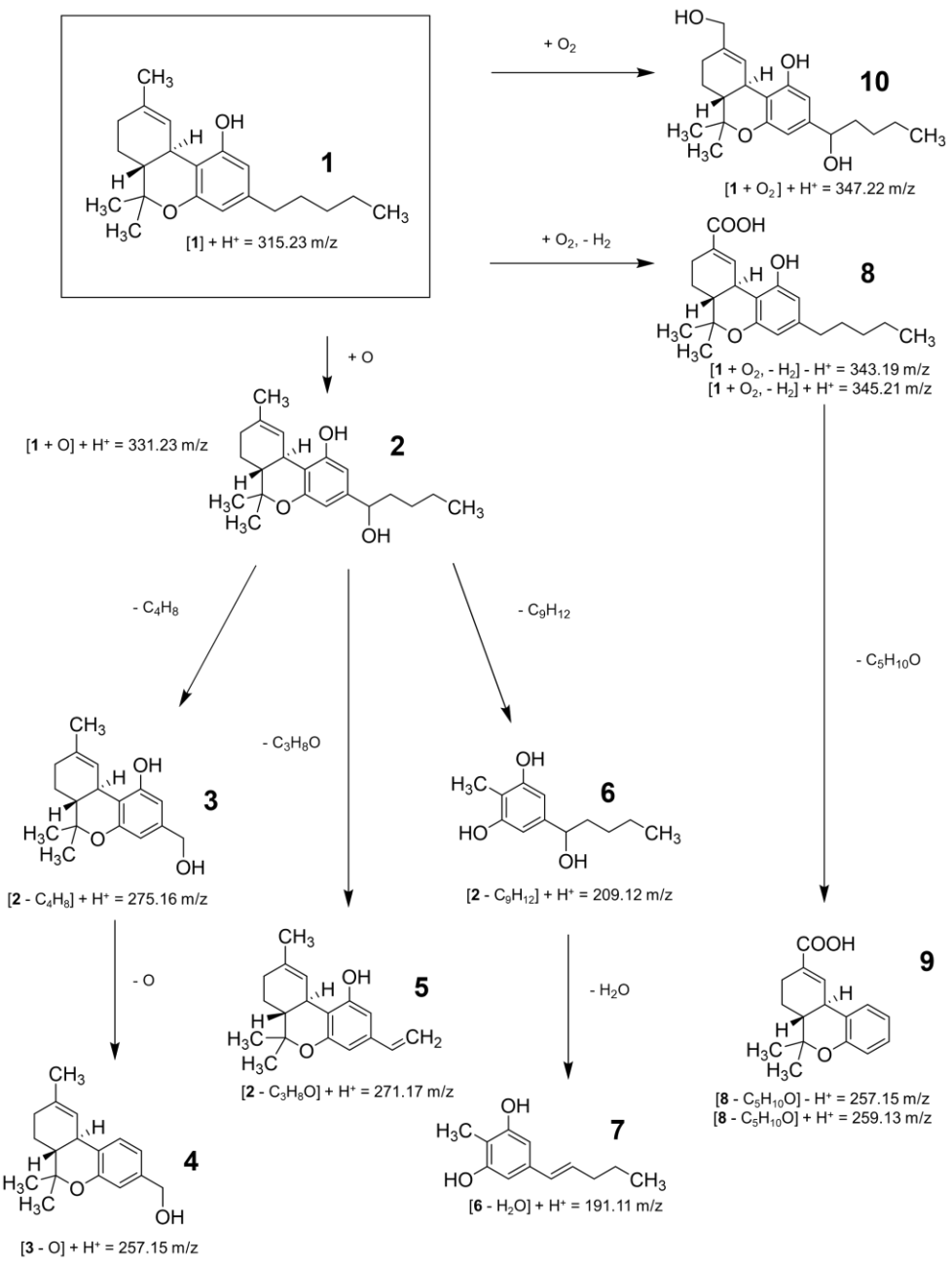

Supplementary Figure 4.1. Fragmentation pathway of Δ9-THC. Parent species as Ion **1**; monohydroxylated species represented as Ions **2-7**; carboxylated species as Ions **8** and **9**; dihydroxylated species as Ion **10**. Corresponding MS/MS data and retention times provided in **Supplementary Table 4.1**.

Supplementary Table 4.1. MS/MS data corresponding to ions distinguishing CYP2J2-Δ9-THC metabolism.

pCB	Modification	Ion #	Formula	Mode	Retention Time	m/z	Intensity	Rel. Abundance in MS/MS spectrum (%)
Delta-9-tetrahydrocannabinol	Parent*	1	$C_{21}H_{30}O_2$	+	24.09	315.23	75162304.00	100.00
	1'-OH	2	$C_{21}H_{30}O_3$	+	20.42	331.23	3504953.25	7.64
				+	21.05	331.22	556748.44	2.51
		3	$C_{17}H_{22}O_3$	+	20.42	275.16	3191566.25	6.96
				+	21.05	275.16	103704.74	0.47
		4	$C_{17}H_{22}O_2$	+	20.42	257.15	45883472.00	100.00
				+	21.05	257.15	22224676.00	100.00
		5	$C_{18}H_{22}O_2$	+	20.42	271.17	1603232.25	3.49
				+	21.05	271.17	302656.03	1.36
		6	$C_{12}H_{18}O_3$	+	20.42	209.12	4297215.00	9.37
				+	21.05	209.12	113166.77	0.51
		7	$C_{12}H_{16}O_2$	+	20.42	191.11	24560034.00	53.53
				+	21.05	191.11	6284094.00	28.28
	11-COOH	8	$C_{21}H_{28}O_4$	+	18.76	345.20	29737.60	4.88
				-	18.89	343.19	1077148.75	100.00
				+	19.4	345.21	169284.34	70.20
				-	22.67	343.19	506196.88	58.80
		9	$C_{16}H_{18}O_3$	+	18.76	259.13	23468.31	3.85
				-	18.89	257.15	202751.48	18.82
				+	19.4	259.13	6911.84	2.87
	DiOH	10	$C_{21}H_{30}O_4$	+	20.71	347.22	52726.88	6.51

*Parent Ion data gathered from MS/MS data of Δ9-THC standard.

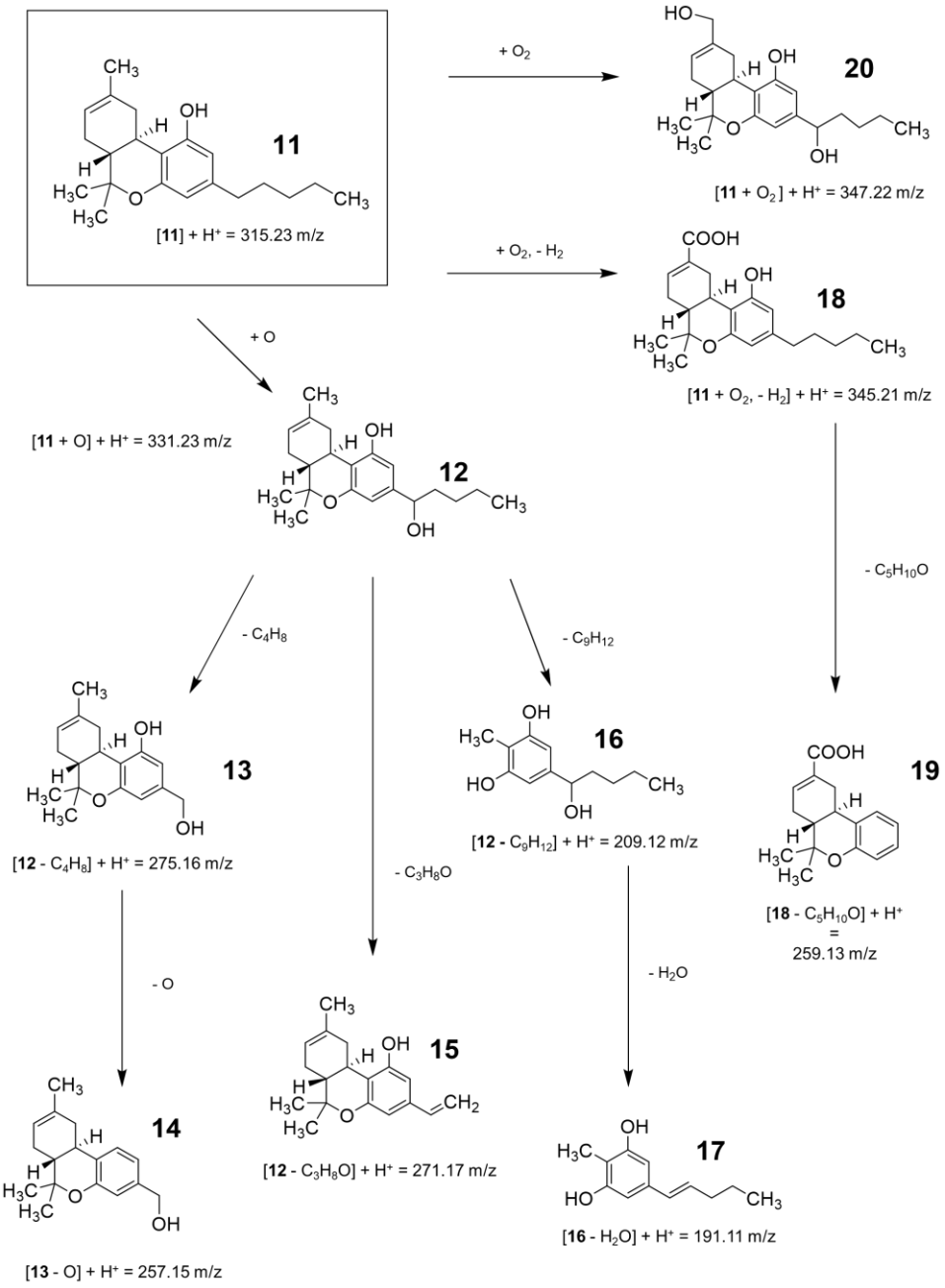

Supplementary Figure 4.2. Fragmentation pathway of Δ8-THC. Parent species as Ion **11**; monohydroxylated species represented as Ions 1**2-17**; carboxylated species as Ions **18** and 1**9**; dihydroxylated species as Ion **20**. Corresponding MS/MS data and retention times provided in **Supplementary Table 4.2**.

Supplementary Table 4.2. MS/MS data corresponding to ions distinguishing CYP2J2-Δ8-THC metabolism.

pCB	Modification	Ion #	Formula	Mode	Retention Time	m/z	Intensity	Rel. Abundance in MS/MS spectrum (%)
Delta-8-tetrahydrocannabinol	Parent*	11	$C_{21}H_{30}O_2$	+	24.16	315.23	63499332.00	100.00
	1'-OH	12	$C_{21}H_{30}O_3$	+	20.84	331.23	6163016.00	7.20
				+	21.4	331.23	714990.75	1.70
		13	$C_{17}H_{22}O_3$	+	20.84	275.16	16755311.00	19.58
				+	21.4	275.16	181899.47	0.43
		14	$C_{17}H_{22}O_2$	+	20.84	257.15	85588832.00	100.00
				+	21.4	257.15	42145924.00	100.00
		15	$C_{18}H_{22}O_2$	+	20.84	271.17	1189927.88	1.39
				+	21.4	271.17	329652.75	0.78
		16	$C_{12}H_{18}O_3$	+	20.84	209.12	24819734.00	29.00
				+	21.4	209.12	330217.00	0.78
		17	$C_{12}H_{16}O_2$	+	20.84	191.11	42031644.00	49.11
				+	21.4	191.11	13706612.00	32.52
	11-COOH**	18	$C_{21}H_{28}O_4$	+	19.17	345.21	43102268.00	100.00
		19	$C_{16}H_{18}O_3$	+	19.17	259.13	94450.52	21.91
	DiOH	20	$C_{21}H_{30}O_4$	+	16.4	347.22	756208.25	17.06

*Parent Ion data gathered from MS/MS data of Δ8-THC standard.

**Δ8-THC-11-COOH data gathered from MS data, as MS/MS spectra did not provide any ions with a mass corresponding to the unfragmented 11-carboxylated fragment.

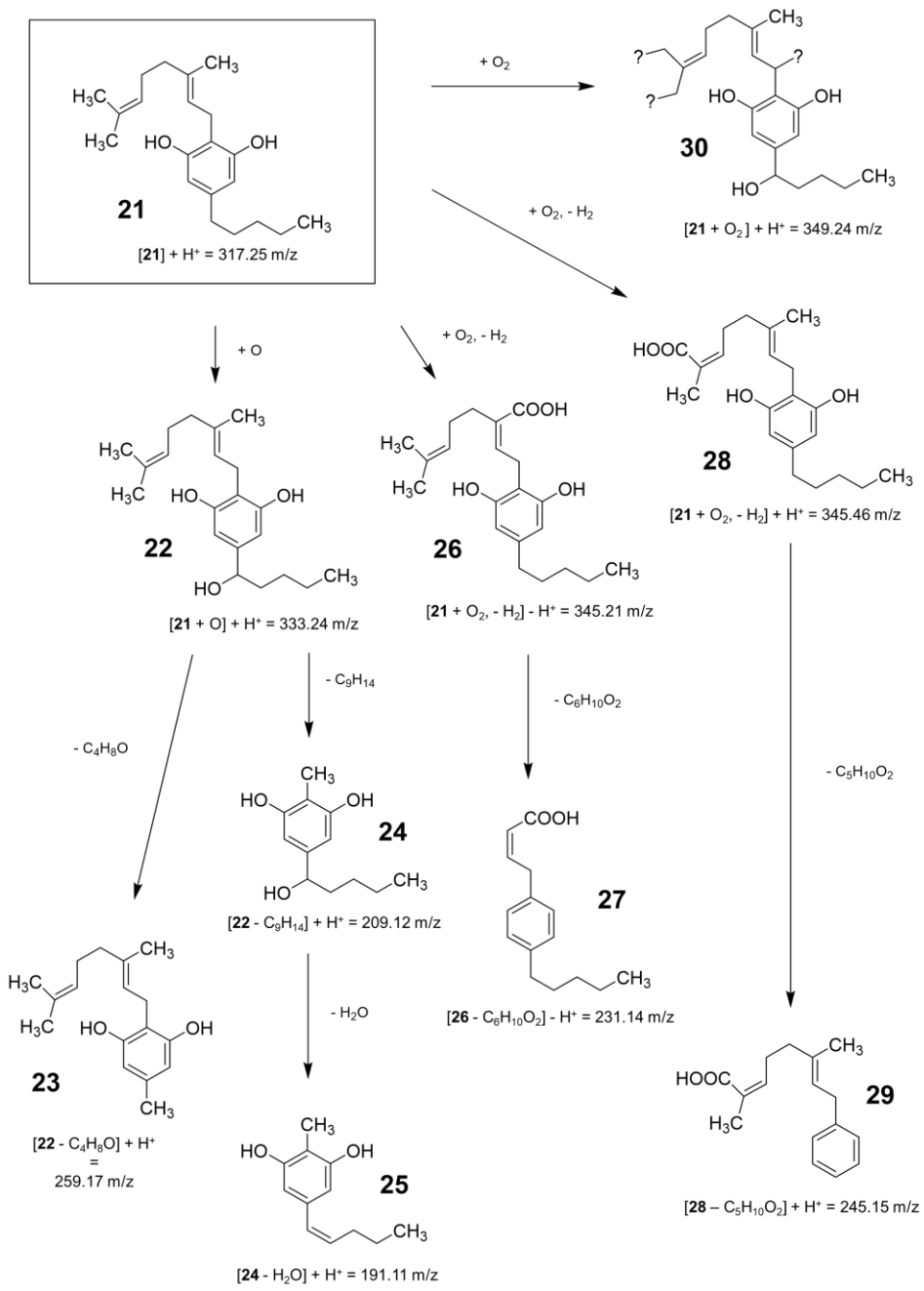

Supplementary Figure 4.3. Fragmentation pathway of CBG. Parent species as Ion **21**; monohydroxylated species represented as Ions **22-25**; 9'-carboxylated species as Ions **26** and **27**; 5"-carboxylated species as Ions **28** and **29**; dihydroxylated species as Ion **30**, where question marks represent potential positions for subsequent hydroxylation, in addition to the 1" position. Corresponding MS/MS data and retention times provided in **Supplementary Table 4.3**.

Supplementary Table 4.3. MS/MS data corresponding to ions distinguishing CYP2J2-CBG metabolism.

pCB	Modification	Ion #	Formula	Mode	Retention Time	m/z	Intensity	Rel. Abundance in MS/MS spectrum (%)
Cannabigerol	Parent*	21	$C_{21}H_{32}O_2$	+	20.86	317.25	15646022.00	15.04
	1"-OH	22	$C_{21}H_{32}O_3$	+	19.03	333.24	80101.83	0.88
		23	$C_{17}H_{24}O_2$	+	19.03	259.17	361966.63	3.99
		24	$C_{12}H_{18}O_3$	+	19.03	209.12	9062598.00	100.00
		25	$C_{12}H_{16}O_2$	+	19.03	191.11	6411131.50	70.74
	9'-COOH	26	$C_{21}H_{30}O_4$	-	14.35	345.21	363732.16	8.56
				-	17.96	345.21	209334.03	5.63
				-	22.32	345.21	1130435.75	100.00
		27	$C_{15}H_{20}O_2$	-	17.96	231.14	10928.57	0.29
	8'/10'-COOH	28	$C_{21}H_{30}O_4$	+	18.09	345.46	6156.17	0.09
		29	$C_{16}H_{20}O_2$	+	18.09	245.15	9129.97	0.13
	DiOH	30	$C_{21}H_{32}O_4$	+	15.07	349.24	16091.57	0.96
				+	15.26	349.20	11280.58	0.85
				+	18.33	349.24	4345.53	0.20

*Parent Ion data gathered from MS/MS data of CBG standard.

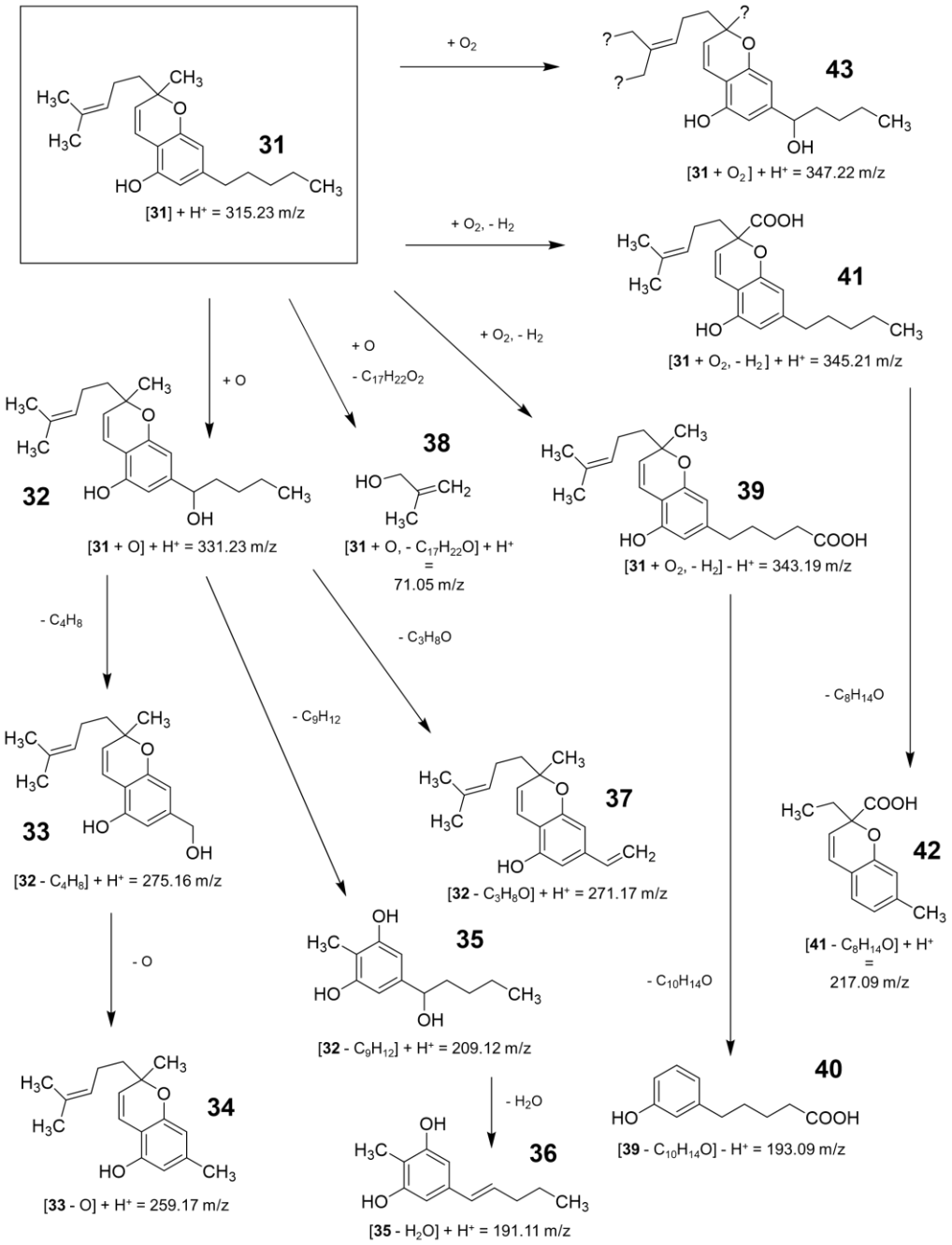

Supplementary Figure 4.4. Fragmentation pathway of CBC. Parent species as Ion **31**; 1”-monohydroxylated species represented as Ions **32-37**; 8’/10’-monohydroxylated species represented as Ion **38**; 9’-carboxylated species as Ions **41** and **42**; 5”-carboxylated species as Ions **39** and **40**; dihydroxylated species as Ion **43**, where question marks represent potential positions for hydroxylation other than at the 1” position. Corresponding MS/MS data and retention times provided in **Supplementary Table 4.4**.

Supplementary Table 4.4. MS/MS data corresponding to ions distinguishing CYP2J2-CBC metabolism.

pCB	Modification	Ion #	Formula	Mode	Retention Time	m/z	Intensity	Rel. Abundance in MS/MS spectrum (%)
Cannabichromene	Parent*	31	$C_{21}H_{30}O_2$	+	24.98	315.23	99115136.00	100.00
	1"-OH	32	$C_{21}H_{30}O_3$	+	21.95	331.23	2570219.00	28.33
				+	25.91	331.23	12169246.00	100.00
		33	$C_{17}H_{22}O_3$	+	21.95	275.16	3260814.25	35.94
		34	$C_{17}H_{22}O_2$	+	25.91	259.17	413954.13	3.40
		35	$C_{12}H_{18}O_3$	+	21.95	209.12	6257679.50	68.98
		36	$C_{12}H_{16}O_2$	+	21.95	191.11	7630927.00	84.11
		37	$C_{18}H_{22}O_2$	+	21.95	271.17	314709.53	3.47
				+	25.91	271.17	1348963.75	11.09
	8'/10'-OH	38	C_4H_8O	+	25.91	71.05	34044.07	0.28
	5"-COOH	39	$C_{21}H_{28}O_4$	-	14.56	343.19	1065349.00	100.00
				-	15.72	343.19	481593.59	19.80
		40	$C_{11}H_{14}O_3$	-	14.56	193.09	75317.45	7.07
	9'-COOH	41	$C_{21}H_{28}O_4$	+	15.85	345.21	150768.06	3.01
				+	20.67	345.2	21276.88	5.92
		42	$C_{13}H_{14}O_3$	+	15.85	217.09	182060.16	3.63
	DiOH	43	$C_{21}H_{30}O_4$	+	20.07	347.22	628388.19	75.86
				+	15.51	347.22	36306.39	3.56

*Parent Ion data gathered from MS/MS data of CBC standard.

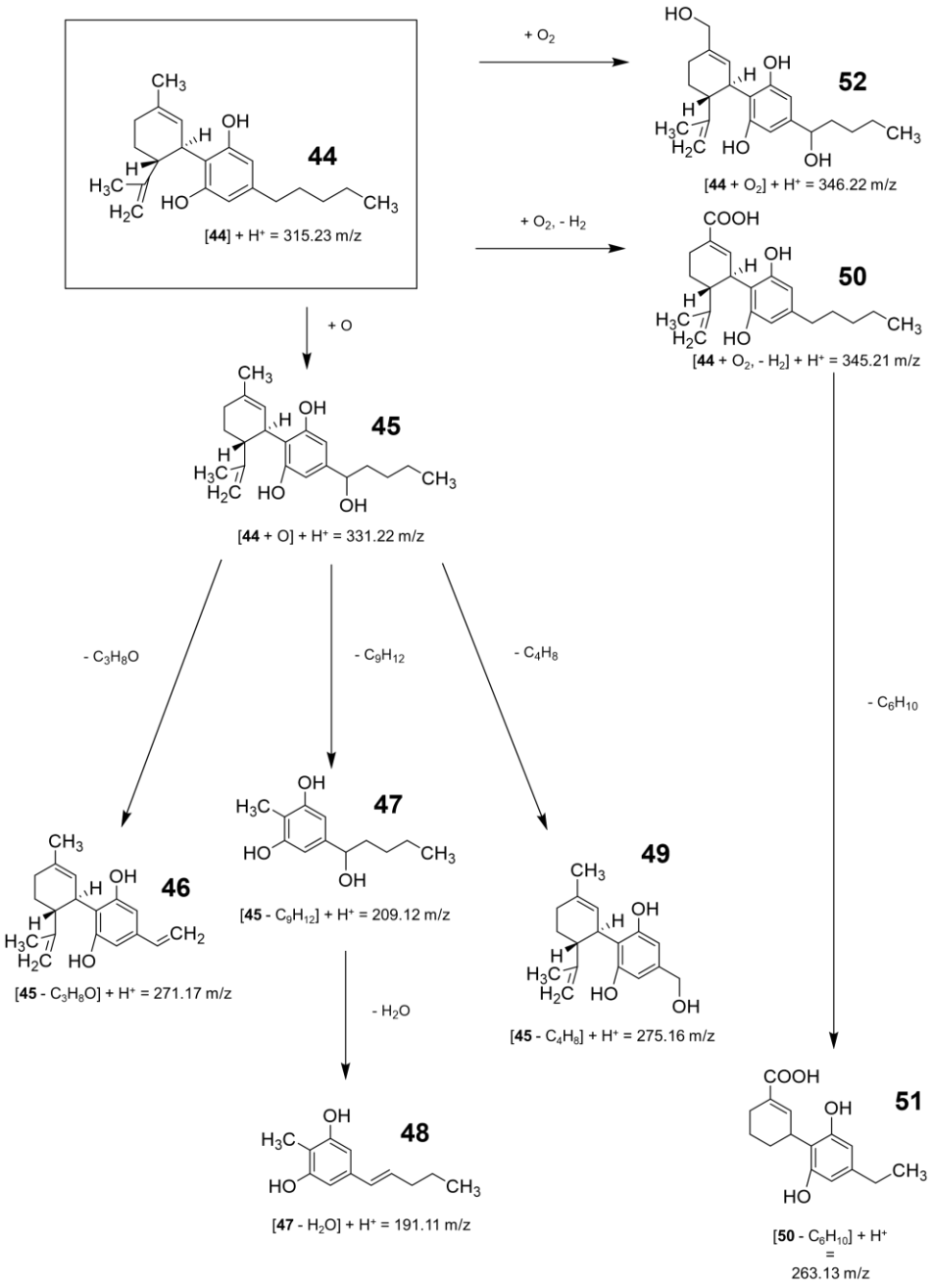

Supplementary Figure 4.5. Fragmentation pathway of CBD. Parent species as Ion **44**; monohydroxylated species represented as Ions **45-49**; **c**arboxylated species as Ions **50** and **51**; dihydroxylated species as Ion **52**. Corresponding MS/MS data and retention times provided in **Supplementary Table 4.5**.

Supplementary Table 4.5. MS/MS data corresponding to ions distinguishing CYP2J2-CBD metabolism.

pCB	Modification	Ion #	Formula	Mode	Retention Time	m/z	Intensity	Rel. Abundance in MS/MS spectrum (%)
Cannabidiol	Parent*	44	$C_{21}H_{30}O_2$	+	21.24	315.23	236230496.00	100.00
	1"-OH	45	$C_{21}H_{30}O_3$	+	17.97	331.22	22309.22	5.28
		46	$C_{18}H_{22}O_2$	+	17.97	271.17	37226.14	8.82
		47	$C_{12}H_{18}O_3$	+	17.97	209.12	13521.62	3.20
		48	$C_{12}H_{16}O_2$	+	17.97	191.11	60162.30	14.25
		49	$C_{17}H_{22}O_3$	+	17.97	275.16	6640.29	1.57
	7-COOH	50	$C_{21}H_{28}O_4$	+	18.01	345.2	92596.23	21.40
				+	18.81	345.21	87302.59	20.17
				+	20.31	345.2	97335.08	65.87
				-	20.44	343.19	1490278.00	100.00
		51	$C_{15}H_{18}O_4$	+	18.81	263.13	39798.00	9.20
	DiOH**	52	$C_{21}H_{30}O_4$	+	11.60	347.22	9769595.00	49.97

*Parent Ion data gathered from MS/MS data of CBD standard.

**CBD-DiOH data gathered from MS data, as MS/MS spectra did not provide any ions with a mass corresponding to the unfragmented dehydroxylated fragment.

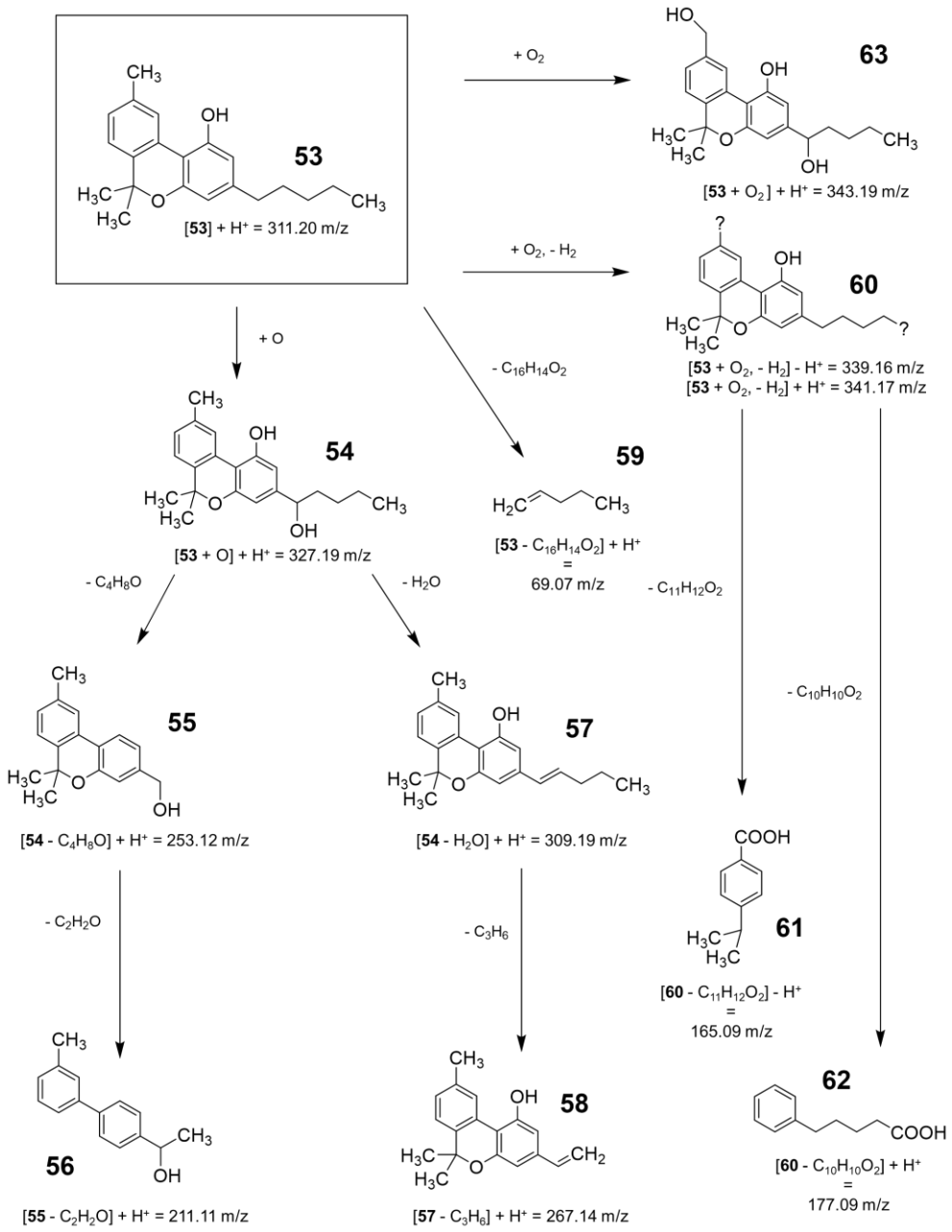

Supplementary Figure 4.6. Fragmentation pathway of CBN. Parent species as Ion **53**; monohydroxylated species represented as Ions **54-59**; parent 11/5”-carboxylated species is represented as Ion **60**, with question marks corresponding to either type of carboxylation, depending on the ionization mode used; 11-carboxylation (negative ion mode) represented as Ion **61** and 5’-carboxylation (positive ion mode) represented as Ion **62**; dihydroxylated species as Ion **63**. Corresponding MS/MS data and retention times provided in **Supplementary Table 4.6**.

Supplementary Table 4.6. MS/MS data corresponding to ions distinguishing CYP2J2-CBN metabolism.

pCB	Modification	Ion #	Formula	Mode	Retention Time	m/z	Intensity	Rel. Abundance in MS/MS spectrum (%)
Cannabinol	Parent*	53	$C_{21}H_{26}O_2$	+	23.04	311.20	72421216.00	100.00
	1'-OH	54	$C_{21}H_{26}O_3$	+	19.31	327.19	7484971.00	4.42
		55	$C_{17}H_{18}O_2$	+	19.31	253.12	169165280.00	100.00
		56	$C_{15}H_{16}O$	+	19.31	211.11	6758462.50	4.00
		57	$C_{21}H_{24}O_2$	+	19.31	309.19	75666080.00	44.73
		58	$C_{18}H_{19}O_2$	+	19.31	267.14	9962170.00	5.89
		59	C_5H_{10}	+	19.31	69.07	2100366.75	1.24
	11-COOH	60	$C_{21}H_{24}O_4$	-	17.38	339.16	58063432.00	100.00
	11-COOH	61	$C_{10}H_{12}O_2$	-	17.38	165.09	321084.72	6.01
	5"-COOH	60	$C_{21}H_{24}O_4$	+	18.86	341.17	50217104.00	100.00
	5"-COOH	62	$C_{11}H_{14}O_2$	+	18.86	177.09	74082.51	0.15
	DiOH	63	$C_{21}H_{26}O_4$	+	15.34	343.19	19536.93	0.53

*Parent Ion data gathered from MS/MS data of CBN standard.

Ions **54-59 suggestive of CBN-1'-OH, though may also represent CBN-11-OH, for reasons stated in the main text.

Chapter 5: Endovanilloid metabolism by CYP2J2 is potentiated by anandamide

5.1 Introduction

Opioids are highly addictive pain medications that are susceptible for abuse. The age-adjusted death rate by opioid overdose was determined to be nearly 20 per 100,000 people in the United States in 2016, according to a report by the Centers for Disease Control and Prevention[364]. Hence, there is a need for therapeutic alternatives to opioids that combat inflammation and the associated pain.

Pain is regulated primarily by sensory afferent neuronal cells and immune cells. Both of these cell types are rich sources of lipid mediators. Lipid mediators are generated via the enzymatic oxidation of dietary omega-3 and omega-6 polyunsaturated fatty acids (PUFAs). The pro-inflammatory lipid mediators contribute to pain sensitivity by activating the GPCRs in the sensory neurons to increase membrane excitability and pain response[365]. For instance, cyclooxygenases generate pro-inflammatory lipids such as prostaglandin E_2 (PGE_2) at the sites of inflammation. NSAIDs are used to inhibit cyclooxygenases, leading to a decrease in the synthesis of pro-inflammatory lipid metabolites, thereby decreasing inflammatory pain[4]. On the other hand, anti-inflammatory and pro-resolving lipid mediators suppress and resolve the inflammatory process, and thus attenuate pain[37,366]. Hence, lipid mediators can fine-tune the pain response and have been at the center for the development of alternative non-opioid pain therapeutics[367,368].

Additionally, cannabis has been used for centuries to reduce nociceptive pain either alone or in combination with opioids[369]. The primary components of cannabis interact in the body with cannabinoid receptors 1 and 2 (CB1 and CB2) and other GPCRs[84-86]. A class of bioactive lipid mediators, known as endocannabinoids (eCBs), activate cannabinoid receptors and suppresses inflammation and pain sensitization[370,371]. These eCBs are generated by damaged neurons and inflamed tissues and are derivatives of dietary omega-3 and omega-6 PUFAs. CB1 receptors are highly expressed in the central nervous system, mostly in the presynaptic region, and there is substantial CB1 expression in the nociceptive sensory neurons. It has been shown that under different pain conditions, there is a concomitant increase in CB1 expression[372,373]. Hence, there is sufficient evidence that CB1 mediates the psychotropic effects of cannabinoids such as modulating nociceptive pain, as well as modulating inflammation[84,97-101,374]. CB2 is mostly expressed in

immune cells and mediates the anti-inflammatory effects of cannabinoids, which indirectly contributes to the anti-nociception of acute inflammatory pain[100,102,108,374]. CB2 receptor activation exerts profound anti-nociceptive effects in animal models of acute, inflammatory, and neuropathic pain[375].

In addition to CB1 and CB2, eCBs act through transient receptor potential vanilloid 1 (TRPV1)[360,376,377]. TRPV1 is activated by noxious temperatures, pH, and chemical stimuli such as inflammatory agents[147-150]. TRPV1 has been associated with the nociceptive pain of these stimuli, and thus antagonizing TRPV1 can reduce pain. Paradoxically, the activation of TRPV1 by small molecules such as capsaicin can also alleviate pain by desensitizing TRPV1 signaling and creating a numbing effect[378,379]. In addition to mediating the pain associated with these stimuli, TRPV1 exhibits pro- and anti-inflammatory effects[152-155].

Recently, it has been postulated that there is a crosstalk between CB1 and TRPV1 receptors, which are co-localized in dorsal root ganglion and in neuron-enriched mesencephalic cultures, hippocampus, and cerebellum[380]. Therefore, the endocannabinoid system and TRPV1 axis provides a promising target to develop pain and inflammation therapeutics. For example, CMX-020 (Patent US8658632B2) is a novel drug based on the structure of eCBs and is in development to alleviate pain by binding to both cannabinoid receptors and TRPV1. Moreover, several other lipid metabolites such as synthetic resolvins RvD1 and RvD2 have been shown to reduce pain by the inhibition of specific TRPV channels[37,381]. However, to further exploit the potential of the TRPV1-eCB axis for pain therapeutics, we need to better understand the endogenous eCB-like ligands and their derivatives that modulate pain by acting through the TRPV1-eCB axis.

The best-studied eCB is anandamide (N-arachidonoyl-ethanolamine: AEA), which is derived from arachidonic acid (AA)[87-90]. Besides AEA, other eCBs such as N-arachidonoyl-dopamine (NADA) and N-arachidonoyl-serotonin (NA5HT) are also derivatives of AA (Figure 5.1). These dopamine (DA)[382-384] and serotonin (5HT)[385-387] derivatives were identified *in vivo* in brain and intestinal tissues. It was shown that NADA binds with a higher affinity to CB1 than to CB2[382]; however, conclusive evidence for NA5HT binding to CB1/2 has yet to emerge. Additionally, NADA was shown to be an agonist of TRPV1[142,143] and NA5HT is an antagonist of TRPV1, which results in analgesia[144]. Hence, NADA and NA5HT are classified as endovanilloids (eVDs) for their actions at the TRPV1 “vanilloid” receptor. Interestingly, NADA has low-affinity binding to DA

receptors[382], and the stimulation of degranulation in mast cells by NA5HT suggests it does not activate the 5HT receptors[388]. Therefore, NADA and NA5HT do not display typical DA or 5HT responses and are instead regulators of TRPV1.

To add to the complexity of lipid metabolism, oxygenases transform lipids such as eCBs into oxy-metabolites that exhibit distinct pharmacology compared to their parent molecules. For instance, the oxidized products of AA by cyclooxygenase lead to the formation of prostaglandins that modulate TRPV1 activity and subsequently pain[389]. Cytochromes P450 (CYPs) epoxidize AA and omega-3 PUFAs into epoxy-PUFAs that have been shown to decrease pain[57,58,390]. Recently, the CYP-mediated metabolism of eCBs was shown to produce epoxy-eCBs that exhibit CB2 receptor selectivity and are anti-inflammatory and anti-tumorigenic[161,163,164]. For instance, CYPs epoxidize AEA into epoxyeicosatrienoyl ethanolamides (EET-EAs) that bind to CB2 receptors[161,246,391]. Similarly, omega-3 eCBs are also converted by CYPs into epoxide metabolites that are anti-inflammatory and anti-tumorigenic[163].

Overall, there is strong evidence in the literature for pain modulation by eCB and PUFA epoxides through multiple receptors. Herein, we report the discovery of a novel class of dual-functional epoxides of NADA and NA5HT (epoNADA and epoNA5HT, respectively) that reciprocally regulate both cannabinoid receptors (CB1 and CB2) and TRPV1 (Figure 5.1). We synthesize epoNADA and epoNA5HT and determine their endogenous levels in porcine brains using targeted lipidomics. We then show that epoNADA and epoNA5HT are formed under inflammatory conditions by CYP epoxygenases and show that AEA potentiates the formation of 14',15'-epoNADA in microglial cells. We show that the potentiation can be explained by the fact that NADA, NA5HT, and AEA bind to multiple sites to CYP-Nanodiscs (nanoscale bilayers) using *in vitro* kinetics methods and molecular dynamics (MD) simulations. Together, we show that epoNADA and epoNA5HT act as dual CB1/2 and TRPV1 ligands and exhibit anti-inflammatory activity and are by virtue of their pharmacological properties are likely to exhibit anti-pain activity.

5.2 Experimental procedures

Materials, RT-qPCR, IL-6, NO, MTT, protein expression, nanodisc, in vitro *metabolism, and full-scan metabolism protocols can be found in the supplementary information.*

Synthesis of NADA [(5Z,8Z,11Z,14Z)-N-(3,4-dihydroxyphenethyl)icosa-5,8,11,14-tetraenamide] and NA5HT [(5Z,8Z,11Z,14Z)-N-(2-(5-hydroxy-1H-indol-3-yl)ethyl)icosa-5,8,11,14-tetraenamide]. Dopamine hydrochloride (24.9 mg, 0.131 mmol, 2.0 equiv.) or serotonin hydrochloride (27.9 mg, 0.131 mmol, 2.0 equiv.) were added to N,N-diisopropylethylamine (DIPEA, 27.4 μL, 0.145 mmol, 2.2 equiv.) in an anhydrous solution of DMF/CH_2Cl_2 (1/1 v/v, 25 mL) under an argon atmosphere. This mixture was cooled in an ice-water bath and then AA (21.7 μL, 0.066 mmol, 1.0 equiv.), 1-ethyl-3-(3-dimethylaminopropyl)-carbodiimide (EDC, 63 mg, 0.33 mmol, 5.0 equiv.), and 4-dimethylaminopyridine (DMAP, 2 mg, 0.0099 mmol, 0.15 equiv.) were added. After 1 hour, the reaction was warmed to room temperature and allowed to incubate at the same temperature for 8 hours. Afterwards, toluene was added, and the reaction was concentrated under reduced pressure. The product was extracted 3× from water with CH_2Cl_2 and then washed 1× with brine. The organic layer was dried over sodium sulfate and concentrated under reduced pressure to yield a yellow-brown oil. NADA and NA5HT were purified using HPLC Method 2 below. Products were dried under reduced pressure, stored in ethanol, and quantified via HPLC as stated below. Yields were 13.0 mg NADA (45%) and 12.8 mg NA5HT (45%). **[NADA]** ^{1}H NMR (400 MHz, $CDCl_3$) δ 6.96 (s, 1H); 6.80 (d, *J* = 8.0 Hz, 1H); 6.74 (d, *J* = 2.0 Hz, 1H); 6.58 (dd, *J* = 8.1, 2.0 Hz, 1H); 5.61 (s, 1H); 5.54 (d, J = 6.5 Hz, 1H); 5.44 – 5.27 (m, 8H); 4.12 (q, J = 7.1 Hz, 1H) (ethyl acetate); 3.48 (q, *J* = 6.7 Hz, 2H); 2.88 – 2.75 (m, 6H); 2.70 (t, *J* = 7.1 Hz, 2H); 2.19 – 2.12 (m, 2H); 2.12 – 1.99 (m, 6H); 1.68 (p, *J* = 7.4 Hz, 2H); 1.41 – 1.19 (m, 8H) (part ethanol); 0.88 (t, *J* = 6.7 Hz, 3H). HRMS (m/z): [M + H^+] cal'd 440.3165, observed 440.3161 (-0.9 ppm); $C_{28}H_{42}NO_3$. **[NA5HT].** ^{1}H NMR (500 MHz, $CDCl_3$) δ 7.90 (s, 1H); 7.04 – 6.98 (m, 2H); 6.82 – 6.76 (m, 1H); 5.53 (s, 1H); 5.44 – 5.29 (m, 8H); 3.57 (q, J = 6.6 Hz, 2H); 2.90 (t, J = 6.8 Hz, 2H); 2.80 (dt, J = 18.2, 5.9 Hz, 6H); 2.08 (ddt, J = 31.1, 14.6, 7.4 Hz, 6H); 1.73 – 1.63 (m, 2H); 1.40 – 1.16 (m, 7H) (part ethanol); 0.88 (t, J = 6.7 Hz, 3H). HRMS (m/z): [M + H^+] cal'd 463.3325, observed 463.3322 (-0.6 ppm); $C_{30}H_{43}N_2O_2$.

Synthesis of 14',15'-epoNADA [(5Z,8Z,11Z)-N-(3,4-dihydroxyphenethyl)-13-(3-pentyloxiran-2-yl)trideca-5,8,11-trienamide] and 14',15'-epoNA5HT [(5Z,8Z,11Z)-N-(2-(5-hydroxy-1H-indol-3-yl)ethyl)-13-(3-pentyloxiran-2-yl)trideca-5,8,11-trienamide]. Synthesis of EETs was performed using *m*CPBA as previously described, which yields 4-8 mg of 14,15-EET (7.6-15% yield)[163]. 14,15-epoNADA and 14,15-epoNA5HT were synthesized by coupling DA and 5HT to 14,15-EET using the above coupling method. Yield from 14,15-EET: 3.6 mg (65%) 14',15'-epoNADA, 4.7

mg (40%) 14',15'-epoNA5HT. **[14',15'-epoNADA]** 1H NMR (400 MHz, $CDCl_3$) δ 6.80 (d, *J* = 8.1 Hz, 1H); 6.72 (s, 1H); 6.58 (d, *J* = 7.9 Hz, 1H); 5.81 (s, 1H); 5.65 – 5.25 (m, 6H); 3.47 (q, *J* = 6.5 Hz, 2H); 3.01 (d, *J* = 5.4 Hz, 1H); 2.80 (d, *J* = 20.6 Hz, 4H); 2.69 (t, *J* = 6.8 Hz, 2H); 2.45 (m, *J* = 7.3 Hz, 1H); 2.24 (m, *J* = 6.8 Hz 1H); 2.17 – 1.92 (m, 4H); 1.79 – 1.62 (m, 2H); 1.34 (q, *J* = 5.1, 3.7 Hz, 4H); 0.98 – 0.77 (m, 3H). HRMS (m/z): [M + H^+] cal'd 456.3114, observed 456.3104 (-2.2 ppm); $C_{28}H_{42}NO_4$. **[14',15'-epoNA5HT]** 1H NMR (500 MHz, $CDCl_3$) δ 7.97 (s, 1H); 7.13 – 6.89 (m, 2H); 6.79 (dd, J = 8.7, 2.5 Hz, 1H); 5.60 (s, 1H); 5.55 – 5.29 (m, 7H); 5.23 (s, 1H); 3.56 (p, J = 8.1, 7.3 Hz, 2H); 2.96 (d, J = 7.2 Hz, 2H); 2.89 (q, J = 7.0 Hz, 2H); 2.79 (dt, J = 23.0, 6.3 Hz, 4H); 2.42 (d, J = 6.7 Hz, 1H); 2.21 (dt, J = 13.8, 6.8 Hz, 1H); 2.09 (dq, J = 20.9, 7.4 Hz, 4H); 1.68 (p, J = 7.6 Hz, 2H); 1.47 – 1.19 (m, 6H), 0.89 (d, J = 7.1 Hz, 3H). HRMS (m/z): [M + H^+] cal'd 479.3274, observed 479.3269 (-1.0 ppm); $C_{30}H_{43}N_2O_3$.

Extraction of NADA and NA5HT from porcine brain regions. Porcine brains were obtained from the Meat Science Laboratory at the University of Illinois at Urbana-Champaign. The brains were dissected into regions (cerebellum; "central core" comprising the hippocampus, hypothalamus, and thalamus; and the cerebrum) and diced immediately after removal from the pig. The tissue was then flash frozen and stored at -80° C until used. For extraction, the tissue was homogenized in 5 volumes of ice-cold methanol (MeOH) containing 0.03 mM of the soluble epoxide hydrolase inhibitor 4-[[trans-4-[[(tricyclo[3.3.1.13,7]dec-1-ylamino)carbonyl]amino]cyclohexyl]oxy]-benzoic acid (t-AUCB) and 1 mM of FAAH inhibitor phenylmethylsulfonyl fluoride (PMSF). Debris was filtered using a filter column. The extract was then dried under reduced pressure and resuspended in 50% MeOH. The extracts were then loaded onto 1-gram Bond Elut C-18 cartridges (Varian, Harbor City, CA) (one column per gram of tissue), preconditioned with 25% MeOH. Cartridges were washed with 4 mL of 10% MeOH and eluted with 4 mL of 100% acetonitrile. The eluates were dried under reduced pressure in amber vials and stored under $Ar_{(g)}$ at -80° C until resuspended in 180-proof ethanol for LC-MS/MS analysis (the day after). Samples of tissue were spiked with 1 µg of NADA or NA5HT standards to test the recovery of this method, and we were able to recover 40% of the material.

HPLC analysis of NADA, NA5HT, and metabolites. Compounds were analyzed via high-performance liquid chromatography (HPLC) consisting of an Alliance 2695 analytical separation module (Waters, Milford, MA) and a Waters 996 photodiode diode array detector (Waters). Epoxy-eVDs for synthesis purification were separated in reverse phase using a SunFire™ Prep

C_{18} OBD™ 5 µm 19 x 50 mm column (Waters) and a 3.0 mL/min flow rate, and for quantification using a Phenomenex Prodigy® 5µm ODS-2, 150 x 4.60 mm column (Phenomenex, PN 00F-3300-E0, Torrance, CA) with a 1 mL/min flow rate. Mobile Phase A consisted of 95:5% H_2O (0.1% acetic acid):acetonitrile and Mobile Phase B consisted of 5:95% H_2O (0.1% acetic acid):acetonitrile. A full-scan method (Method 1) was developed to investigate all potential products from *in vitro* enzyme reactions as follows: 0-1 min, 100% A; 1-60 min, linear gradient of 100% A to 100% B; 60-65 min, 100% B. NADA and NA5HT elution times were confirmed using authentic standards (59.5 min and 60 min, respectively). A shorter method (Method 2) was developed to analyze the hydrophobic products and for synthesis purification and quantification. 0-30 min: 100% A to 100% B; 30-40 min: 100% B. All wavelengths from 190-600 nm were monitored. 14',15'-epoNADA and 14',15'-epoNA5HT were quantified at 281 nm and 277 nm wavelengths, respectively, using a NADA and NA5HT standard curve, respectively.

LC-MS/MS quantification of NADA, NA5HT, and AEA from tissue. Samples were analyzed with the 5500 QTRAP LC/MS/MS system (Sciex, Foster City, CA) in Metabolomics Lab of Roy J. Carver Biotechnology Center, University of Illinois at Urbana-Champaign. Software Analyst 1.6.2 was used for data acquisition and analysis. The 1200 series HPLC system (Agilent Technologies, Santa Clara, CA) includes a degasser, an autosampler, and a binary pump. The LC separation was performed on an Agilent SB-Aq column (4.6 x 50mm, 5µm) with mobile phase A (0.1% formic acid in water) and mobile phase B (0.1% formic acid in acetontrile). The flow rate was 0.3 mL/min. The linear gradient was as follows: 0-1min, 90%A; 8-13min, 0%A; 13.5-18min, 90%A. The autosampler was set at 10°C. The injection volume was 10 µL. Mass spectra were acquired under positive electrospray ionization (ESI) with the ion spray voltage of 5500 V. The source temperature was 450 °C. The curtain gas, ion source gas 1, and ion source gas 2 were 32 psi, 50 psi, and 65 psi, respectively. Multiple reaction monitoring (MRM) was used for quantitation: AEA m/z 348.3 --> m/z 203.2; NADA m/z 440.2 --> m/z 287.1; 14',15'-epoNADA m/z 456.3 --> m/z 137.1; 14',15'-epoNA5HT m/z 479.3 --> m/z 160.1; NA5HT m/z 463.3 --> m/z 287.2. Internal standard AEA-d4 was monitored at m/z 352.3 --> m/z 287.2.

Cell culture. HEK cells stably transfected with human TRPV1 (HEK-hTRPV1) were a gift from Prof. Bradshaw (University of Indiana, Bloomington), which were originally constructed by Merck Research. Cells were grown in Eagle Minimum Essential Media supplemented with L-glutamine (EMEM) (ATCC) and 10% fetal bovine serum (FBS) and were incubated at 37°C with

5% CO_2. Cells were sub-cultured at 80-90% confluency by trypsinization in a 1:6-1:10 ratio. HTLA cells for PRESTO-TANGO and BV-2 microglia were grown as previously described[163].

Metabolism of NADA and NA5HT by BV-2 microglia with and without lipopolysaccharide (LPS) stimulation. BV-2 microglia were plated on 6-well plates at 5 x 10^5 cells per well and grown to 80-90% confluency. Cell growth media was exchanged for 2 mL of serum-free DMEM and cells were then stimulated with 100 ng/mL of LPS for 12 hours; control cells were without LPS stimulation. Afterwards, 1 μM of t-AUCB with or without 1 μM of the CYP inhibitor SKF 525A were added for 30 min. 10 μM of NADA or NA5HT were then added for 30 min with or without 10 μM or 30 μM AEA. Cells were scraped into media and combined with 2 mL ice-cold methanol. Cells were lysed using three consecutive 30-second on/off cycles on a water-bath sonicator. Cell debris was pelleted via centrifugation and the supernatant was purified using 100-mg Bond Elut C-18 cartridges (Varian, Harbor City, CA) and analyzed as stated above for tissue extractions.

TRPV1 binding/activation measurements. Binding of NADA, NA5HT, and epoxy-eVDs to TRPV1 was determined using an intracellular Ca^{2+} fluorescent quantification method. HEK-hTRPV1 cells were grown for 3 passages after recovery from frozen stocks before plating on Corning CellBind black, clear-bottom 96-well fluorescence plates coated with poly-L-lysine. After 24 hrs, media was removed, and cells were loaded with 3 μM Fura-2 AM dye (Molecular Probes) in sterile-filtered HEPES-Tyrode Buffer (HTB) (Alfa Aesar) supplemented with 0.01% Plurionic F-127 (Molecular Probes) for 20 min at room temperature. Analytes were prepared from DMSO stocks in 150 μL HTB on separate 96-well plates so that <0.1% DMSO was introduced to the cells. Dye was removed and cells were washed twice with HTB and 100 μL of HTB was added to the cells for the assay. To confirm binding to TRPV1, 0.5 μM of the TRPV1-specific antagonist AMG-9810 was added to this 100 μL of HTB prior to stimulating with agonists. Cells were then incubated at room temperature for 20 min to allow for the de-acetylation of the dye. Fluorescence readings were conducted on a SpectraMax Gemini EM (Molecular Devices, San José, Ca) plate reader using the following settings: bottom-read; channel 1—340 nm excitation, 510 nm emission; channel 2—380 nm excitation, 510 nm emission; 2-sec mix before experiment; read every 14 sec; 5-min experiment. The assays were conducted at room temperature (25° C). 100 μL of agonists were transferred in triplicate via multi-channel pipette to initiate the assay and the fluorescence intensities of both channels were measured over 5 min. The intensity from channel 1 (Ca^{2+}-bound Fura-2) was divided by the intensity from channel 2 (Ca^{2+}-free Fura-2) to achieve the Fluorescence

Ratio $\left(\frac{I_{340ex/510em}}{I_{380ex/510em}}\right)$. The Fluorescence Ratio was then plotted over time. Due to variations in the activation, the AUC of the Fluorescence Ratio from 84-252 seconds was used to determine activation. The average AUC of DMSO from 84-252 seconds was considered "baseline" and subtracted from each data point. The AUCs were plotted as a function of concentration and fitted to a dose-response curve (Equation 5) using OriginPro. CAP was used as a full-agonist positive control, and the B_{max} of the CAP was defined as 100% activation. Antagonism experiments for NA5HT, 14',15'-epoNA5HT, and AMG-9810 were determined by adding varying concentrations of antagonist in 100 μL of HTB 15 min prior to stimulating with 250 nM capsaicin.

PRESTO-TANGO binding with CB1 and CB2. Binding of eVDs to CB1 and CB2 was performed using the PRESTO-TANGO assay as previously described[163]. CP-55940 was used as a full-agonist positive control for both receptors, and its B_{max} was defined as 100% activity. Cells were incubated with 1 μM of t-AUCB for 30 minutes prior to stimulation with analyte for 8 hrs. Luminescence readings were then recorded and processed as previously described.[163] For antagonism experiments, analytes were co-administered at varying concentrations with 50 nM CP-55940.

Quantitation of 14',15'-epoNADA and 14',15'-epoNA5HT using LC-MS/MS. Samples were analyzed with the 5500 QTRAP LC/MS/MS system (Sciex, Framingham, MA) in Metabolomics Lab of Roy J. Carver Biotechnology Center, University of Illinois at Urbana-Champaign. Software Analyst 1.6.2 was used for data acquisition and analysis. The 1200 series HPLC system (Agilent Technologies, Santa Clara, CA) includes a degasser, an autosampler, and a binary pump. The LC separation was performed on an Agilent SB-Aq (4.6 x 50mm, 5μm) with mobile phase A (0.1% formic acid in water) and mobile phase B (0.1% formic acid in acetonitrile). The flow rate was 0.3 mL/min. The linear gradient was as follows: 0-1min, 90%A; 8-13min, 0%A; 13.5-18min, 90%A. The autosampler was set at 10°C. The injection volume was 10 μL. Mass spectra were acquired under positive electrospray ionization (ESI) with the ion spray voltage of +5000 V. The source temperature was 450 °C. The curtain gas, ion source gas 1, and ion source gas 2 were 30, 65, and 55, respectively. Multiple reaction monitoring (MRM) was used for quantitation: 14',15'-epoNA5HT m/z 479.3 → m/z 160.0; 14',15'-epoNADA m/z 456.3 → m/z 137.1. Internal standard Anadamide-d4 was monitored at m/z 352.3 → m/z 287.2.

Quantitation of EET-EAs and either 14',15'-epoNADA or 14',15'-epoNA5HT using LC-MS/MS. Samples were analyzed with the 5500 QTRAP LC/MS/MS system (Sciex, Framingham, MA) in Metabolomics Lab of Roy J. Carver Biotechnology Center, University of Illinois at Urbana-Champaign. Software Analyst 1.6.2 was used for data acquisition and analysis. The 1200 series HPLC system (Agilent Technologies, Santa Clara, CA) includes a degasser, an autosampler, and a binary pump. The LC separation was performed on an Agilent Agilent Eclipse XDB-C18 (4.6 x 150mm, 5μm) with mobile phase A (0.1% formic acid in water) and mobile phase B (0.1% formic acid in acetonitrile). The flow rate was 0.4 mL/min. The linear gradient was as follows: 0-2min, 90%A; 8min, 55%A; 13-25min, 40%A; 30min, 30%A; 35min, 25%A; 36-44min, 0%A; 45-50min, 90%A. The autosampler was set at 10°C. The injection volume was 10 μL. Mass spectra were acquired under positive electrospray ionization (ESI) with the ion spray voltage of +5000 V. The source temperature was 450 °C. The curtain gas, ion source gas 1, and ion source gas 2 were 32, 65, and 55, respectively. Multiple reaction monitoring (MRM) was used for quantitation: 14,15-epoNA5HT m/z 479.3 → m/z 160.0; 14,15-epoNADA m/z 456.3 → m/z 137.1; 5,6-EET-EA, 8,9-EET-EA, 11,12-EET-EA, and 14,15-EET-EA are all measured with m/z 264.2 → m/z 62.0. Internal standards Anadamide-d4 and 14,15-EET-EA-d8 were monitored at m/z 352.3 → m/z 287.2 and m/z 372.2 → m/z 63.0, respectively.

Binding equations. The general one-site binding equation used was Equation 1 below

$$B = B_0 + \frac{B_{max}[S]}{K+[S]} \qquad \text{(Equation 5.1)}$$

where B_o is the baseline response, B_{max} is the maximum response, K is the binding parameter, and $[S]$ is the substrate concentration. For kinetic experiments, B and K represent velocity and K_m, respectively; for Soret binding experiments, B and K represent ΔA and K_D, respectively. For metabolism and Soret experiments, $B_o = 0$; for NADPH metabolism B_o is a nonzero value.

Inhibition experiments were described by either a competitive model (Equation 5.2) or noncompetitive model (Equation 5.3)

$$B = \frac{B_{max}[S]}{K\left(1+\frac{[I]}{K_i}\right)+[S]} \qquad \text{(Equation 5.2)}$$

$$B = \frac{B_{max}[S]}{(K+[S])\left(1+\frac{[I]}{K_i}\right)} \qquad \text{(Equation 5.3)}$$

where K_i is the affinity of the inhibitor and $[I]$ is the concentration of the inhibitor.

A general two-site binding equation (Equation 5.4) was used to describe the metabolism of NADA and NA5HT

$$B = \frac{\frac{B_1[S]}{K_1} + \frac{B_2[S]^2}{K_1 \cdot K_2}}{1 + \frac{[S]}{K_1} + \frac{[S]^2}{K_1 \cdot K_2}} \quad \text{(Equation 5.4)}$$

where B_1 and B_2 are the maximum metabolism at the first site and second site, respectively, and K_1 and K_2 are the affinities at the first site and second site, respectively.

In cellulo data were fitted to a dose-response equation (Equation 5.5)

$$B = B_0 + \frac{B_{max} - B_o}{1 + 10^{[(B_{50} - [L])p]}} \qquad \text{(Equation 5.5)}$$

where $[L]$ is the concentration of the ligand, p is the Hill coefficient, B_{50} is the half-maximal response (EC_{50} for agonism and IC_{50} for antagonism experiments), B_o is the baseline response (bottom asymptote), and B_{max} is the maximum response (top asymptote).

Statistical analysis. Statistical significance was determined by a one-way ANOVA followed by a Tukey's post-hoc analysis. P values < 0.05 were considered statistically significant.

Modeling and simulation of membrane-bound CYP2J2 with AEA and NADA or NA5HT. Initial structural models of membrane-bound CYP2J2 bound to AEA and NADA or NA5HT were generated with molecular docking performed with AutoDock Vina[259] in a stepwise manner as described below. A grid box of dimension 22 Å in x, y and z and centered in the active site of CYP2J2 was employed for docking. We first docked NADA or NA5HT to our previous membrane-bound models of CYP2J2 [245,289]. From this docking step, configurations of AEA/NADA/NA5HT in which the main epoxidation site (carbons C14, C15) were close to the heme (with distance < 5 ˚A) and with a high docking score, resulting in over 100 initial structures of each molecule in complex with CYP2J2. The resulting structures were then employed as receptors for docking of a second molecule (AEA for NADA/NA5HT in active site, or NADA/NA5HT for AEA in active site). This second step allowed us to explore potential peripheral binding sites (i.e., not the central active site cavity of CYP2J2), which were hypothesized from the experimental. From docking, two potential peripheral binding sites were identified. For each peripheral binding configuration, the corresponding CYP2J2 complexes with two molecules were

sorted by docking score, and the models with the highest score were employed as starting configurations for molecular dynamics (MD) simulations. Each simulation system was minimized for 2,000 steps, and equilibrated for 1 ns with the Cα of CYP2J2 and the heavy atoms of the ligands (AEA, NADA and NA5HT) harmonically restrained (with force constant k=1 kcal/mol/˚A2). Following this preparation step, the 2-molecule systems were simulated for 50 ns.

Simulation protocol. The simulations were performed using NAMD2[260]. The CHARMM27 force field with cMAP[299,300] corrections was used for CYP2J2. The CHARMM36[262,301] force field was used for lipids. Force field parameters for AEA, NADA and NA5HT were generated by analogy from the CHARMM General Force Field[263]. The TIP3P model was used for water[265]. Simulations were performed with the NPT ensemble with a time step of 2 fs. A constant pressure of 1 atm was maintained using the Nosé-Hoover Langevin piston method[266,267]. Temperature was maintained at 310 K using Langevin dynamics with a damping coefficient γ of 0.5 ps^{-1}applied to all atoms. Nonbonded interactions were cut off at 12 Å, with smoothing applied at 10 Å. The particle mesh Ewald (PME) method[269] was used for long-range electrostatic calculations with a grid density of > 1 $Å^{-3}$.

5.3 Results

Biosynthesis of epoxy-endovanilloids by microglial cells and their endogenous levels in porcine brains. We first determined the levels of NADA and NA5HT in porcine brain, as pigs have close anatomy to humans and express similar CYP isozymes. To achieve this, we synthesized the authentic standards (Figure 5.2a). As the epoxidation of PUFAs and eCBs by CYPs occurs mainly on the terminal alkene[163,232,289,391], we synthesized 14',15'-epoNADA and 14',15'-epoNA5HT (Figure 5.2a) and separated them using a reverse-phase HPLC-UV method and confirmed the structures using NMR and LC-MS/MS (Supplementary Figure 5.1-5.5). As shown in Figure 5.2b Method 1, we developed an LC-MS/MS quantitation method in the selected reaction monitoring (SRM) mode to quantify NADA, NA5HT, 14',15'-epoNADA, 14',15'-epoNA5HT, and AEA from brain tissue and microglial cells. Previously, NADA was found in the cerebellum and hippocampus/thalamus regions in bovine and rat brains[385,392,393], while NA5HT was identified in bovine brain extracts and in the intestine[386,387]. The levels of NADA and NA5HT have been reported to be <1-10 pmol $\cdot$ g^{-1} in these brain tissues, which is lower than literature AEA levels

(~20-80 pmol · g^{-1})[394] and lower than our reported levels for AEA in rat brains (150 pmol · g^{-1}) and pig brains (2800 pmol · g^{-1})[163]. It is important to note that AEA levels are known to rise postmortem due to denaturation of the enzymes that degrade AEA[395]. Additionally, during tissue extraction, NADA and NA5HT are unstable due to the potential oxidation of the headgroups. Hence, the levels of the NADA and NA5HT are expected to be lower than AEA. Herein, we measured 1.7 and 1.9 pmol of NADA (0.182 ± 0.081 pmol · g^{-1} wet tissue) and 11.3 and 4.9 pmol of NA5HT (0.686 ± 0.006 pmol · g^{-1} wet tissue) from the cerebella of two pig brains. From the hippocampus-thalamus-hypothalamus regions, we recovered 0.4 and 0.5 pmol of NADA (0.039 ± 0.009 pmol · g^{-1} wet tissue) and 0.2 and 0.1 pmol of NA5HT (0.010 ± 0.003 pmol · g^{-1} wet tissue) in two brains. From tissue samples spiked with 1 µg of NADA or NA5HT standards, we were able to recover 40% of the eVDs, and so the levels from the tissue are likely 2.5-fold higher. The epoxy-eVDs were below detection limit due to the low abundance of the parent molecules. Moreover, two different extraction methods were used to detect eVDs and AEA. Whereas the methanol/C-18 cartridge method was able to extract the eVDs, AEA was undetectable. AEA was previously determined using ethyl acetate:hexanes extract followed by purification on silica column[163], which we determined quickly degrades the eVDs. Overall, the levels of NADA and NA5HT are much less than AEA in rat and pig brains reported from our laboratory[163].

In the field of lipid metabolites, there is strong evidence that the production of lipid metabolites is localized at the site of action and then these metabolites are rapidly degraded. This leads to low plasma/tissue levels of most lipid metabolites. Hence, we studied the endogenous production of these lipid metabolites in microglial cells. Microglial cells are brain macrophages that are activated during neuroinflammation and play important roles in pain modulation[396,397]. Previously, it was demonstrated that CYPs are upregulated during neuroinflammation[361]. Hence, we used BV2 microglial cells to determine the production of eVD epoxides from NADA or NA5HT under an inflammatory stimulus. We stimulated microglial cells with lipopolysaccharide (LPS), followed by the addition of NADA or NA5HT[163]. There was a rapid formation of 14',15'-epoNADA or 14',15'-epoNA5HT under LPS stimulation. Interestingly, these molecules are also produced without LPS stimulation showing that these molecules are made spontaneously by resting microglial cells (Figure 5.2c). Importantly, the production of these metabolites were inhibited in the presence of SKF 525A (a reversible CYP epoxygeanse inhibitor) demonstrating that the eVD epoxides are produced partly by enzymatic oxidation by CYP epoxygenases[398] (Figure 5.2c).

Epoxygenation of NADA or NA5HT by cytochromes P450. We determined that the endogenous levels of AEA are much higher than NADA and NA5HT. Previously, others including us have shown that various brain CYPs such as CYP2J2 and CYP2D6 convert AEA into AEA epoxides (EET-EAs). Therefore, to understand the substrate specificity of CYPs when both substrates (AEA and NADA or NA5HT) are present, we further used the activated microglial cells to study the co-metabolism of AEA with NADA or NA5HT (Figure 5.3a and b). Interestingly, we observed that AEA potentiated the formation of 14',15'-epoNADA (~ 2-fold) in a concentration-dependent manner (Figure 5.3a). Contrariwise, AEA inhibited 14',15'-epoNA5HT formation (~0.5-fold) (Figure 5.3b). Hence, AEA increases the metabolism of NADA and inhibits the CYPs responsible for NA5HT formation, indicating the involvement of similar CYPs in metabolism of AEA and eVDs. To further understand this observation, we delineated the mechanism of eVD metabolism using a recombinantly expressed CYP.

Of the common CYP epoxygenases in mouse, CYP2J9 and CYP2J12 were shown to be highly expressed in mouse brain tissues while CYP2Cs showed low expression[195,399]. We confirmed that CYP2J9 and CYP2J12 are expressed in the BV2 microglial cells used for our studies (Supplementary Figure 5.6). CYP2J9 and CYP2J12 are highly homologous to human CYP2J2, which is the only CYP2J found in humans. CYP2J2 is also the most highly express CYP epoxygenase of the human brain[204,205,400]. Hence, we elucidated the biochemistry of eVD metabolism in the presence and absence of AEA by human CYP2J2.

Human CYP2J2 epoxidizes NADA and NA5HT to form epoNADA and epoNA5HT. CYP2J2 is highly expressed in the brain, cardiovascular, and cerebrovascular systems and is one of the major epoxygenases in these tissues[196,204,205,400]. Additionally, CYP2J2 is known to epoxygenate several endocannabinoids including AEA[163,165,246]. Therefore, we recombinantly expressed human CYP2J2 and its redox partner cytochrome P450 reductase (CPR) and studied the metabolism of eVDs by CYP2J2.

In order to study the direct metabolism of NADA and NA5HT, we incubated CYP2J2 with each eVD and detected the metabolites using UV-Vis HPLC and LC-MS/MS. All the oxidized products of NADA and NA5HT are detailed in the supplementary material (Supplementary Figures 5.7-5.26 and Supplementary Table 5.2). The metabolism of NADA resulted in the formation of eight mono-oxygenated products (PD1-8), which show masses that indicated alkene oxygenation such as epoNADAs and hydroxyl products (Supplementary Figure 5.7-5.9 and

Supplementary Table 5.2). We determined that 14',15'-epoNADA (PD5) is a product based on the fragmentation and co-elution with the synthesized standard. Two di-oxygenated products were also found (PD9 and PD10) (Supplementary Figure 5.10). Additionally, a hydroxyquinone product of NADA (PD11) was detected within 6 ppm of the expected mass (Supplementary Figure 5.11). UV-Vis HPLC demonstrates that PD11 has an absorbance profile between 270 and 310 nm that is typical of hydroxyquinones (Supplementary Figure 5.11c). It is known that dopamine is oxidized to form 6-hydroxy-*p*-quinone,[401,402] and therefore, NADA-6-hydroxy-*p*-quinone is likely the identity of PD11 (Supplementary Figure 5.7c).

The metabolism of NA5HT by CYP2J2 produced 4 mono-oxygenated products (PS1-4) (Supplementary Figure 5.12-5.14 and Supplementary Table 5.2). The MS/MS spectra indicate the formation of epoxides/hydroxides (PS1 and PS2). PS2 was confirmed to be 14',15'-epoNA5HT. The oxidation of the serotonin moiety was also observed (PS3 and PS4) (Supplementary Figure 5.13d-e and Supplementary Figure 5.14b-c). Di-oxygenated and quinonized products of the serotonin headgroup were also observed (Supplementary Figures 5.15-5.18). To confirm that CYP2J2 oxidizes the headgroups of the eVDs, we also investigated capsaicin (CAP) as a substrate, and found headgroup-oxidized products among other oxygenated products (Supplementary Figures 5.19-5.26 and Supplementary Table 5.2). After establishing eVDs as substrates of CYP2J2, we then proceeded to measure the kinetics of metabolism by CYP2J2-CPR-Nanodiscs.

Kinetics of NADA and NA5HT metabolism by CYP2J2-CPR-Nanodiscs. We next incorporated CYP2J2 and CPR into stable nanoscale lipid bilayers known as Nanodiscs (ND) and proceeded to determine the kinetics of eVD metabolism (Figure 5.3c). The kinetics of eVD metabolism by CYP2J2-CPR-ND was monitored by measuring the primary epoxide metabolites, which were 14',15'-epoNADA and 14',15'-epoNA5HT (Figure 5.3d and e). The metabolism of NA5HT by CYP2J2 is in a similar range as the metabolism of AEA and other lipid PUFAs,[289,391] but the rate of 14',15'-epoNADA formation is low. Interestingly, the data demonstrate the presence of multiple binding sites, as the kinetics plots strongly deviate from a typical Michaelis-Menten model. The plots resemble the beginning of a sigmoidal curve indicating positive binding interactions. However, saturation was not achieved as the eVDs are insoluble beyond 100 μM (Figure 5.3d and e). We therefore hypothesized that there are at least two binding sites. To further probe the kinetics of eVD metabolism, we measured the rate of NADPH oxidation by CYP2J2-CPR-ND in the presence of the eVDs.

CPR shuttles electrons from NADPH to CYPs to facilitate the metabolism of substrates. Therefore, the rate of NADPH oxidation increases in the presence of CYP substrates. In this case, NADPH oxidation in the presence of NA5HT showed biphasic kinetics (Supplementary Figure 5.27). During Phase I, the rates are close to the baseline (without NA5HT). In Phase II (after one minute) the rates increase to produce a second linear phase that demonstrate a hyperbolic curve as a function of the NA5HT concentration (Equation 5.1) (Supplementary Figure 5.27). This increase in NADPH oxidation is dependent on CYP2J2 (Supplementary Figure 5.27c). The K_m and V_{max} of Phase II are 27.3 $\pm$ 11.3 μM and 178 $\pm$ 28 $nmol_{NADPH} \cdot min^{-1} \cdot nmol_{CYP2J2}{}^{-1}$, respectively. Therefore, the increase in NADPH oxidation supports NA5HT binds to two sites, where one is silent for the formation of 14',15'-epoNA5HT and the other increases NADPH oxidation. Although the drug ebastine (EBS) shows monophasic NADPH oxidation with similar kinetics as NA5HT (K_m = 18.9 $\pm$ 9.5 μM and V_{max} = 64.8 $\pm$ 12.1 $nmol_{NADPH} \cdot min^{-1} \cdot nmol_{CYP2J2}{}^{-1}$), AA, AEA, and NADA do not increase NADPH oxidation and therefore the biphasic NADPH kinetics is unique to NA5HT (Supplementary Figure 5.27a).

Relative binding affinities of NADA and NA5HT as determined by ebastine (EBS) binding inhibition. Substrate binding to CYPs is typically measured by observing direct spectroscopic changes to the heme Soret band at 417 nm. As eCBs do not produce substantial Soret shift upon binding, we used an ebastine competitive inhibition assay to measure the binding affinity of NADA and NA5HT[61,64]. Both NADA and NA5HT displayed competitive inhibition of EBS binding (Equation 5.2) suggesting that they bind to the same binding site as EBS (K_i for NADA is 71.1 $\pm$ 20.0 μM and K_i for NA5HT is 49.3 $\pm$ 6.2 μM).

Co-metabolism of AEA with NADA or NA5HT. As AEA potentiates the metabolism of NADA and inhibits NA5HT metabolism (Figure 5.3a and b), we next determined the co-substrate kinetics to understand the crosstalk of eVD metabolism with AEA. We first developed an LC-MS/MS method to simultaneously measure the four different regioisomers of AEA epoxides (EET-EA)s and either 14',15'-epoNADA or 14',15'-epoNA5HT (Figure 5.2b, Method 2). We had previously determined the kinetics of AEA metabolism by CYP2J2-CPR-NDs[391], and we repeated these experiments using increasing concentrations (25 and 75 μM) of NADA and NA5HT. NADA inhibited AEA metabolism following a competitive inhibition model (Figure 5.3f). A 3D global fit of the data (Supplementary Figure 5.28) yields a K_i of 7.50 $\pm$ 0.88 μM for the inhibition of AEA by NADA, which is the strongest inhibition of CYP2J2 by an endogenous ligand as

compared to virodhamine[403]. NA5HT was a noncompetitive inhibitor (Equation 5.3) at 25 μM (K_i = 21.4 ± 3.6 μM) and a competitive inhibitor at 75 μM (K_i = 86.6 ± 18.5 μM) (Figure 5.3g). Interestingly, NADA and NA5HT also altered the regioselectivity of AEA epoxidation in a concentration-dependent manner (Supplementary Figure 5.29).

Interestingly, AEA showed a biphasic potentiation of NADA and NA5HT metabolism (Figure 5.3h and i). With increasing concentrations of AEA, the metabolism of NADA and NA5HT slightly decreases but then increases at higher concentrations of AEA. AEA significantly and hyperbolically increases 75 μM NA5HT metabolism by almost 100-fold with an apparent V_{max} and K_m of 5,460 ± 1,910 pmol · min^{-1} · nmol$_{CYP2J2}^{-1}$ and 53.7 ± 35.7 μM, respectively (Figure 5.3h). NADA is potentiated by almost 200% at the highest concentrations of AEA (Figure 5.3i). Overall, the potentiation of eVD metabolism by AEA and the altered AEA regioselectivity in the presence of eVDs demonstrate that eVDs and AEA are binding to CYP2J2 at multiple sites. Furthermore, these data support the observed crosstalk of AEA and eVDs in microglial cells (Figure 5.3a and b), as at similar concentrations within each experiment AEA potentiates NADA and inhibits NA5HT.

Molecular dynamics (MD) simulations demonstrate AEA stabilizes eVD binding to CYP2J2. In order to understand the molecular basis of the multi-site kinetics observed with the eVDs, we performed molecular dynamics (MD) simulations starting from membrane-bound structures of CYP2J2 in complex with substrates (AEA, NADA or NA5HT). Initial molecular docking was performed with AEA and either NADA or NA5HT in a stepwise manner[404]. These models allowed us to identify the binding mode of a second molecule to CYP2J2 while a molecule is bound in the active site in an unbiased manner (i.e., without any assumptions about location of peripheral binding pockets). Two distinct configurations of peripheral AEA binding, with either NADA or NA5HT in the active site, were identified (Figure 5.4a and b). In Configuration 1, AEA was docked in a pocket located below the I-helix, with its ethanolamine group near one of the residues (R321) that we have previously identified to modulate PUFA binding[289] (Figure 5.4a). In Configuration 2, AEA was located closer to the membrane interface (Figure 5.4b). For the two identified AEA binding configurations, the initial orientation of NADA or NA5HT in the active site were similar, with the main epoxidation site (carbons C14, C15) close to the heme (distance < 5 Å), and the headgroup (DA or 5HT) pointing away from the heme. These docking results suggested that NADA/NA5HT binding was not modulated by the same PUFA-interacting residues previously

reported (T318, R321 and S493)[289]. Due to the larger headgroups of NADA/NA5HT compared to other PUFAs (i.e., DA/5HT vs. carboxylic acid), a different binding orientation (not interacting with the PUFA triad) was required to fit these molecules in the active site.

The MD simulations (Figure 5.4c, Supplementary Tables 5.3-5.6) revealed that stable NADA/NA5HT binding (i.e, with the epoxidation site distance to the heme < 5 Å) was only achieved when AEA is bound in Configuration 2 (Figure 5.4b). When AEA is located in the I-helix pocket (Configuration 1), NADA or NA5HT in the active site gradually move away from the heme, which results in a displacement of its epoxidation site (with the distance to heme between 7.5 and 10 Å during the simulations) (Figure 5.4c). In contrast, AEA in Configuration 2 constrains the motion of NADA or NA5HT in the active site, which maintain their potentially productive orientation close to the heme (epoxidation site to heme distance < 5 Å) during the simulation (Figure 5.4c). In these simulations, the ethanolamine group of AEA interacted with Q228, located near the membrane interface, and remained locked in its binding site. Positioning of AEA in turn constrained the mobility of the molecule in the active site (NADA or NA5HT). NADA/NA5HT are further stabilized by hydrophobic interactions (mainly with F310) and transient electrostatic interactions (i.e., NA5HT serotonin group with D307 and E222). These observations suggest that NADA/NA5HT binding is enhanced by concurrent AEA binding to a peripheral site near the membrane interface, and provide insights into the protein residues involved in this binding (e.g., Q228 for AEA and F310 for NADA/NA5HT). Overall, the MD simulations in conjunction with the kinetics data concur with the observations from the cell culture studies that AEA enhances the metabolism of NADA.

Estimate of NA5HT binding at the second site. We can definitively demonstrate that the eVDs bind to at least two sites in CYP2J2 from the kinetic curves; however, due to the solubility issues of the lipids, we cannot determine the kinetic parameters of their metabolism. Notwithstanding, we can obtain approximate values for the kinetic parameters of NA5HT based on a two-site binding equation using assumptions from other data (Equation 5.4). The assumptions are the following. (A) No metabolism occurs at the unproductive site ($B_1 = 0$). (B) The EBS competitive binding and NADPH oxidation data represent the affinity at the first site and can be averaged to obtain $K_1 = 38$ µM. (C) The apparent V_{max} as AEA potentiates the metabolism of NA5HT represents the V_{max} of NA5HT metabolism (i.e., $B_2 = 5{,}460$ pmol · min^{-1} · nmol$_{CYP2J2}^{-1}$). Substituting these values into Equation 4, K_2 is determined to be 5.36 ± 0.27 mM (Supplementary

Figure 5.30). This shows that the affinity of the eVDs for the second site is weak. Due to lack of kinetic details in the data, a similar analysis cannot be done for NADA, though the binding to the second site is likely as weak.

Anti-inflammatory action of the epoxy-NADA and epoxy-NA5HT in microglial cells. Primarily sensory afferent neuronal cells and immune cells are rich sources of lipid mediators that regulate pain due to inflammation. Previous studies have demonstrated the anti-inflammatory actions of eVDs[405-407]; thus, we hypothesize that epoxy-eVDs would also be anti-inflammatory. Microglial cells play an important role in neuroinflammation and neuropathic pain. Microglial cells are strongly activated after injury and release proinflammatory cytokines such as IL-6. Therefore, there is a strong interest in discovering lipid-based molecules that decrease microglial activation. Herein, we show that the two novel lipid mediators, epoNADA and epoNA5HT, exhibit anti-inflammatory action in microglial cells. To investigate the actions of eVDs and epoxy-eVDs, we measured the levels of pro-inflammatory nitric oxide (NO) and IL-6 in lipopolysaccharide- (LPS)-stimulated BV2 cells. All eVDs and epoxy-eVDs dose-dependently reduced NO and IL-6 production (Figure 5.5a-d) and the IC_{50} values are tabulated in Table 5.1. 14',15'-epoNA5HT was slightly more potent at inhibiting NO production compared to NA5HT (Figure 5.5a); however, NA5HT was better at downregulating IL-6 (Figure 5.5b). Similar trends are observed with NADA and 14',15'-epoNADA, where 14'15'-epoNADA inhibited NO production more than NADA (Figure 5.5c) and NADA was better at inhibiting IL-6 production (Figure 5.5d). Together, these data demonstrate that the eVDs and the epoxy-eVDs are anti-inflammatory mediators. As determined by MTT assays, these compounds were not toxic at their effective concentrations, though NA5HT and 14',15'-epoNA5HT increased cell viability in the presence of LPS suggesting they may be pro-proliferative (Supplementary Figure 5.31).

In addition to measuring IL-6 protein levels and NO, we also measured the mRNA expression of *Il-6* and *Il-10* to determine the transition of the pro-inflammatory phenotype of BV2 to the anti-inflammatory phenotype. Whereas IL-6 is pro-inflammatory, IL-10 is an anti-inflammatory cytokine that facilitates the resolution of inflammation. Concentrations around the IC_{50} of the IL-6 and NO experiments (1 and 2.5 μM of each compound) were tested and compared to a no-treatment control. All of the eVDs and epoxy-eVDs downregulated *Il-6* with 14',15'-epo-NA5HT being the most effective overall (Figure 5.5e). The eVDs and epoxy-eVDs concomitantly upregulated *Il-10* (Figure 5.5f). NADA upregulated *Il-10* by almost 550% at 2.5 μM and 14',15'-

epoNADA was the second best at upregulating *Il-10* (Figure 5.5f). 14',15'-epoNA5HT was more effective than NA5HT at upregulating *Il-10* at 2.5 µM and more effective at 1 µM overall (Figure 5.5f). Therefore, the eVDs and epoxy-eVDs decrease *Il-6* expression and increase *Il-10* mRNA expression in activated microglial cells, demonstrating that these compounds are anti-inflammatory.

Most eCBs and eVDs mediate anti-inflammation and anti-pain via polypharmacology through CB1, CB2, and TRPV1 receptors. We determined that the mRNA of *Cnr1* (CB1 gene), *Cnr2* (CB2 gene), and *Trpv1* are expressed in the BV2 cells (Supplementary Figure 5.32). Since these receptors are known targets of eVDs and mediate inflammation and pain, we proceeded to measure the activation of CB1, CB2, and TRPV1 by epoxy-eVDs.

Activation of TRPV1 by eVDs and epoxy-eVDs. Previous studies have shown that NADA mediates anti-inflammation via TRPV1[405]. Therefore, we next investigated the actions of eVDs and epoxy-eVDs at TRPV1 using HEK cells stably expressing human TRPV1. As TRPV1 is a non-selective cation channel, activation was determined by measuring the relative Ca^{2+} influx (Supplementary Figure 5.33 and Table 5.1). Capsaicin (CAP) was used as a full-agonist positive control and was found to have an EC_{50} of 6.88 $\pm$ 3.36 nM, in accordance with reported values[408] (Supplementary Figure 5.34a). We determined that NADA and 14',15'-epoNADA are full agonists, with ~80% activation compared to CAP (Figure 5.5g). The EC_{50} of 14',15'-epoNADA is about 6.5-fold tighter than NADA. 14',15'-epoNADA also promoted a broader duration of TRPV1 opening compared to NADA, which suggests a slower opening and closing of the channels (Supplementary Figure 5.33). The TRPV1-selective antagonist AMG-9810 was able to fully antagonize the signal from CAP, the eVDs, and the epoxy-eVDs, confirming the Ca^{2+} influx is TRPV1-mediated (Supplementary Figure 5.34b and c).

On the contrary, 14'15'-epoNA5HT was found to be a partial agonist of TRPV1 up to 250 nM, with a 24% activation compared to CAP (Figure 5.5h). This signal was antagonized by AMG-9810, demonstrating it is TRPV1-mediated (Supplementary Figure 5.34c). Concentrations above 250 nM, however, resulted in a reduction of the signal, signifying that 14',15'-epoNA5HT is an antagonist of TRPV1 at higher concentrations (Figure 5.5h). Previously, NA5HT had been shown to be an antagonist of TRPV1[144]; therefore, we measured the antagonism of TRPV1 by 14'15'-epoNA5HT and compared it to NA5HT. 14'15'-epoNA5HT functioned as an antagonist of CAP at all concentrations, with an IC_{50} of 254 $\pm$ 38 nM (Figure 5.5i). Of note, this IC_{50} correlates to the

concentration at which the self-antagonism was observed for 14',15'-epoNA5HT (Figure 5.5h). From Table 5.1, we see that 14'15'-epoNA5HT is a 30-fold stronger antagonist of TRPV1 than NA5HT.

Activation of CB1 and CB2 by eVDs and epoxy-eVDs using a β-arrestin recruitment PRESTO-Tango assay. Previously, we have shown that epoxy-eCBs show an increased activation of CB2 compared to the parent eCBs[163,164]. Therefore, we determined the activation of CB1 and CB2 by eVDs and the epoxy-eVDs using the PRESTO-Tango assay[163]. CP55940 was used as a positive control, which is a full agonist at both CB1 and CB2 (Supplementary Figure 5.35a and b). The EC_{50} values for CP55940 were 0.91 ± 0.38 nM and 5.16 ± 1.91 nM at CB1 and CB2, respectively, which agree with previously reported data[163,164,409].

Herein, NADA, 14',15'-epoNADA, and 14',15'-epoNA5HT, but not NA5HT, demonstrated full-agonism binding to CB1 (~100% activation as compared to CP55940) (Figure 5.5j and k, Table 5.1). Of these, NADA activates CB1 2-fold more potently as compared to 14',15'-epoNADA. 14',15'-epoNA5HT activated CB1 with an EC_{50} of 16.5 ± 11.7 nM. Only NA5HT activated CB2. The measured EC_{50} was 8.80 ± 5.57 nM with 19.2% activation compared to CP55940, which makes it a partial agonist.

We further tested if NA5HT is an antagonist for CB1 and if NADA, 14',15'-epoNADA, and 14',15'-epoNA5HT are antagonists for CB2. None of these antagonized 50 nM CP55940 binding at these receptors (Supplementary Figure 5.35c). Therefore, NA5HT does not bind CB1, and NADA, 14',15'-epoNADA, and 14',15'-epoNA5HT do not bind CB2. This interesting dichotomy could be exploited to design pain therapeutics that specifically target one receptor. Overall, our data shows that 14',15'-epoNA5HT is anti-inflammatory, is an agonist of CB1, and is an antagonist of TRPV1, thereby making it the most efficacious of the eVDs for the development of pain therapeutics.

5.4 Discussion

The endocannabinoid (eCB) system is a promising target to mitigate pain as an alternative to the opioid system. There is also evidence that there is a synergism between the eCB and opioid system that reduces the need for high doses of opioids[369]. Hence, it is important to understand the function of eCBs and their metabolites as endogenous ligands of the receptors that are involved in pain response modulation. It has been shown previously that the activation of CB1 and CB2 is

associated with anti-nociceptive and anti-inflammatory actions[370,371]. Control of TRPV1 can also modulate pain by mostly antagonizing TRPV1. While there are ample examples of drugs that target cannabinoid receptors or TRPV1, there is dearth of molecules that are rheostat regulators (varying strength of agonism or antagonism) of both cannabinoid receptors and TRPV1. The primary difference between drugs and endogenous molecules is that these lipids are functionally plastic and capable of binding both receptors. For example, anandamide is an agonist TRPV1 and cannabinoid receptors (mostly CB1) and exhibits this type of site-specific functional plasticity. NADA and NA5HT, which are AA derivatives of neurotransmitters—dopamine (DA) and serotonin (5HT). NADA is an agonist of both CB1 and TRPV1[142,143]. NA5HT is an antagonist of TRPV1. PUFAs, through parallel pathways, are converted into epoxide mediators that have been shown to reduced pain, and anti-pain drugs have been developed that prevent the degradation of these molecules[57]. Overall, there is strong evidence for pain modulation by eCB and PUFA epoxides through multiple receptors.

Using a combined physical biochemistry and cell-based approach, we report the discovery of NADA and NA5HT epoxides that are produced by the CYP epoxygenase pathway in microglial cells. These molecules are dual functional molecules and can function through the eCB-TRPV1 axis, which makes them potential anti-pain molecules. The overall findings of this work are outlined in Figure 5.6 and discussed below.

The biosynthesis of the epoxy-eVDs is facilitated primarily by CYP epoxygenases as the inhibiton of CYP enzymes in microglial cells reduce the levels of these metabolites. In the pig brain, we were able to detect the parent compounds NADA and NA5HT, whose levels were much lower than that of AEA. The epoNADA and epoNA5HT were spontaneously formed by microglia cells in the presence and absence of inflammatory stimulus. As the levels of AEA were high and eVDs were low, we tested the effect of eVD metabolism by CYPs in the presence of AEA. Interestingly, the metabolism of NADA by CYPs is potentiated by AEA in the microglial cells. This was an interesting observation as there are very few examples where the binding of one ligand at the enzyme active site potentiates the metabolism of another ligand. However, this is common for CYPs with a large active sites such as CYP3A4[191-193].

To translate the CYP-mediated biosynthesis studies from mice microglial cells to humans, we studied the biochemical mechanism of eVD metabolism by a human CYP. Of the common CYP epoxygenases in mouse, CYP2J9 and CYP2J12 were shown to be highly expressed in mouse brain

while CYP2Cs showed low expression[195,399]. We confirmed the presence of CYP2J9 and CYP2J12 in the microglial cells. CYP2J9 and CYP2J12 are highly homologous to human CYP2J2, the only CYP2J enzyme in humans. Hence, we elucidated the biochemistry of the formation of eVD epoxides in the presence and absence of AEA using human CYP2J2, which is also the most highly expressed CYP epoxygenase in the human brain[204,205,400].

Comparing the *in cellulo* metabolism data to the *in vitro* kinetic measurements with CYP2J2-NDs reveals a complex network of substrate-substrate interactions. CYPs are known to display complex heterotropic cooperativity due to the concurrent binding of multiple substrates[191-193]. Likewise, the metabolism of eVDs by CYP2J2 in our study shows complex substrate-substrate interactions. Previously, we had determined that PUFAs bind CYP2J2 into two main sites: the substrate access channel and the PUFA binding pocket. Since PUFAs adopt similar conformations, their binding to CYP2J2 is competitive[289]. AEA binds to CYP2J2 with "PUFA-like" properties: that is, by binding similar sites in the substrate access channel and PUFA binding pocket as shown by the MD simulations and support by kinetic observations. However, NADA and NA5HT bind distinctly compared to PUFAs and AEA due to their large headgroups. They do not bind the PUFA binding pocket and have unstable binding to the substrate access channel. The eVDs, therefore, bind to distinct sites and can bind simultaneously in the CYP2J2 active site along with AEA. The MD simulations support that up to three overlapping binding sites are possible, which can help to explain the observed complex AEA and eVD interactions, such as the regioselectivity change in the AEA metabolites (Supplementary Figure 5.29) and the potentiation of eVD metabolism (Figures 5.3 and 5.4). We have previously observed complex inhibition and regioselectivity changes for endogenous substrates of CYP2J2[391,403,404]; however, this is the first report of a potentiation of CYP2J2 metabolism. Due to poor solubility of the lipid substrates used in these studies, we could not accurately determine the binding constants to understand the cooperative nature of the potentiation. However, it is evident from the kinetic curves that there is a homotropic potentiation of eVD metabolism and a heterotropic potentiation by AEA. Overall, the finding implies that the co-substrate AEA potentiates the metabolism of NADA and NA5HT by CYP2J2. We have recently determined that virodhamine, is an endogenous inhibitor of CYP2J2[403]. Herein we report that AEA may be an endogenous potentiator of CYP2J2. Therefore, this study provides another therapeutic route where drugs can potentiate CYP2J2's epoxidation of endogenous lipids.

There are very few reports on the study of eVD and eCB metabolism by CYPs. One common observation is that the oxidized eVD metabolites always exhibit different pharmacology compared to the parent molecules. NA5HT was previously shown to be metabolized to a 2-oxo derivative by CYP2U1, an orphaned CYP highly expressed in the brain[386]. This 2-oxo-NA5HT was shown to be a weaker FAAH inhibitor compared to NA5HT[386]. In a separate study, NADA was shown to be hydroxylated at the ω and ω-1 positions by rat liver microsomes[142]. The NADA-OH metabolites were weaker agonists of TRPV1 compared to NADA[142]. Therefore, the 2-oxo-NA5HT and NADA-OH metabolites may represent a degradation pathway of NADA and NA5HT. However, we show that the epoxy-eVDs are potently anti-inflammatory, as they lower IL-6 and NO levels while increasing IL-10 levels in activated microglial cells, and therefore may represent an activation pathway.

A key observation is that the epoxidation of eVDs increases their ability to activate TRPV1. 14',15'-epoNADA is a 6.5-fold stronger agonist than NADA and 14',15'-epoNA5HT is a 30-fold stronger antagonist than NA5HT at TRPV1, while also showing partial agonism at lower concentrations. Based on the cyro-EM structure of TRPV1, it has been proposed that agonists binding at the capsaicin-binding pocket facilitate channel opening by promoting the lateral movement of the S4-S5 linker[410]. The epoxide could be forming some interactions with H-bond donating groups such as Tyr or Asp residues that populate this linker, which facilitates the channel opening. Since TRPV1 exists as a tetramer, the binding of 14',15'-epoNA5HT to different sites and perhaps different monomers may help to explain its dual agonism/antagonism. However, since the activation of TRPV1 is self-antagonized at concentrations greater than 250 nM (around the IC_{50}), the 14',15'-epoNA5HT functions overall as an antagonist. Another interesting characteristic is that 14',15'-epoNADA influxes the same amount of Ca^{2+} as NADA or CAP, but the duration of the influx is broader. That is, the area under the curve (AUC) of the Ca^{2+} influx at B_{max} is the same as NADA or CAP but the peaks are broader (Supplementary Figure 5.33). This signifies that 14',15'-epoNADA is slower to open and close the channel and may have pronounced effects on the Ca^{2+}-mediated signaling in the cell.

The epoxidation of NA5HT changes it from being a partial CB2 agonist to a full CB1 agonist. This is intriguing given that 14',15'-epoNA5HT and NA5HT differ only by an epoxide yet bind potently to the two different receptors. Contrariwise, the epoxidation of NADA does not greatly alter their potency towards CB1 receptor activation. Previously it was shown that the epoxidation

of omega-6 and omega-3 eCBs have preferential binding towards CB2[163,165]. Herein, we show that eVD epoxides target CB1 receptors. While NADA and 14',15'-epoNADA are TRPV1 and CB1 agonists, NA5HT and 14',15'-epoNA5HT are TRPV1 antagonists. The complex functional crosstalk of CB1 and TRPV1 is still being elucidated,[411,412] but the studies suggest that the plasticity exhibited by endogenous lipids indirectly contributes to this crosstalk.

Overall, the eVDs and epoxy-eVDs lower pro-inflammatory IL-6 and NO levels while increasing anti-inflammatory IL-10. They also bind very potently to cannabinoid receptors, with affinities between 40 pM and 20 nM, and are potent ligands of TRPV1. The epoxidation of eVDs increases their potency at TRPV1 and alters their pharmacology at cannabinoid receptors. In particular, 14',15'-epoNA5HT is the most effective epoxy-eVD at reducing pro-inflammatory markers and increasing IL-10 while also avoiding toxicity. 14',15'-epoNA5HT is also a potent antagonist of TRPV1 and a potent full agonist of CB1. Lastly, the formation of epoxy-eVDs by CYPs is potentiated by the co-substrate AEA, which is also metabolized by CYPs to form EET-EA that are potent CB2 ligands. Hence, inflammation and related pain response is accompanied by a storm of epoxy-eVDs and epoxy-eCBs that are multi-faceted endogenous molecules capable of influencing the activity of CB1, CB2 and TRPV1 receptors. The discovery of these molecules will serve as templates for new multi-target therapeutic drugs that will prove useful for the treatment of inflammatory pain as well as of other conditions in which these receptors are targeted in other clinical studies.

5.5 Figures and tables

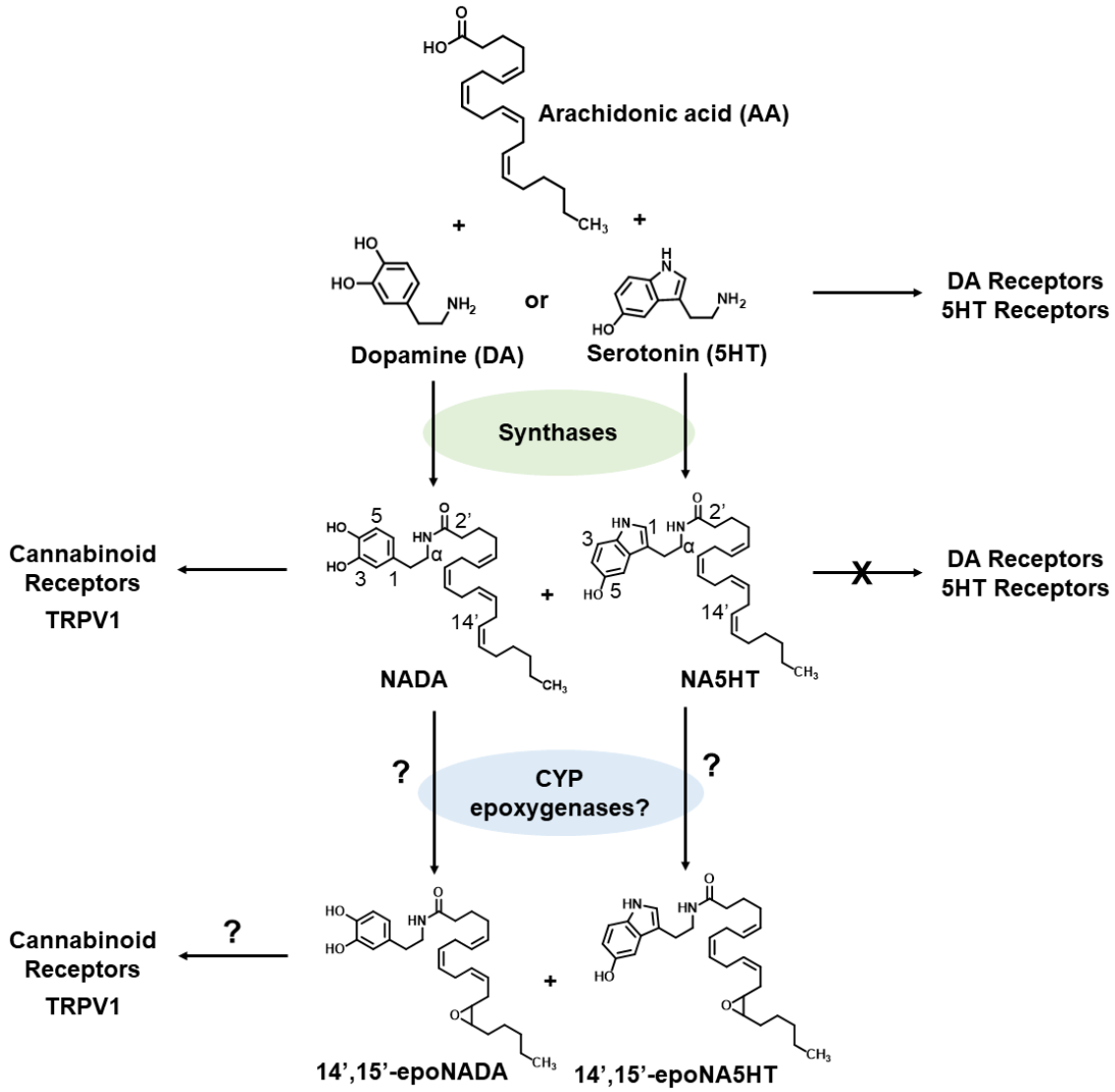

Figure 5.1. The endovanilloid (eVD) pathway and structures of 14',15'-epoNADA and 14',15'-epoNA5HT.

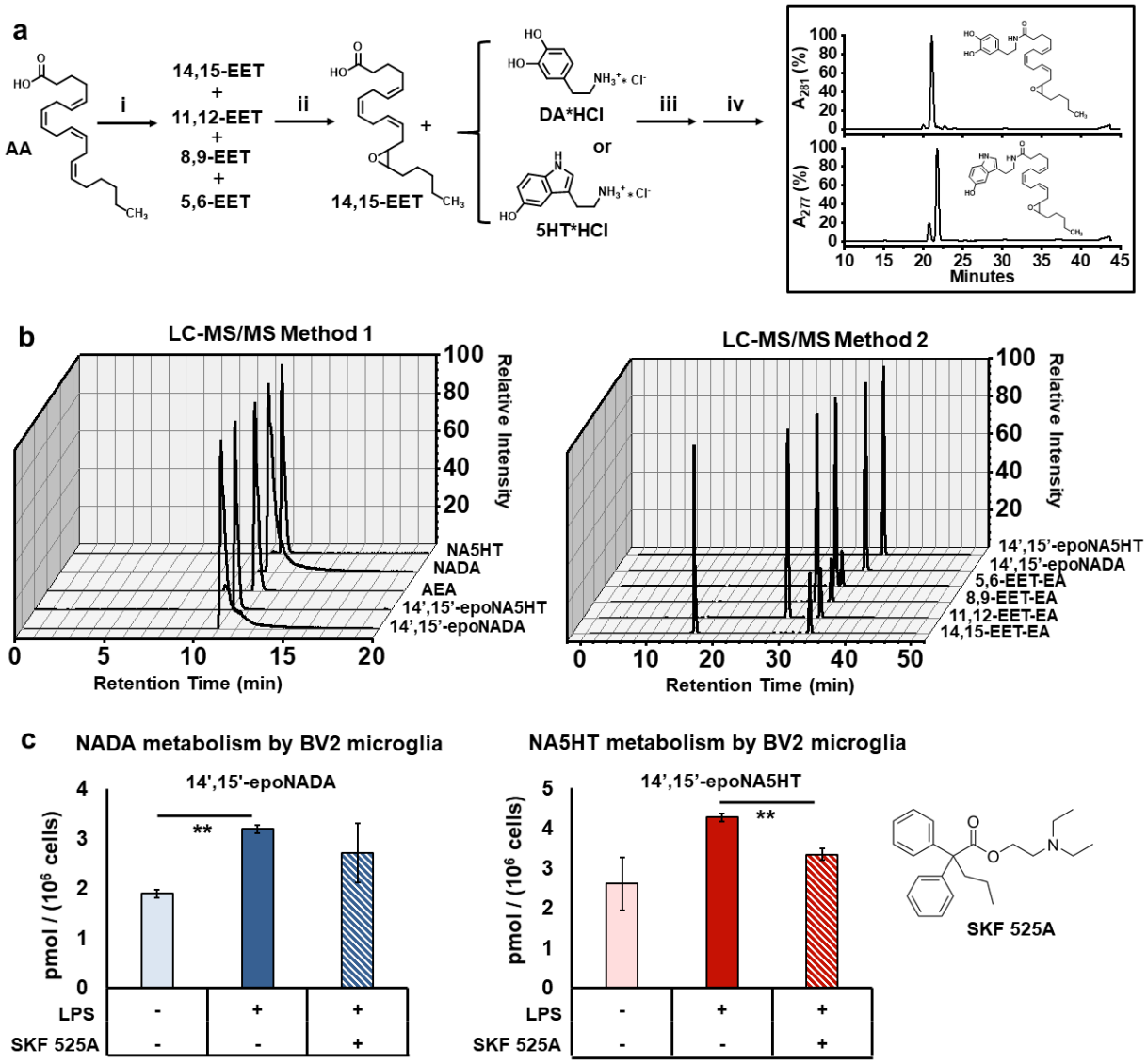

Figure 5.2. *Synthesis of authentic standards, targeted lipidomics method, and production of epo-NADA and epo-NA5HT by microglial cells*. **(a)** Authentic standards 14',15'-epoNADA and 14',15'-epoNA5HT of were synthesized. (i) *m*-CPBA, RT, 1 hr, MeCN (ii) reverse-phase HPLC purify (iii) EDC, DMAP, DIPEA; ice bath 1 hr; RT 8 hrs; 50:50 DCM:DMF (iv) reverse-phase HPLC purify. **(b)** Development of LC-MS/MS method for the separation of NADA, epo-NADA, NA5HT, epo-NA5HT and AEA (Method 1) and the differen regioisomers of EET-EAs and epo-NADA and epo-NA5HT (Method 2). AEA m/z 348.3 → m/z 203.2; NADA m/z 440.2 → m/z 287.1; 14',15'-epoNADA m/z 456.3 → m/z 137.1; 14',15'-epoNA5HT m/z 479.3 → m/z 160.1; NA5HT m/z 463.3 → m/z 287.2; EET-EA m/z 264.2 → m/z 62.0. **(c)** NADA and NA5HT metabolism by BV2 microglial cells under lipopolysaccharide (LPS) stimulation in the presence of 1 μM t-AUCB (sEH inhibitor) and 10 μM NADA or NA5HT. The reversible CYP epoxygenase inhibitor SKF 525A was used to demonstrate CYP-mediated metabolism. Data represents SEM of 3 experiments.

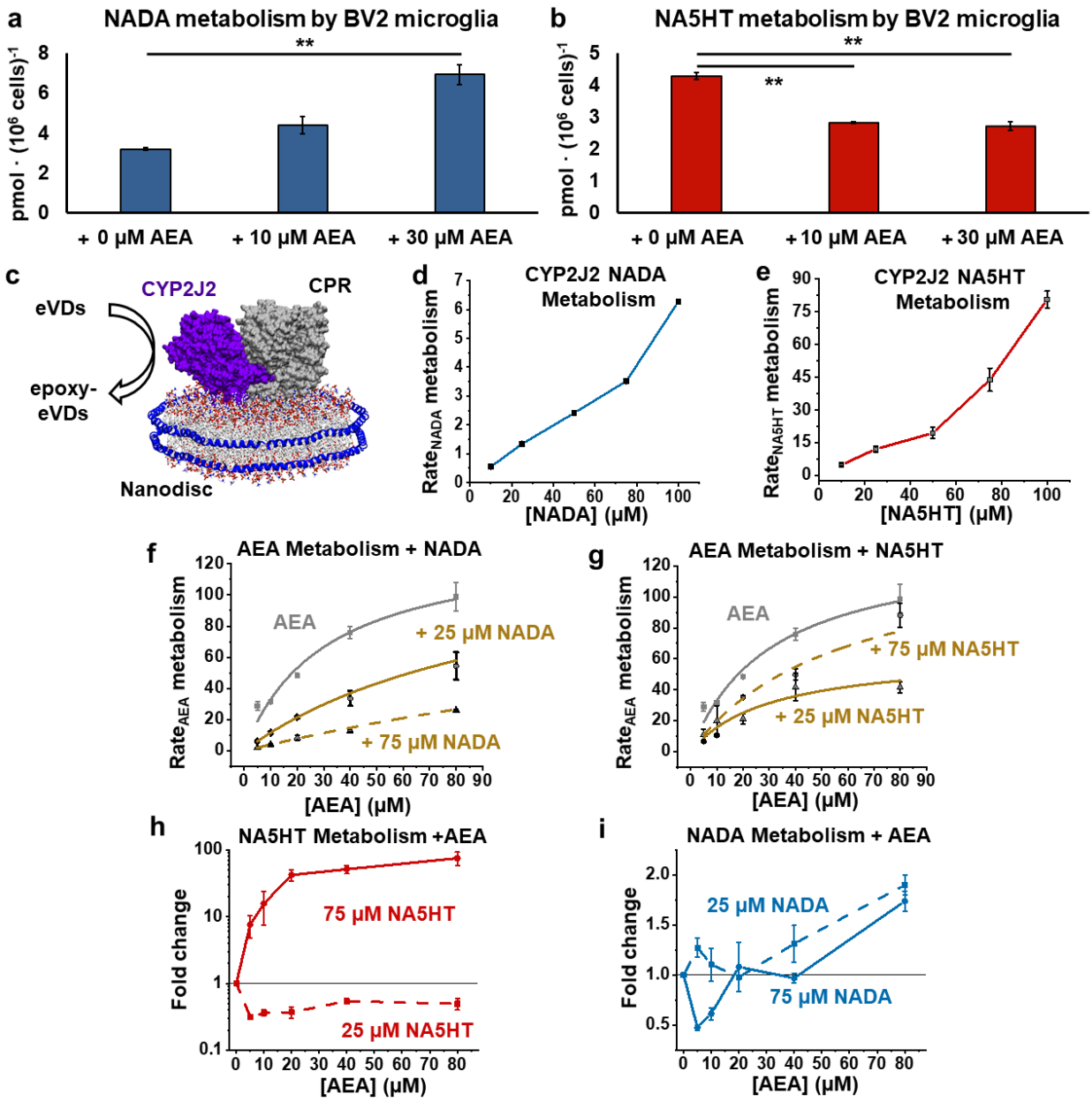

Figure 5.3. *Potentiation of eVD metabolism by AEA.* **(a)** Metabolism 10 µM NADA and **(b)** 10 µM NA5HT in the presence of increasing concentrations of AEA by BV2 microglia. Metabolism as conducted similarly to data in Figure 2c. Data shown are the SEM of n = 6 (two sets of triplicate performed on separate days). **p < 0.01. **(c)** Schematic of the CYP2J2-CPR-Nanodisc. **(d-e)** Metabolism of NADA and NA5HT by CYP2J2-CPR-NDs. Rates are in $pmol_{epoxy\text{-}eVD} \cdot min^{-1} \cdot nmol_{CYP2J2}^{-1}$ and data represents the SEM of 3 experiments. **(f-i)** Co-substrate metabolism of eVDs with AEA. Data represents the SEM of 3 experiments. **(f)** AEA metabolism in the presence of NADA and **(g)** NA5HT. Rates are in $pmol_{EET\text{-}EAs} \cdot min^{-1} \cdot nmol_{CYP2J2}^{-1}$. AEA data shown without NADA and NA5HT (grey squares) was previously published as described in the text. **(h)** Fold change of NA5HT metabolism and **(i)** NADA metabolism in the presence of increasing AEA concentrations compared to the metabolism without AEA.

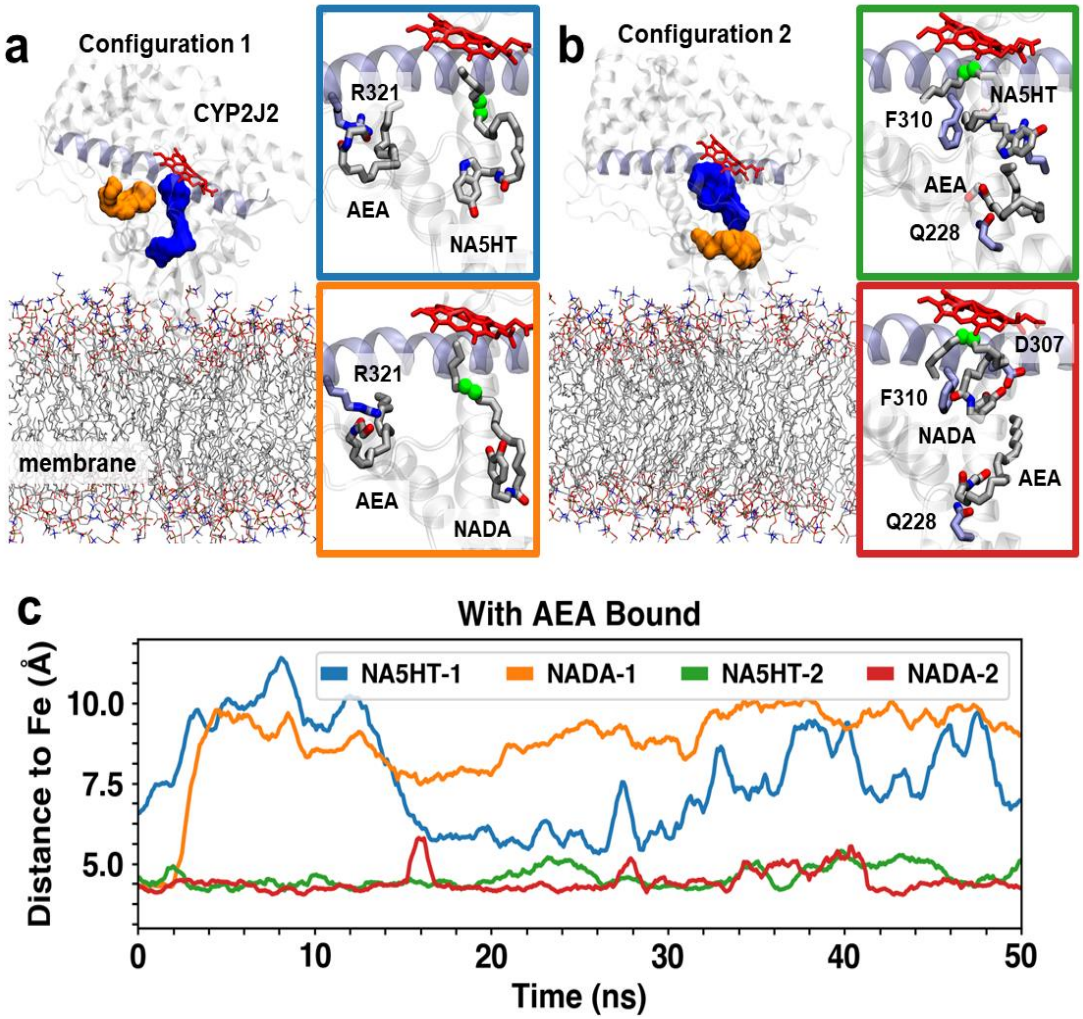

Figure 5.4. *Concurrent CYP2J2 binding of AEA and NADA/NA5HT in MD simulations*. Representative snapshots of two distinct configurations of AEA and NADA/NA5HT identified with molecular docking and with MD simulations: **(a)** peripheral binding pocket located near helix I (shown in purple cartoon) and **(b)** peripheral binding site near the membrane interface. In both panels, peripheral and active binding site cavity are shown as orange and blue surfaces, respectively. Lipids are shown in stick representation and CYP2J2 in cartoon representation. AEA, NADA, and NA5HT molecules are shown as sticks. Notable residues involved in AEA/NADA/NA5HT interactions are also shown as sticks. Carbons involved in expoxidation are highlighted as green spheres. **(c)** Time series of carbon-to-heme distances obtained from 50 ns MD simulations for the main epoxidation sites of NADA/NA5HT. Colors correspond to the subpanels shown in **(a)** and **(b).**

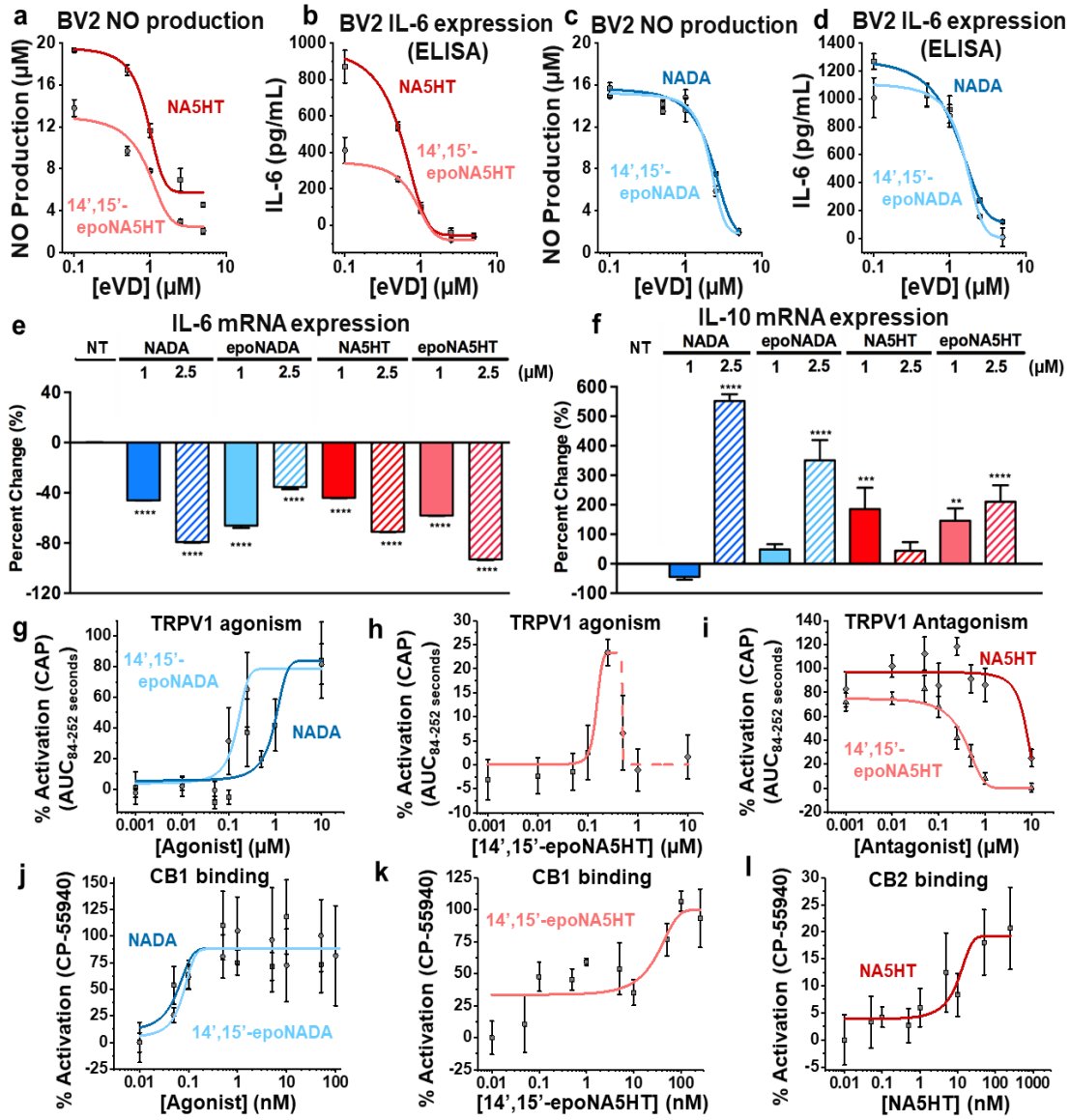

Figure 5.5. *Anti-inflammatory actions of eVDs and receptor binding*. **(a-d)** Anti-inflammatory effects of eVDs and epoxy-eVDs were determined by pre-incubating eVDs and epoxy-eVDs with BV2 cells for 4 hrs prior to stimulation by 25 ng/mL LPS. Data represents the SEM of n = 3. **(a)** Dose-dependent inhibiton of nitric oxide (NO) production by NA5HT as determined by Griess Assay. **(b)** Dose-dependent reduction of IL-6 protein expression (ELISA) by NA5HT. **(c)** Dose-dependent inhibition of NO production and **(d)** IL-6 protein expression by NADA. **(e-f)** Anti-inflammation experiments were repeated to measure pro-inflammatory *Il-6* and anti-inflammatory *Il-10* mRNA expression. Data is shown as a percent change compared to no treatment (NT) under LPS stimulation. Data represents the SEM of n = 3 technical replicates. **p ≤ 0.01, ***p ≤ 0.001 ****p ≤ 0.0001. **(g-i)** eVD binding to TRPV1-transfected HEK cells was determined using a Fura 2-AM Ca^{2+}-influx assay. The B_{max} of capsaicin (CAP) binding is defined as 100%. Data represents the SEM of n = 6 (two sets of triplicate experiments on separate days). **(i)** Antagonism was determined by preincubating cells with antagonist prior to stimulating with 250 nM CAP. **(j-l)** eVD binding to CB1 and CB2 was determined by the PRESTO-Tango assay. B_{max} of CP-55940 is defined as 100%. Data represents the SEM of n = 6 (two sets of triplicate experiments on separate days).

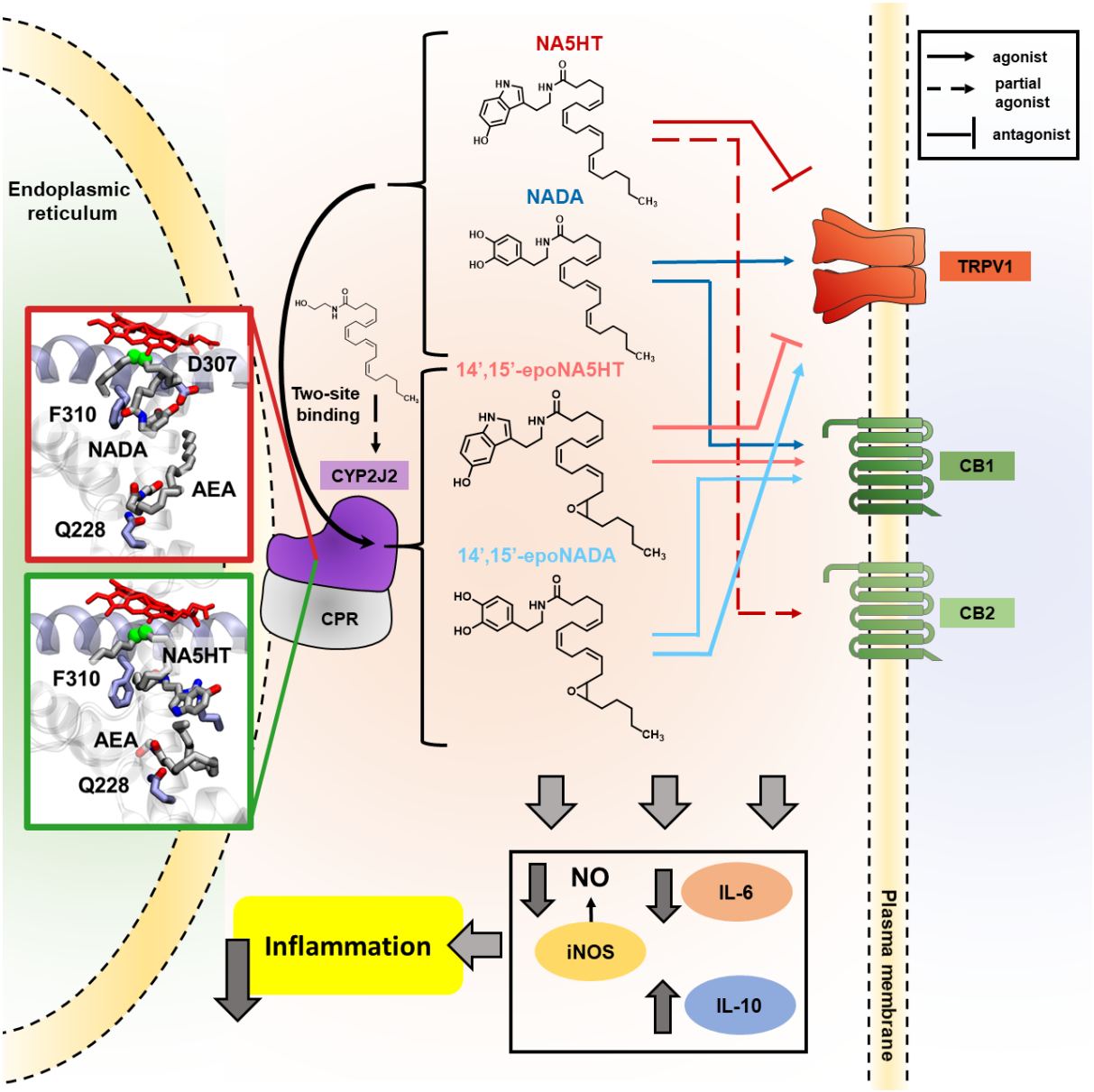

Figure 5.6. *Summary of the eVD metabolism pathway and pharmacology*. The eVDs bind in a two-site model to CYP2J2 and other epoxygenases and are metabolized to form epoxy-eVDs. AEA potentiates the metabolism of eVDs as revealed by BV2 metabolism assays, *in vitro* CYP2J2 kinetics, and molecular dynamics simulations. 14',15'-epoNADA is a better TRPV1 agonist and slightly weaker CB1 agonist compared to NADA. 14',15'-epoNA5HT is a better TRPV1 antagonist compared to NA5HT, and is a CB1 full agonists as opposed to NA5HT, which is a partial CB2 agonist. Overall, the eVDs and epoxy-eVDs potently downregulate pro-inflammatory NO production and IL-6 expression while increasing IL-10 expression, thereby demonstrating that they are potently anti-inflammatory.

Table 5.1. Anti-inflammatory marker inhibition and receptor binding parameters of eVDs and epoxy-eVDs.

	IC_{50} (μM)		TRPV1		CB1		CB2	
	NO production	IL-6 expression	% Activation[a]	EC_{50} (IC_{50})[b]	% Activation[c]	EC_{50}[b]	% Activation[c]	EC_{50}[b]
NADA	0.909 ± 0.076	0.507 ± 0.065	83.8 ± 13.6	962 ± 249	83.9 ± 9.2	0.045 ± 0.01	---	DNB[d]
14',15'-epoNADA	0.888 ± 0.135	0.807 ± 0.440	79.7 ± 9.8	156 ± 36	92.3 ± 11.2	0.080 ± 0.03	---	DNB[d]
NA5HT	2.14 ± 0.06	1.06 ± 0.49	---	(7,650 ± 1,300)	---	DNB[d]	19.2 ± 3.4	8.80 ± 5.57
14',15'-epoNA5HT	2.07 ± 0.18	1.56 ± 0.22	23.6 ± 4.4 ---	120 ± 27 (254 ± 38)	99.9 ± 13.1	16.5 ± 11.7	---	DNB[d]

[a] Percent activation compared to the B_{max} of CAP

[b] nM

[c] Percent activation compared to the B_{max} of CP-55940

[d] DNB: Does not bind. Compounds up to 1 μM in concentration do not agonize the receptor and do not antagonize 50 nM of CP-55940.

5.6 Supplementary information

Materials and Methods

Materials. Human CYP2J2 cDNA was obtained from OriGene (Catalog No. SC321730) and modified as published before[250]. Ampicillin, arabinose, chloramphenicol, isopropyl β-D-1-thiogalactopyranoside (IPTG), and Ni-NTA resin were obtained from Gold Biotechnology. δ-aminolevulinic acid was obtained from Frontier Scientific. NADPH and $NADP^+$ were obtained from P212121.com. 1-palmitoyl-2-oleoyl-sn-glycero-3-phosphocholine (POPC) and 1-hexadecanoyl-2-(9Z-octadecenoyl)-sn-glycero-3-phospho-L serine (POPS) were purchased from Avanti Polar Lipids, Inc. AA, NADA, and NA5HT, SKF 525A (α-phenyl-α-propyl-benzeneacetic acid, 2-(diethylamino)ethyl ester, monohydrochloride), AMG-9810 ((2E)-N-(2,3-dihydro-1,4-benzodioxin-6-yl)-3-[4-(1,1-dimethylethyl)phenyl]-2-propenamide), capsaicin (N-[(4-hydroxy-3-methoxyphenyl)methyl]-6E-8-methyl-nonenamide), and CP55940 (*rac*-5-(1,1-dimethylheptyl)-2-[(1R,2R,5R)-5-hydroxy-2-(3-hydroxypropyl)cyclohexyl]-phenol) were obtained from Cayman Chemical. AA for syntheses was obtained from NuChek. All other materials and reagents used were purchased from Sigma-Aldrich and Fisher Scientific.

Reverse Transcription quantitative Polymerase Chain Reaction (RT-qPCR). To measure IL-6, IL-10, CYP2J9, CYP2J12, GAPDH, TRPV1, CB1, and CB2 mRNA, total RNA was isolated from BV-2 microglial cells using the Direct-zol RNA Kit, according to the manufacturer's instructions (Zymo Research). One microgram of RNA and random primers were used to synthesize the first strand of cDNA using the High-Capacity cDNA Reverse Transcription Kit (Applied Biosciences). Total cDNA reaction samples were diluted 5-fold in RNAse/DNase-free water and were used as templates for amplification of each gene using the 7500 Real Time PCR System (Applied Biosciences). In addition, corresponding primers purchased from Integrated DNA Technologies (Supplementary Table 5.1) and the Power SYBR green PCR Master Mix (Applied Biosciences) were utilized during each qPCR reaction. The mRNA levels of IL-6, IL-10, CYP2J9, CYP2J12, TRPV1, CB1, and CB2 were normalized to those of GAPDH, the internal control, and were analyzed using the $2^{-\Delta\Delta C_T}$ method[413]. Relative mRNA expression was reported as a percent change versus control. For the quantification of TRPV1, CB1, and CB2, each data set was analyzed using

one-way ANOVA with a subsequent multiple comparisons test (GraphPad Prism version 6.00). The following p values correspond to the reported number of asterisks above each bar. *$p \leq 0.05$, **$p \leq 0.01$, ***$p \leq 0.001$ ****$p \leq 0.0001$. Primers used were designed as shown in Supplementary Table 1.

BV2 anti-inflammation assays (NO Griess assay, IL-6 ELISA, and MTT). Assays were performed as previously described[163]. BV-2 cells were seeded in 24-well plates (200,000 cells/mL) and grown to 80-90% confluency. For eVD screening and dose response studies, media was replaced with serum-free media and the cells were pre-incubated with eVDs for 4 hours prior to stimulation with 25 ng/mL LPS (Sigma-Aldrich, USA). For epoxy-eVDs studies, BV-2 were treated with the sEH inhibitor, t-AUCB (1 μM), for 30 min prior to addition of epoxy-eVDs. For inhibition studies, CB1 antagonist, Rimonabant (1 μM), CB2 inverse agonist, AM630 (1 μM), TRPV1 antagonist, AMG 9810 (1 μM), were pre-incubated 30 min before addition of eVDs (1 μM) for 4 hrs. Media was collected after 24 hours and measured for NO levels (Griess assay) and IL-6 levels (ELISA) as previously described[163]. Cellular proliferation/cytotoxicity was assessed by testing the media with a commercially available MTT kit (Cayman Chemical Item No: #10009365).

Expression and purification of recombinant CYP2J2 in E. coli. Recombinant D34-CYP2J2 containing a His_5 tag was expressed and purified as previously performed[243,250]. The D34-CYP2J2 is a 34-residue N-terminal truncation (residues 3-37) of CYP2J2 with a substitution of Leu2 for an Ala residue. These modifications have been previously shown to increase protein yield without affecting activity[38, 45].

Expression and purification of cytochrome P450 reductase. Expression of cytochrome P450 reductase (CPR) was performed as described previously[250].

Use of reactive oxygen species (ROS) scavengers. All *In vitro* metabolism data were performed using ROS scavengers as previously described[404].

CYP2J2-mediated metabolism of NADA and NA5HT. Metabolism of NADA and NA5HT was performed in a lipid reconstituted system as previously described[391,404]. Briefly, 0.6 μM CYP2J2 and 0.6 μM CPR were incubated in a 20% POPS reconstituted system in 0.5 mL of 0.1 M potassium phosphate buffer, pH 7.4 at 37^o C with 100 μM NADA or NA5HT for 10 min. Reactions were initiated with 1 mM NADPH (final) and reacted for 60 min. Reactions were terminated by

vortexing with 0.5 mL ethyl acetate. 10 mg of $NaCl_{(s)}$ was added to facilitate layer separation. Metabolites were extracted thrice by vortexing the reactions for 1 min with 0.5 mL ethyl acetate followed by centrifugation at 3K RPM at 4° C to separate the layers. The organic layers were dried under a stream of $N_2(g)$ and resuspended in 0.1 mL of acetonitrile for HPLC and LC-MS/MS analysis. For all other experiments, CYP2J2 was incorporated into Nanodiscs.

Incorporation of CYP2J2 into Nanodiscs. Nanodiscs (NDs) containing CYP2J2 were prepared in 20% POPS Nanodiscs as previously described[289]. NDs were used for all experiments using *in vitro* CYP2J2 except for initial product determination.

Kinetics of NADA and NA5HT metabolism. The kinetics of NADA and NA5HT metabolism was determined using a CYP2J2- ND/CPR system as previous described[289] with the following modifications. Reactions were performed with ROS scavengers as stated above. NADA and NA5HT (10-100 μM in DMSO) were incubated with CYP2J2-ND/CPR in 0.5 mL of 0.1 M potassium phosphate buffer (pH 7.4) for 10 min. Reactions were initiated with the addition of 0.5 mM NADPH. The formation of epoxy-eVDs was determined to be linear up to 45 min, and so a 30-min reaction was utilized. Reactions were terminated upon the addition of 0.5 mL ethyl acetate and 10 mg $NaCl_{(s)}$ to facilitate layer separation. The products were extract thrice with ethyl acetate, dried under a stream of $N_{2(g)}$, and resuspended in 180-proof ethanol for LC-MS/MS quantification.

NADPH kinetics. The rate of NADPH oxidation by CYP2J2-ND/CPR was determined using UV-Vis spectroscopy as previously described[257]. The rate of the NADPH oxidation with CYP2J2-ND/CPR without substrates was considered the "baseline" rate.

AEA metabolism inhibition. AEA metabolism was determined as previously described[391] with the following modifications. Reactions were performed in the presence of ROS scavengers as stated above and were terminated using 0.5 mL ethyl acetate and $NaCl_{(s)}$. 25 μM and 75 μM of NADA or NA5HT were used to inhibit AEA metabolism. 40 μM of AEA without inhibitor was used as a control for each set of experiments and we did not observe significant variation in the metabolism of AEA. EET-EAs and epoxy-eVDs were simultaneously quantified using LC-MS/MS.

Ebastine competitive binding. Relative binding affinities of eVDs binding to CYP2J2 were determined using an ebastine competitive binding assay as previously described.[289]

LC-MS and LC-MS/MS analysis of CYP2J2 metabolites. CYP2J2 metabolism products were determined using HPLC Method 1. The Phenomenex column was used. LC-MS/MS detection was performed as previously described[391].

Figures

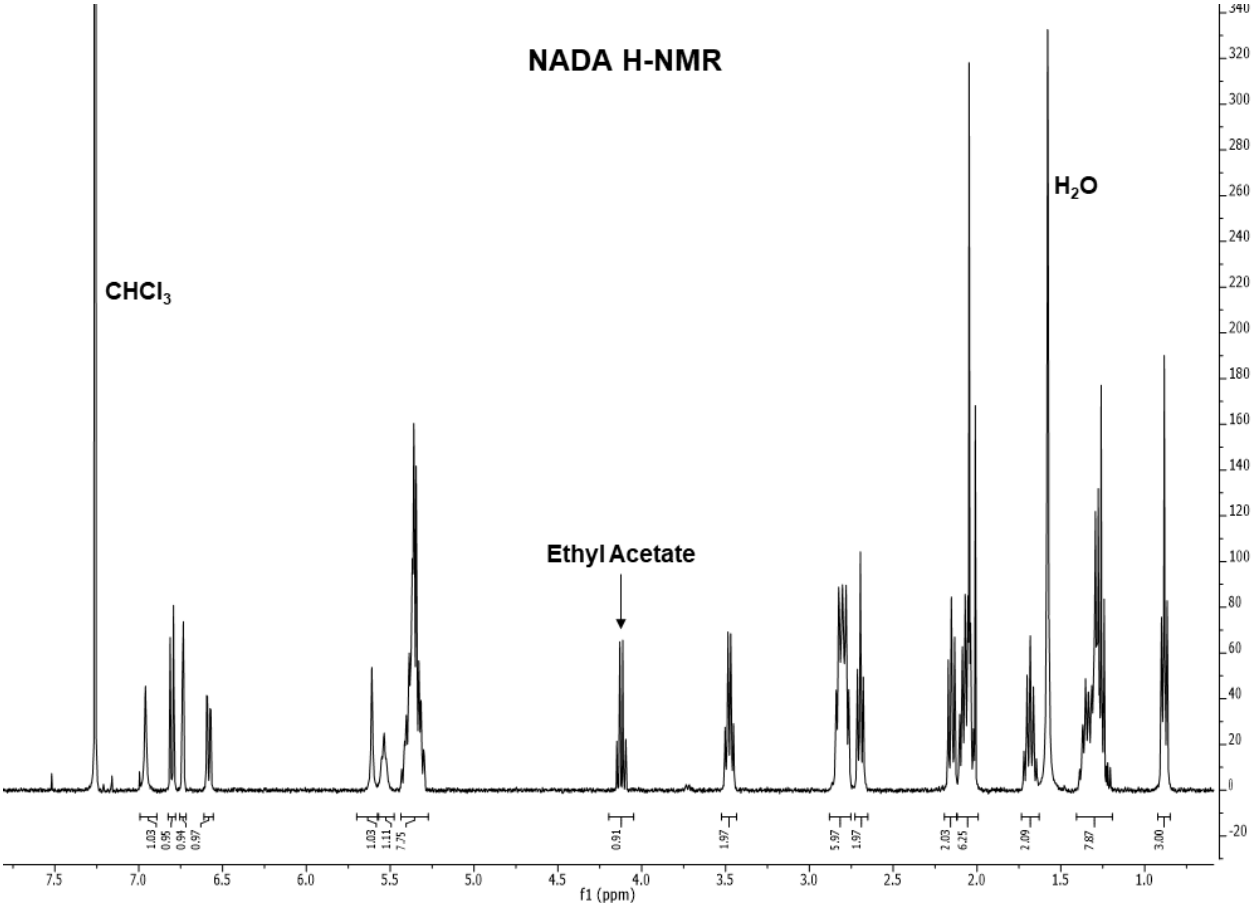

Supplementary Figure 5.1. ^{1}H-NMR spectrum for NADA (400 Hz, $CDCl_3$).

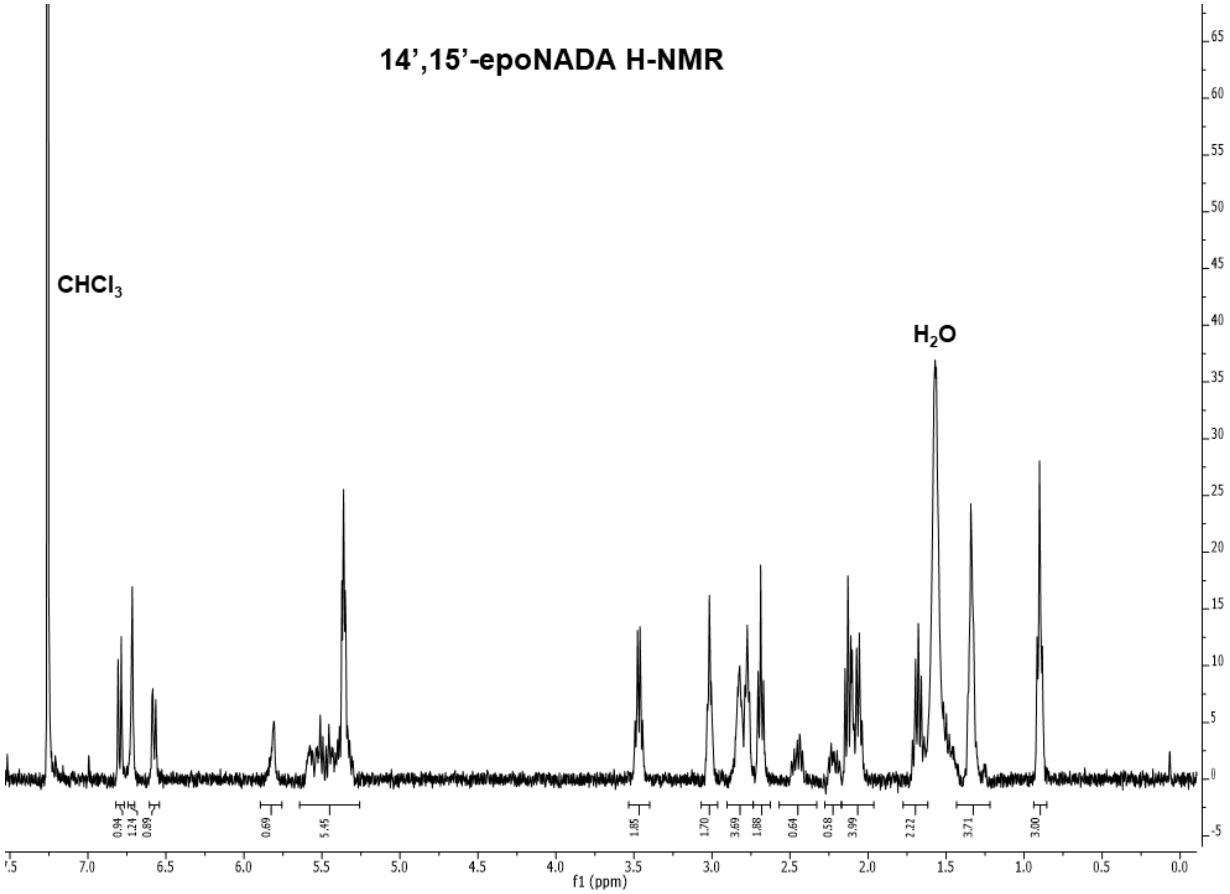

Supplementary Figure 5.2. ^{1}H-NMR spectrum for 14',15'-epoNADA (400 Hz, $CDCl_3$).

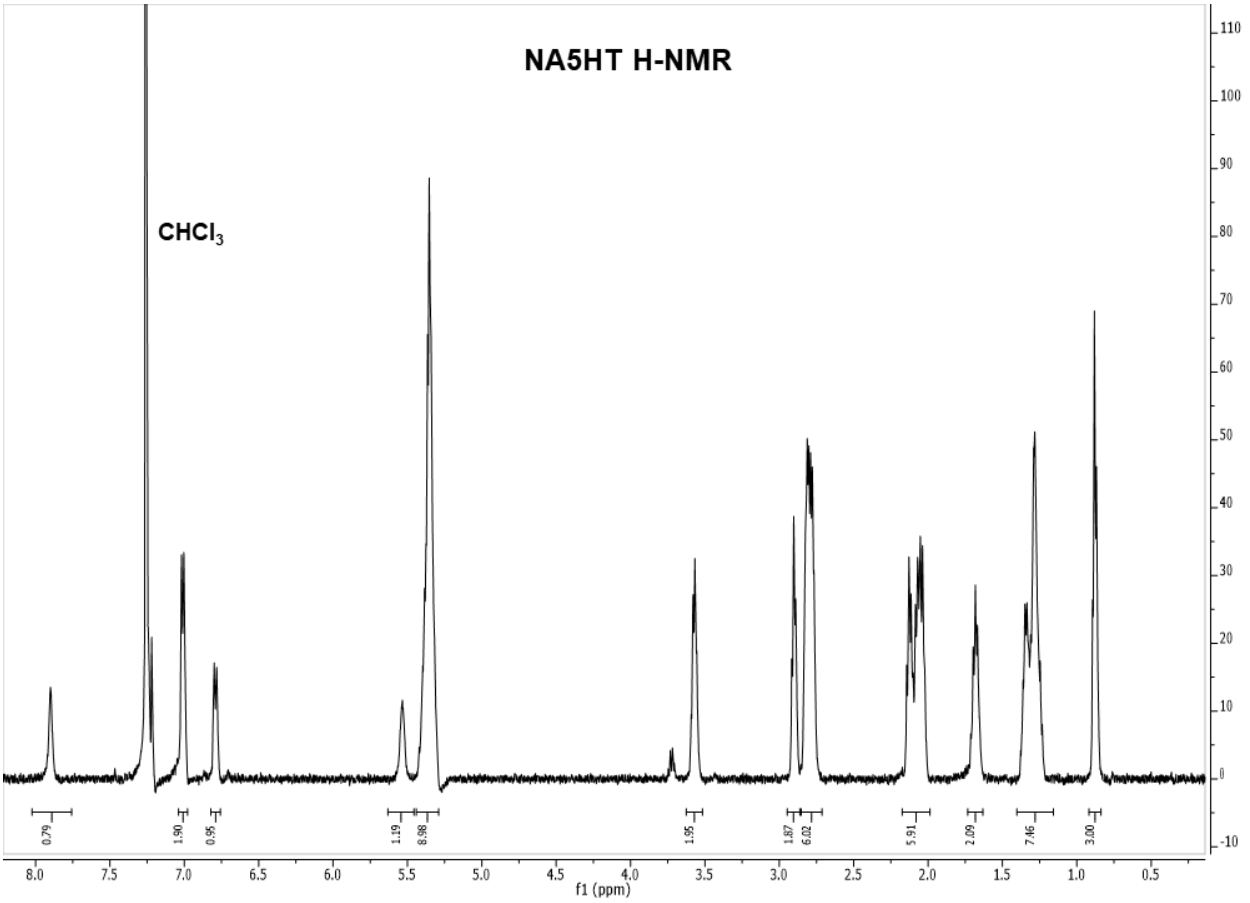

Supplementary Figure 5.3. ^{1}H-NMR spectrum for NA5HT (400 Hz, $CDCl_3$).

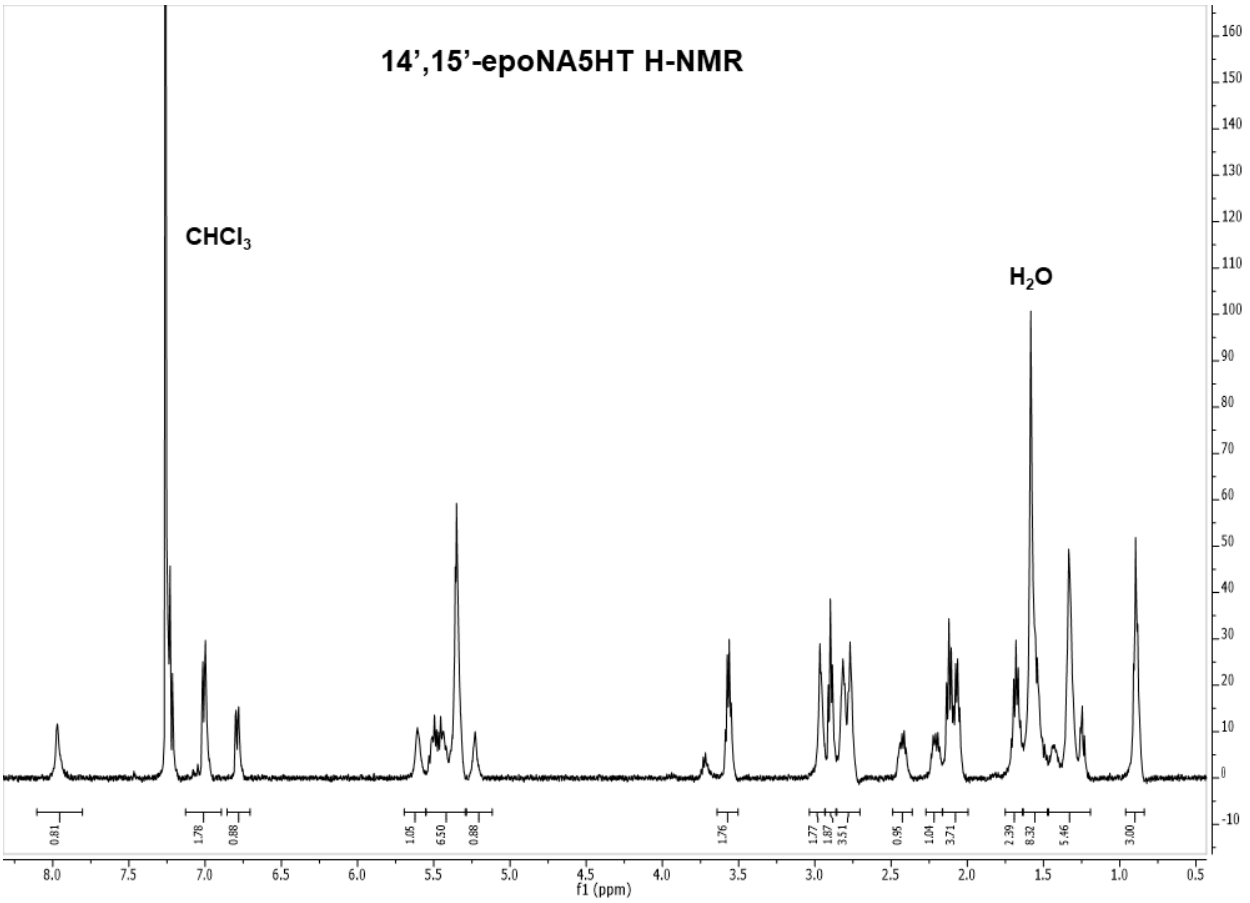

Supplementary Figure 5.4. ^{1}H-NMR spectrum for 14',15'-epoNA5HT (500 Hz, $CDCl_3$).

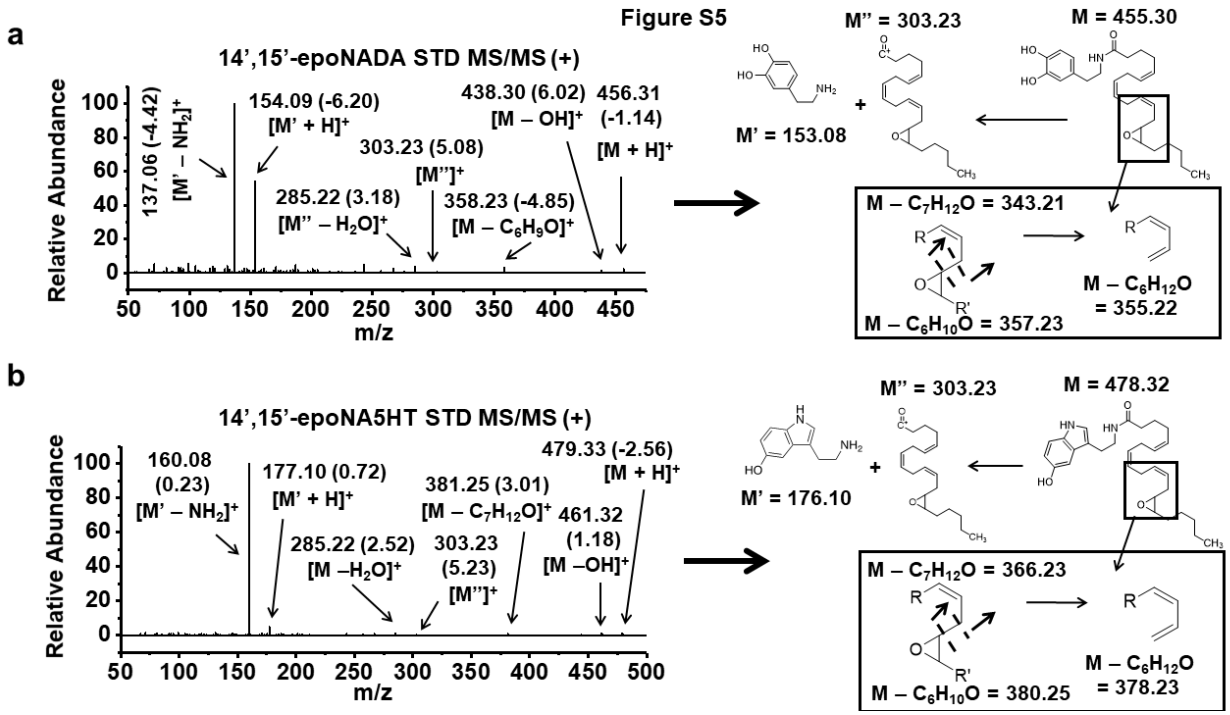

Supplementary Figure 5.5. MS/MS spectra of synthesized **(a)** 14',15'-epoNADA and **(b)** 14',15'-epoNA5HT standards along with fragmentation schemes. Data are obtained from LC-MS/MS analysis. Fragment m/z values are given with deviation from the calculated m/z values (± ppm) given in parentheses.

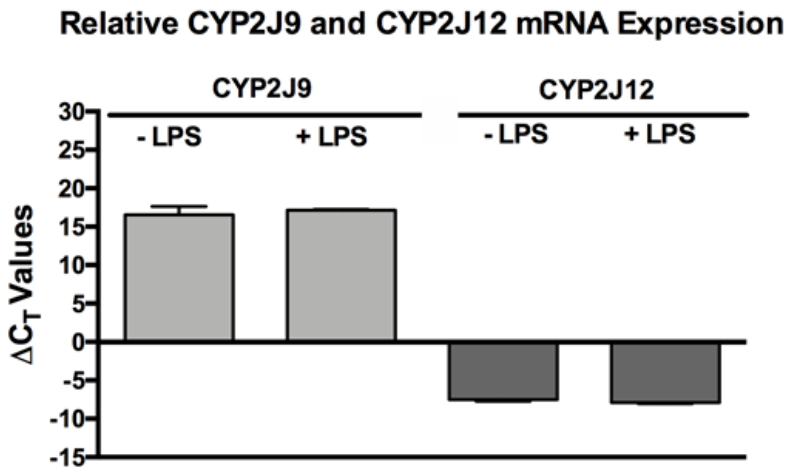

Supplementary Figure 5.6. *Effect of LPS in BV-2 microglial cells on the relative mRNA expression of CYP2J9 and CYP2J12.* BV-2 microglial cells seeded at 200,000 cells/well in a 24-well plate were treated with 100 ng/mL LPS for 3 hours. ΔCT values are inversely related to expression levels. Quantitative PCR showed no significant increase in CYP2J9 or CYP2J12 mRNA expression with LPS stimulation. Data were from 3 pooled wells and performed in technical triplicate.

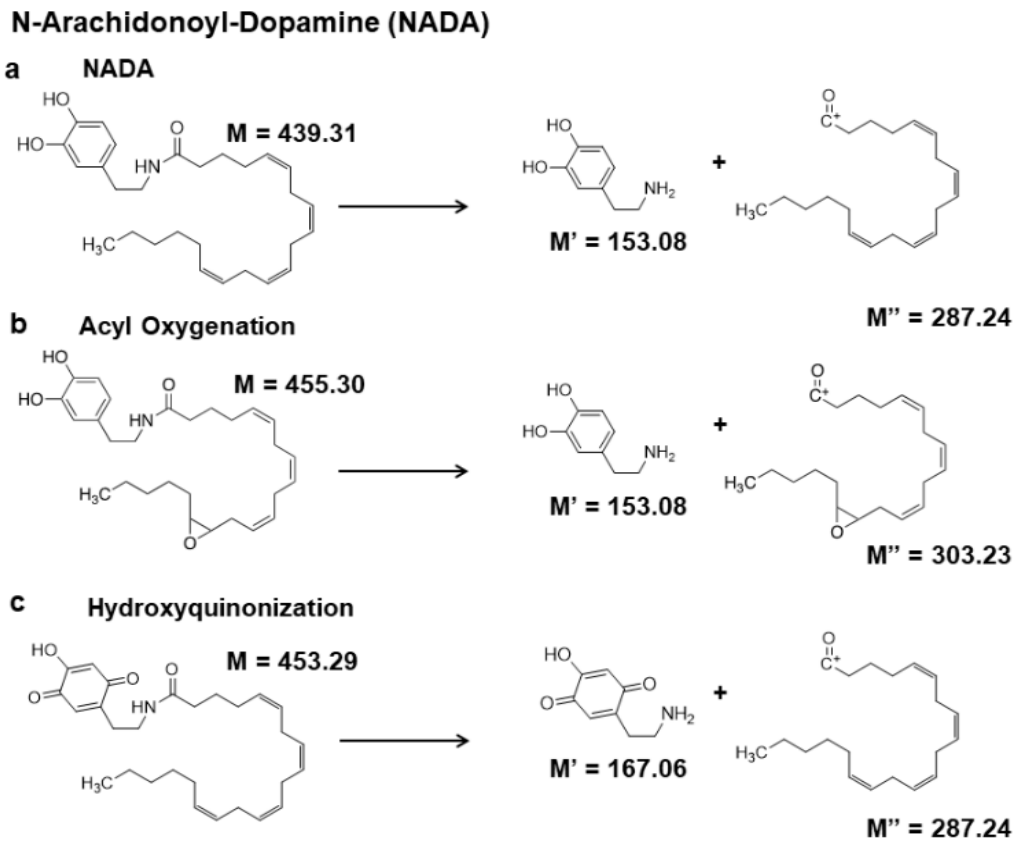

Supplementary Figure 5.7. Fragmentation scheme of **(a)** NADA, **(b)** acyl oxygenation of NADA (14',15'-epoNADA shown as an example), and **(c)** NADA-HQ.

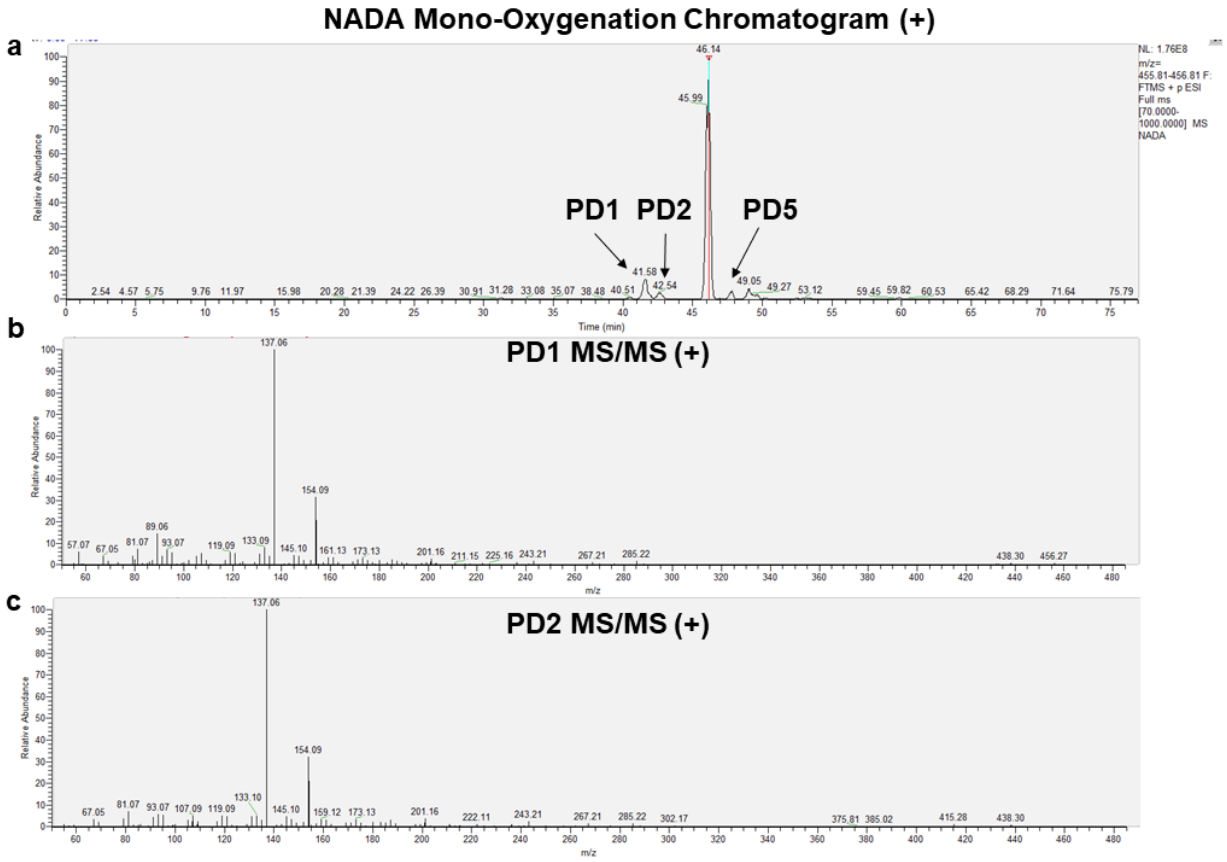

Supplementary Figure 5.8. *Mono-oxygenation of NADA by CYP2J2*. **(a)** LC-MS/MS chromatogram in positive ion mode. Mass range is ± 5 ppm of the predicted product. **(b-c)** MS/MS spectra obtained from each corresponding product.

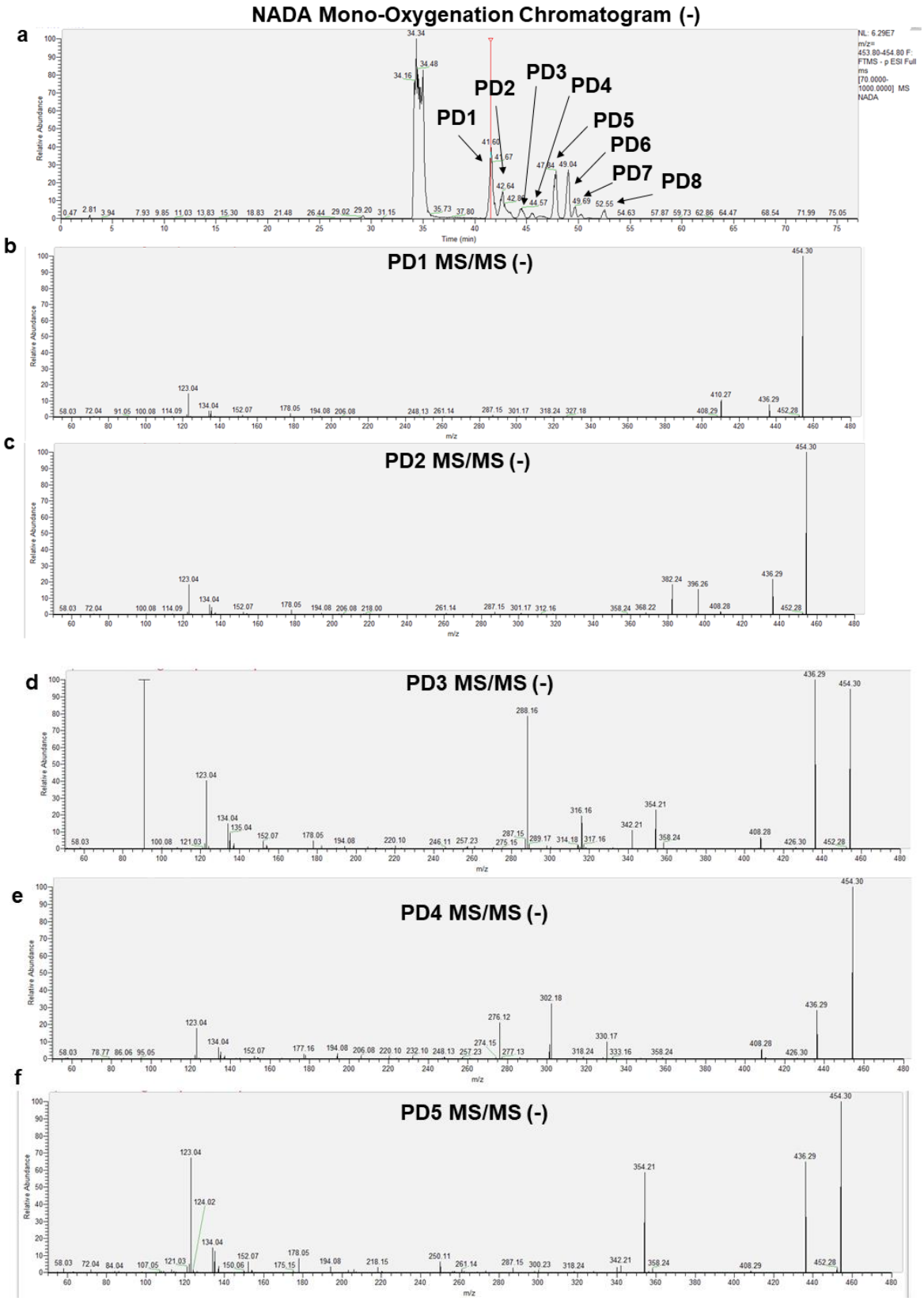

Supplementary Supplementary Figure 5.9 cont.

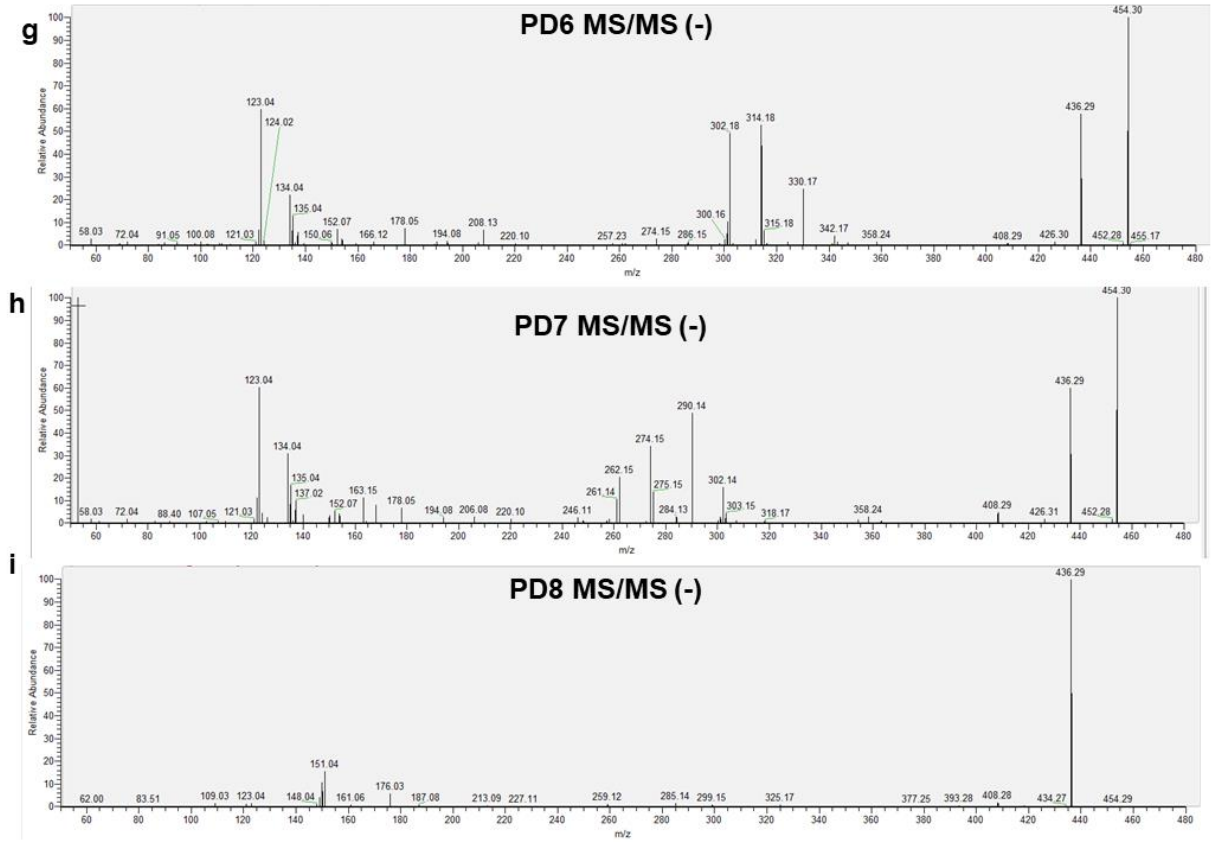

Supplementary Figure 5.9. *Mono-oxygenation of NADA by CYP2J2*. **(a)** LC-MS/MS chromatogram in negative ion mode. Mass range is ± 5 ppm of the predicted product. **(b-i)** MS/MS spectra obtained from each corresponding product.

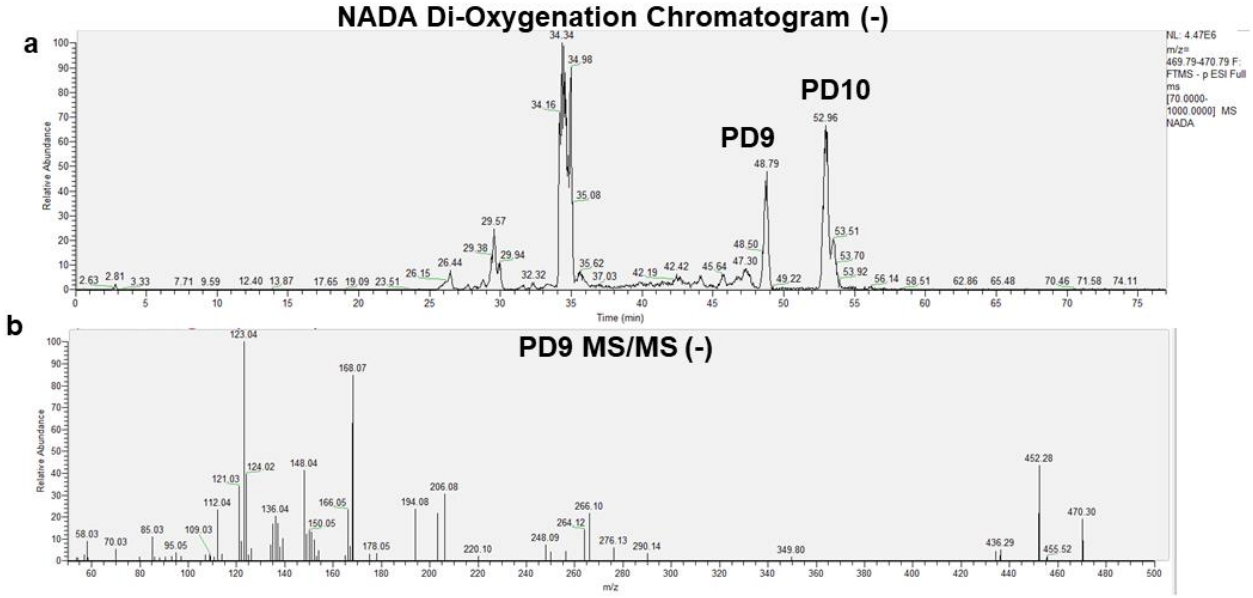

Supplementary Figure 5.10. *Di-oxygenation of NADA by CYP2J2*. **(a)** LC-MS/MS chromatogram in negative ion mode. Mass range is ± 5 ppm of the predicted product. **(b)** MS/MS spectrum obtained from PD9.

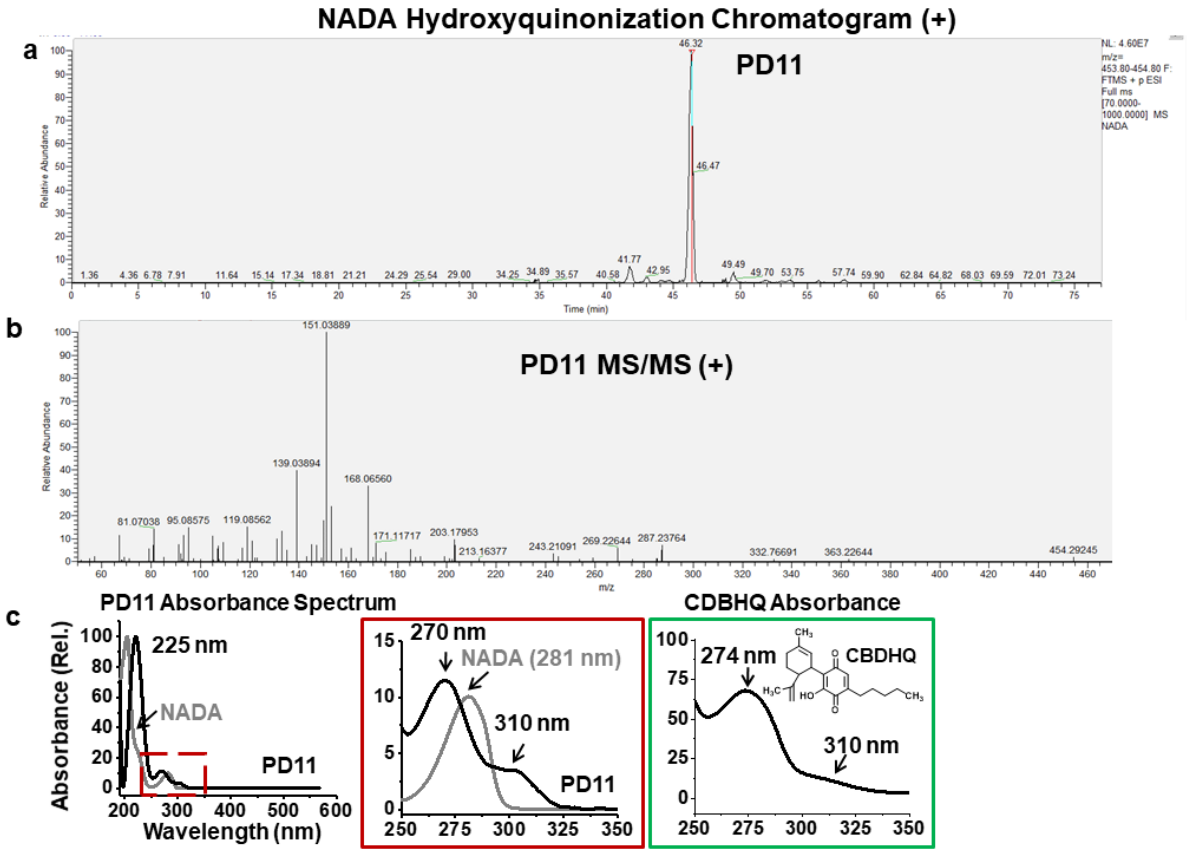

Supplementary Figure 5.11. *Hydroxyquinonization of NADA by CYP2J2*. **(a)** LC-MS/MS chromatogram in positive ion mode. Mass range is ± 5 ppm of the predicted product. **(b)** MS/MS spectrum of PD11. **(c)** Absorbance spectrum of PD11 obtained by UV-Vis HPLC analysis. NADA and cannabidiol hydroxyquinone (CBDHQ) were analyzed using a similar method and their absorbance spectra are given for comparison.

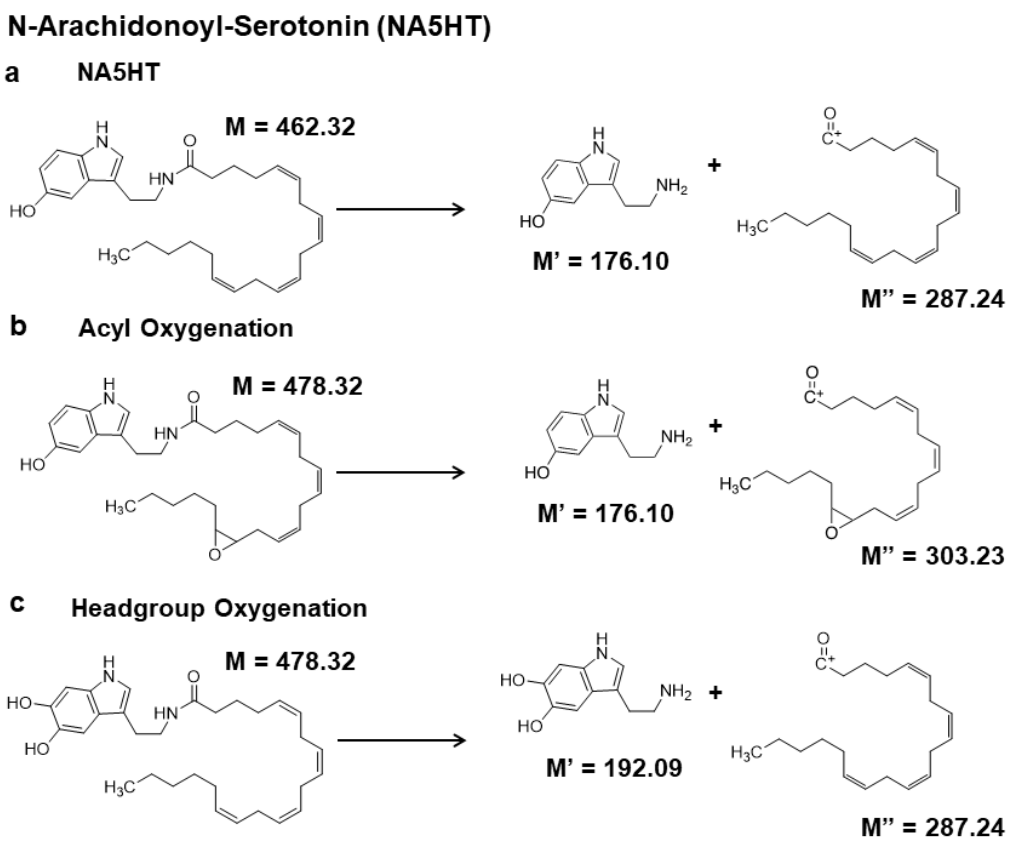

Supplementary Figure 5.12. Fragmentation scheme of **(a)** NA5HT, **(b)** acyl oxygenation of NA5HT (14',15'-epoNA5HT shown as an example), and **(c)** Headgroup oxygenation of NA5HT.

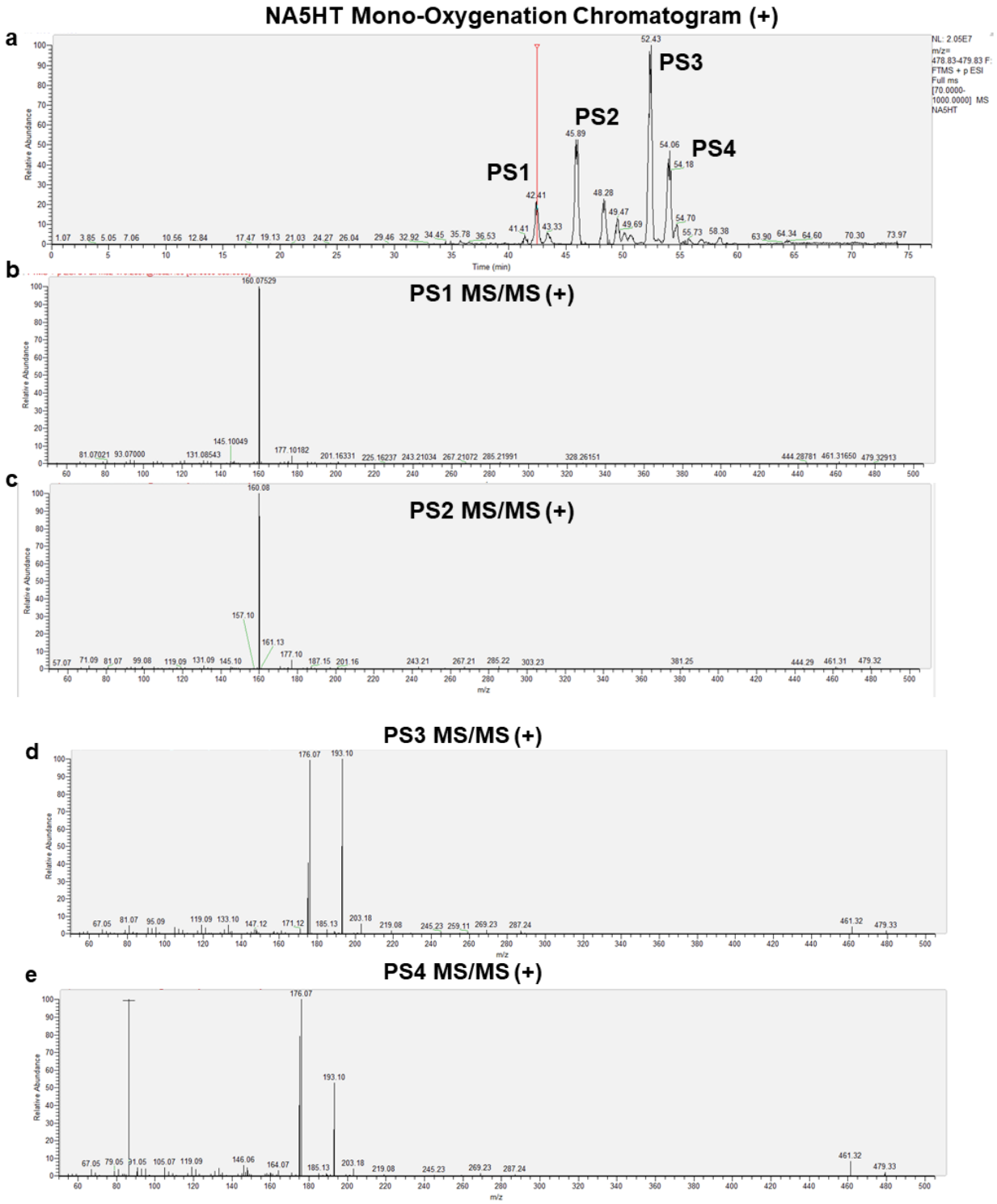

Supplementary Figure 5.13. *Mono-oxygenation of NA5HT by CYP2J2*. **(a)** LC-MS/MS chromatogram in positive ion mode. Mass range is ± 5 ppm of the predicted product. **(b-e)** MS/MS spectra obtained from each corresponding product.

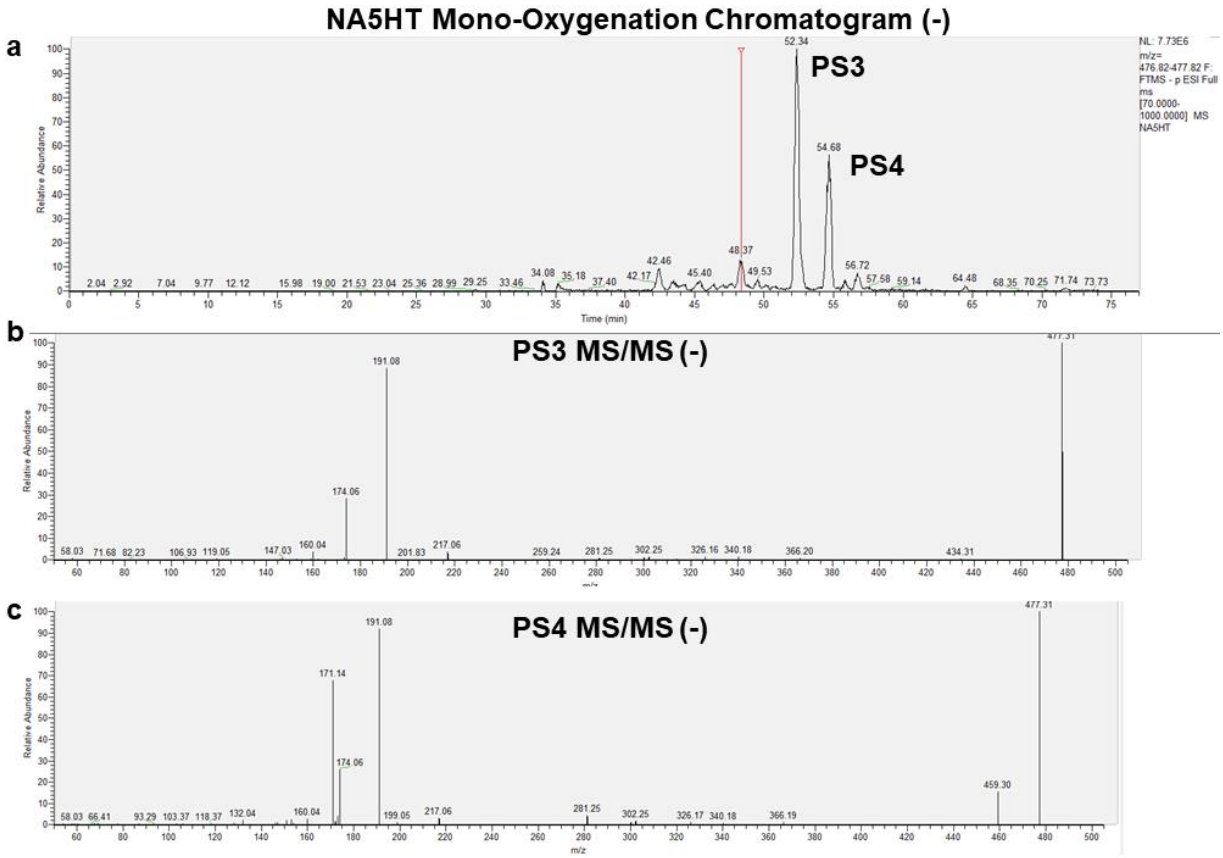

Supplementary Figure 5.14. *Mono-oxygenation of NA5HT by CYP2J2*. **(a)** LC-MS/MS chromatogram in negative ion mode. Mass range is ± 5 ppm of the predicted product. **(b-c)** MS/MS spectra obtained from each corresponding product.

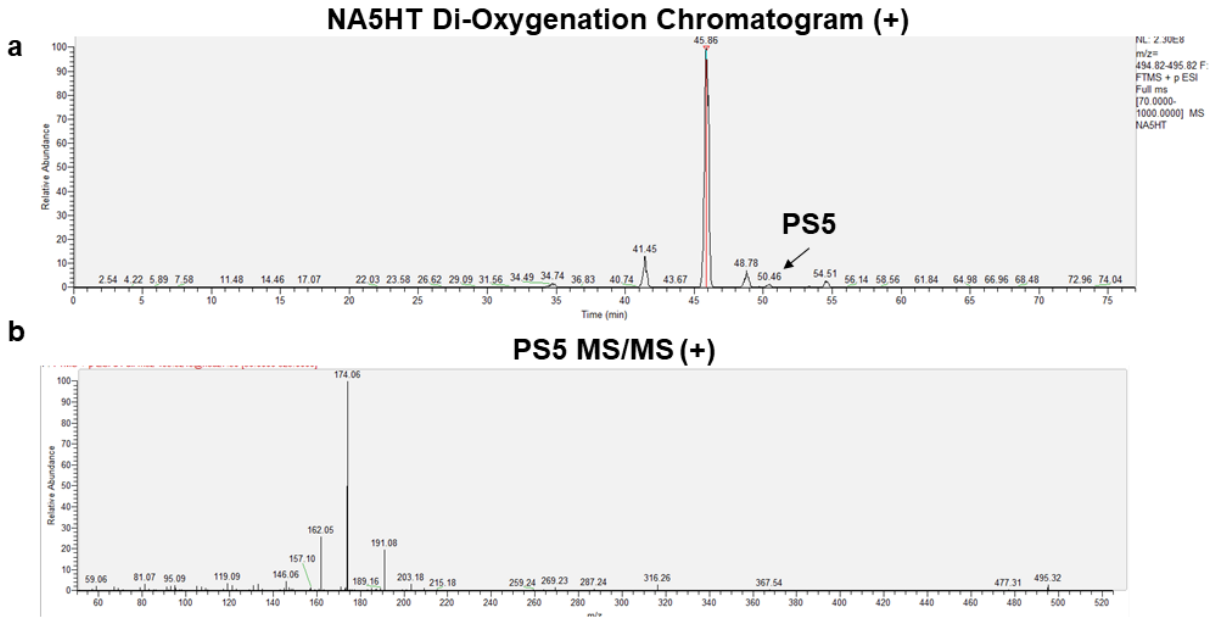

Supplementary Figure 5.15. *Di-oxygenation of NA5HT by CYP2J2*. **(a)** LC-MS/MS chromatogram in positive ion mode. Mass range is ± 5 ppm of the predicted product. **(b)** MS/MS spectrum of PS5.

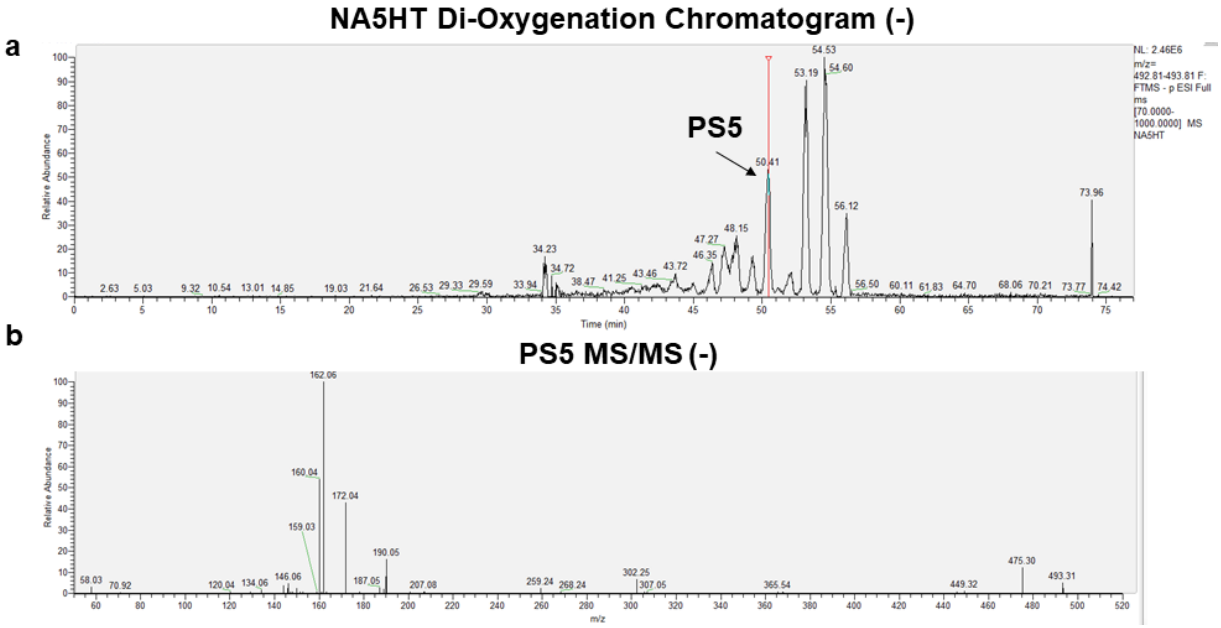

Supplementary Figure 5.16. *Di-oxygenation of NA5HT by CYP2J2*. **(a)** LC-MS/MS chromatogram in negative ion mode. Mass range is ± 5 ppm of the predicted product. **(b)** MS/MS spectrum of PS5.

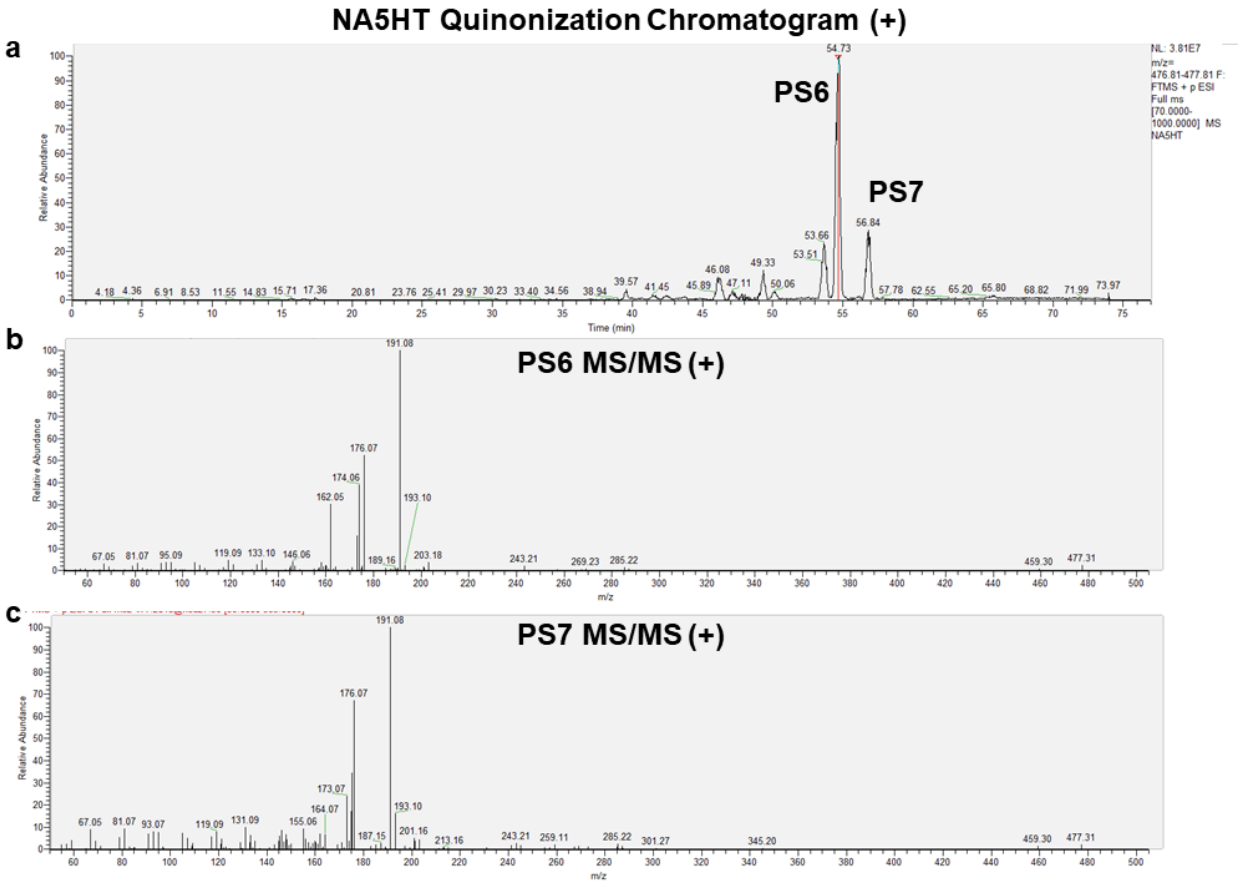

Supplementary Figure 5.17. *Quinonization of NA5HT by CYP2J2*. Quinonization was determined from the apparent oxygenation of the mono-oxygenation products (PS3 and PS4) indicated by a loss of 2 hydrogen atoms. **(a)** LC-MS/MS chromatogram in positive ion mode. Mass range is ± 5 ppm of the predicted product. **(b-c)** MS/MS spectra obtained from the indicated product.

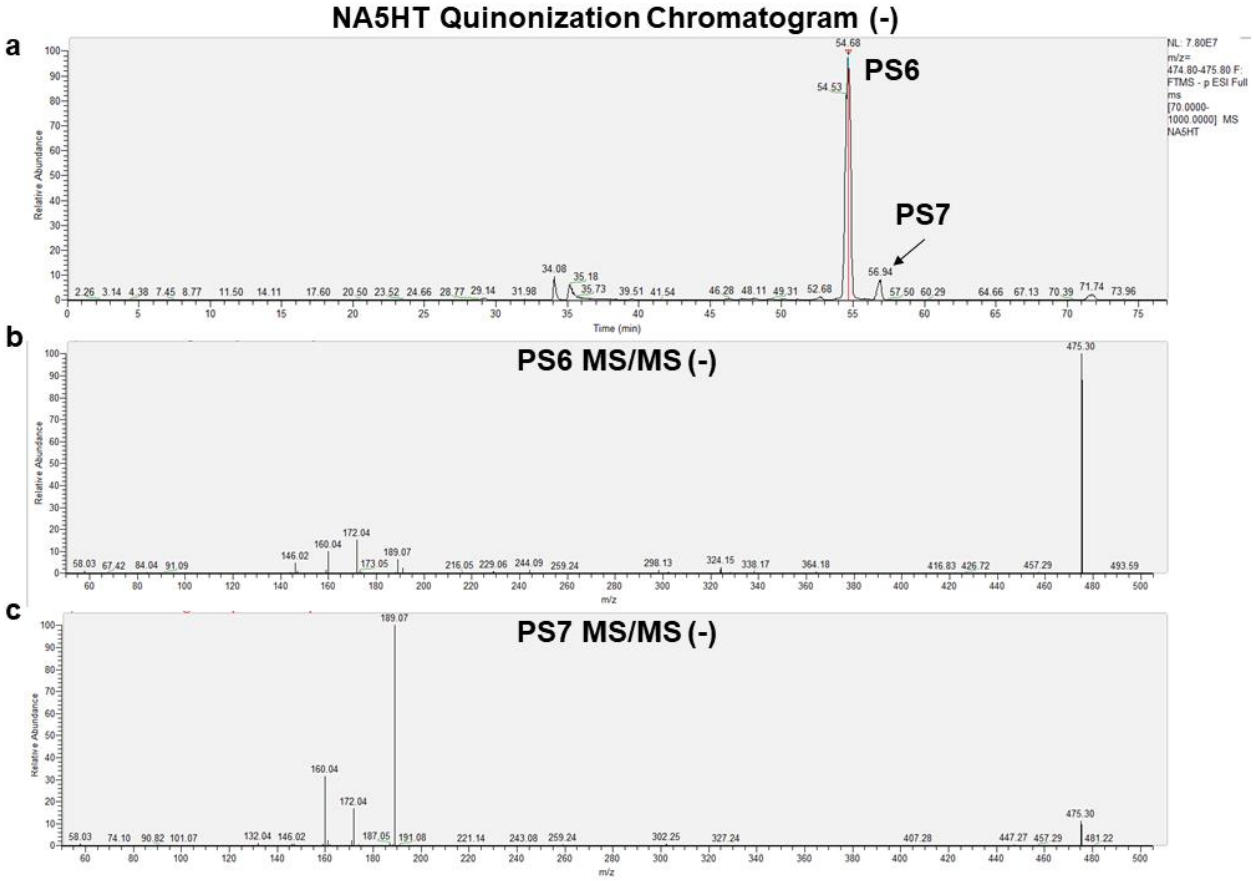

Supplementary Figure 5.18. *Quinonization of NA5HT by CYP2J2*. Quinonization was determined from the apparent oxygenation of the mono-oxygenation products (PS3 and PS4) indicated by a loss of 2 hydrogen atoms. **(a)** LC-MS/MS chromatogram in negative ion mode. Mass range is ± 5 ppm of the predicted product. **(b-c)** MS/MS spectra obtained from the indicated product.

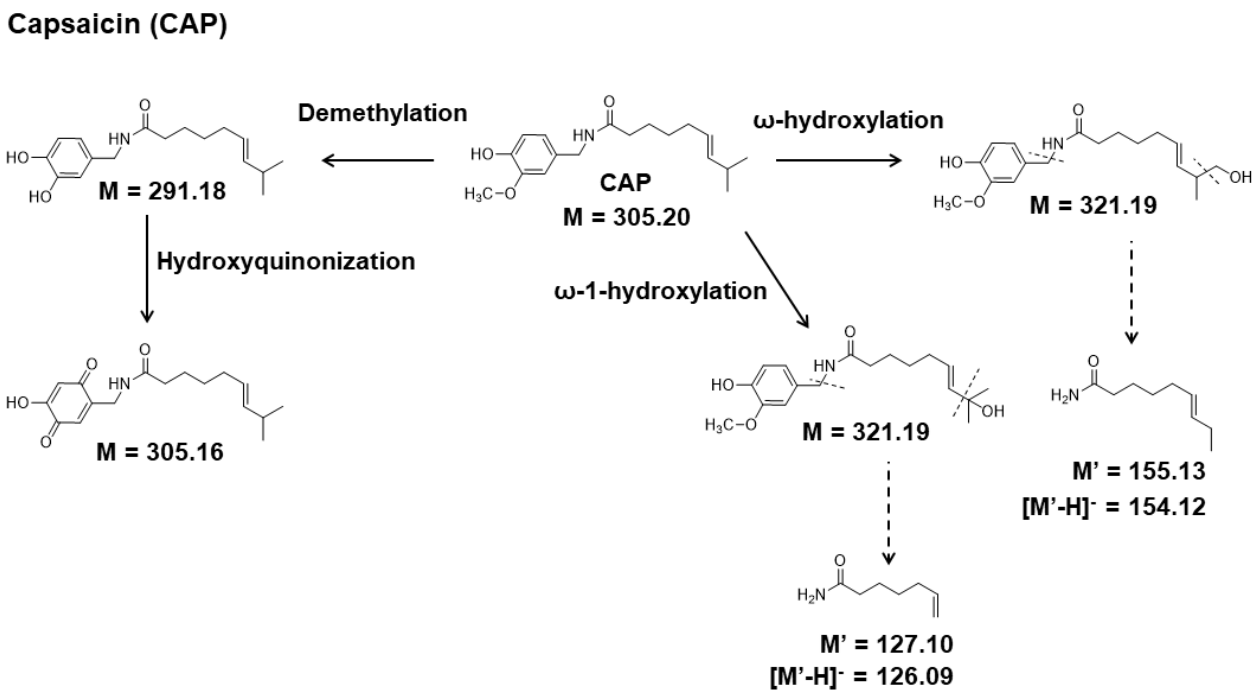

Supplementary Figure 5.19. Fragmentation scheme of capsaicin oxygenation.

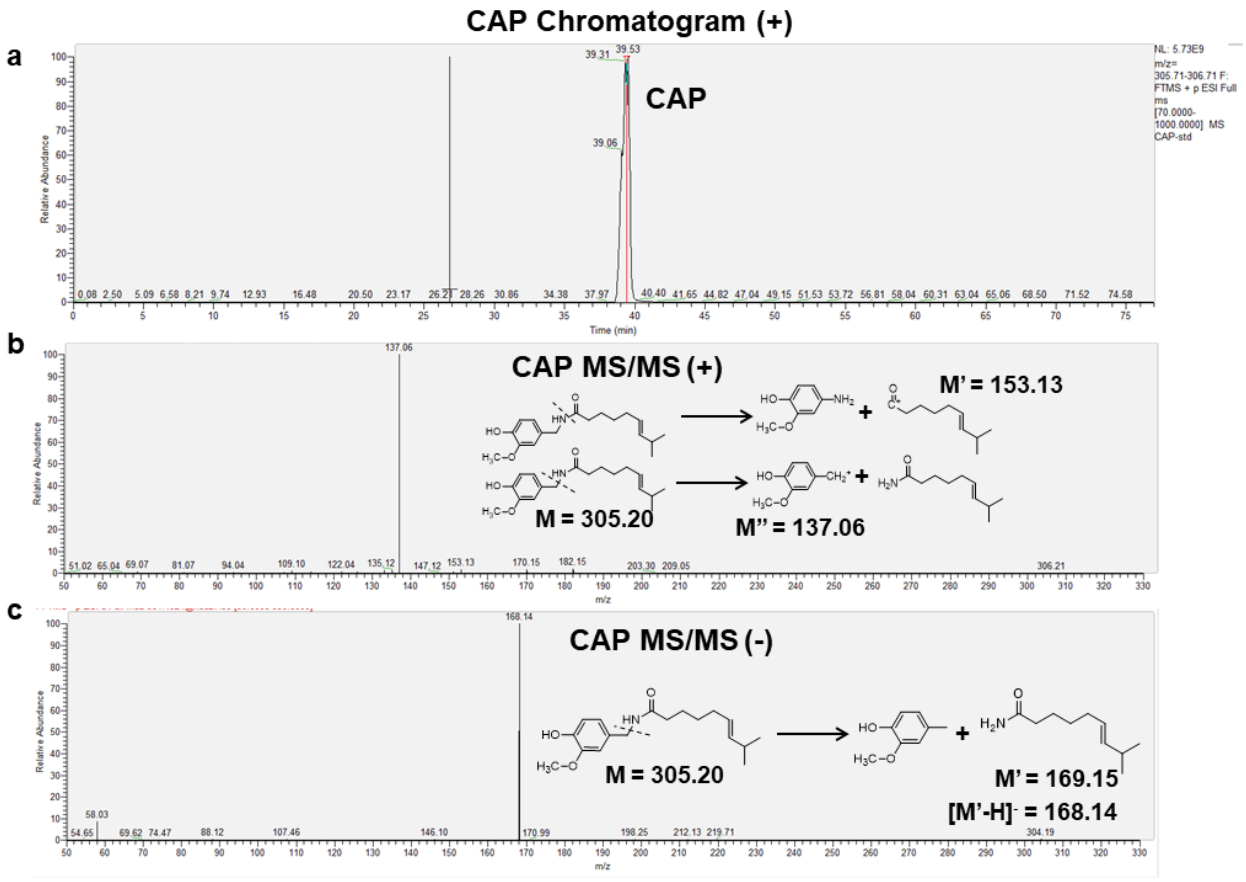

Supplementary Figure 5.20. *LC-MS/MS analysis of capsaicin (CAP).* **(a)** LC-MS/MS chromatogram in positive ion mode. Mass range is ± 5 ppm of the predicted product. **(b)** MS/MS spectrum of CAP in positive ion mode. **(c)** MS/MS spectrum of CAP in negative ion mode.

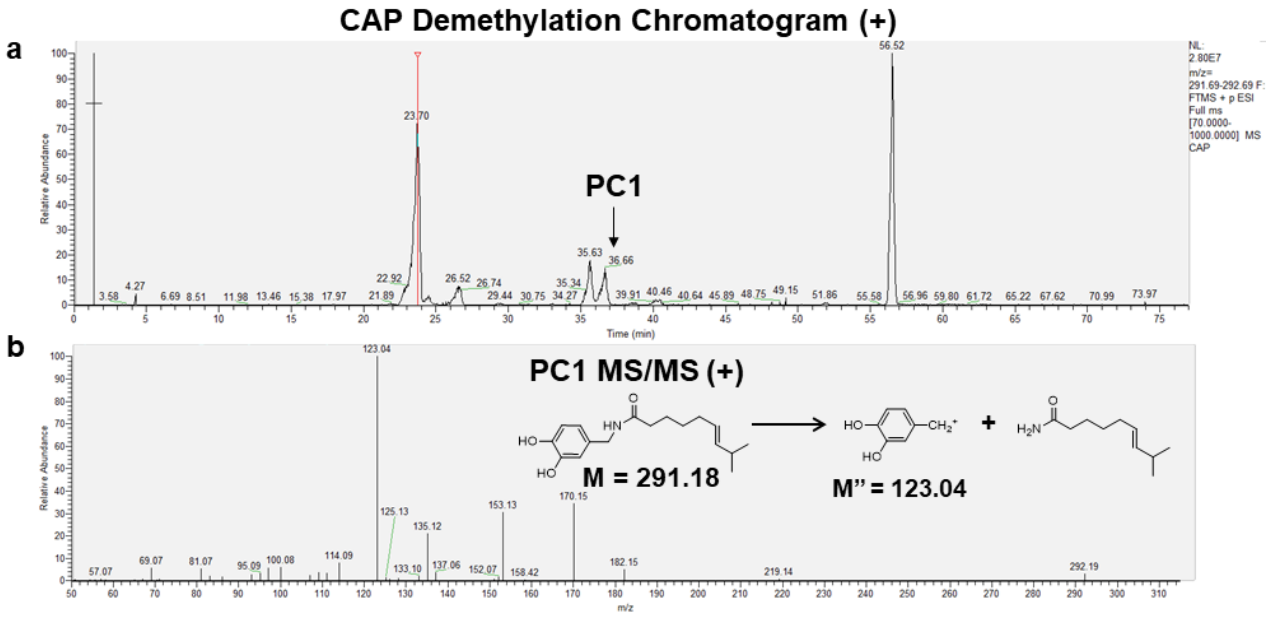

Supplementary Figure 5.21. *Demethylation of CAP by CYP2J2*. **(a)** LC-MS/MS chromatogram in positive ion mode. Mass range is ± 5 ppm of the predicted product. **(b)** MS/MS spectrum of PC1.

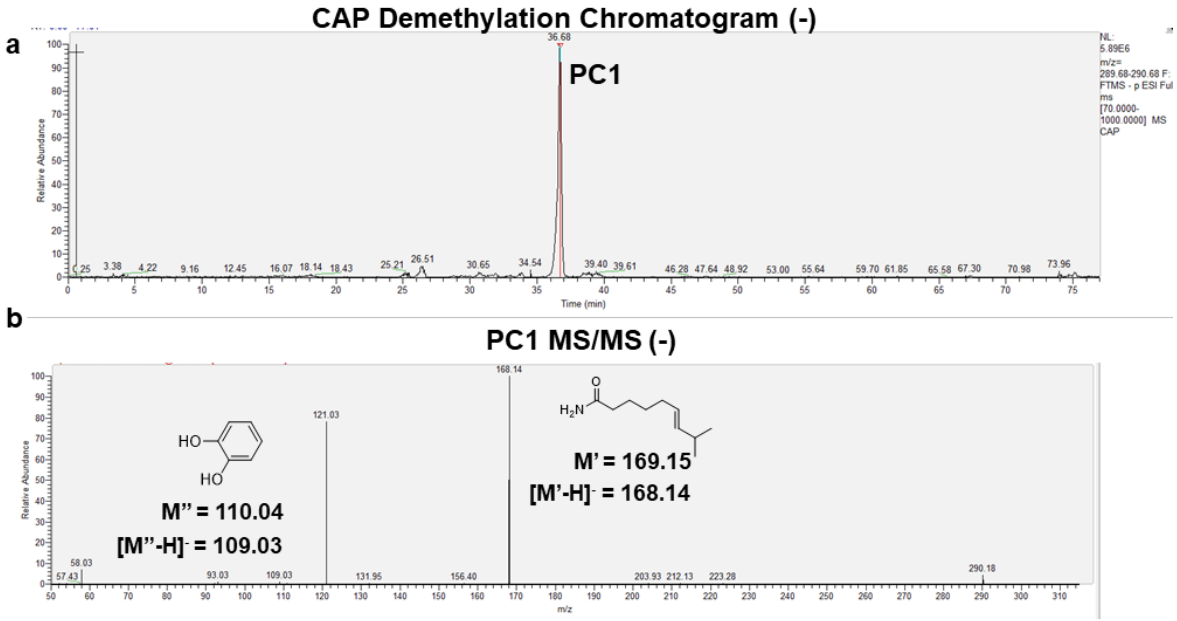

Supplementary Figure 5.22. *Demethylation of CAP by CYP2J2*. **(a)** LC-MS/MS chromatogram in negative ion mode. Mass range is ± 5 ppm of the predicted product. **(b)** MS/MS spectrum of PC1.

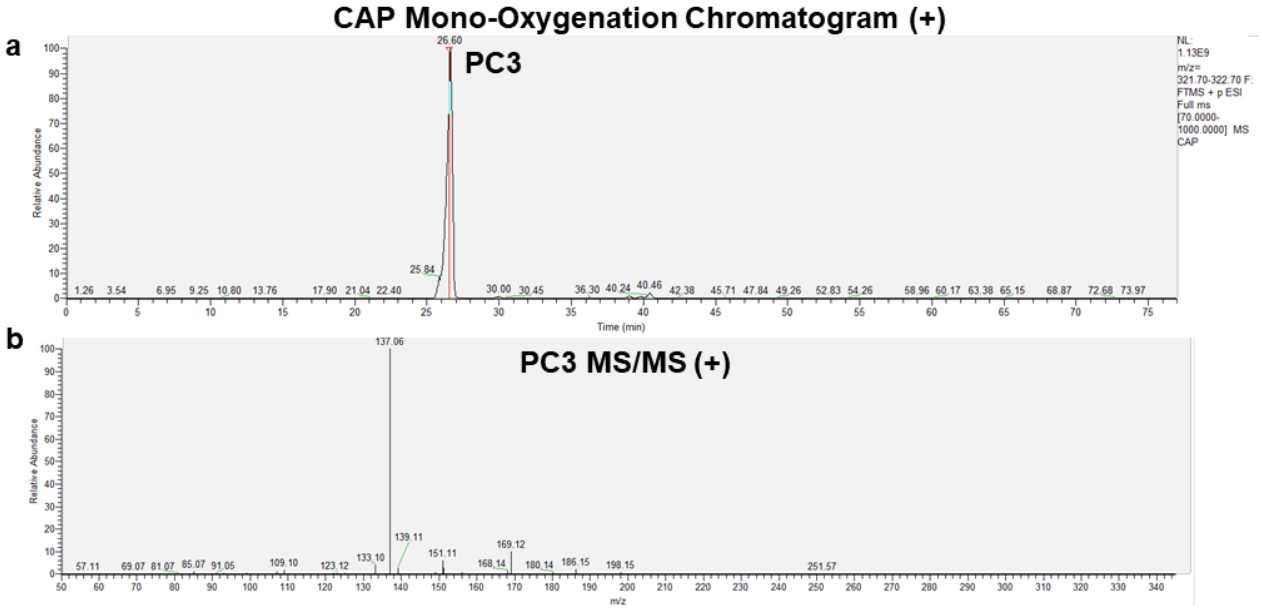

Supplementary Figure 5.23. *Mono-oxygenation of CAP by CYP2J2*. **(a)** LC-MS/MS chromatogram in positive ion mode. Mass range is ± 5 ppm of the predicted product. **(b)** MS/MS spectrum of PC3.

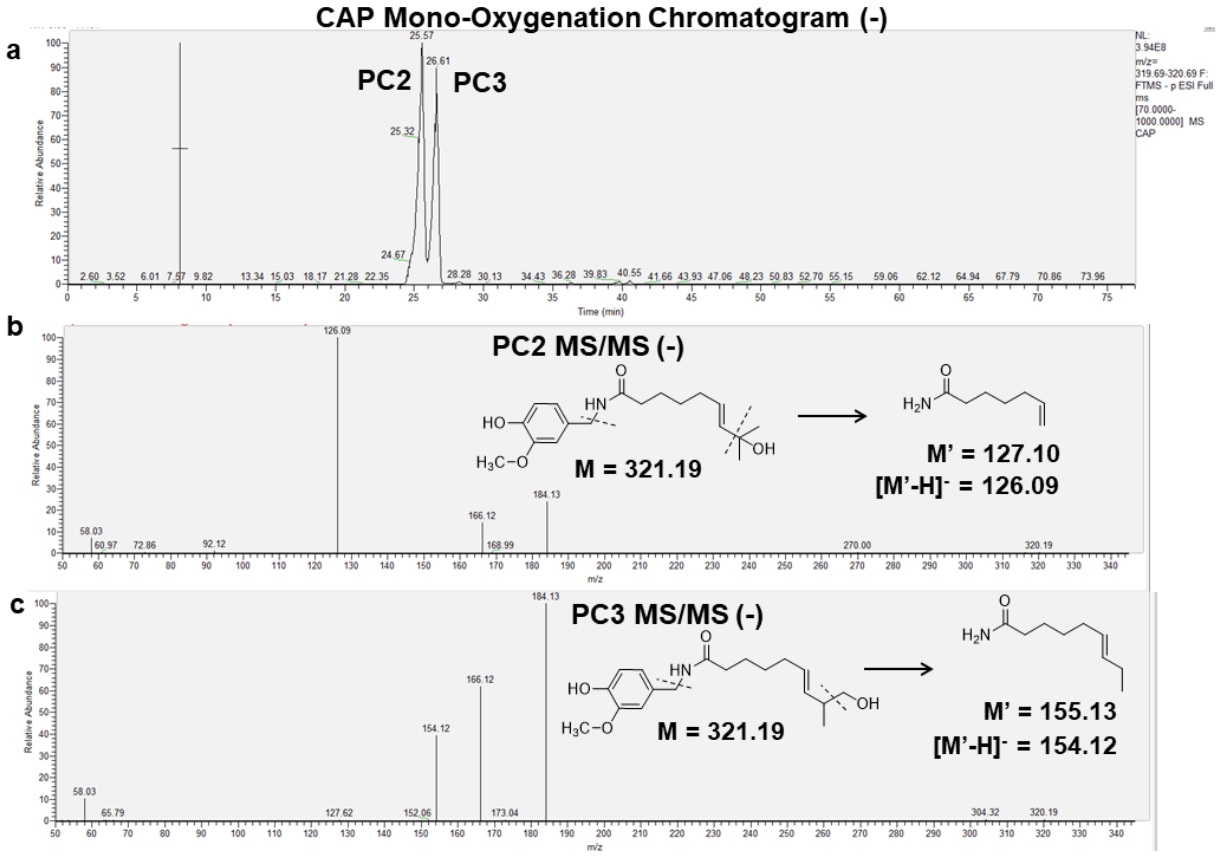

Supplementary Figure 5.24. *Mono-oxygenation of CAP by CYP2J2*. **(a)** LC-MS/MS chromatogram in negative ion mode. Mass range is ± 5 ppm of the predicted product. **(b-c)** MS/MS spectra of indicated products.

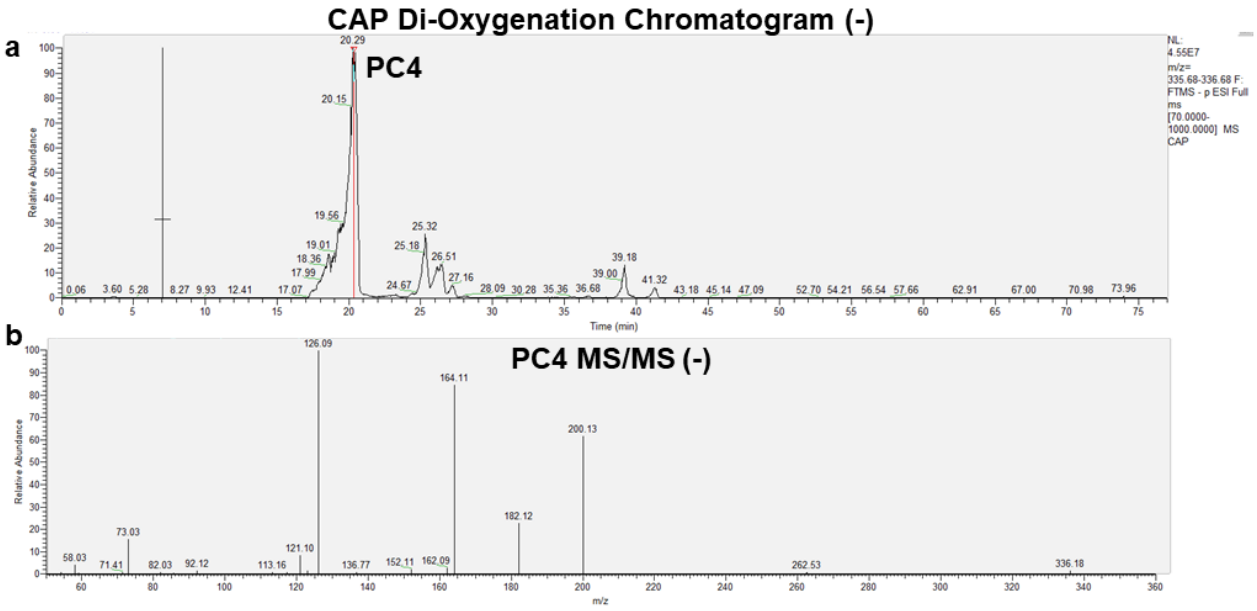

Supplementary Figure 5.25. *Di-oxygenation of CAP by CYP2J2*. **(a)** LC-MS/MS chromatogram in negative ion mode. Mass range is ± 5 ppm of the predicted product. **(b)** MS/MS spectrum of PC4.

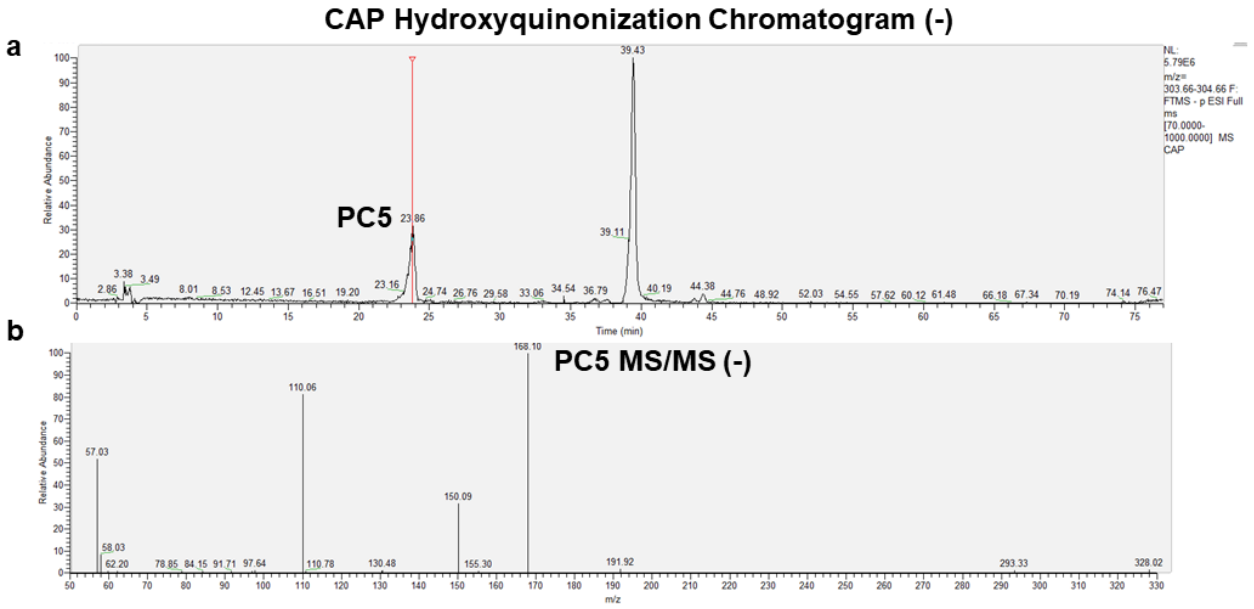

Supplementary Figure 5.26. *Hydroxyquinonization of CAP by CYP2J2*. Hydroxyquinonization is determined by an oxidation of the demethylated CAP (PC1) indicated by the loss of two hydrogen atoms. **(a)** LC-MS/MS chromatogram in negative ion mode. Mass range is ± 5 ppm of the predicted product. **(b)** MS/MS spectrum of PC5.

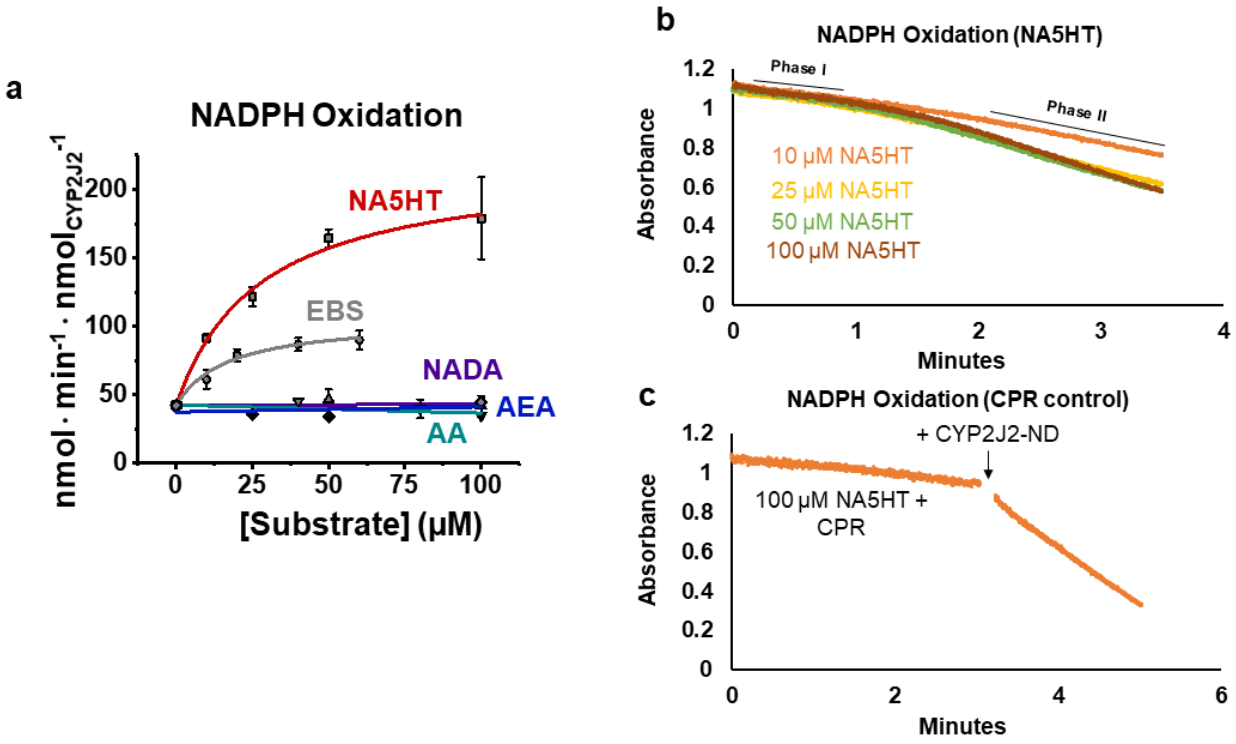

Supplementary Figure 5.27. *Biphasic NADPH oxidation in the presence of NA5HT*. NADPH oxidation as CYP2J2-ND metabolizes NA5HT was determined by the absorbance of NADPH at 340 nm. Data represents the SEM of three independent experiments. Representative spectra are shown. **(a)** NADPH oxidation rates with the indicated substrates. NA5HT showed biphasic NADPH oxidation kinetics and the rates of Phase II are plotted. Ebastine (EBS) is monophasic. **(b)** Absorbance at 340 nm in the presence of the indicated amounts of NA5HT. Phase I rates are similar to those obtained with CPR and CYP2J2-ND alone. Phase II shows a decrease in NADPH as a function of NA5HT concentration. **(c)** Experiments were repeated with NA5HT and CPR only. Rate of NADPH oxidation is similar to CPR alone. Adding CYP2J2-ND results in a rate of NADPH oxidation similar to Phase II with 100 μM NA5HT as seen in **(b)**.

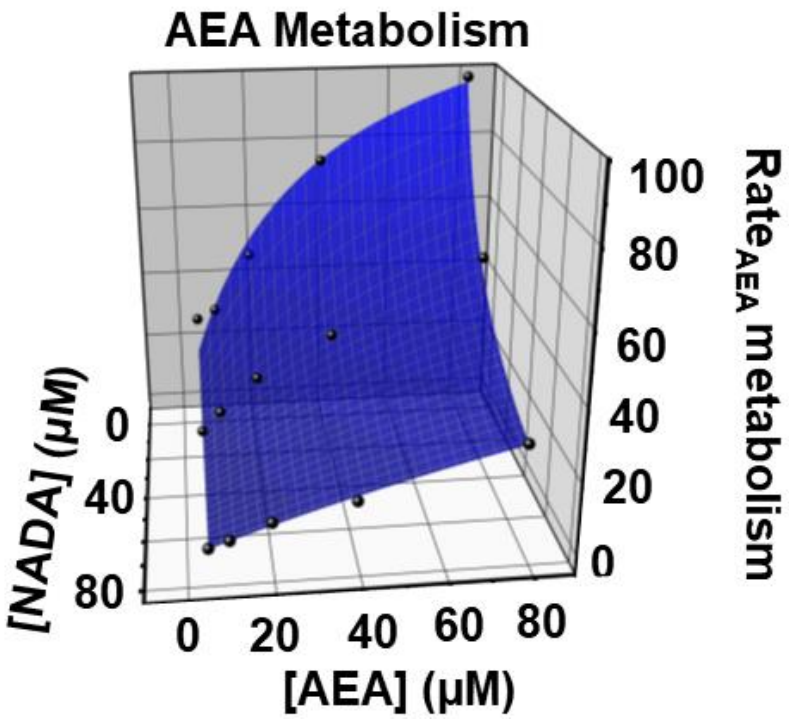

Supplementary Figure 5.28. 3D global fit of AEA inhibition by NADA as shown in Figure 3f. Rates are in $pmol_{EET\text{-}EAs} \cdot min^{-1} \cdot nmol_{CYP2J2}^{-1}$.

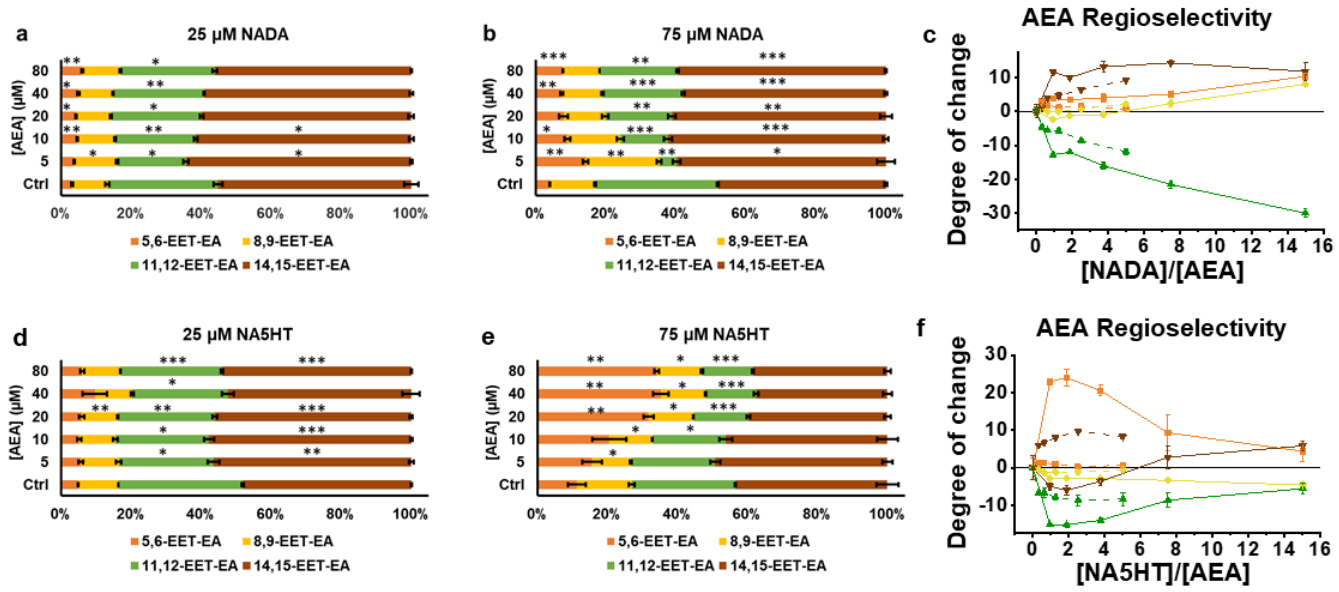

Supplementary Figure 5.29. *Regioselectivity of AEA epoxidation in the presence of eVDs*. **(a-c)** Regioselectivity in the presence of NADA and **(d-f)** NA5HT at the indicated concentrations. Regioselectivity is shown as a percentage of the total EET-EAs. Control (Ctrl) refers to 40 µM AEA samples without eVDs, which was ran along with each experiment. *p < 0.05; **p < 0.01, ***p < 0.001. Data in **(c)** and **(f)** show the dependence of the regioselectivity change on the concentrations of the eVDs as a function of an increasing ratio of the eVD:AEA. Degree of change is defined as the change in percentage value compared to control. Data from the 25 µM datasets are shown as dashed lines and the data from the 75 µM datasets are shown as solid lines.

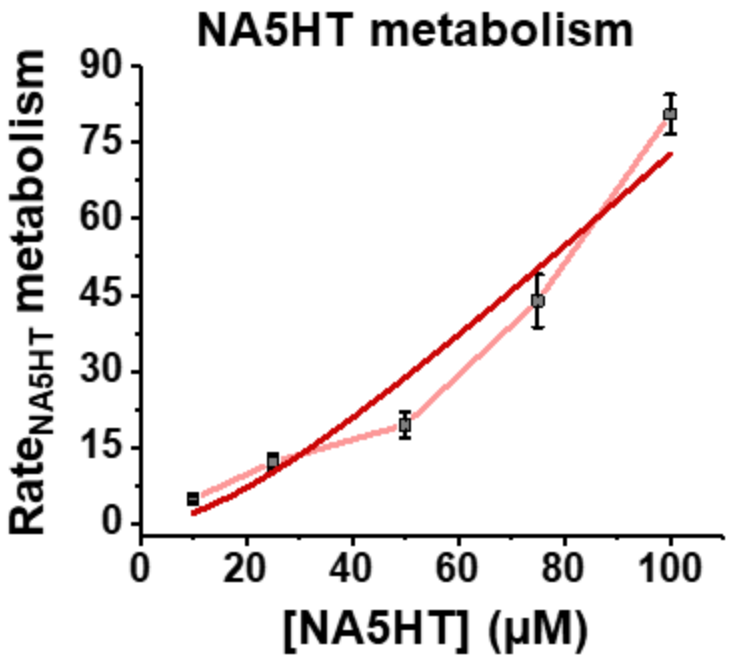

Supplementary Figure 5.30. NA5HT metabolism data fitted to a two-site (Equation 4) binding equation as detailed in the Results section.

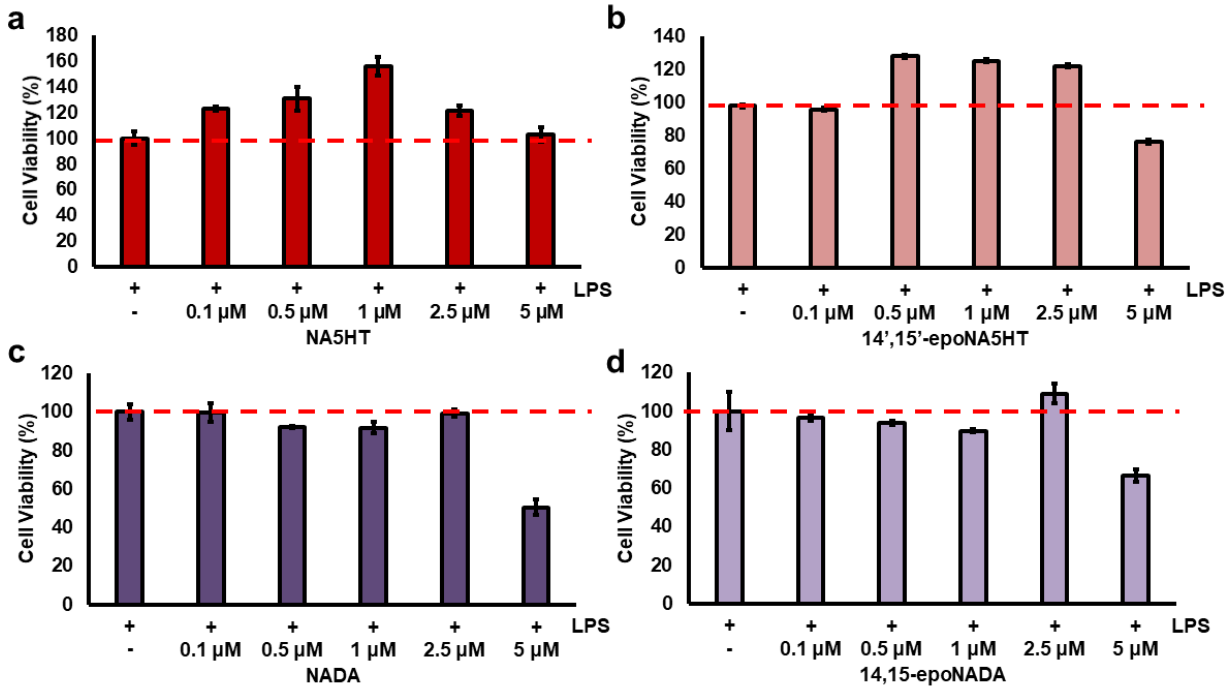

Supplementary Figure 5.31. *MTT assay to determine cell viability*. BV2 microglial cells seeded at 200,000 cells/well in a 24-well plate were treated with 25 ng/mL LPS for 24 hours and an MTT cell proliferation assay was performed to determine cell viability. Viability was determined as a percent of the formazan absorbance at 570 nm compared to LPS treatment only (100%) in the presence of **(a)** NA5HT, **(b)** 14',15'-epoNA5HT, **(c)** NADA, and **(d)** 14',15'-epoNADA. Data represents the SEM of 3 independent experiments.

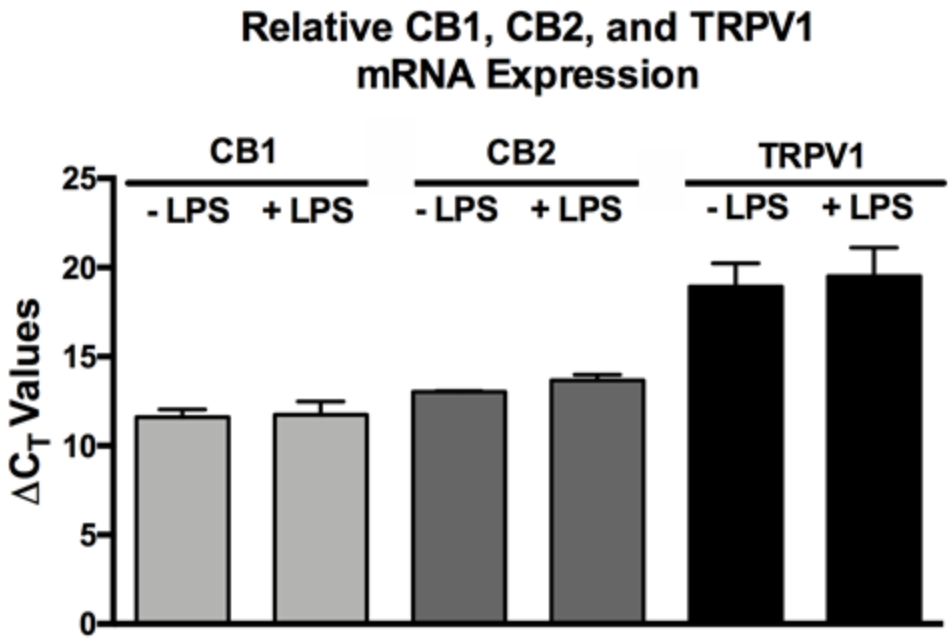

Supplementary Figure 5.32. Effect of *LPS in BV-2 microglial cells on the relative mRNA expression of CB1, CB2, and TRPV1*. BV-2 microglial cells seeded at 200,000 cells/well in a 24-well plate were treated with 25 ng/mL LPS for 24 hours. ΔCT values are inversely related to expression levels. Quantitative PCR showed no significant increase in TRPV1, CB1, or mRNA expression with LPS stimulation. Data is from 3 pooled wells and is performed in technical replicates.

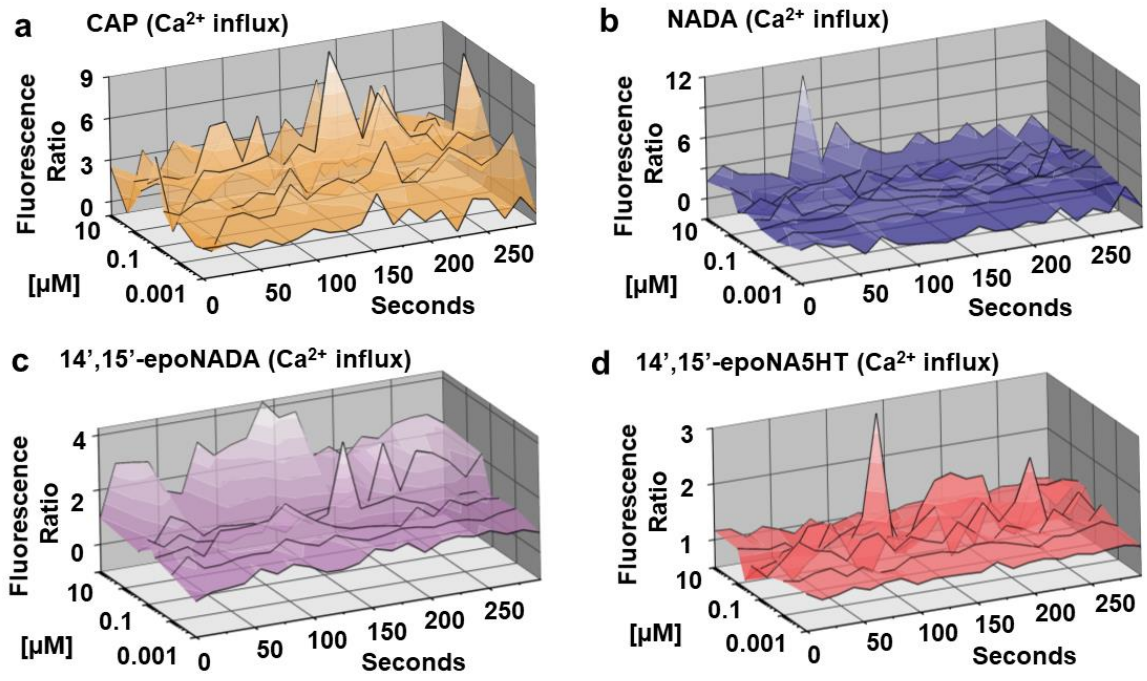

Supplementary Figure 5.33. *TRPV1 activation by vanilloids.* Relative Ca^{2+} influx upon TRPV1 activation was measured using a Fura-2 AM fluorescence assay. The fluorescence intensity at 510 nm from the Ca^{2+}-bound (excitation 340 nm) and Ca^{2+}-free (excitation 380 nm) dye was measured over time at varying concentrations of ligands and are reported as a ratio (Fluorescence Ratio). Representative plots of **(a)** Capsaicin (CAP), **(b)** NADA, **(c)** 14',15'-epoNADA, and **(d)** 14',15'-epoNA5HT from 4-6 separate experiments (2 sets of triplicate on separate days) are shown.

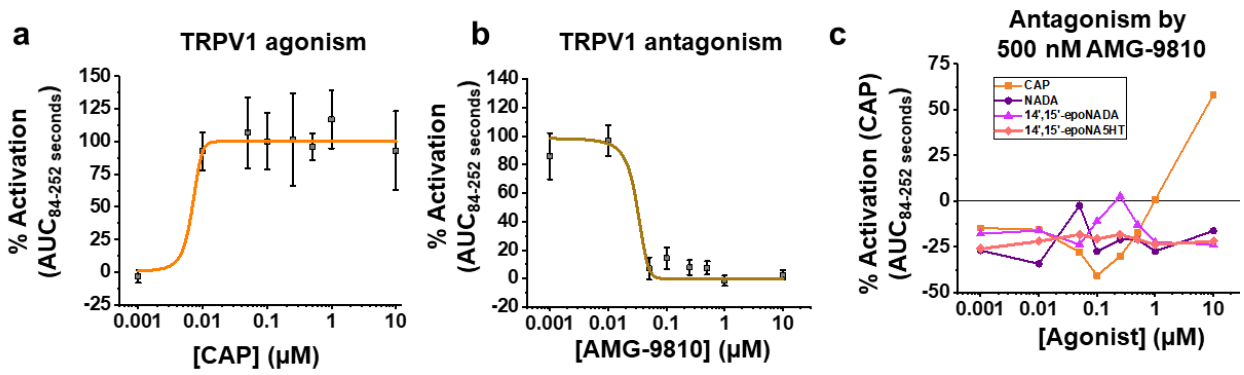

Supplementary Figure 5.34. *TRPV1-mediated Ca^{2+} influx agonized by CAP and antagonized by AMG-9810.* A Fura 2-AM fluorescence assay was used to determine TRPV1 binding in transfected HEK cells. 100% is defined as the B_{max} of CAP binding. **(a)** CAP agonism data. **(b)** Antagonism of TRPV1 by AMG-9810. 250 nM of CAP was used to activate TRPV1. Data in **(a-b)** is shown as the SEM of 4-6 experiments (2 sets of triplicate performed on separate days). **(c)** HEK-TRPV1 cells were treated with 500 nM of reversible antagonist AMG-9810 30 min prior to stimulating with the indicated agonists. AMG-9810 prevented agonism of TRPV1 for all compounds. Data represents the SEM of 3 independent experiments.

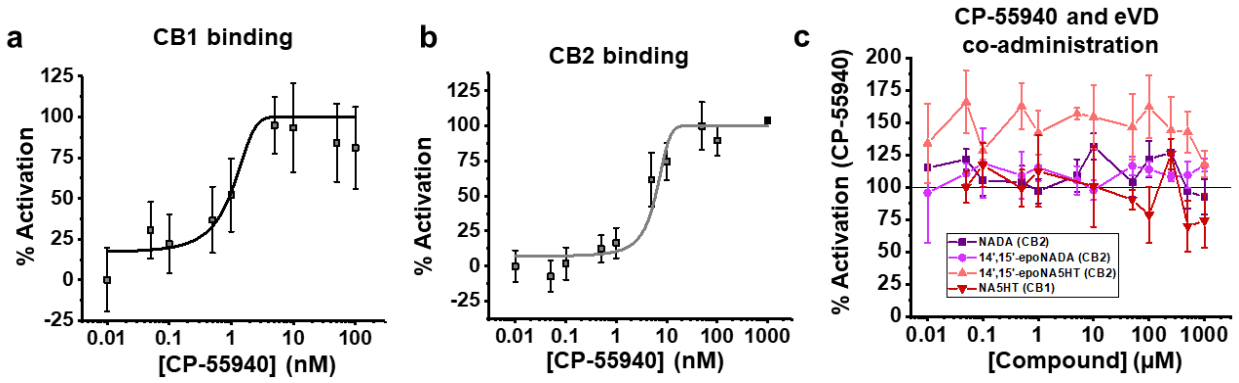

Supplementary Figure 5.35. *PRESTO-Tango assays of CB1 and CB2 binding.* **(a)** Agonism of CB1 and **(b)** CB2 by CP-55940. Data respresents the SEM of 4-6 separate experiments (2 sets of triplicates from separate days). **(c)** Co-administration of eVDs and CP-55940 to determine eVD binding to CB1 and 2. CB1 and CB2 were stimulated with 50 nM of CP-55940 to determine antagonism by NADA (CB2), 14',15'-epoNADA (CB2), 14',15'-epoNA5HT (CB2), and NA5HT (CB1). 100% is defined as the B_{max} of CP-55940 binding. Data represents the SEM of 3 independent experiments.

Tables

Supplementary Table 5.1. Primers for Quantitative Polymerase Chain Reaction

Gene	Forward Primer (5' → 3')	Reverse Primer (5' → 3')	Reference
Cyp2j9	AACCGTTTCCCCAGTCAGTC	ATTGCACGCACTCTCTGTCA	[399]
Cyp2j12	ATGGAAGACAGCCAAGCACA	AGCCAGTGTGCTATCAGCTG	(designed in-house)
Il-6	CCAGAGATACAAAGAAATGATGG	ACTCCAGAAGACCAGAGGAAAT	[414]
Il-10	CATGGCCCAGAAATCAAGGA	GGAGAAATCGATGACAGCGC	[414]
Cnr1	TGAAGTCGATCTTAGACGGCC	GTGGTGATGGTACGGAAGGTA	[415]
Cnr2	TGAATGAGCAGACCGACA GG	AGAGATGTTTGCTGG GTGGC	[415]
Trpv1	TCGTCTACCTCGTGTTCTTGTTTG	CCAGATGTTCTTGCTCTCTTGTGC	[416]
Gapdh	TCACCACCATGGAGAAGGC	GCTAAGCAGTTGGTGGTGCA	[417]

Supplementary Table 5.2. LC-MS/MS metabolite identification

Substrate	Product	Formulae	m/z (+) m/z (-)	Retention Times (Min)	Metabolite ID
NADA	Parent	$C_{28}H_{41}NO_3$	440.3159 438.3014	55.4	
	-O	$C_{28}H_{41}NO_4$	456.3108 454.2963	41.6; 42.6; 44.6; 45.6; 47.8; 49.0; 49.6; 52.6	PD1-PD8
	$-O_2$	$C_{28}H_{41}NO_5$	472.3057 470.2912	48.8 53.0	PD9 & PD10
	-HQ	$C_{28}H_{39}NO_4$	454.2952 452.2806	46.3	PD11
NA5HT	Parent	$C_{30}H_{42}N_2O_2$	463.3319 461.3174	55.6	
	-O	$C_{30}H_{42}N_2O_3$	479.3268 477.3122	42.4; 48.3; 52.4; 54.1	PS1-PS4
	$-O_2$	$C_{30}H_{42}N_2O_4$	495.3217 493.3072	50.5	PS5
	-Q	$C_{30}H_{40}N_2O_3$	477.3112 475.2969	54.7 56.8	PS6 & PS7
CAP	Parent	$C_{18}H_{27}NO_3$	306.2064 304.1918	39.5	
	-*O*-de-CH_3	$C_{17}H_{25}NO_3$	292.1907 290.1762	36.7	PC1
	-O	$C_{18}H_{27}NO_4$	322.2013 320.1867	25.6 26.6	PC2 & PC3
	$-O_2$	$C_{18}H_{27}NO_5$	338.1962 336.1816	20.3	PC4
	-HQ	$C_{17}H_{23}NO_4$	306.1700 304.1554	23.8	PC5

Supplementary Table 5.3. Binding interaction energies for AEA and NADA in Configure 1.

AEA

Residue	Interaction energy (kJ/mol)	Error (±kJ/mol)
ARG321	-8.92481	3.47937
ARG495	-4.72929	1.37637
ARG484	-3.76565	5.08937
ASN185	-3.6608	0.91729
LEU215	-3.13021	0.90826
HIS494	-3.10337	2.63799
HIS181	-2.99208	1.25837
SER493	-2.98903	1.15341
PRO491	-2.91059	2.22862
TRP322	-2.7051	1.87051
VAL492	-2.34359	0.69187
LEU212	-2.29354	0.802
THR313	-2.29139	0.656
LEU481	-2.25677	2.00732
LEU496	-1.88488	0.98401
SER480	-1.76965	1.92706
THR219	-1.65714	0.72366
ASP216	-1.53383	0.59384
PHE483	-1.15568	1.16863

NADA

Residue	Interaction energy (kJ/mol)	Error (±kJ/mol)
ILE489	-3.25625	0.96471
GLU222	-2.81904	7.20851
THR114	-2.64145	1.26045

Supplementary Table 5.3 cont.

ILE127	-2.4887	0.672
THR488	-2.42929	1.62007
PHE310	-2.33006	0.68078
ASN231	-2.13378	1.40423
ILE487	-2.12379	1.17521
ARG117	-2.0808	1.03731
MET400	-2.0443	0.97651
ILE86	-1.86892	0.99568
VAL380	-1.86384	0.53806
ALA311	-1.75345	0.60574
MET128	-1.71349	0.69304
PRO381	-1.52613	0.65021
LEU83	-1.51171	0.79452
GLN228	-1.16917	1.08287
GLU314	-1.15822	0.47136
THR315	-0.98946	0.40637

Supplementary Table 5.4. Binding interaction energies for AEA and NADA in Configure 2.

AEA

Residue	Interaction energy (kJ/mol)	Error (±kJ/mol)
ILE487	-5.89876	1.21444
GLN228	-5.83744	2.55033
GLY486	-4.4337	0.85385
ILE489	-3.73012	1.80267
THR488	-2.86717	1.23994
LEU83	-2.66672	1.22142
PRO381	-2.01531	0.5883
MET400	-1.92187	0.59975
ARG111	-1.86332	0.65592
PHE61	-1.76106	0.70389
PRO112	-1.56523	0.63967
THR114	-1.38301	0.59581
VAL380	-1.31937	0.42989
LEU81	-1.29664	0.75077
ILE86	-1.23497	0.69801
ASN231	-1.23156	0.70985
GLU82	-1.21236	0.75533
ILE127	-0.93357	0.4817
MET485	-0.90994	0.50495

NADA

Residue	Interaction energy (kJ/mol)	Error (±kJ/mol)
ASP307	-24.8669	9.39773
PHE310	-5.45818	1.08501
SER490	-4.84377	2.57133

Supplementary Table 5.4 cont.

ILE489	-3.81991	1.27441
ALA311	-2.55907	0.64457
GLU222	-2.43978	6.04616
THR315	-2.4274	0.79848
GLU314	-1.99078	0.60895
ILE127	-1.74117	0.56921
VAL380	-1.56889	0.67457
ILE376	-1.45199	0.64053
ILE375	-1.40588	0.55081
THR318	-1.24705	0.4895
TRP251	-1.15856	0.49279
PHE121	-1.06322	0.47599
THR219	-0.99602	0.86035
PRO491	-0.87034	0.55172
LEU126	-0.76823	0.67118
ARG111	-0.72046	0.51937

Supplementary Table 5.5. Binding interaction energies for AEA and NA5HT in Configure 1.

AEA

Residue	Interaction energy (kJ/mol)	Error (±kJ/mol)
ARG321	-21.757	3.21232
TRP322	-4.69984	1.39869
PRO491	-4.12342	1.47182
ARG495	-3.77759	1.6088
VAL492	-3.66875	0.78594
SER493	-2.94951	0.78101
ASN185	-2.82361	0.97184
THR318	-2.74648	0.88867
LEU215	-2.29793	0.59603
LEU496	-2.1508	0.48536
THR219	-1.81981	0.54936
ASP216	-1.45737	0.6174
THR313	-1.44611	0.63856
HSD181	-1.23107	0.92312
LEU212	-1.22474	0.5249
SER317	-1.13683	0.42019
SER480	-1.12392	0.50546
SER490	-1.05437	0.5769
LEU325	-0.94713	0.42667

NA5HT

Residue	Interaction energy (kJ/mol)	Error (±kJ/mol)
GLU222	-5.78558	3.11688
THR488	-3.52051	2.94825
ILE489	-3.40178	1.07731

Supplementary Table 5.5

VAL380	-3.0252	0.61197
GLN228	-3.00795	2.10628
ARG117	-2.86239	1.37033
THR114	-2.8041	0.76497
ARG111	-2.58118	0.899
ILE127	-2.16936	0.67201
ASN231	-1.96704	0.91609
PRO112	-1.8457	0.72025
PHE310	-1.78344	0.73298
ALA311	-1.49405	0.50818
PRO381	-1.43143	0.66267
SER490	-1.38003	0.99802
MET400	-1.26626	0.51045
ILE487	-1.22545	1.01001
THR315	-1.11141	0.64492
GLY486	-1.00512	0.58716

Supplementary Table 5.6. Binding interaction energies for AEA and NA5HT in Configure 2.

AEA

Residue	Interaction energy (kJ/mol)	Error (±kJ/mol)
GLN228	-6.5189	1.61495
ILE487	-6.4654	1.07545
GLY486	-5.05945	0.69118
ASN231	-3.30921	1.13293
THR488	-2.75129	0.70766
MET400	-2.60969	0.64574
LEU83	-2.51603	0.82828
ILE86	-2.41382	0.70615
ILE489	-2.06282	0.60377
PHE61	-1.61387	0.53751
GLU222	-1.59248	1.60739
LEU81	-1.54611	0.58844
SER490	-1.37099	0.95213
GLU82	-1.32141	0.53585
ALA88	-1.07485	0.34869
MET485	-1.04278	0.39769
ALA223	-1.02855	0.51492
THR114	-1.0283	0.63714
VAL232	-0.97153	0.50219

NA5HT

Residue	Interaction energy (kJ/mol)	Error (±kJ/mol)
ARG117	-4.62722	1.01273
PHE310	-4.25033	0.78785
ILE489	-3.79065	0.7503

Supplementary Table 5.6

PRO112	-3.53451	2.60917
ILE127	-3.16155	0.66233
VAL380	-3.0195	0.73603
ARG111	-2.8175	0.86368
ALA311	-2.54837	0.69605
GLU314	-2.41186	0.5614
THR315	-2.06731	0.79649
THR114	-1.5682	0.61104
ILE376	-1.48917	0.57733
THR318	-1.26557	0.42192
ILE375	-1.19388	0.4528
GLU222	-0.95049	0.97809
VAL113	-0.87465	0.51344
SER490	-0.83479	0.43952
THR488	-0.62754	0.11655
PRO491	-0.60725	0.5804

Chapter 6: Concluding remarks and future directions

Some CYPs have evolved to perform specialized functions in the body, such as vitamin synthesis and steroidogenesis. Other CYPs, such as those involved in drug metabolism, have been purposed by evolution to metabolize a pool of substrates and do not bind specific substrates. As a result, substrate recognition by these CYPs is often complicated by the binding of multiple ligands. CYP epoxygenases spearhead an important biosynthetic pathway, and because their promiscuity gives rise to complex substrate-substrate interactions, it is important to understand ligands may affect their lipid metabolism. Understanding these interactions can give valuable insight into drug develop that either potentiates or avoids interfering with their endogenous activity. Furthermore, the regulation of CYP epoxygenases may occur through the direct binding of other endogenous ligands. Based on the findings from Chapters 2-5, we can create a map of binding sites to CYP2J2 and understand how ligand binding can affect substrate metabolism at each site (Figure 6.1).

6.1 Ligand binding sites in CYP2J2

The catalytic site. CYP substrates must bind proficiently near the heme in order to be oxidized. The heme forms the roof of the active site buried within the protein and is positioned between the substrate access channel and the PUFA binding pocket. The binding of substrates to the substrate access channel and the PUFA binding pocket will determine how they bind into the catalytic site. It is generally accepted that substrates must bind a distance less than 5 Å from the heme for an efficient catalysis to occur. Certain substrates such as ebastine will bind conformationally constrained near the heme of CYP2J2, providing only one site for metabolism. The constrained binding of ebastine also allows it to be more efficiently metabolized. Substrates that bind fluidly, such as AA, present multiple sites of metabolism to the heme. Owing to their malleability, these substrates are especially susceptible to direct ligand-induced conformational changes resulting in altered sites of metabolism.

The substrate access channel. CYPs have a putative substrate access channel, in which substrates also bind to be metabolized. This channel is gated at the protein-membrane interface and leads towards the heme. Ebastine and terfenadine have been shown to bind to the substrate access channel[298,418], and our studies (Chapter 3) confirm that this is the binding site for ebastine.

Clusters 1-3 of the PUFA molecular dynamics simulations (Chapter 2) are all within this channel. PUFA binding is mostly governed by hydrophobic interactions with residues lining the channel. Similarly, AEA binds the substrate access channel with the headgroup interacting with Q228 (Chapter 5). Endovanilloids bind preferentially to this channel, albeit weakly and in a non-productive confirmation for epoxidation (Chapter 5).

The PUFA binding pocket. In addition to the substrate access channel, substrates, notably PUFAs, can bind into a pocket next to the heme and substrate access channel. PUFAs form specific interactions to this site and have a higher binding affinity than binding to the substrate access channel, and as such we have termed this site as the PUFA binding pocket (Chapter 2). When PUFAs bind this site, they are bound in a conformation that facilitates terminal oxidation of the acyl chain. R321 forms ionic interactions with the carboxyl head of the PUFAs and greatly directs their binding to the active site. The headgroup of anandamide also forms stable hydrogen bonds with R321 (Chapter 5). Along with R321, T318 and S493 triangulate the carboxyl headgroup of PUFAs further stabilizing their binding. Mutating these residues undermines the binding of PUFAs to CYP2J2 (Chapter 2). Other residues may contribute to the binding of specific substrates, such as R484, which facilitates the egression of EPA from the active site.

6.2 Effects of multiple ligands binding to CYP2J2

The similarities between the structures and binding positions of substrates will overall determine substrate-substrate interactions. The binding sites, binding affinities, and structures of PUFAs are very similar to each other and likely explains their competitive binding to CYP2J2 (Chapter 2). Likewise, ebastine binds tightly to the substrate access channel and competes with PUFA binding. However, since it is also sufficiently overlaps the heme site, it prevents PUFAs binding to the PUFA binding pocket (Chapter 3). Doxorubicin occupies much of active site volume and therefore shuts down substrate binding to CYP2J2 (Chapter 3). The binding sites of CYP2J2 overlap significantly and many substrates occupy a majority of the active site volume. It is likely, therefore, that a majority of substrate-substrate interactions are competitive.

Ligands that do not share similar binding sites may concurrently bind and effect substrate metabolism. 7-deoxydoxorubicin aglycone is a highly compact and rigid polycyclic compound that binds the PUFA binding pocket. However, since it does not fully occlude the active site, AA

is capable of binding to CYP2J2 concurrently with 7-deoxydoxorubicin aglycone. This alters the positioning of AA and changes the preferred site of metabolism (Chapter 3). Phytocannabinoids also contain compact polycyclic structures, which minimizes their footprint in the CYP2J2 active site. Preliminary binding of Δ9-THC near the heme suggests that there is ample room for anandamide to bind concurrently to CYP2J2 (data not shown). This may help to explain the noncompetitive inhibition of anandamide metabolism by phytocannabinoids (Chapter 4). Finally, positive cooperativity is possible if the binding of a second ligand stabilizes the binding of the first ligand. Endovanilloids preferentially bind into the substrate access channel but have poor binding to the heme site. However, a second molecule, either anandamide or the endovanilloid itself, can stabilize endovanilloid binding near the heme (Chapter 5). It is therefore possible to develop drugs that which potentiate lipid metabolism by promoting a productive conformation of the substrate in the CYP2J2. For example, a drug could bind into the substrate access channel, promoting PUFA binding to the PUFA binding pocket and positioning the 14,15 position more stably to the heme.

Overall, these data demonstrate that complex substrate-substrate interactions can occur in CYP2J2 and alter the metabolism of endogenous substrates. These data have implications for drug design, toxicity, and endogenous regulation. Importantly, these data confirm the notion that substrate interactions are specific to the analytes of the experiment. For example, 7-deoxydoxrubicin affects AA metabolism but does not affect ebastine metabolism. Furthermore, PUFAs display one-site binding and endovanilloids appear *prima facie* to be PUFA-like in their structure. A naïve assertion would be that they would, likewise, show one-site binding. However, endovanilloids differ greatly in their molecular interactions with CYP2J2 compared to PUFAs, namely that they do not bind the PUFA binding pocket and display cooperative two-site binding. Therefore, results obtained from a probe substrate cannot be directly translated to the substrate of interest and studies investigating the physiological impact of CYP2J2 activity must be conducted using the endogenous ligands.

6.3 Future directions: physiological differences among regioisomers and enantiomers of epoxide mediators

There has been a lot of focus on understanding the physiological effects of epoxide mediators from different lipids, e.g. epoxides of AA vs. DHA. However, the physiological effects of different regioisomers and enantiomers of epoxide mediators from the same lipid is poorly

understood. This is partly due to the difficulty of synthesizing and purifying the different regioisomers and especially the enantiomers of each epoxidation. Each site of unsaturation presents a unique site for epoxidation (regioselectivity). Additionally, each site can have two common enantiomers. Therefore, for every lipid with *n* sites of unsaturation there are 2*n* possible unique epoxide mediators that can be formed. Enantiomer effects of compounds have been well documented throughout biochemistry, which is often mediated by how receptors interact with each enantiomer. The quintessential example is thalidomide, in which the *S*- enantiomer is teratogenic whereas the *R*- enantiomer is safer. Due to the relative nonspecificity of CYPs compared to other enzymes, changes in the regio- and enantioselectivity of CYP metabolism may occur through substrate-substrate interactions or through polymorphic variance. For example, 7-deoxydoxorubicin alters the site of AA metabolism by CYP2J2, and it is reasonable that if the binding position of AA is altered then perhaps the enantioselectivity is also altered. These changes in the positioning of the epoxide can therefore have profound effects on the downstream signaling mechanisms and is an area that should be investigated further.

6.3.1 Synthetic and quantification methods for epoxide enantiomers

Synthesizing racemic mixtures of epoxide regioisomers can be done in a one-pot synthesis using *m*-chloroperoxybenzoic acid[163]. However, this method produces a mixture of oxygenated products, including different regioisomers and di-oxygenated products. Methods have been developed to achieve regioselective epoxidation of the terminal alkene, such as using urea hydrogen peroxide to produce 14,15-EET[419] and using a hydrogen peroxide intermediate on the PUFA to produce[420].

Achieving enantioselective methods is more difficult than racemic mixtures. One method for producing enantioselective epoxide mediators is through directed evolution of enzymes. CYP-BM3 (BM3) metabolizes PUFAs with high turnover rate and often produces highly optically pure metabolites. From AA, BM3 produces mostly 18-HETE as the product with a minor production of 14,15-EET. However, BM3-F87V is a mutant that increases the terminal epoxidation of PUFAs and produces 14(S),15(R)-EET as 99% of the total metabolites from AA and has been used for the enantioselective epoxidation of PUFAs and other organic molecules[421-423]. Organic synthetic methods have also been developed to achieve enantio- as well as regioselectivity. Many methods have been developed by Falck and coworkers for the total synthesis of epoxide enantiomers. These

include using dimethyl D- or L-malate to produce 8,9- and 11,12-EET enantiomers[424]; and 14(R),15(S)-EET from methyl furanoside and 5,6-EET enantiomers from methyl furanoside but with different lactone opening methods[425]. Falck and coworkers have also developed enatioselective epoxidation methods using semi-total synthesis methods[426,427].

Determining the enantiomer of an unknown epoxide can be achieved through common chemistry methods such as circular dichroism and NMR. However, these procedures can only be reasonably performed on synthesized compounds in high quantity. Measuring the enantiomers from biochemical or pharmacological samples is a much more difficult task due to the limited quantities of the epoxides present, in addition to these samples often containing a heterogeneous mixture of various oxygenated products. For these samples, the best method is LC-MS/MS detection and using chiral columns to separate the enantiomers. Various chiral columns are capable of separating epoxide enantiomers of small organic compounds[428]. However, the separation of PUFA epoxides often requires chemical derivation to facilitate enantiomer separation[429]. EETs can be converted to a methyl ester analogue, followed by conversing to a HETE analogue and modified with a dehydroabiethylisocyanate group[430]. Alternatively, they can be converted to pentafluorobenzyl ester derivatives or methyl esters, and analyzed directly or using radiolabeled PUFA[431-433].

6.3.2 Regio- and enantioselectivity of epoxygenases

Seminal work on CYP2C8's epoxygenase activity by Zeldin, et al.[434] showed that the regioselectivity of AA epoxidation by recombinant CYP2C8 was 48% 14,15-EET and 52% 11,12-EET. 8,9-EET and 5,6-EET were not detected. CYP2C8 showed a remarkable optical purity for its metabolism of AA, with the (R,S):(S,R) configuration being 82:18 for both 14,15-EET and 11,12-EET. Daikh, B. E., et al.[435] reported similar results for CYP2C8. For CYP2C9, they also reported that 14,15-EET; 11,12-EET; and 8,9-EET were produced in a ratio of 2.3:1:0.5, respectively. CYP2C9 was less enantioselective than CYP2C8, producing the regioisomers with an (R,S):(S,R) ratio of 62.5:37.5 for 14,15-EET and 30.5:69.4 for 11,12-EET. The enantioselectivity of 8,9-EET was not investigated. Of note, the enantioselectivity of CYP2C9 is opposite that of CYP2C8 at the 11,12- position. In regards to the epoxidation of EPA at the 17,18 position, CYP2C8 and CYP2C9 also displayed opposite enantioselectivity. The (R,S):(S,R) ratio

was 28:72 for CYP2C8 and 68:32 for CYP2C9[436]. CYP2C8 was also shown to have about a similar (~30:70) (R,S):(S,R) selectivity for the terminal epoxidation of DHA[433].

Evidence towards the fact that CYP2J2 is the primary epoxygenase of the heart comes from comparing the EETs produced by recombinant CYP2J2 and the EETs produced in the human heart. In the seminal work identifying CYP2J2 as an epoxygenase, Wu, et al.[196] reported that the regioselectivity of AA epoxidation by CYP2J2 was 37% 14,15-EET; 18% 11,12-EET; 24% 8,9-EET; and 21% for 5,6-EET. The enantioselectivity, (R,S):(S,R), was 74:26 for 14,15-EET; 49:51 for 11,12-EET; and 47:53 for 8,9-EET (5,6-EET was not determined). Therefore, CYP2J2 is less enantioselective for its AA epoxidation compared to CYP2C8 or CYP2C9. The reported regioselectivity from human heart samples was 39% 14,15-EET; 24% 11,12-EET; and 37% 8,9-EET (5,6-EET was not determined). The corresponding enantioselectivity was 63:37 for 14,15-EET; 44:56 for 11,12-EET; and 43:57 for 8,9-EET. The authors concluded that since the regioselectivity and importantly enantioselectivity of CYP2J2 closely match those of EETs obtained from heart tissues, CYP2J2 must be the predominant epoxygenase of the heart. CYP2J2 was also shown to have an enantioselectivity for the terminal epoxidation of EPA and DHA of about 60:40[433]. We determined that the regioselecitivity of CYP2J2-D34 (a 34-residue N-terminal truncation used for *E. coli* expression) for AA was 49% 14,15-EET; 25% 11,12-EET; 16% 8,9-EET; and 9% for 5,6-EET[289,404]. In the presence of 7-deoxydoxorubicin, the regioselectivity is significantly altered to 42% 14,15-EET; 26% 11,12-EET; 21% 8,9-EET; and 13% for 5,6-EET[404]. This is the first and only reported change in regioselectivity induced directly by the binding of a ligand to an epoxygenase.

6.3.3 Regio- and enantioselective effects on downstream signaling

Many biological studies do not investigate all regioisomers of epoxides, which makes cross-comparisons difficult. Nevertheless, there are distinct functions among the different regioisomers. Much more is known regarding the effects of the different EETs. One of the most pronounced differences is that 5,6-EET and 8,9-EET are COX substrates and have been shown to exhibit pro-inflammatory responses, in contrast to 11,12-EET and 14,15-EET, which are not COX-2 substrates[292,293]. 11,12-EET was found to most potently decrease TNF-α levels in human endothelial cells, with 5,6-EET being the weakest; 14,15-EET had no effect[42]. Regarding cardioprotection, 11,12- and 14,15-EET reduce myocardial infarct size, whereas 8,9-EET did

not[68]. Further, it was shown that 5,6-EET increases the beating rate of neonatal cardiomyocytes, which was suggested to be through its conversion to 5,6-epoxythromboxane A1[437,438]. Although each regioisomer can regulate similar physiological responses, differences exist by which downstream pathway is activitated. Proliferation is mediated by 8,9-EET and 11,12-EET through the p38 MAPK pathway, whereas 5,6-EET and 14,15-EET mediate proliferation through the PI3K pathway[310]. Activation of ion channels is another important function of EETs. Hyperpolarization of the membrane results in the release of hyperpolarization factors that dilate blood vessels. 11,12-EET has been shown to be the most effective at activating Ca^{2+}-activated potassium channels, which is mediated by the putative unknown EET receptor[61,439]. TRPV4 is activated both by 5,6-EET and 8,9-EET, which influxes Ca^{2+} and leads to vasodilation[64,65,440]. The preference of EETs as substrates of sEH, the main degradative enzyme of EETs, are 14,15-EET > 11,12-EET > 8,9-EET > 5,6-EET with an enantioselectivity of 14(R),15(S)-EET, 11(S),l2(R)-EET, and 8(S),9(R)-EET[441]. Finally, regarding activation of the putative unknown EET receptor, 14,15-EET was shown to bind similarly, albeit slightly better, compared to 11,12-EET, and 8,9-EET had a much weaker affinity[78].

Not much is currently known regarding the biological effects of epoxide enantiomers, likely due to the difficulty of synthesizing and detecting them. Many of the downstream effects of EETs are thought to be mediated by the putative unknown EET receptor. Although the identity of the receptor is yet to be elucidated, the receptor is known to exhibit enantioselectivity. 14(R),15(S)-EET was about twice as effective than 14(S),15(R)-EET at displacing [^{3}H]-14,15-EET from U-937 cell membranes[77]. In a competitive binding assay to guinea pig monocytes, 14(R),15(S)-EET (K_i = 226.3 nM) inhibited [^{3}H]-14,15-EET binding more effectively than 14(S),15(R)-EET or 11(R),12(S)-EET ($K_i \approx$ 600 nM)[75]. Translocation of TRPC6-V5 fusion protein and angiogenesis were stimulated by racemic 11,12-EET and 11(R),12(S)-EET, but not by 11(S),12(R)-EET[63]. These effects were eliminated by knocking down $G_{\alpha s}$, thus suggesting that these effects are mediated by the putative EET receptor[63].

Enantiomer differences have been mostly observed concerning cardiovascular function. Vasodilatory effects on bovine arteries were shown to be stronger with 14(S),15(R)-EET than 14(R),15(S)-EET[80], which is the opposite selectivity exhibited by the [^{3}H]-14,15-EET binding assays of the putative EET receptor. Minor effects of 14,15-EET enantiomers were also observed

with canine or porcine coronary arterioles, though overall there were not any significant differences observed among regioisomers or enantiomers in the study, even from different PUFAs[442]. Interestingly, (R,S)- or (S,R)-11,12-EET were shown to be equally effective in canine arterioles, but 11(S),12(R)-EET was slightly (but not significantly) more effective in porcine arterioles[442]. 11(S),12(R)-EET was shown to inhibit rat epithelial sodium channel, but 11(R),12(S)-EET was ineffective[443]. Contrariwise, 11(R),12(S)-EET was more effective at activating Ca^{2+}-activated potassium channels in rat renal arteries[444]. Further effects on cardiac activity include 17(R),18(S)-EEQ, which was shown to be as equally anti-arrhythmic as racemic mixtures, whereas 17(S),18(R)-EEQ was ineffective[445]. Cardiovascular effects are known to occur via the putative endothelial receptor[8]. Though many of these enantiomers show the opposite selectivity of the putative EET receptor, it is possible that the putative receptor exhibits ligand bias similarly as seen with the cannabinoid receptors. The different enantiomers could perhaps control which pathway, inflammation vs. vascular, by inducing different conformational changes to the putative receptor. However, more studies would have to be performed in order to shape this hypothesis.

6.4 Figure

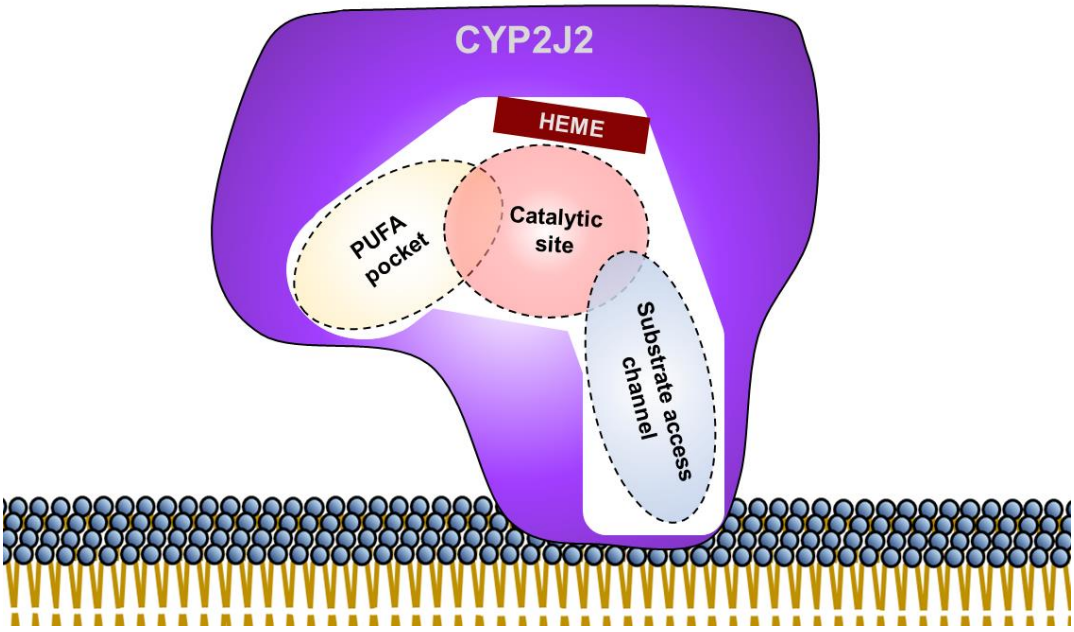

Figure 6.1. Stylized representation of the 3 binding sites of CYP2J2.

References

1 Spector, A. A. Arachidonic acid cytochrome P450 epoxygenase pathway. *Journal of Lipid Research* **50**, S52-S56, doi:10.1194/jlr.R800038-JLR200 (2009).

2 Brash, A. R. Arachidonic acid as a bioactive molecule. *J Clin Invest* **107**, 1339-1345, doi:Doi 10.1172/Jci13210 (2001).

3 Spector, A. A. & Kim, H. Y. Cytochrome P450 epoxygenase pathway of polyunsaturated fatty acid metabolism. *Biochim Biophys Acta* **1851**, 356-365, doi:10.1016/j.bbalip.2014.07.020 S1388-1981(14)00153-X [pii] (2015).

4 Cashman, J. N. The mechanisms of action of NSAIDs in analgesia. *Drugs* **52 Suppl 5**, 13-23 (1996).

5 Magazine, R., Shahul, H. A., Chogtu, B. & Kamath, A. Comparison of oral montelukast with oral zileuton in acute asthma: A randomized, double-blind, placebo-controlled study. *Lung India : official organ of Indian Chest Society* **33**, 281-286, doi:10.4103/0970-2113.180805 (2016).

6 Hwang, S. H., Wecksler, A. T., Wagner, K. & Hammock, B. D. Rationally designed multitarget agents against inflammation and pain. *Curr Med Chem* **20**, 1783-1799 (2013).

7 Spector, A. A., Fang, X., Snyder, G. D. & Weintraub, N. L. Epoxyeicosatrienoic acids (EETs): metabolism and biochemical function. *Prog Lipid Res* **43**, 55-90 (2004).

8 Xu, X., Zhang, X. A. & Wang, D. W. The roles of CYP450 epoxygenases and metabolites, epoxyeicosatrienoic acids, in cardiovascular and malignant diseases. *Adv Drug Deliv Rev* **63**, 597-609, doi:10.1016/j.addr.2011.03.006 S0169-409X(11)00054-8 [pii] (2011).

9 Harris, T. R., Li, N., Chiamvimonvat, N. & Hammock, B. D. The potential of soluble epoxide hydrolase inhibition in the treatment of cardiac hypertrophy. *Congestive heart failure* **14**, 219-224 (2008).

10 Yokoyama, C. & Tanabe, T. Cloning of human gene encoding prostaglandin endoperoxide synthase and primary structure of the enzyme. *Biochem Biophys Res Commun* **165**, 888-894 (1989).

11 Funk, C. D., Funk, L. B., Kennedy, M. E., Pong, A. S. & Fitzgerald, G. A. Human platelet/erythroleukemia cell prostaglandin G/H synthase: cDNA cloning, expression, and gene chromosomal assignment. *FASEB journal : official publication of the Federation of American Societies for Experimental Biology* **5**, 2304-2312 (1991).

12 Xie, W. L., Chipman, J. G., Robertson, D. L., Erikson, R. L. & Simmons, D. L. Expression of a Mitogen-Responsive Gene Encoding Prostaglandin Synthase Is Regulated by Messenger-Rna Splicing. *P Natl Acad Sci USA* **88**, 2692-2696, doi:DOI 10.1073/pnas.88.7.2692 (1991).

13 Vane, J. R., Bakhle, Y. S. & Botting, R. M. Cyclooxygenases 1 and 2. *Annual review of pharmacology and toxicology* **38**, 97-120, doi:10.1146/annurev.pharmtox.38.1.97 (1998).

14 Simmons, D. L., Botting, R. M. & Hla, T. Cyclooxygenase isozymes: the biology of prostaglandin synthesis and inhibition. *Pharmacol Rev* **56**, 387-437, doi:10.1124/pr.56.3.3 (2004).

15 Ricciotti, E. & FitzGerald, G. A. Prostaglandins and inflammation. *Arterioscler Thromb Vasc Biol* **31**, 986-1000, doi:10.1161/ATVBAHA.110.207449 (2011).

16 Smyth, E. M., Grosser, T., Wang, M., Yu, Y. & FitzGerald, G. A. Prostanoids in health and disease. *J Lipid Res* **50 Suppl**, S423-428, doi:10.1194/jlr.R800094-JLR200 (2009).
17 Smyth, E. M. Thromboxane and the thromboxane receptor in cardiovascular disease. *Clinical lipidology* **5**, 209-219, doi:10.2217/clp.10.11 (2010).
18 Tilley, S. L., Coffman, T. M. & Koller, B. H. Mixed messages: modulation of inflammation and immune responses by prostaglandins and thromboxanes. *J Clin Invest* **108**, 15-23, doi:10.1172/JCI13416 (2001).
19 Kawahara, K., Hohjoh, H., Inazumi, T., Tsuchiya, S. & Sugimoto, Y. Prostaglandin E2-induced inflammation: Relevance of prostaglandin E receptors. *Biochim Biophys Acta* **1851**, 414-421, doi:10.1016/j.bbalip.2014.07.008 (2015).
20 Nakanishi, M. & Rosenberg, D. W. Multifaceted roles of PGE2 in inflammation and cancer. *Seminars in immunopathology* **35**, 123-137, doi:10.1007/s00281-012-0342-8 (2013).
21 Murata, T. & Maehara, T. Discovery of anti-inflammatory role of prostaglandin D2. *The Journal of veterinary medical science* **78**, 1643-1647, doi:10.1292/jvms.16-0347 (2016).
22 Malkowski, M. G. *et al.* Structure of eicosapentaenoic and linoleic acids in the cyclooxygenase site of prostaglandin endoperoxide H synthase-1. *J Biol Chem* **276**, 37547-37555, doi:10.1074/jbc.M105982200 (2001).
23 Wada, M. *et al.* Enzymes and receptors of prostaglandin pathways with arachidonic acid-derived versus eicosapentaenoic acid-derived substrates and products. *J Biol Chem* **282**, 22254-22266, doi:10.1074/jbc.M703169200 (2007).
24 Obata, T., Nagakura, T., Masaki, T., Maekawa, K. & Yamashita, K. Eicosapentaenoic acid inhibits prostaglandin D2 generation by inhibiting cyclo-oxygenase-2 in cultured human mast cells. *Clin Exp Allergy* **29**, 1129-1135 (1999).
25 Bagga, D., Wang, L., Farias-Eisner, R., Glaspy, J. A. & Reddy, S. T. Differential effects of prostaglandin derived from omega-6 and omega-3 polyunsaturated fatty acids on COX-2 expression and IL-6 secretion. *Proc Natl Acad Sci U S A* **100**, 1751-1756, doi:10.1073/pnas.0334211100 (2003).
26 Rodriguez-Lagunas, M. J., Ferrer, R. & Moreno, J. J. Effect of eicosapentaenoic acid-derived prostaglandin E3 on intestinal epithelial barrier function. *Prostaglandins, leukotrienes, and essential fatty acids* **88**, 339-345, doi:10.1016/j.plefa.2013.02.001 (2013).
27 Ringbom, T. *et al.* Cox-2 inhibitory effects of naturally occurring and modified fatty acids. *Journal of natural products* **64**, 745-749 (2001).
28 Dong, L. *et al.* Different Fatty Acids Compete with Arachidonic Acid for Binding to the Allosteric or Catalytic Subunits of Cyclooxygenases to Regulate Prostanoid Synthesis. *J Biol Chem* **291**, 4069-4078, doi:10.1074/jbc.M115.698001 (2016).
29 Das, U. N. COX-2 inhibitors and metabolism of essential fatty acids. *Medical science monitor : international medical journal of experimental and clinical research* **11**, RA233-237 (2005).
30 Mashima, R. & Okuyama, T. The role of lipoxygenases in pathophysiology; new insights and future perspectives. *Redox biology* **6**, 297-310, doi:10.1016/j.redox.2015.08.006 (2015).
31 Haeggstrom, J. Z. & Funk, C. D. Lipoxygenase and leukotriene pathways: biochemistry, biology, and roles in disease. *Chemical reviews* **111**, 5866-5898, doi:10.1021/cr200246d (2011).

32 Dobrian, A. D. *et al.* Functional and pathological roles of the 12- and 15-lipoxygenases. *Prog Lipid Res* **50**, 115-131, doi:10.1016/j.plipres.2010.10.005 (2011).
33 Henderson, W. R., Jr. The role of leukotrienes in inflammation. *Annals of internal medicine* **121**, 684-697 (1994).
34 Powell, W. S. & Rokach, J. The eosinophil chemoattractant 5-oxo-ETE and the OXE receptor. *Prog Lipid Res* **52**, 651-665, doi:10.1016/j.plipres.2013.09.001 (2013).
35 Goetzl, E. J., Hill, H. R. & Gorman, R. R. Unique aspects of the modulation of human neutrophil function by 12-L-hydroperoxy-5,8,10,14-eicosatetraenoic acid. *Prostaglandins* **19**, 71-85 (1980).
36 Feltenmark, S. *et al.* Eoxins are proinflammatory arachidonic acid metabolites produced via the 15-lipoxygenase-1 pathway in human eosinophils and mast cells. *Proc Natl Acad Sci U S A* **105**, 680-685, doi:10.1073/pnas.0710127105 (2008).
37 Serhan, C. N. Pro-resolving lipid mediators are leads for resolution physiology. *Nature* **510**, 92-101 (2014).
38 Eickmeier, O. *et al.* Pro-resolving lipid mediator Resolvin D1 serves as a marker of lung disease in cystic fibrosis. *Plos One* **12**, doi:Artn E0171249 10.1371/Journal.Pone.0171249 (2017).
39 Chandrasekharan, J. A. & Sharma-Walia, N. Lipoxins: nature's way to resolve inflammation. *Journal of inflammation research* **8**, 181-192, doi:10.2147/JIR.S90380 (2015).
40 Fischer, R. *et al.* Dietary omega-3 fatty acids modulate the eicosanoid profile in man primarily via the CYP-epoxygenase pathway. *J Lipid Res* **55**, 1150-1164, doi:jlr.M047357 [pii] 10.1194/jlr.M047357 (2014).
41 Ozawa, T. *et al.* Biosynthesis of Leukotoxin, 9, 10-Epoxy-12 Octadecenoate, by Leukocytes in Lung Lavages of Rat after Exposure to Hyperoxia. *Biochemical and Biophysical Research Communications* **134**, 1071-1078, doi:Doi 10.1016/0006-291x(86)90360-8 (1986).
42 Node, K. *et al.* Anti-inflammatory properties of cytochrome P450 epoxygenase-derived eicosanoids. *Science* **285**, 1276-1279, doi:7768 [pii] (1999).
43 Roman, R. J. P-450 Metabolites of Arachidonic Acid in the Control of Cardiovascular Function. *Physiol Rev* **82**, 131-185, doi:10.1152/physrev.00021.2001 (2002).
44 Capdevila, J. H., Falck, J. R. & Harris, R. C. Cytochrome P450 and arachidonic acid bioactivation: molecular and functional properties of the arachidonate monooxygenase. *Journal of Lipid Research* **41**, 163-181 (2000).
45 Tunaru, S., Chennupati, R., Nusing, R. M. & Offermanns, S. Arachidonic Acid Metabolite 19(S)-HETE Induces Vasorelaxation and Platelet Inhibition by Activating Prostacyclin (IP) Receptor. *PLoS One* **11**, e0163633, doi:10.1371/journal.pone.0163633 (2016).
46 Fan, F. *et al.* Molecular mechanisms and cell signaling of 20-hydroxyeicosatetraenoic acid in vascular pathophysiology. *Frontiers in bioscience* **21**, 1427-1463 (2016).
47 Ishizuka, T. *et al.* 20-Hydroxyeicosatetraenoic acid stimulates nuclear factor-kappaB activation and the production of inflammatory cytokines in human endothelial cells. *J Pharmacol Exp Ther* **324**, 103-110, doi:10.1124/jpet.107.130336 (2008).
48 Kim, D. H. *et al.* Cyclooxygenase-2 dependent metabolism of 20-HETE increases adiposity and adipocyte enlargement in mesenchymal stem cell-derived adipocytes. *J Lipid Res* **54**, 786-793, doi:10.1194/jlr.M033894 (2013).

49 Escalante, B., Sessa, W. C., Falck, J. R., Yadagiri, P. & Schwartzman, M. L. Vasoactivity of 20-Hydroxyeicosatetraenoic Acid Is Dependent on Metabolism by Cyclooxygenase. *Journal of Pharmacology and Experimental Therapeutics* **248**, 229-232 (1989).

50 Schwartzman, M. L., Falck, J. R., Yadagiri, P. & Escalante, B. Metabolism of 20-Hydroxyeicosatetraenoic Acid by Cyclooxygenase - Formation and Identification of Novel Endothelium-Dependent Vasoconstrictor Metabolites. *Journal of Biological Chemistry* **264**, 11658-11662 (1989).

51 Pillarisetti, S. & Khanna, I. Targeting soluble epoxide hydrolase for inflammation and pain - an overview of pharmacology and the inhibitors. *Inflammation & allergy drug targets* **11**, 143-158 (2012).

52 Zhao, G. *et al.* Delivery of AAV2-CYP2J2 protects remnant kidney in the 5/6-nephrectomized rat via inhibition of apoptosis and fibrosis. *Human gene therapy* **23**, 688-699, doi:10.1089/hum.2011.135 (2012).

53 Bystrom, J. *et al.* Endogenous epoxygenases are modulators of monocyte/macrophage activity. *PLoS One* **6**, e26591, doi:10.1371/journal.pone.0026591 (2011).

54 Thomson, S. J., Askari, A. & Bishop-Bailey, D. Anti-inflammatory effects of epoxyeicosatrienoic acids. *Int J Vasc Med* **2012**, 605101, doi:10.1155/2012/605101 (2012).

55 Mitra, R. *et al.* CYP3A4 Mediates Growth of Estrogen Receptor-positive Breast Cancer Cells in Part by Inducing Nuclear Translocation of Phospho-Stat3 through Biosynthesis of (+/-)-14, 15-Epoxyeicosatrienoic Acid (EET). *Journal of Biological Chemistry* **286**, 17543-17559, doi:10.1074/jbc.M110.198515 (2011).

56 Williams, L., Bradley, L., Smith, A. & Foxwell, B. Signal transducer and activator of transcription 3 is the dominant mediator of the anti-inflammatory effects of IL-10 in human macrophages. *J Immunol* **172**, 567-576, doi:DOI 10.4049/jimmunol.172.1.567 (2004).

57 Zhang, G., Kodani, S. & Hammock, B. D. Stabilized epoxygenated fatty acids regulate inflammation, pain, angiogenesis and cancer. *Prog Lipid Res* **53**, 108-123, doi:10.1016/j.plipres.2013.11.003 (2014).

58 Schunck, W. H., Konkel, A., Fischer, R. & Weylandt, K. H. Therapeutic potential of omega-3 fatty acid-derived epoxyeicosanoids in cardiovascular and inflammatory diseases. *Pharmacol Ther* **183**, 177-204, doi:10.1016/j.pharmthera.2017.10.016 (2018).

59 Morin, C., Sirois, M., Echave, V., Albadine, R. & Rousseau, E. 17,18-Epoxyeicosatetraenoic Acid Targets PPAR gamma and p38 Mitogen-Activated Protein Kinase to Mediate Its Anti-inflammatory Effects in the Lung. *American Journal of Respiratory Cell and Molecular Biology* **43**, 564-575, doi:10.1165/rcmb.2009-0155OC (2010).

60 Campbell, W. B., Gebremedhin, D., Pratt, P. F. & Harder, D. R. Identification of epoxyeicosatrienoic acids as endothelium-derived hyperpolarizing factors. *Circ Res* **78**, 415-423 (1996).

61 Li, P. L. & Campbell, W. B. Epoxyeicosatrienoic acids activate K+ channels in coronary smooth muscle through a guanine nucleotide binding protein. *Circ Res* **80**, 877-884 (1997).

62 Yang, C., Kwan, Y. W., Seto, S. W. & Leung, G. P. Inhibitory effects of epoxyeicosatrienoic acids on volume-activated chloride channels in rat mesenteric arterial smooth muscle. *Prostaglandins Other Lipid Mediat* **87**, 62-67, doi:10.1016/j.prostaglandins.2008.08.003 (2008).

63 Ding, Y. *et al.* The biological actions of 11,12-epoxyeicosatrienoic acid in endothelial cells are specific to the R/S-enantiomer and require the G(s) protein. *J Pharmacol Exp Ther* **350**, 14-21, doi:10.1124/jpet.114.214254 (2014).

64 Berna-Erro, A. *et al.* Structural determinants of 5',6'-epoxyeicosatrienoic acid binding to and activation of TRPV4 channel. *Sci Rep* **7**, 10522, doi:10.1038/s41598-017-11274-1 (2017).

65 Watanabe, H. *et al.* Anandamide and arachidonic acid use epoxyeicosatrienoic acids to activate TRPV4 channels. *Nature* **424**, 434-438, doi:10.1038/nature01807 (2003).

66 Wang, H. *et al.* Up-regulation of endothelial nitric-oxide synthase by endothelium-derived hyperpolarizing factor involves mitogen-activated protein kinase and protein kinase C signaling pathways. *J Pharmacol Exp Ther* **307**, 753-764, doi:10.1124/jpet.103.052787 (2003).

67 Jiang, J. G. *et al.* Regulation of endothelial nitric-oxide synthase activity through phosphorylation in response to epoxyeicosatrienoic acids. *Prostag Oth Lipid M* **82**, 162-174, doi:10.1016/j.prostaglandins.2006.08.005 (2007).

68 Gross, G. J., Hsu, A., Falck, J. R. & Nithipatikom, K. Mechanisms by which epoxyeicosatrienoic acids (EETs) elicit cardioprotection in rat hearts. *J Mol Cell Cardiol* **42**, 687-691, doi:S0022-2828(06)01069-8 [pii] 10.1016/j.yjmcc.2006.11.020 (2007).

69 Guengerich, F. P. Cytochrome p450 and chemical toxicology. *Chem Res Toxicol* **21**, 70-83, doi:10.1021/tx700079z (2008).

70 Nithipatikom, K., Moore, J. M., Isbell, M. A., Falck, J. R. & Gross, G. J. Epoxyeicosatrienoic acids in cardioprotection: ischemic versus reperfusion injury. *Am J Physiol Heart Circ Physiol* **291**, H537-542, doi:00071.2006 [pii] 10.1152/ajpheart.00071.2006 (2006).

71 Oni-Orisan, A., Alsaleh, N., Lee, C. R. & Seubert, J. M. Epoxyeicosatrienoic acids and cardioprotection: the road to translation. *J Mol Cell Cardiol* **74**, 199-208, doi:10.1016/j.yjmcc.2014.05.016 S0022-2828(14)00192-8 [pii] (2014).

72 Spector, A. A. & Norris, A. W. Action of epoxyeicosatrienoic acids on cellular function. *Am J Physiol Cell Physiol* **292**, C996-1012 (2007).

73 El-Sikhry, H. E., Alsaleh, N., Dakarapu, R., Falck, J. R. & Seubert, J. M. Novel Roles of Epoxyeicosanoids in Regulating Cardiac Mitochondria. *PLoS One* **11**, e0160380, doi:10.1371/journal.pone.0160380 (2016).

74 Zhang, Y. *et al.* Overexpression of CYP2J2 provides protection against doxorubicin-induced cardiotoxicity. *Am J Physiol Heart Circ Physiol* **297**, H37-46, doi:10.1152/ajpheart.00983.2008 00983.2008 [pii] (2009).

75 Wong, P. Y. K. *et al.* 14(R),15(S)-Epoxyeicosatrienoic Acid (14(R),15(S)-Eet) Receptor in Guinea-Pig Mononuclear Cell-Membranes. *J Lipid Mediator* **6**, 199-208 (1993).

76 Wong, P. Y., Lai, P. S., Shen, S. Y., Belosludtsev, Y. Y. & Falck, J. R. Post-receptor signal transduction and regulation of 14(R),15(S)-epoxyeicosatrienoic acid (14,15-EET) binding in U-937 cells. *J Lipid Mediat Cell Signal* **16**, 155-169 (1997).

77 Wong, P. Y., Lai, P. S. & Falck, J. R. Mechanism and signal transduction of 14 (R), 15 (S)-epoxyeicosatrienoic acid (14,15-EET) binding in guinea pig monocytes. *Prostag Oth Lipid M* **62**, 321-333 (2000).

78 Chen, Y., Falck, J. R., Manthati, V. L., Jat, J. L. & Campbell, W. B. 20-Iodo-14,15-epoxyeicosa-8(Z)-enoyl-3-azidophenylsulfonamide: photoaffinity labeling of a 14,15-epoxyeicosatrienoic acid receptor. *Biochemistry* **50**, 3840-3848, doi:10.1021/bi102070w (2011).

79 Chen, Y., Falck, J. R., Tuniki, V. R. & Campbell, W. B. 20-125Iodo-14,15-epoxyeicosa-5(Z)-enoic acid: a high-affinity radioligand used to characterize the epoxyeicosatrienoic acid antagonist binding site. *J Pharmacol Exp Ther* **331**, 1137-1145 (2009).

80 Falck, J. R. *et al.* Comparison of vasodilatory properties of 14,15-EET analogs: structural requirements for dilation. *Am J Physiol Heart Circ Physiol* **284**, H337-349 (2003).

81 Liu, X. *et al.* Functional screening for G protein-coupled receptor targets of 14,15-epoxyeicosatrienoic acid. *Prostaglandins Other Lipid Mediat* **132**, 31-40, doi:S1098-8823(16)30109-5 [pii] 10.1016/j.prostaglandins.2016.09.002 (2017).

82 Yang, W. *et al.* Characterization of 14,15-epoxyeicosatrienoyl-sulfonamides as 14,15-epoxyeicosatrienoic acid agonists: use for studies of metabolism and ligand binding. *J Pharmacol Exp Ther* **321**, 1023-1031 (2007).

83 Yang, W. *et al.* Characterization of epoxyeicosatrienoic acid binding site in U937 membranes using a novel radiolabeled agonist, 20-125i-14,15-epoxyeicosa-8(Z)-enoic acid. *J Pharmacol Exp Ther* **324**, 1019-1027, doi:10.1124/jpet.107.129577 jpet.107.129577 [pii] (2008).

84 Devane, W. A., Dysarz, F. A., Johnson, M. R., Melvin, L. S. & Howlett, A. C. Determination and characterization of a cannabinoid receptor in rat brain. *Molecular Pharmacology* **34**, 605-613 (1988).

85 Matsuda, L. A., Lolait, S. J., Brownstein, M. J., Young, A. C. & Bonner, T. I. Structure of a cannabinoid receptor and functional expression of the cloned cDNA. *Nature* **346**, 561-564 (1990).

86 Munro, S., Thomas, K. L. & Abu-Shaar, M. Molecular characterization of a peripheral receptor for cannabinoids. *Nature* **365**, 61-65 (1993).

87 Devane, W. A. *et al.* Isolation and structure of a brain constituent that binds to the cannabinoid receptor. *Science* **258**, 1946+ (1992).

88 Mechoulam, R. *et al.* Identification of an endogenous 2-monoglyceride, present in canine gut, that binds to cannabinoid receptors. *Biochemical Pharmacology* **50**, 83-90, doi:http://dx.doi.org/10.1016/0006-2952(95)00109-D (1995).

89 Sugiura, T. *et al.* 2-Arachidonoylgylcerol: A Possible Endogenous Cannabinoid Receptor Ligand in Brain. *Biochemical and Biophysical Research Communications* **215**, 89-97, doi:http://dx.doi.org/10.1006/bbrc.1995.2437 (1995).

90 Leishman, E. & Bradshaw, H. B. N-Acyl Amides: Ubiquitous Endogenous Cannabimimetic Lipids That Are in the Right Place at the Right Time. *Endocannabinoidome: The World of Endocannabinoids and Related Mediators*, 33-48 (2015).

91 Balvers, M. G. *et al.* Docosahexaenoic acid and eicosapentaenoic acid are converted by 3T3-L1 adipocytes to N-acyl ethanolamines with anti-inflammatory properties. *Biochim Biophys Acta* **1801**, 1107-1114, doi:10.1016/j.bbalip.2010.06.006 (2010).

92 Berger, A. *et al.* Anandamide and diet: inclusion of dietary arachidonate and docosahexaenoate leads to increased brain levels of the corresponding N-

acylethanolamines in piglets. *Proc Natl Acad Sci U S A* **98**, 6402-6406, doi:10.1073/pnas.101119098 (2001).
93 Saghatelian, A., McKinney, M. K., Bandell, M., Patapoutian, A. & Cravatt, B. F. A FAAH-regulated class of N-acyl taurines that activates TRP ion channels. *Biochemistry* **45**, 9007-9015, doi:10.1021/bi0608008 (2006).
94 Laprairie, R. B., Bagher, A. M. & Denovan-Wright, E. M. Cannabinoid receptor ligand bias: implications in the central nervous system. *Current opinion in pharmacology* **32**, 32-43, doi:10.1016/j.coph.2016.10.005 (2017).
95 Ibsen, M. S., Connor, M. & Glass, M. Cannabinoid CB1 and CB2 Receptor Signaling and Bias. *Cannabis and cannabinoid research* **2**, 48-60, doi:10.1089/can.2016.0037 (2017).
96 Soethoudt, M. *et al.* Cannabinoid CB2 receptor ligand profiling reveals biased signalling and off-target activity. *Nature communications* **8**, 13958, doi:10.1038/ncomms13958 (2017).
97 Croci, T. *et al.* In vitro functional evidence of neuronal cannabinoid CB1 receptors in human ileum. *Brit J Pharmacol* **125**, 1393-1395, doi:10.1038/sj.bjp.0702190 (1998).
98 El-Talatini, M. R. *et al.* Localisation and Function of the Endocannabinoid System in the Human Ovary. *PLoS ONE* **4**, e4579, doi:10.1371/journal.pone.0004579 (2009).
99 Fride, E. Endocannabinoids in the central nervous system-an overview. *Prostaglandins, Leukotrienes and Essential Fatty Acids* **66**, 221-233, doi:http://dx.doi.org/10.1054/plef.2001.0360 (2002).
100 Galiègue, S. *et al.* Expression of Central and Peripheral Cannabinoid Receptors in Human Immune Tissues and Leukocyte Subpopulations. *European Journal of Biochemistry* **232**, 54-61, doi:10.1111/j.1432-1033.1995.tb20780.x (1995).
101 Lazenka, M. F., Selley, D. E. & Sim-Selley, L. J. Brain regional differences in CB1 receptor adaptation and regulation of transcription. *Life Sciences* **92**, 446-452, doi:http://dx.doi.org/10.1016/j.lfs.2012.08.023 (2013).
102 Manzanares, J., Julian, M. D. & Carrascosa, A. Role of the cannabinoid system in pain control and therapeutic implications for the management of acute and chronic pain episodes. *Curr Neuropharmacol* **4**, 239-257, doi:Doi 10.2174/157015906778019527 (2006).
103 Moreira, F. A., Grieb, M. & Lutz, B. Central side-effects of therapies based on CB1 cannabinoid receptor agonists and antagonists: focus on anxiety and depression. *Best practice & research. Clinical endocrinology & metabolism* **23**, 133-144, doi:10.1016/j.beem.2008.09.003 (2009).
104 Mackie, K. Mechanisms of CB1 receptor signaling: endocannabinoid modulation of synaptic strength. *International journal of obesity* **30 Suppl 1**, S19-23, doi:10.1038/sj.ijo.0803273 (2006).
105 Mackie, K. Distribution of cannabinoid receptors in the central and peripheral nervous system. *Handbook of experimental pharmacology*, 299-325 (2005).
106 Piomelli, D. The molecular logic of endocannabinoid signalling. *Nat Rev Neurosci* **4**, 873-884, doi:10.1038/nrn1247 (2003).
107 Marsicano, G. & Lutz, B. Neuromodulatory functions of the endocannabinoid system. *Journal of endocrinological investigation* **29**, 27-46 (2006).
108 Clayton, N., Marshall, F. H., Bountra, C. & O'Shaughnessy, C. T. CB1 and CB2 cannabinoid receptors are implicated in inflammatory pain. *Pain* **96**, 253-260 (2002).

109 Pacher, P., Batkai, S. & Kunos, G. Cardiovascular pharmacology of cannabinoids. *Handbook of experimental pharmacology*, 599-625 (2005).
110 Dhopeshwarkar, A. & Mackie, K. CB2 Cannabinoid receptors as a therapeutic target-what does the future hold? *Mol Pharmacol* **86**, 430-437, doi:10.1124/mol.114.094649 (2014).
111 Slipetz, D. M. *et al.* Activation of the human peripheral cannabinoid receptor results in inhibition of adenylyl cyclase. *Mol Pharmacol* **48**, 352-361 (1995).
112 Herrera, B., Carracedo, A., Diez-Zaera, M., Guzman, M. & Velasco, G. P38 MAPK is involved in CB2 receptor-induced apoptosis of human leukaemia cells. *Febs Lett* **579**, 5084-5088, doi:10.1016/j.febslet.2005.08.021 (2005).
113 Ho, B. Y., Uezono, Y., Takada, S., Takase, I. & Izumi, F. Coupling of the expressed cannabinoid CB1 and CB2 receptors to phospholipase C and G protein-coupled inwardly rectifying K+ channels. *Receptor Channel* **6**, 363-374 (1999).
114 McAllister, S. D., Griffin, G., Satin, L. S. & Abood, M. E. Cannabinoid receptors can activate and inhibit G protein-coupled inwardly rectifying potassium channels in a Xenopus oocyte expression system. *Journal of Pharmacology and Experimental Therapeutics* **291**, 618-626 (1999).
115 McPartland, J. M., Glass, M. & Pertwee, R. G. Meta-analysis of cannabinoid ligand binding affinity and receptor distribution: interspecies differences. *Br J Pharmacol* **152**, 583-593, doi:10.1038/sj.bjp.0707399 (2007).
116 Trillou, C. R. *et al.* Anti-obesity effect of SR141716, a CB1 receptor antagonist, in diet-induced obese mice. *Am J Physiol-Reg I* **284**, R345-R353, doi:10.1152/ajpregu.00545.2002 (2003).
117 Hillard, C. J. *et al.* Synthesis and characterization of potent and selective agonists of the neuronal cannabinoid receptor (CB1). *Journal of Pharmacology and Experimental Therapeutics* **289**, 1427-1433 (1999).
118 Lan, R. X. *et al.* Design and synthesis of the CB1 selective cannabinoid antagonist AM281: A potential human SPECT ligand. *Aaps Pharmsci* **1** (1999).
119 Hanus, L. *et al.* HU-308: A specific agonist for CB2, a peripheral cannabinoid receptor. *P Natl Acad Sci USA* **96**, 14228-14233, doi:DOI 10.1073/pnas.96.25.14228 (1999).
120 Gertsch, J. *et al.* Beta-caryophyllene is a dietary cannabinoid. *P Natl Acad Sci USA* **105**, 9099-9104, doi:10.1073/pnas.0803601105 (2008).
121 Mackie, K., Devane, W. A. & Hille, B. Anandamide, an Endogenous Cannabinoid, Inhibits Calcium Currents as a Partial Agonist in N18 Neuroblastoma-Cells. *Molecular Pharmacology* **44**, 498-503 (1993).
122 Sugiura, T. *et al.* Evidence that the cannabinoid CB1 receptor is a 2-arachidonoylglycerol receptor - Structure-activity relationship of 2-arachidonoylglycerol ether-linked analogues, and related compounds. *Journal of Biological Chemistry* **274**, 2794-2801, doi:DOI 10.1074/jbc.274.5.2794 (1999).
123 Savinainen, J. R., Jarvinen, T., Laine, K. & Laitinen, J. T. Despite substantial degradation, 2-arachidonoylglycerol is a potent full efficacy agonist mediating CB1 receptor-dependent G-protein activation in rat cerebellar membranes. *Brit J Pharmacol* **134**, 664-672, doi:DOI 10.1038/sj.bjp.0704297 (2001).
124 Sugiura, T. *et al.* Evidence that 2-arachidonoylglycerol but not N-palmitoylethanolamine or anandamide is the physiological ligand for the cannabinoid CB2 receptor - Comparison of the agonistic activities of various cannabinoid receptor ligands in HL-60 cells. *Journal of Biological Chemistry* **275**, 605-612, doi:DOI 10.1074/jbc.275.1.605 (2000).

125 Gonsiorek, W. *et al.* Endocannabinoid 2-arachidonyl glycerol is a full agonist through human type 2 cannabinoid receptor: Antagonism by anandamide. *Molecular Pharmacology* **57**, 1045-1050 (2000).
126 Bosier, B., Hermans, E. & Lambert, D. M. Differential modulation of AP-1- and CRE-driven transcription by cannabinoid agonists emphasizes functional selectivity at the CB(1) receptor. *Brit J Pharmacol* **155**, 24-33, doi:10.1038/bjp.2008.230 (2008).
127 Bosier, B., Lambert, D. M. & Hermans, E. Reciprocal influences of CB1 cannabinoid receptor agonists on ERK and JNK signalling in N1E-115 cells. *Febs Lett* **582**, 3861-3867, doi:10.1016/j.febslet.2008.10.022 (2008).
128 Bosier, B., Tilleux, S., Najimi, M., Lambert, D. M. & Hermans, E. Agonist selective modulation of tyrosine hydroxylase expression by cannabinoid ligands in a murine neuroblastoma cell line. *Journal of neurochemistry* **102**, 1996-2007, doi:10.1111/j.1471-4159.2007.04679.x (2007).
129 Bosier, B. *et al.* Differential modulations of striatal tyrosine hydroxylase and dopamine metabolism by cannabinoid agonists as evidence for functional selectivity in vivo. *Neuropharmacology* **62**, 2328-2336, doi:10.1016/j.neuropharm.2012.02.003 (2012).
130 Bosier, B. *et al.* Revisiting the complex influences of cannabinoids on motor functions unravels pharmacodynamic differences between cannabinoid agonists. *Neuropharmacology* **59**, 503-510, doi:10.1016/j.neuropharm.2010.07.005 (2010).
131 Bosier, B., Hermans, E. & Lambert, D. M. Concomitant activation of adenylyl cyclase suppresses the opposite influences of CB1 cannabinoid receptor agonists on tyrosine hydroxylase expression. *Biochemical Pharmacology* **77**, 216-227, doi:10.1016/j.bcp.2008.10.010 (2009).
132 Maneuf, Y. P. & Brotchie, J. M. Paradoxical action of the cannabinoid WIN 55,212-2 in stimulated and basal cyclic AMP accumulation in rat globus pallidus slices. *Brit J Pharmacol* **120**, 1397-1398, doi:DOI 10.1038/sj.bjp.0701101 (1997).
133 Bonhaus, D. W., Chang, L. K., Kwan, J. & Martin, G. R. Dual activation and inhibition of adenylyl cyclase by cannabinoid receptor agonists: Evidence for agonist-specific trafficking of intracellular responses. *Journal of Pharmacology and Experimental Therapeutics* **287**, 884-888 (1998).
134 Smoum, R. *et al.* CB2 cannabinoid receptor agonist enantiomers HU-433 and HU-308: An inverse relationship between binding affinity and biological potency. *P Natl Acad Sci USA* **112**, 8774-8779, doi:10.1073/pnas.1503395112 (2015).
135 McHugh, D. *et al.* N-arachidonoyl glycine, an abundant endogenous lipid, potently drives directed cellular migration through GPR18, the putative abnormal cannabidiol receptor. *Bmc Neurosci* **11**, doi:Artn 44 10.1186/1471-2202-11-44 (2010).
136 Ryberg, E. *et al.* The orphan receptor GPR55 is a novel cannabinoid receptor. *Brit J Pharmacol* **152**, 1092-1101, doi:10.1038/sj.bjp.0707460 (2007).
137 Kohno, M. *et al.* Identification of N-arachidonylglycine as the endogenous ligand for orphan G-protein-coupled receptor GPR18. *Biochemical and Biophysical Research Communications* **347**, 827-832, doi:10.1016/j.bbrc.2006.06.175 (2006).
138 Kapur, A. *et al.* Atypical Responsiveness of the Orphan Receptor GPR55 to Cannabinoid Ligands. *Journal of Biological Chemistry* **284**, 29817-29827, doi:10.1074/jbc.M109.050187 (2009).
139 McHugh, D., Tanner, C., Mechoulam, R., Pertwee, R. G. & Ross, R. A. Inhibition of human neutrophil chemotaxis by endogenous cannabinoids and phytocannabinoids:

Evidence for a site distinct from CB1 and CB2. *Molecular Pharmacology* **73**, 441-450, doi:10.1124/mol.107.041863 (2008).

140 Begg, M. *et al.* Evidence for novel cannabinoid receptors. *Pharmacol Ther* **106**, 133-145, doi:10.1016/j.pharmthera.2004.11.005 (2005).

141 Mackie, K. & Stella, N. Cannabinoid receptors and endocannabinoids: evidence for new players. *The AAPS journal* **8**, E298-306, doi:10.1208/aapsj080234 (2006).

142 Rimmerman, N. *et al.* Microsomal omega-hydroxylated metabolites of N-arachidonoyl dopamine are active at recombinant human TRPV1 receptors. *Prostag Oth Lipid M* **88**, 10-17, doi:10.1016/j.prostaglandins.2008.08.004 (2009).

143 De Petrocellis, L. & Di Marzo, V. N-Acyldopamines and N-Acylserotonins: From Synthetic Pharmacological Tools to Endogenous Multitarget Mediators. *Endocannabinoidome: The World of Endocannabinoids and Related Mediators*, 67-84 (2015).

144 Maione, S. *et al.* Analgesic actions of N-arachidonoyl-serotonin, a fatty acid amide hydrolase inhibitor with antagonistic activity at vanilloid TRPV1 receptors. *Brit J Pharmacol* **150**, 766-781, doi:10.1038/sj.bjp.0707145 (2007).

145 Ryskamp, D. A., Redmon, S., Jo, A. O. & Krizaj, D. TRPV1 and Endocannabinoids: Emerging Molecular Signals that Modulate Mammalian Vision. *Cells* **3**, 914-938, doi:10.3390/cells3030914 (2014).

146 Toth, A., Blumberg, P. M. & Boczan, J. Anandamide and the vanilloid receptor (TRPV1). *Vitamins and hormones* **81**, 389-419, doi:10.1016/S0083-6729(09)81015-7 (2009).

147 Caterina, M. J. *et al.* Impaired nociception and pain sensation in mice lacking the capsaicin receptor. *Science* **288**, 306-313, doi:8443 [pii] (2000).

148 Tominaga, M. & Caterina, M. J. Thermosensation and pain. *J Neurobiol* **61**, 3-12, doi:10.1002/neu.20079 (2004).

149 Szallasi, A. & Blumberg, P. M. Vanilloid (Capsaicin) receptors and mechanisms. *Pharmacological Reviews* **51**, 159-212 (1999).

150 Choi, S. I., Yoo, S., Lim, J. Y. & Hwang, S. W. Are sensory TRP channels biological alarms for lipid peroxidation? *Int J Mol Sci* **15**, 16430-16457, doi:10.3390/ijms150916430 (2014).

151 Chen, Y. S., Lu, M. J., Huang, H. S. & Ma, M. C. Mechanosensitive transient receptor potential vanilloid type 1 channels contribute to vascular remodeling of rat fistula veins. *J Vasc Surg* **52**, 1310-1320, doi:10.1016/j.jvs.2010.05.095 (2010).

152 Wang, Y. & Wang, D. H. TRPV1 ablation aggravates inflammatory responses and organ damage during endotoxic shock. *Clin Vaccine Immunol* **20**, 1008-1015, doi:10.1128/CVI.00674-12 CVI.00674-12 [pii] (2013).

153 Tsuji, F. & Aono, H. Role of transient receptor potential vanilloid 1 in inflammation and autoimmune diseases. *Pharmaceuticals (Basel)* **5**, 837-852, doi:10.3390/ph5080837 ph5080837 [pii] (2012).

154 Yoshida, A. *et al.* TRPV1 is crucial for proinflammatory STAT3 signaling and thermoregulation-associated pathways in the brain during inflammation. *Sci Rep-Uk* **6**, doi:Artn 26088 10.1038/Srep26088 (2016).

155 Schwartz, E. S. *et al.* TRPV1 and TRPA1 antagonists prevent the transition of acute to chronic inflammation and pain in chronic pancreatitis. *J Neurosci* **33**, 5603-5611, doi:10.1523/JNEUROSCI.1806-12.201333/13/5603 [pii] (2013).

156 Randhawa, P. K. & Jaggi, A. S. TRPV1 channels in cardiovascular system: A double edged sword? *Int J Cardiol* **228**, 103-113, doi:S0167-5273(16)33636-1 [pii]10.1016/j.ijcard.2016.11.205 (2017).

157 Zygmunt, P. M. *et al.* Vanilloid receptors on sensory nerves mediate the vasodilator action of anandamide. *Nature* **400**, 452-457 (1999).

158 Hao, X. *et al.* TRPV1 activation prevents high-salt diet-induced nocturnal hypertension in mice. *Pflugers Arch* **461**, 345-353, doi:10.1007/s00424-011-0921-x (2011).

159 Wang, L. & Wang, D. H. TRPV1 gene knockout impairs postischemic recovery in isolated perfused heart in mice. *Circulation* **112**, 3617-3623, doi:CIRCULATIONAHA.105.556274 [pii]10.1161/CIRCULATIONAHA.105.556274 (2005).

160 Sun, Z. W. *et al.* TRPV1 Activation Exacerbates Hypoxia/Reoxygenation-Induced Apoptosis in H9C2 Cells via Calcium Overload and Mitochondrial Dysfunction. *International Journal of Molecular Sciences* **15**, 18362-18380, doi:10.3390/ijms151018362 (2014).

161 Zelasko, S., Arnold, W. R. & Das, A. Endocannabinoid metabolism by cytochrome P450 monooxygenases. *Prostag Oth Lipid M* **116**, 112-123, doi:10.1016/j.prostaglandins.2014.11.002 (2015).

162 Maccarrone, M. Metabolism of the Endocannabinoid Anandamide: Open Questions after 25 Years. *Front Mol Neurosci* **10**, 166, doi:10.3389/fnmol.2017.00166 (2017).

163 McDougle, D. R. *et al.* Anti-inflammatory omega-3 endocannabinoid epoxides. *Proc Natl Acad Sci U S A* **114**, E6034-E6043, doi:10.1073/pnas.1610325114 (2017).

164 Roy, J., Watson, J. E., Hong, I., Fan, T. M. & Das, A. Anti-Tumorigenic Properties of Omega-3 Endocannabinoid Epoxides. *J Med Chem*, doi:10.1021/acs.jmedchem.8b00243 (2018).

165 Snider, N. T., Nast, J. A., Tesmer, L. A. & Hollenberg, P. F. A cytochrome P450-derived epoxygenated metabolite of anandamide is a potent cannabinoid receptor 2-selective agonist. *Mol Pharmacol* **75**, 965-972, doi:10.1124/mol.108.053439 (2009).

166 Gonzalez, F. J. & Gelboin, H. V. Human cytochromes P450: evolution and cDNA-directed expression. *Environmental health perspectives* **98**, 81-85, doi:10.1289/ehp.929881 (1992).

167 Guengerich, F. P., Wu, Z. L. & Bartleson, C. J. Function of human cytochrome P450s: characterization of the orphans. *Biochem Biophys Res Commun* **338**, 465-469, doi:S0006-291X(05)01794-8 [pii] 10.1016/j.bbrc.2005.08.079 (2005).

168 Rittle, J. & Green, M. T. Cytochrome P450 compound I: capture, characterization, and C-H bond activation kinetics. *Science* **330**, 933-937, doi:10.1126/science.1193478 (2010).

169 Guengerich, F. P. Common and uncommon cytochrome P450 reactions related to metabolism and chemical toxicity. *Chem Res Toxicol* **14**, 611-650 (2001).

170 Lu, A. Y., Junk, K. W. & Coon, M. J. Resolution of the cytochrome P-450-containing omega-hydroxylation system of liver microsomes into three components. *J Biol Chem* **244**, 3714-3721 (1969).

171 Hanukoglu, I. Steroidogenic enzymes: structure, function, and role in regulation of steroid hormone biosynthesis. *The Journal of steroid biochemistry and molecular biology* **43**, 779-804, doi:10.1016/0960-0760(92)90307-5 (1992).

172 Estrada, D. F., Laurence, J. S. & Scott, E. E. Substrate-modulated cytochrome P450 17A1 and cytochrome b5 interactions revealed by NMR. *J Biol Chem* **288**, 17008-17018, doi:10.1074/jbc.M113.468926 (2013).
173 Duggal, R., Denisov, I. G. & Sligar, S. G. Cytochrome b5 enhances androgen synthesis by rapidly reducing the CYP17A1 oxy-complex in the lyase step. *Febs Lett* **592**, 2282-2288, doi:10.1002/1873-3468.13153 (2018).
174 Duggal, R. *et al.* Evidence that cytochrome b5 acts as a redox donor in CYP17A1 mediated androgen synthesis. *Biochem Biophys Res Commun* **477**, 202-208, doi:10.1016/j.bbrc.2016.06.043 (2016).
175 Porter, T. D. The roles of cytochrome b5 in cytochrome P450 reactions. *Journal of biochemical and molecular toxicology* **16**, 311-316, doi:10.1002/jbt.10052 (2002).
176 Hall, P. F. Cytochrome P-450 C21scc: one enzyme with two actions: hydroxylase and lyase. *The Journal of steroid biochemistry and molecular biology* **40**, 527-532 (1991).
177 Glubb, D. M., O'Mara, T. A., Shamsani, J. & Spurdle, A. B. The Association of CYP19A1 Variation with Circulating Estradiol and Aromatase Inhibitor Outcome: Can CYP19A1 Variants Be Used to Predict Treatment Efficacy? *Frontiers in pharmacology* **8**, 218, doi:10.3389/fphar.2017.00218 (2017).
178 Hanukoglu, I., Privalle, C. T. & Jefcoate, C. R. Mechanisms of ionic activation of adrenal mitochondrial cytochromes P-450scc and P-45011 beta. *J Biol Chem* **256**, 4329-4335 (1981).
179 Cheng, J. B., Levine, M. A., Bell, N. H., Mangelsdorf, D. J. & Russell, D. W. Genetic evidence that the human CYP2R1 enzyme is a key vitamin D 25-hydroxylase. *Proc Natl Acad Sci U S A* **101**, 7711-7715, doi:10.1073/pnas.0402490101 (2004).
180 Takeyama, K. *et al.* 25-Hydroxyvitamin D3 1alpha-hydroxylase and vitamin D synthesis. *Science* **277**, 1827-1830 (1997).
181 Yokoyama, C., Miyata, A., Ihara, H., Ullrich, V. & Tanabe, T. Molecular cloning of human platelet thromboxane A synthase. *Biochem Biophys Res Commun* **178**, 1479-1484 (1991).
182 Yokoyama, C. *et al.* Human gene encoding prostacyclin synthase (PTGIS): genomic organization, chromosomal localization, and promoter activity. *Genomics* **36**, 296-304, doi:10.1006/geno.1996.0465 (1996).
183 Howell, A. *et al.* Results of the ATAC (Arimidex, Tamoxifen, Alone or in Combination) trial after completion of 5 years' adjuvant treatment for breast cancer. *Lancet* **365**, 60-62, doi:10.1016/S0140-6736(04)17666-6 (2005).
184 de Ronde, W. & de Jong, F. H. Aromatase inhibitors in men: effects and therapeutic options. *Reproductive biology and endocrinology : RB&E* **9**, 93, doi:10.1186/1477-7827-9-93 (2011).
185 McDonnell, A. M. & Dang, C. H. Basic review of the cytochrome p450 system. *Journal of the advanced practitioner in oncology* **4**, 263-268 (2013).
186 Galetin, A. & Houston, J. B. Intestinal and hepatic metabolic activity of five cytochrome P450 enzymes: impact on prediction of first-pass metabolism. *J Pharmacol Exp Ther* **318**, 1220-1229, doi:10.1124/jpet.106.106013 (2006).
187 Liston, H. L., Markowitz, J. S. & DeVane, C. L. Drug glucuronidation in clinical psychopharmacology. *Journal of clinical psychopharmacology* **21**, 500-515 (2001).
188 Haddad, A., Davis, M. & Lagman, R. The pharmacological importance of cytochrome CYP3A4 in the palliation of symptoms: review and recommendations for avoiding adverse drug interactions. *Supportive care in cancer : official journal of the Multinational*

Association of Supportive Care in Cancer **15**, 251-257, doi:10.1007/s00520-006-0127-5 (2007).

189 Klein, K. & Zanger, U. M. Pharmacogenomics of Cytochrome P450 3A4: Recent Progress Toward the "Missing Heritability" Problem. *Frontiers in genetics* **4**, 12, doi:10.3389/fgene.2013.00012 (2013).

190 Zanger, U. M. & Schwab, M. Cytochrome P450 enzymes in drug metabolism: regulation of gene expression, enzyme activities, and impact of genetic variation. *Pharmacol Ther* **138**, 103-141, doi:10.1016/j.pharmthera.2012.12.007 (2013).

191 Denisov, I. G., Frank, D. J. & Sligar, S. G. Cooperative properties of cytochromes P450. *Pharmacol Ther* **124**, 151-167, doi:10.1016/j.pharmthera.2009.05.011S0163-7258(09)00117-X [pii] (2009).

192 Atkins, W. M. Non-Michaelis-Menten kinetics in cytochrome P450-catalyzed reactions. *Annual review of pharmacology and toxicology* **45**, 291-310, doi:10.1146/annurev.pharmtox.45.120403.100004 (2005).

193 Korzekwa, K. R. *et al.* Evaluation of atypical cytochrome P450 kinetics with two-substrate models: evidence that multiple substrates can simultaneously bind to cytochrome P450 active sites. *Biochemistry* **37**, 4137-4147, doi:10.1021/bi9715627 (1998).

194 Roberts, A. G. *et al.* The structural basis for homotropic and heterotropic cooperativity of midazolam metabolism by human cytochrome P450 3A4. *Biochemistry* **50**, 10804-10818, doi:10.1021/bi200924t (2011).

195 Graves, J. P. *et al.* Characterization of the Tissue Distribution of the Mouse Cyp2c Subfamily by Quantitative PCR Analysis. *Drug Metab Dispos* **45**, 807-816, doi:10.1124/dmd.117.075697 (2017).

196 Wu, S., Moomaw, C. R., Tomer, K. B., Falck, J. R. & Zeldin, D. C. Molecular cloning and expression of CYP2J2, a human cytochrome P450 arachidonic acid epoxygenase highly expressed in heart. *J Biol Chem* **271**, 3460-3468 (1996).

197 Michaud, V., Frappier, M., Dumas, M. C. & Turgeon, J. Metabolic activity and mRNA levels of human cardiac CYP450s involved in drug metabolism. *PLoS One* **5**, e15666, doi:10.1371/journal.pone.0015666 (2010).

198 Chaudhary, K. R., Batchu, S. N. & Seubert, J. M. Cytochrome P450 enzymes and the heart. *IUBMB life* **61**, 954-960, doi:10.1002/iub.241 (2009).

199 DeLozier, T. C. *et al.* Detection of Human CYP2C8, CYP2C9, and CYP2J2 in Cardiovascular Tissues. *Drug Metabolism and Disposition* **35**, 682-688, doi:10.1124/dmd.106.012823 (2007).

200 Drolet, B. *et al.* Altered Protein Expression of Cardiac CYP2J and Hepatic CYP2C, CYP4A, and CYP4F in a Mouse Model of Type II Diabetes-A Link in the Onset and Development of Cardiovascular Disease? *Pharmaceutics* **9**, doi:10.3390/pharmaceutics9040044 (2017).

201 Ma, B. *et al.* Cardiac-specific overexpression of CYP2J2 attenuates diabetic cardiomyopathy in male streptozotocin-induced diabetic mice. *Endocrinology* **154**, 2843-2856, doi:10.1210/en.2012-2166 (2013).

202 Yang, B. *et al.* Overexpression of cytochrome P450 CYP2J2 protects against hypoxia-reoxygenation injury in cultured bovine aortic endothelial cells. *Mol Pharmacol* **60**, 310-320 (2001).

203 Ferguson, C. S. & Tyndale, R. F. Cytochrome P450 enzymes in the brain: emerging evidence of biological significance. *Trends Pharmacol Sci* **32**, 708-714, doi:10.1016/j.tips.2011.08.005 (2011).
204 Nishimura, M., Yaguti, H., Yoshitsugu, H., Naito, S. & Satoh, T. Tissue distribution of mRNA expression of human cytochrome P450 isoforms assessed by high-sensitivity real-time reverse transcription PCR. *Yakugaku zasshi : Journal of the Pharmaceutical Society of Japan* **123**, 369-375 (2003).
205 Dutheil, F. *et al.* Xenobiotic-Metabolizing Enzymes and Transporters in the Normal Human Brain: Regional and Cellular Mapping as a Basis for Putative Roles in Cerebral Function. *Drug Metabolism and Disposition* **37**, 1528-1538, doi:10.1124/dmd.109.027011 (2009).
206 Liu, M. Z. *et al.* Glutamate affects the production of epoxyeicosanoids within the brain: The up -regulation of brain CYP2J through the MAPK-CREB signaling pathway. *Toxicology* **381**, 31-38, doi:10.1016/j.tox.2017.02.008 (2017).
207 Qu, W. *et al.* Cytochrome P450 CYP2J9, a new mouse arachidonic acid omega-1 hydroxylase predominantly expressed in brain. *J Biol Chem* **276**, 25467-25479, doi:10.1074/jbc.M100545200 (2001).
208 Graves, J. P. *et al.* Characterization of four new mouse cytochrome P450 enzymes of the CYP2J subfamily. *Drug Metab Dispos* **41**, 763-773, doi:10.1124/dmd.112.049429 (2013).
209 Li, Y. *et al.* The Protective Role of Brain CYP2J in Parkinson's Disease Models. *Oxidative medicine and cellular longevity* **2018**, 2917981, doi:10.1155/2018/2917981 (2018).
210 Si, D. *et al.* Mechanism of CYP2C9 inhibition by flavones and flavonols. *Drug Metab Dispos* **37**, 629-634, doi:10.1124/dmd.108.023416dmd.108.023416 [pii] (2009).
211 Segel, I. H. *Enzyme Kinetics: Behavior and Analysis of Rapid Equilibrium and Steady-State Enzyme Systems*. (John Wiley & Sons, 1975).
212 Fontana, E., Dansette, P. M. & Poli, S. M. Cytochrome p450 enzymes mechanism based inhibitors: common sub-structures and reactivity. *Current drug metabolism* **6**, 413-454 (2005).
213 Zhou, S. *et al.* Mechanism-based inhibition of cytochrome P450 3A4 by therapeutic drugs. *Clinical pharmacokinetics* **44**, 279-304 (2005).
214 Di Cera, E. Site-specific thermodynamics: Understanding cooperativity in molecular recognition. *Chemical reviews* **98**, 1563-1591, doi:Doi 10.1021/Cr960135g (1998).
215 Weiss, J. N. The Hill equation revisited: uses and misuses. *FASEB journal : official publication of the Federation of American Societies for Experimental Biology* **11**, 835-841 (1997).
216 Denisov, I. G., Baas, B. J., Grinkova, Y. V. & Sligar, S. G. Cooperativity in cytochrome P450 3A4: linkages in substrate binding, spin state, uncoupling, and product formation. *Journal of Biological Chemistry* **282**, 7066-7076, doi:M609589200 [pii]10.1074/jbc.M609589200 (2007).
217 Frank, D. J., Denisov, I. G. & Sligar, S. G. Analysis of heterotropic cooperativity in cytochrome P450 3A4 using alpha-naphthoflavone and testosterone. *J Biol Chem* **286**, 5540-5545, doi:10.1074/jbc.M110.182055 (2011).
218 Denisov, I. G., Grinkova, Y. V., Baylon, J. L., Tajkhorshid, E. & Sligar, S. G. Mechanism of drug-drug interactions mediated by human cytochrome P450 CYP3A4 monomer. *Biochemistry* **54**, 2227-2239, doi:10.1021/acs.biochem.5b00079 (2015).

219 Calder, P. C. n-3 polyunsaturated fatty acids, inflammation, and inflammatory diseases. *Am J Clin Nutr* **83**, 1505S-1519S (2006).
220 Gilroy, D. W. *et al.* Inducible cyclooxygenase may have anti-inflammatory properties. *Nat Med* **5**, 698-701, doi:10.1038/9550 (1999).
221 Greene, E. R., Huang, S., Serhan, C. N. & Panigrahy, D. Regulation of inflammation in cancer by eicosanoids. *Prostaglandins Other Lipid Mediat* **96**, 27-36, doi:10.1016/j.prostaglandins.2011.08.004 (2011).
222 Korotkova, M. & Jakobsson, P. J. Persisting eicosanoid pathways in rheumatic diseases. *Nat Rev Rheumatol* **10**, 229-241, doi:10.1038/nrrheum.2014.1 (2014).
223 Harizi, H., Corcuff, J. B. & Gualde, N. Arachidonic-acid-derived eicosanoids: roles in biology and immunopathology. *Trends Mol Med* **14**, 461-469, doi:10.1016/j.molmed.2008.08.005 (2008).
224 Ihara, A. *et al.* Blockade of leukotriene B-4 signaling pathway induces apoptosis and suppresses cell proliferation in colon cancer. *J Pharmacol Sci* **103**, 24-32, doi:10.1254/jphs.FP0060651 (2007).
225 Bertagnolli, M. M. *et al.* Celecoxib for the prevention of sporadic colorectal adenomas. *N Engl J Med* **355**, 873-884, doi:10.1056/NEJMoa061355 (2006).
226 Kinsella, J. E., Lokesh, B. & Stone, R. A. Dietary n-3 polyunsaturated fatty acids and amelioration of cardiovascular disease: possible mechanisms. *Am J Clin Nutr* **52**, 1-28 (1990).
227 Kris-Etherton, P. M., Harris, W. S. & Appel, L. J. Fish consumption, fish oil, omega-3 fatty acids, and cardiovascular disease. *Circulation* **106**, 2747-2757 (2002).
228 Simopoulos, A. P. Omega-3 fatty acids in health and disease and in growth and development. *Am J Clin Nutr* **54**, 438-463 (1991).
229 Wall, R., Ross, R. P., Fitzgerald, G. F. & Stanton, C. Fatty acids from fish: the anti-inflammatory potential of long-chain omega-3 fatty acids. *Nutr Rev* **68**, 280-289, doi:10.1111/j.1753-4887.2010.00287.xNURE287 [pii] (2010).
230 Vonschacky, C., Fischer, S. & Weber, P. C. Long-Term Effects of Dietary Marine Omega-3 Fatty-Acids Upon Plasma and Cellular Lipids, Platelet-Function, and Eicosanoid Formation in Humans. *J Clin Invest* **76**, 1626-1631, doi:Doi 10.1172/Jci112147 (1985).
231 Harris, W. S. *et al.* Omega-6 fatty acids and risk for cardiovascular disease: a science advisory from the American Heart Association Nutrition Subcommittee of the Council on Nutrition, Physical Activity, and Metabolism; Council on Cardiovascular Nursing; and Council on Epidemiology and Prevention. *Circulation* **119**, 902-907, doi:10.1161/CIRCULATIONAHA.108.191627 (2009).
232 Arnold, C. *et al.* Arachidonic Acid-metabolizing Cytochrome P450 Enzymes Are Targets of ω-3 Fatty Acids. *Journal of Biological Chemistry* **285**, 32720-32733, doi:10.1074/jbc.M110.118406 (2010).
233 Sudhahar, V., Shaw, S. & Imig, J. D. Epoxyeicosatrienoic acid analogs and vascular function. *Curr Med Chem* **17**, 1181-1190, doi:BSP/CMC/E-Pub/ 074 [pii] (2010).
234 Simpkins, A. N. *et al.* Soluble epoxide hydrolase inhibition modulates vascular remodeling. *Am J Physiol Heart Circ Physiol* **298**, H795-806, doi:10.1152/ajpheart.00543.200900543.2009 [pii] (2010).

235 Moran, J. H. *et al.* Analysis of the cytotoxic properties of linoleic acid metabolites produced by renal and hepatic P450s. *Toxicol Appl Pharmacol* **168**, 268-279, doi:10.1006/taap.2000.9053S0041-008X(00)99053-7 [pii] (2000).

236 Fer, M. *et al.* Metabolism of eicosapentaenoic and docosahexaenoic acids by recombinant human cytochromes P450. *Archives of Biochemistry and Biophysics* **471**, 116-125, doi:10.1016/j.abb.2008.01.002S0003-9861(08)00004-0 [pii] (2008).

237 Morin, C., Sirois, M., Échavé, V., Albadine, R. & Rousseau, E. 17,18-Epoxyeicosatetraenoic Acid Targets PPARγ and p38 Mitogen–Activated Protein Kinase to Mediate Its Anti-inflammatory Effects in the Lung. *American Journal of Respiratory Cell and Molecular Biology* **43**, 564-575 (2010).

238 Spector, A. A. & Kim, H.-Y. Cytochrome P450 epoxygenase pathway of polyunsaturated fatty acid metabolism. *Biochimica et Biophysica Acta (BBA) - Molecular and Cell Biology of Lipids* **1851**, 356-365, doi:10.1016/j.bbalip.2014.07.020 (2015).

239 Lee, T. H. *et al.* Effects of exogenous arachidonic, eicosapentaenoic, and docosahexaenoic acids on the generation of 5-lipoxygenase pathway products by ionophore-activated human neutrophils. *J Clin Invest* **74**, 1922-1933, doi:10.1172/JCI111612 (1984).

240 Vecchio, A. J., Simmons, D. M. & Malkowski, M. G. Structural basis of fatty acid substrate binding to cyclooxygenase-2. *J Biol Chem* **285**, 22152-22163, doi:10.1074/jbc.M110.119867 (2010).

241 Zanger, U. M. & Schwab, M. Cytochrome P450 enzymes in drug metabolism: Regulation of gene expression, enzyme activities, and impact of genetic variation. *Pharmacology & Therapeutics* **138**, 103-141, doi:http://dx.doi.org/10.1016/j.pharmthera.2012.12.007 (2013).

242 Furge, L. L. & Guengerich, F. P. Cytochrome P450 enzymes in drug metabolism and chemical toxicology: An introduction. *Biochem Mol Biol Educ* **34**, 66-74, doi:10.1002/bmb.2006.49403402066 (2006).

243 Zelasko, S., Palaria, A. & Das, A. Optimizations to achieve high-level expression of cytochrome P450 proteins using Escherichia coli expression systems. *Protein Expres Purif* **92**, 77-87, doi:DOI 10.1016/j.pep.2013.07.017 (2013).

244 Das, A., Varma, S., Mularczyk, C., and Meling, D. Functional Investigations of Thromboxane Synthase (CYP5A1) in Lipid Bilayers of Nanodiscs. *ChemBioChem*, doi:10.1002/cbic.201300646 (2014).

245 McDougle, D. R. *et al.* Incorporation of charged residues in the CYP2J2 F-G loop disrupts CYP2J2-lipid bilayer interactions. *Biochim Biophys Acta* **1848**, 2460-2470, doi:S0005-2736(15)00237-0 [pii]10.1016/j.bbamem.2015.07.015 (2015).

246 McDougle, D. R., Kambalyal, A., Meling, D. D. & Das, A. Endocannabinoids Anandamide and 2-Arachidonoylglycerol Are Substrates for Human CYP2J2 Epoxygenase. *J Pharmacol Exp Ther* **351**, 616-627, doi:10.1124/jpet.114.216598 jpet.114.216598 [pii] (2014).

247 Meling, D. D., McDougle, D. R. & Das, A. CYP2J2 epoxygenase membrane anchor plays an important role in facilitating electron transfer from CPR. *Journal of inorganic biochemistry* **142**, 47-53, doi:http://dx.doi.org/10.1016/j.jinorgbio.2014.09.016 (2015).

248 Meling, D. D., Zelasko, S., Roy, J., Kambayal, A. & Das, A. Functional Role of the Conserved I-Helix Residue I346 in CYP5A1-Nanodiscs. *Biophysical Chemistry* **(In Press)** (2015).

249 Zelasko, S., Arnold, W. R. & Das, A. Endocannabinoid metabolism by cytochrome P450 monooxygenases. *Prostaglandins Other Lipid Mediat*, doi:S1098-8823(14)00074-4 [pii] 10.1016/j.prostaglandins.2014.11.002 (2014).

250 McDougle, D. R., Palaria, A., Magnetta, E., Meling, D. D. & Das, A. Functional studies of N-terminally modified CYP2J2 epoxygenase in model lipid bilayers. *Protein Sci* **22**, 964-979, doi:10.1002/pro.2280 (2013).

251 Rizzuti, B., Bartucci, R., Sportelli, L. & Guzzi, R. Fatty acid binding into the highest affinity site of human serum albumin observed in molecular dynamics simulation. *Archives of Biochemistry and Biophysics* **579**, 18-25, doi:10.1016/j.abb.2015.05.018 (2015).

252 Cui, Y. L., Zheng, Q. C., Zhang, J. L. & Zhang, H. X. Molecular Basis of the Recognition of Arachidonic Acid by Cytochrome P450 2E1 Along Major Access Tunnel. *Biopolymers* **103**, 53-66, doi:10.1002/bip.22567 (2015).

253 Mugnai, M. L., Shi, Y., Keatinge-Clay, A. T. & Elber, R. Molecular dynamics studies of modular polyketide synthase ketoreductase stereospecificity. *Biochemistry* **54**, 2346-2359, doi:10.1021/bi501401g (2015).

254 Boddupalli, S. S., Estabrook, R. W. & Peterson, J. A. Fatty acid monooxygenation by cytochrome P-450BM-3. *J Biol Chem* **265**, 4233-4239 (1990).

255 Meling, D. D., McDougle, D. R. & Das, A. CYP2J2 epoxygenase membrane anchor plays an important role in facilitating electron transfer from CPR. *Journal of inorganic biochemistry* **142C**, 47-53, doi:S0162-0134(14)00258-X [pii] 10.1016/j.jinorgbio.2014.09.016 (2014).

256 Omura, T. & Sato, R. The Carbon Monoxide-Binding Pigment of Liver Microsomes. Ii. Solubilization, Purification, and Properties. *Journal of Biological Chemistry* **239**, 2379-2385 (1964).

257 Capdevila, J. H. *et al.* The highly stereoselective oxidation of polyunsaturated fatty acids by cytochrome P450BM-3. *J Biol Chem* **271**, 22663-22671 (1996).

258 Liu, K. H. *et al.* Characterization of ebastine, hydroxyebastine, and carebastine metabolism by human liver microsomes and expressed cytochrome P450 enzymes: major roles for CYP2J2 and CYP3A. *Drug Metab Dispos* **34**, 1793-1797, doi:dmd.106.010488 [pii] 10.1124/dmd.106.010488 (2006).

259 Trott, O. & Olson, A. J. AutoDock Vina: improving the speed and accuracy of docking with a new scoring function, efficient optimization, and multithreading. *J Comput Chem* **31**, 455-461, doi:10.1002/jcc.21334 (2010).

260 Phillips, J. C. *et al.* Scalable molecular dynamics with NAMD. *J Comput Chem* **26**, 1781-1802, doi:10.1002/jcc.20289 (2005).

261 Best, R. B. *et al.* Optimization of the additive CHARMM all-atom protein force field targeting improved sampling of the backbone phi, psi and side-chain chi(1) and chi(2) dihedral angles. *J Chem Theory Comput* **8**, 3257-3273, doi:10.1021/ct300400x (2012).

262 Klauda, J. B. *et al.* Update of the CHARMM all-atom additive force field for lipids: validation on six lipid types. *J Phys Chem B* **114**, 7830-7843, doi:10.1021/jp101759q (2010).

263 Vanommeslaeghe, K. *et al.* CHARMM general force field: A force field for drug-like molecules compatible with the CHARMM all-atom additive biological force fields. *J Comput Chem* **31**, 671-690, doi:10.1002/jcc.21367 (2010).
264 Feller, S. E., Gawrisch, K. & MacKerell, A. D. Polyunsaturated fatty acids in lipid bilayers: Intrinsic and environmental contributions to their unique physical properties. *J Am Chem Soc* **124**, 318-326, doi:10.1021/ja0118340 (2002).
265 Jorgensen, W. L., Chandrasekhar, J., Madura, J. D., Impey, R. W. & Klein, M. L. Comparison of Simple Potential Functions for Simulating Liquid Water. *J Chem Phys* **79**, 926-935, doi:Doi 10.1063/1.445869 (1983).
266 Feller, S. E., Zhang, Y. H., Pastor, R. W. & Brooks, B. R. Constant-Pressure Molecular-Dynamics Simulation - the Langevin Piston Method. *J Chem Phys* **103**, 4613-4621, doi:Doi 10.1063/1.470648 (1995).
267 Martyna, G. J., Tobias, D. J. & Klein, M. L. Constant-Pressure Molecular-Dynamics Algorithms. *J Chem Phys* **101**, 4177-4189, doi:Doi 10.1063/1.467468 (1994).
268 Ryckaert, J. P., Ciccotti, G. & Berendsen, H. J. C. Numerical-Integration of Cartesian Equations of Motion of a System with Constraints - Molecular-Dynamics of N-Alkanes. *J Comput Phys* **23**, 327-341, doi:Doi 10.1016/0021-9991(77)90098-5 (1977).
269 Darden, T., York, D. & Pedersen, L. Particle Mesh Ewald - an N.Log(N) Method for Ewald Sums in Large Systems. *J Chem Phys* **98**, 10089-10092, doi:Doi 10.1063/1.464397 (1993).
270 Eisenberg, D. & McLachlan, A. D. Solvation energy in protein folding and binding. *Nature* **319**, 199-203, doi:10.1038/319199a0 (1986).
271 Noble, M. A. *et al.* Roles of key active-site residues in flavocytochrome P450 BM3. *Biochem J* **339 (Pt 2)**, 371-379 (1999).
272 Copeland, R. A. *Enzymes: A Practical Introduction to Structure, Mechanism, and Data Analysis*. 136 (John Wiley & Sons, 2004).
273 Dhar, M., Sepkovic, D. W., Hirani, V., Magnusson, R. P. & Lasker, J. M. Omega oxidation of 3-hydroxy fatty acids by the human CYP4F gene subfamily enzyme CYP4F11. *J Lipid Res* **49**, 612-624, doi:10.1194/jlr.M700450-JLR200 (2008).
274 Yao, H. T. *et al.* The inhibitory effect of polyunsaturated fatty acids on human CYP enzymes. *Life Sci* **79**, 2432-2440, doi:10.1016/j.lfs.2006.08.016 (2006).
275 Singh, Y., Ulrich, L., Katz, D., Bowen, P. & Krishna, G. Structural requirements for anthracycline-induced cardiotoxicity and antitumor effects. *Toxicol Appl Pharmacol* **100**, 9-23 (1989).
276 Minotti, G., Menna, P., Salvatorelli, E., Cairo, G. & Gianni, L. Anthracyclines: molecular advances and pharmacologic developments in antitumor activity and cardiotoxicity. *Pharmacological Reviews* **56**, 185-229, doi:10.1124/pr.56.2.6 56/2/185 [pii] (2004).
277 Di Marco, A., Cassinelli, G. & Arcamone, F. The discovery of daunorubicin. *Cancer Treat Rep* **65 Suppl 4**, 3-8 (1981).
278 Arcamone, F. *et al.* Adriamycin, 14-hydroxydaunomycin, a new antitumor antibiotic from S. peucetius var. caesius. *Biotechnol Bioeng* **11**, 1101-1110, doi:10.1002/bit.260110607 (1969).
279 Rabbani, A., Finn, R. M. & Ausio, J. The anthracycline antibiotics: antitumor drugs that alter chromatin structure. *Bioessays* **27**, 50-56, doi:10.1002/bies.20160 (2005).
280 Volkova, M. & Russell, R., 3rd. Anthracycline cardiotoxicity: prevalence, pathogenesis and treatment. *Curr Cardiol Rev* **7**, 214-220, doi:CCR-7-4-214 [pii] (2011).

281 Nohl, H. Identification of the site of adriamycin-activation in the heart cell. *Biochemical Pharmacology* **37**, 2633-2637, doi:0006-2952(88)90257-2 [pii] (1988).
282 Unverferth, D. V., Leier, C. V., Balcerzak, S. P. & Hamlin, R. L. Usefulness of a free radical scavenger in preventing doxorubicin-induced heart failure in dogs. *Am J Cardiol* **56**, 157-161, doi:0002-9149(85)90585-5 [pii] (1985).
283 Minotti, G. *et al.* Paradoxical inhibition of cardiac lipid peroxidation in cancer patients treated with doxorubicin. Pharmacologic and molecular reappraisal of anthracycline cardiotoxicity. *J Clin Invest* **98**, 650-661, doi:10.1172/JCI118836 (1996).
284 Chatterjee, K., Zhang, J., Honbo, N. & Karliner, J. S. Doxorubicin cardiomyopathy. *Cardiology* **115**, 155-162, doi:10.1159/000265166000265166 [pii] (2010).

285 Doroshow, J. H. & Davies, K. J. Redox cycling of anthracyclines by cardiac mitochondria. II. Formation of superoxide anion, hydrogen peroxide, and hydroxyl radical. *Journal of Biological Chemistry* **261**, 3068-3074 (1986).
286 Goeptar, A. R., Te Koppele, J. M., Lamme, E. K., Pique, J. M. & Vermeulen, N. P. Cytochrome P450 2B1-mediated one-electron reduction of adriamycin: a study with rat liver microsomes and purified enzymes. *Mol Pharmacol* **44**, 1267-1277 (1993).
287 Bartoszek, A. Metabolic activation of adriamycin by NADPH-cytochrome P450 reductase; overview of its biological and biochemical effects. *Acta Biochim Pol* **49**, 323-331 (2002).
288 Deng, S. *et al.* Gp91phox-containing NAD(P)H oxidase increases superoxide formation by doxorubicin and NADPH. *Free Radic Biol Med* **42**, 466-473, doi:S0891-5849(06)00751-9 [pii] 10.1016/j.freeradbiomed.2006.11.013 (2007).

289 Arnold, W. R., Baylon, J. L., Tajkhorshid, E. & Das, A. Asymmetric Binding and Metabolism of Polyunsaturated Fatty Acids (PUFAs) by CYP2J2 Epoxygenase. *Biochemistry* **55**, 6969-6980, doi:10.1021/acs.biochem.6b01037 (2016).
290 Spector, A. A. & Norris, A. W. Action of epoxyeicosatrienoic acids on cellular function. *Am J Physiol Cell Physiol* **292**, C996-1012, doi:00402.2006 [pii] 10.1152/ajpcell.00402.2006 (2007).

291 Gross, G. J. *et al.* Effects of the selective EET antagonist, 14,15-EEZE, on cardioprotection produced by exogenous or endogenous EETs in the canine heart. *Am J Physiol Heart Circ Physiol* **294**, H2838-2844, doi:10.1152/ajpheart.00186.2008 00186.2008 [pii] (2008).

292 Fulton, D., Balazy, M., McGiff, J. C. & Quilley, J. Possible contribution of platelet cyclooxygenase to the renal vascular action of 5,6-epoxyeicosatrienoic acid. *J Pharmacol Exp Ther* **277**, 1195-1199 (1996).
293 Takahashi, K. *et al.* Cytochrome P-450 arachidonate metabolites in rat kidney: characterization and hemodynamic responses. *American Journal of Physiology* **258**, F781-789 (1990).
294 Evangelista, E. A., Kaspera, R., Mokadam, N. A., Jones, J. P., 3rd & Totah, R. A. Activity, inhibition, and induction of cytochrome P450 2J2 in adult human primary cardiomyocytes. *Drug Metab Dispos* **41**, 2087-2094, doi:10.1124/dmd.113.053389 dmd.113.053389 [pii] (2013).

295 Kaspera, R. *et al.* Investigating the contribution of CYP2J2 to ritonavir metabolism in vitro and in vivo. *Biochem Pharmacol* **91**, 109-118, doi:10.1016/j.bcp.2014.06.020 S0006-2952(14)00363-3 [pii] (2014).

296 Lee, C. A. *et al.* Identifying a selective substrate and inhibitor pair for the evaluation of CYP2J2 activity. *Drug Metab Dispos* **40**, 943-951, doi:10.1124/dmd.111.043505 dmd.111.043505 [pii] (2012).

297 Karkhanis, A. *et al.* Multiple modes of inhibition of human cytochrome P450 2J2 by dronedarone, amiodarone and their active metabolites. *Biochemical Pharmacology* **107**, 67-80, doi:10.1016/j.bcp.2016.03.005 S0006-2952(16)00158-1 [pii] (2016).

298 Lafite, P., Andre, F., Zeldin, D. C., Dansette, P. M. & Mansuy, D. Unusual regioselectivity and active site topology of human cytochrome P450 2J2. *Biochemistry* **46**, 10237-10247, doi:10.1021/bi700876a (2007).

299 MacKerell, A. D. *et al.* All-atom empirical potential for molecular modeling and dynamics studies of proteins. *J Phys Chem B* **102**, 3586-3616, doi:10.1021/jp973084f (1998).

300 Mackerell, A. D., Jr., Feig, M. & Brooks, C. L., 3rd. Extending the treatment of backbone energetics in protein force fields: limitations of gas-phase quantum mechanics in reproducing protein conformational distributions in molecular dynamics simulations. *J Comput Chem* **25**, 1400-1415, doi:10.1002/jcc.20065 (2004).

301 Hart, K. *et al.* Optimization of the CHARMM additive force field for DNA: Improved treatment of the BI/BII conformational equilibrium. *J Chem Theory Comput* **8**, 348-362, doi:10.1021/ct200723y (2012).

302 Rahman, A. M., Yusuf, S. W. & Ewer, M. S. Anthracycline-induced cardiotoxicity and the cardiac-sparing effect of liposomal formulation. *Int J Nanomedicine* **2**, 567-583 (2007).

303 Barpe, D. R., Rosa, D. D. & Froehlich, P. E. Pharmacokinetic evaluation of doxorubicin plasma levels in normal and overweight patients with breast cancer and simulation of dose adjustment by different indexes of body mass. *Eur J Pharm Sci* **41**, 458-463, doi:10.1016/j.ejps.2010.07.015 S0928-0987(10)00282-4 [pii] (2010).

304 Jelic, S. *et al.* [A pilot study of high-dose zorubicin in advanced stages of soft tissue sarcoma in adults]. *Bull Cancer* **83**, 1002-1007 (1996).

305 Husain, N., Agbaria, R. A. & Warner, I. M. Spectroscopic Analysis of the Binding of Doxorubicin to Human Alpha-1-Acid Glycoprotein. *J Phys Chem-Us* **97**, 10857-10861, doi:Doi 10.1021/J100143a054 (1993).

306 Alsaad, A. M., Zordoky, B. N., El-Sherbeni, A. A. & El-Kadi, A. O. Chronic doxorubicin cardiotoxicity modulates cardiac cytochrome P450-mediated arachidonic acid metabolism in rats. *Drug Metab Dispos* **40**, 2126-2135, doi:10.1124/dmd.112.046631 dmd.112.046631 [pii] (2012).

307 Zordoky, B. N., Anwar-Mohamed, A., Aboutabl, M. E. & El-Kadi, A. O. Acute doxorubicin toxicity differentially alters cytochrome P450 expression and arachidonic acid metabolism in rat kidney and liver. *Drug Metab Dispos* **39**, 1440-1450, doi:10.1124/dmd.111.039123 dmd.111.039123 [pii] (2011).

308 Zordoky, B. N., Anwar-Mohamed, A., Aboutabl, M. E. & El-Kadi, A. O. Acute doxorubicin cardiotoxicity alters cardiac cytochrome P450 expression and arachidonic acid metabolism in rats. *Toxicol Appl Pharmacol* **242**, 38-46, doi:10.1016/j.taap.2009.09.012 S0041-008X(09)00404-9 [pii] (2010).

309 Imig, J. D. Eicosanoid regulation of the renal vasculature. *Am J Physiol Renal Physiol* **279**, F965-981 (2000).

310 Pozzi, A. *et al.* Characterization of 5,6- and 8,9-epoxyeicosatrienoic acids (5,6- and 8,9-EET) as potent in vivo angiogenic lipids. *Journal of Biological Chemistry* **280**, 27138-27146, doi:M501730200 [pii] 10.1074/jbc.M501730200 (2005).

311 McDougle, D. R., Palaria, A., Magnetta, E., Meling, D.D, and Das, A. Functional studies of N-terminally modified CYP2J2 epoxygenase in model lipid bilayers. *Protein Science* (2013).

312 Mulrooney, S. B. & Waskell, L. High-level expression in Escherichia coli and purification of the membrane-bound form of cytochrome b(5). *Protein Expr Purif* **19**, 173-178, doi:10.1006/prep.2000.1228 S1046-5928(00)91228-2 [pii] (2000).

313 Matsuda, M., Mizuki, Y. & Terauchi, Y. Simultaneous determination of the histamine H-1-receptor antagonist ebastine and its two metabolites, carebastine and hydroxyebastine, in human plasma using high-performance liquid chromatography (vol B757, pg 173, 2001). *J Chromatogr B* **765**, 205-205, doi:Doi 10.1016/S0378-4347(01)00534-5 (2001).

314 Cheng, Y. & Prusoff, W. H. Relationship between the inhibition constant (K1) and the concentration of inhibitor which causes 50 per cent inhibition (I50) of an enzymatic reaction. *Biochem Pharmacol* **22**, 3099-3108 (1973).

315 Mendizabal, V. E. & Adler-Graschinsky, E. Cannabinoids as therapeutic agents in cardiovascular disease: a tale of passions and illusions. *Brit J Pharmacol* **151**, 427-440, doi:10.1038/sj.bjp.0707261 (2007).

316 Randall, M. D., Kendall, D. A. & O'Sullivan, S. The complexities of the cardiovascular actions of cannabinoids. *Br J Pharmacol* **142**, 20-26, doi:10.1038/sj.bjp.0705725 142/1/20 [pii] (2004).

317 Fredericks, A. B., Benowitz, N. L. & Savanapridi, C. Y. The cardiovascular and autonomic effects of repeated administration of delta-9-tetrahydrocannabinol to rhesus monkeys. *J Pharmacol Exp Ther* **216**, 247-253 (1981).

318 Dewey, W. L. Cannabinoid pharmacology. *Pharmacol Rev* **38**, 151-178 (1986).

319 Adams, M. D., Chait, L. D. & Earnhardt, J. T. Tolerance to the cardiovascular effects of delta9-tetrahydrocannabinol in the rat. *Br J Pharmacol* **56**, 43-48 (1976).

320 Jones, R. T. Cardiovascular system effects of marijuana. *J Clin Pharmacol* **42**, 58s-63s, doi:10.1177/0091270002238795 (2002).

321 Jiang, R., Yamaori, S., Takeda, S., Yamamoto, I. & Watanabe, K. Identification of cytochrome P450 enzymes responsible for metabolism of cannabidiol by human liver microsomes. *Life Sci* **89**, 165-170, doi:10.1016/j.lfs.2011.05.018 S0024-3205(11)00264-5 [pii] (2011).

322 Yamaori, S. *et al.* Structural requirements for potent direct inhibition of human cytochrome P450 1A1 by cannabidiol: role of pentylresorcinol moiety. *Biol Pharm Bull* **36**, 1197-1203, doi:DN/JST.JSTAGE/bpb/b13-00183 [pii] (2013).

323 Yamaori, S., Kushihara, M., Yamamoto, I. & Watanabe, K. Characterization of major phytocannabinoids, cannabidiol and cannabinol, as isoform-selective and potent inhibitors of human CYP1 enzymes. *Biochemical Pharmacology* **79**, 1691-1698, doi:10.1016/j.bcp.2010.01.028 (2010).

324 Yamaori, S., Maeda, C., Yamamoto, I. & Watanabe, K. Differential inhibition of human cytochrome P450 2A6 and 2B6 by major phytocannabinoids. *Forensic Toxicol* **29**, 117-124, doi:10.1007/s11419-011-0112-7 (2011).

325 Bornheim, L. M., Everhart, E. T., Li, J. M. & Correia, M. A. Induction and Genetic-Regulation of Mouse Hepatic Cytochrome-P450 by Cannabidiol. *Biochemical Pharmacology* **48**, 161-171, doi:Doi 10.1016/0006-2952(94)90236-4 (1994).

326 Bland, T. M., Haining, R. L., Tracy, T. S. & Callery, P. S. CYP2C-catalyzed delta9-tetrahydrocannabinol metabolism: kinetics, pharmacogenetics and interaction with phenytoin. *Biochemical Pharmacology* **70**, 1096-1103, doi:S0006-2952(05)00458-2 [pii] 10.1016/j.bcp.2005.07.007 (2005).

327 Jaeger, W., Benet, L. Z. & Bornheim, L. M. Inhibition of cyclosporine and tetrahydrocannabinol metabolism by cannabidiol in mouse and human microsomes. *Xenobiotica* **26**, 275-284 (1996).

328 Yamaori, S. *et al.* Comparison in the in vitro inhibitory effects of major phytocannabinoids and polycyclic aromatic hydrocarbons contained in marijuana smoke on cytochrome P450 2C9 activity. *Drug Metab Pharmacokinet* **27**, 294-300, doi:JST.JSTAGE/dmpk/DMPK-11-RG-107 [pii] (2012).

329 Yamamoto, I., Watanabe, K., Narimatsu, S. & Yoshimura, H. Recent advances in the metabolism of cannabinoids. *Int J Biochem Cell Biol* **27**, 741-746, doi:1357-2725(95)00043-O [pii] (1995).

330 Jiang, R. R., Yamaori, S., Okamoto, Y., Yamamoto, I. & Watanabe, K. Cannabidiol Is a Potent Inhibitor of the Catalytic Activity of Cytochrome P450 2C19. *Drug Metab Pharmacok* **28**, 332-338, doi:10.2133/dmpk.DMPK-12-RG-129 (2013).

331 Yamaori, S., Okamoto, Y., Yamamoto, I. & Watanabe, K. Cannabidiol, a Major Phytocannabinoid, As a Potent Atypical Inhibitor for CYP2D6. *Drug Metabolism and Disposition* **39**, 2049-2056, doi:10.1124/dmd.111.041384 (2011).

332 Gaston, T. E. & Friedman, D. Pharmacology of cannabinoids in the treatment of epilepsy. *Epilepsy Behav* **70**, 313-318, doi:10.1016/j.yebeh.2016.11.016 (2017).

333 Bornheim, L. M. & Grillo, M. P. Characterization of cytochrome P450 3A inactivation by cannabidiol: possible involvement of cannabidiol-hydroxyquinone as a P450 inactivator. *Chem Res Toxicol* **11**, 1209-1216, doi:10.1021/tx9800598 tx9800598 [pii] (1998).

334 Maccarrone, M. Metabolism of the Endocannabinoid Anandamide: Open Questions after 25 Years. *Front Mol Neurosci* **10**, doi:Artn 166 10.3389/Fnmol.2017.00166 (2017).

335 Di Marzo, V. & Piscitelli, F. The Endocannabinoid System and its Modulation by Phytocannabinoids. *Neurotherapeutics* **12**, 692-698, doi:10.1007/s13311-015-0374-6 10.1007/s13311-015-0374-6 [pii] (2015).

336 Maccarrone, M. *et al.* Endocannabinoid signaling at the periphery: 50 years after THC. *Trends Pharmacol Sci* **36**, 277-296, doi:10.1016/j.tips.2015.02.008 (2015).

337 Pacher, P. & Kunos, G. Modulating the endocannabinoid system in human health and disease successes and failures. *Febs J* **280**, 1918-1943, doi:10.1111/febs.12260 (2013).

338 McPartland, J. M., Guy, G. W. & Di Marzo, V. Care and feeding of the endocannabinoid system: a systematic review of potential clinical interventions that upregulate the endocannabinoid system. *PLoS One* **9**, e89566, doi:10.1371/journal.pone.0089566 PONE-D-13-39668 [pii] (2014).

339 Woods, S. C. Role of the endocannabinoid system in regulating cardiovascular and metabolic risk factors. *Am J Med* **120**, S19-25, doi:S0002-9343(07)00034-4 [pii] 10.1016/j.amjmed.2007.01.004 (2007).

340 Ashton, J. C. & Smith, P. F. Cannabinoids and cardiovascular disease: the outlook for clinical treatments. *Curr Vasc Pharmacol* **5**, 175-185 (2007).

341 O'Sullivan, S. E., Kendall, P. J. & Kendall, D. A. Endocannabinoids and the cardiovascular response to stress. *J Psychopharmacol* **26**, 71-82, doi:10.1177/0269881111408457 0269881111408457 [pii] (2012).

342 Pacher, P. *et al.* Modulation of the endocannabinoid system in cardiovascular disease: therapeutic potential and limitations. *Hypertension* **52**, 601-607, doi:10.1161/HYPERTENSIONAHA.105.063651 HYPERTENSIONAHA.105.063651 [pii] (2008).

343 Pacher, P., Steffens, S., Hasko, G., Schindler, T. H. & Kunos, G. Cardiovascular effects of marijuana and synthetic cannabinoids: the good, the bad, and the ugly. *Nat Rev Cardiol*, doi:10.1038/nrcardio.2017.130 nrcardio.2017.130 [pii] (2017).

344 Rezkalla, S., Stankowski, R. & Kloner, R. A. Cardiovascular Effects of Marijuana. *J Cardiovasc Pharmacol Ther* **21**, 452-455, doi:10.1177/1074248415627874 1074248415627874 [pii] (2016).

345 Montecucco, F. & Di Marzo, V. At the heart of the matter: the endocannabinoid system in cardiovascular function and dysfunction. *Trends Pharmacol Sci* **33**, 331-340, doi:10.1016/j.tips.2012.03.002 (2012).

346 Steffens, S. & Pacher, P. Targeting cannabinoid receptor CB2 in cardiovascular disorders: promises and controversies. *Brit J Pharmacol* **167**, 313-323, doi:10.1111/j.1476-5381.2012.02042.x (2012).

347 Zubrzycki, M., Liebold, A., Janecka, A. & Zubrzycka, M. A New Face of Endocannabinoids in Pharmacotherapy Part Ii. Role of Endocannabinoids in Inflammation-Derived Cardiovascular Diseases. *J Physiol Pharmacol* **65**, 183-191 (2014).

348 Bornheim, L. M., Kim, K. Y., Chen, B. & Correia, M. A. The effect of cannabidiol on mouse hepatic microsomal cytochrome P450-dependent anandamide metabolism. *Biochem Biophys Res Commun* **197**, 740-746, doi:S0006291X83725416 [pii] (1993).

349 Arnold, W. R., Baylon, J. L., Tajkhorshid, E. & Das, A. Arachidonic Acid Metabolism by Human Cardiovascular CYP2J2 is Modulated by Doxorubicin. *Biochemistry*, doi:10.1021/acs.biochem.7b01025 (2017).

350 Harvey, D. J. Mass-Spectrometry of the Cannabinoids and Their Metabolites. *Mass Spectrom Rev* **6**, 135-229, doi:DOI 10.1002/mas.1280060104 (1987).

351 Harvey, D. J. Absorption, distribution, and biotransformation of the cannabinoids. *Marihuana and Medicine*, 91-103 (1999).

352 Narimatsu, S. *et al.* Cytochrome P-450 isozymes in metabolic activation of delta 9-tetrahydrocannabinol by rat liver microsomes. *Drug Metab Dispos* **18**, 943-948 (1990).

353 Yamamoto, I. *et al.* Pharmacology and toxicology of major constituents of marijuana - On the metabolic activation of cannabinoids and its mechanism. *J Toxicol-Toxin Rev* **22**, 577-589, doi:10.1081/Txr-120026915 (2003).

354 Watanabe, K. *et al.* Catalytic Activity of Cytochrome-P450 Isozymes Purified from Rat-Liver in Converting 11-Oxo-Delta-8-Tetrahydrocannabinol to Delta-8-Tetrahydrocannabinol-11-Oic Acid. *Biochemical Pharmacology* **42**, 1255-1259, doi:Doi 10.1016/0006-2952(91)90262-4 (1991).

355 Matsunaga, T. *et al.* Characterization of microsomal alcohol oxygenase catalyzing the oxidation of 7-hydroxy-Delta(8)-tetrahydrocannabinol to 7-oxo-Delta(8)-tetrahydrocannabinol in rat liver. *Biological & Pharmaceutical Bulletin* **23**, 43-46 (2000).
356 Watanabe, K., Yamaori, S., Funahashi, T., Kimura, T. & Yamamoto, I. Cytochrome P450 enzymes involved in the metabolism of tetrahydrocannabinols and cannabinol by human hepatic microsomes. *Life Sci* **80**, 1415-1419, doi:10.1016/j.lfs.2006.12.032 (2007).
357 Huestis, M. A. Human cannabinoid pharmacokinetics. *Chem Biodivers* **4**, 1770-1804, doi:DOI 10.1002/cbdv.200790152 (2007).
358 Watanabe, K., Tanaka, T., Yamamoto, I. & Yoshimura, H. Brain Microsomal Oxidation of Delta-8-Tetrahydrocannabinol and Delta-9-Tetrahydrocannabinol. *Biochemical and Biophysical Research Communications* **157**, 75-80, doi:Doi 10.1016/S0006-291x(88)80013-5 (1988).
359 Elmes, M. W. *et al.* Fatty acid-binding proteins (FABPs) are intracellular carriers for Delta9-tetrahydrocannabinol (THC) and cannabidiol (CBD). *J Biol Chem* **290**, 8711-8721, doi:10.1074/jbc.M114.618447 (2015).
360 Bisogno, T. *et al.* Molecular targets for cannabidiol and its synthetic analogues: effect on vanilloid VR1 receptors and on the cellular uptake and enzymatic hydrolysis of anandamide. *Br J Pharmacol* **134**, 845-852, doi:10.1038/sj.bjp.0704327 (2001).
361 Snider, N. T., Nast, J. A., Tesmer, L. A. & Hollenberg, P. F. A Cytochrome P450-Derived Epoxygenated Metabolite of Anandamide Is a Potent Cannabinoid Receptor 2-Selective Agonist. *Molecular Pharmacology* **75**, 965-972, doi:10.1124/mol.108.053439 (2009).
362 Ohlsson, A. *et al.* Synthesis and Psychotropic Activity of Side-Chain Hydroxylated Delta-6-Tetrahydrocannabinol Metabolites. *Acta Pharm Suec* **16**, 21-33 (1979).
363 Piomelli, D. The molecular logic of endocannabinoid signalling. *Nat Rev Neurosci* **4**, 873-884, doi:10.1038/nrn1247 (2003).
364 Hedegaard, H., Warner, M. & Minino, A. M. Drug Overdose Deaths in the United States, 1999-2016. *NCHS data brief*, 1-8 (2017).
365 Park, K. A. & Vasko, M. R. Lipid mediators of sensitivity in sensory neurons. *Trends Pharmacol Sci* **26**, 571-577 (2005).
366 Serhan, C. N. & Chiang, N. Resolution phase lipid mediators of inflammation: agonists of resolution. *Current opinion in pharmacology* **13**, 632-640, doi:10.1016/j.coph.2013.05.012 (2013).
367 Piomelli, D. & Sasso, O. Peripheral gating of pain signals by endogenous lipid mediators. *Nature neuroscience* **17**, 164-174 (2014).
368 Malan, T. P., Jr. & Porreca, F. Lipid mediators regulating pain sensitivity. *Prostaglandins & Other Lipid Mediators* **77**, 123-130 (2005).
369 Gerak, L. R. & France, C. P. Combined Treatment with Morphine and Delta(9)-Tetrahydrocannabinol in Rhesus Monkeys: Antinociceptive Tolerance and Withdrawal. *Journal of Pharmacology and Experimental Therapeutics* **357**, 357-366, doi:10.1124/jpet.115.231381 (2016).
370 Guindon, J. & Hohmann, A. G. The endocannabinoid system and pain. *CNS & neurological disorders drug targets* **8**, 403-421 (2009).
371 Di Marzo, V., Bifulco, M. & De Petrocellis, L. The endocannabinoid system and its therapeutic exploitation. *Nature reviews. Drug discovery* **3**, 771-784, doi:10.1038/nrd1495 (2004).

372 Palazzo, E. *et al.* Changes in cannabinoid receptor subtype 1 activity and interaction with metabotropic glutamate subtype 5 receptors in the periaqueductal gray-rostral ventromedial medulla pathway in a rodent neuropathic pain model. *CNS Neurol Disord Drug Targets* **11**, 148-161 (2012).

373 Amaya, F. *et al.* Induction of CB1 cannabinoid receptor by inflammation in primary afferent neurons facilitates antihyperalgesic effect of peripheral CB1 agonist. *Pain* **124**, 175-183 (2006).

374 Fagerberg, L. *et al.* Analysis of the human tissue-specific expression by genome-wide integration of transcriptomics and antibody-based proteomics. *Mol Cell Proteomics* **13**, 397-406, doi:10.1074/mcp.M113.035600 M113.035600 [pii] (2014).

375 Guindon, J. & Hohmann, A. G. Cannabinoid CB2 receptors: a therapeutic target for the treatment of inflammatory and neuropathic pain. *British Journal of Pharmacology* **153**, 319-334 (2008).

376 Costa, B., Giagnoni, G., Franke, C., Trovato, A. E. & Colleoni, M. Vanilloid TRPV1 receptor mediates the antihyperalgesic effect of the nonpsychoactive cannabinoid, cannabidiol, in a rat model of acute inflammation. *Br J Pharmacol* **143**, 247-250, doi:10.1038/sj.bjp.0705920 (2004).

377 Morales, P., Hurst, D. P. & Reggio, P. H. Molecular Targets of the Phytocannabinoids: A Complex Picture. *Prog Chem Org Nat Pr* **103**, 103-131, doi:10.1007/978-3-319-45541-9_4 (2017).

378 Jara-Oseguera, A., Simon, S. A. & Rosenbaum, T. TRPV1: on the road to pain relief. *Current molecular pharmacology* **1**, 255-269 (2008).

379 Anand, P. & Bley, K. Topical capsaicin for pain management: therapeutic potential and mechanisms of action of the new high-concentration capsaicin 8% patch. *British journal of anaesthesia* **107**, 490-502, doi:10.1093/bja/aer260 (2011).

380 Grabiec, U. & Dehghani, F. N-Arachidonoyl Dopamine: A Novel Endocannabinoid and Endovanilloid with Widespread Physiological and Pharmacological Activities. *Cannabis and cannabinoid research* **2**, 183-196, doi:10.1089/can.2017.0015 (2017).

381 Bang, S., Yoo, S., Yang, T. J., Cho, H. & Hwang, S. W. 17(R)-resolvin D1 specifically inhibits transient receptor potential ion channel vanilloid 3 leading to peripheral antinociception. *British Journal of Pharmacology* **165**, 683-692 (2012).

382 Bisogno, T. *et al.* N-acyl-dopamines: novel synthetic CB(1) cannabinoid-receptor ligands and inhibitors of anandamide inactivation with cannabimimetic activity in vitro and in vivo. *Biochem J* **351 Pt 3**, 817-824 (2000).

383 Bisogno, T. *et al.* Arachidonoylserotonin and other novel inhibitors of fatty acid amide hydrolase. *Biochem Biophys Res Commun* **248**, 515-522, doi:S0006291X9898874X [pii] (1998).

384 Bezuglov, V. V., Bobrov, M. & Archakov, A. V. Bioactive amides of fatty acids. *Biochemistry (Mosc)* **63**, 22-30 (1998).

385 Huang, S. M. *et al.* An endogenous capsaicin-like substance with high potency at recombinant and native vanilloid VR1 receptors. *Proc Natl Acad Sci U S A* **99**, 8400-8405, doi:10.1073/pnas.122196999 99/12/8400 [pii] (2002).

386 Siller, M. *et al.* Oxidation of endogenous N-arachidonoylserotonin by human cytochrome P450 2U1. *Journal of Biological Chemistry* **289**, 10476-10487, doi:10.1074/jbc.M114.550004 M114.550004 [pii] (2014).

387 Verhoeckx, K. C. *et al.* Presence, formation and putative biological activities of N-acyl serotonins, a novel class of fatty-acid derived mediators, in the intestinal tract. *Biochim Biophys Acta* **1811**, 578-586, doi:10.1016/j.bbalip.2011.07.008 S1388-1981(11)00133-8 [pii] (2011).

388 Yoo, J. M., Sok, D. E. & Kim, M. R. Effect of endocannabinoids on IgE-mediated allergic response in RBL-2H3 cells. *Int Immunopharmacol* **17**, 123-131, doi:10.1016/j.intimp.2013.05.013 (2013).

389 Taberner, F. J., Fernandez-Ballester, G., Fernandez-Carvajal, A. & Ferrer-Montiel, A. TRP channels interaction with lipids and its implications in disease. *Biochim Biophys Acta* **1848**, 1818-1827, doi:10.1016/j.bbamem.2015.03.022 (2015).

390 Green, D. *et al.* Central activation of TRPV1 and TRPA1 by novel endogenous agonists contributes to mechanical allodynia and thermal hyperalgesia after burn injury. *Molecular pain* **12**, doi:10.1177/1744806916661725 (2016).

391 Arnold, W. R., Weigle, A. T. & Das, A. Cross-talk of cannabinoid and endocannabinoid metabolism is mediated via human cardiac CYP2J2. *Journal of inorganic biochemistry* **184**, 88-99, doi:10.1016/j.jinorgbio.2018.03.016 (2018).

392 Hu, S. S. *et al.* The biosynthesis of N-arachidonoyl dopamine (NADA), a putative endocannabinoid and endovanilloid, via conjugation of arachidonic acid with dopamine. *Prostaglandins, leukotrienes, and essential fatty acids* **81**, 291-301, doi:10.1016/j.plefa.2009.05.026 (2009).

393 Marinelli, S. *et al.* N-arachidonoyl-dopamine tunes synaptic transmission onto dopaminergic neurons by activating both cannabinoid and vanilloid receptors. *Neuropsychopharmacol* **32**, 298-308, doi:10.1038/sj.npp.1301118 (2007).

394 Buczynski, M. W. & Parsons, L. H. Quantification of brain endocannabinoid levels: methods, interpretations and pitfalls. *Br J Pharmacol* **160**, 423-442, doi:10.1111/j.1476-5381.2010.00787.x (2010).

395 Schmid, P. C. *et al.* Occurrence and postmortem generation of anandamide and other long-chain N-acylethanolamines in mammalian brain. *Febs Lett* **375**, 117-120 (1995).

396 Inoue, K. & Tsuda, M. Microglia in neuropathic pain: cellular and molecular mechanisms and therapeutic potential. *Nat Rev Neurosci* **19**, 138-152, doi:10.1038/nrn.2018.2 (2018).

397 Zhao, H. *et al.* The role of microglia in the pathobiology of neuropathic pain development: what do we know? *Br J Anaesth* **118**, 504-516 (2017).

398 Graber, M. N., Alfonso, A. & Gill, D. L. Recovery of Ca2+ pools and growth in Ca2+ pool-depleted cells is mediated by specific epoxyeicosatrienoic acids derived from arachidonic acid. *Journal of Biological Chemistry* **272**, 29546-29553, doi:DOI 10.1074/jbc.272.47.29546 (1997).

399 Graves, J. P. *et al.* Quantitative Polymerase Chain Reaction Analysis of the Mouse Cyp2j Subfamily: Tissue Distribution and Regulation. *Drug Metab Dispos* **43**, 1169-1180, doi:10.1124/dmd.115.064139 (2015).

400 Ferguson, C. S. & Tyndale, R. F. Cytochrome P450 enzymes in the brain: emerging evidence of biological significance. *Trends Pharmacol Sci* **32**, 708-714, doi:10.1016/j.tips.2011.08.005 (2011).

401 Napolitano, A., Pezzella, A. & Prota, G. New reaction pathways of dopamine under oxidative stress conditions: nonenzymatic iron-assisted conversion to norepinephrine and the neurotoxins 6-hydroxydopamine and 6, 7-dihydroxytetrahydroisoquinoline. *Chem Res Toxicol* **12**, 1090-1097, doi:tx990079p [pii] (1999).

402 Napolitano, A., Crescenzi, O., Pezzella, A. & Prota, G. Generation of the neurotoxin 6-hydroxydopamine by peroxidase/H2O2 oxidation of dopamine. *J Med Chem* **38**, 917-922 (1995).
403 Carnevale, L., Arango, A., Arnold, W. R., Tajkhorshid, E. & Das, A. Endocannabinoid Virodhamine is an Endogenous Inhibitor of Human Cardiovascular CYP2J2 Epoxygenase. *Biochemistry*, doi:10.1021/acs.biochem.8b00691 (2018).
404 Arnold, W. R., Baylon, J. L., Tajkhorshid, E. & Das, A. Arachidonic Acid Metabolism by Human Cardiovascular CYP2J2 Is Modulated by Doxorubicin. *Biochemistry* **56**, 6700-6712, doi:10.1021/acs.biochem.7b01025 (2017).
405 Lawton, S. K. *et al.* N-Arachidonoyl Dopamine Modulates Acute Systemic Inflammation via Nonhematopoietic TRPV1. *J Immunol* **199**, 1465-1475, doi:10.4049/jimmunol.1602151 (2017).
406 Wilhelmsen, K. *et al.* The endocannabinoid/endovanilloid N-arachidonoyl dopamine (NADA) and synthetic cannabinoid WIN55,212-2 abate the inflammatory activation of human endothelial cells. *J Biol Chem* **289**, 13079-13100, doi:10.1074/jbc.M113.536953 (2014).
407 Costa, B. *et al.* The dual fatty acid amide hydrolase/TRPV1 blocker, N-arachidonoyl-serotonin, relieves carrageenan-induced inflammation and hyperalgesia in mice. *Pharmacological research* **61**, 537-546, doi:10.1016/j.phrs.2010.02.001 (2010).
408 Lam, P. M. *et al.* Activation of recombinant human TRPV1 receptors expressed in SH-SY5Y human neuroblastoma cells increases [Ca(2+)](i), initiates neurotransmitter release and promotes delayed cell death. *Journal of neurochemistry* **102**, 801-811, doi:10.1111/j.1471-4159.2007.04569.x (2007).
409 Pertwee, R. G. Pharmacology of cannabinoid receptor ligands. *Curr Med Chem* **6**, 635-664 (1999).
410 Gao, Y., Cao, E., Julius, D. & Cheng, Y. TRPV1 structures in nanodiscs reveal mechanisms of ligand and lipid action. *Nature* **534**, 347-351, doi:10.1038/nature17964 (2016).
411 Chen, J. *et al.* Spatial Distribution of the Cannabinoid Type 1 and Capsaicin Receptors May Contribute to the Complexity of Their Crosstalk. *Sci Rep-Uk* **6**, doi:Artn 33307 10.1038/Srep33307 (2016).
412 Musella, A. *et al.* A novel crosstalk within the endocannabinoid system controls GABA transmission in the striatum. *Sci Rep-Uk* **7**, doi:Artn 7363 10.1038/S41598-017-07519-8 (2017).
413 Schmittgen, T. D. & Livak, K. J. Analyzing real-time PCR data by the comparative C(T) method. *Nature protocols* **3**, 1101-1108 (2008).
414 Oh, D. Y. *et al.* GPR120 Is an Omega-3 Fatty Acid Receptor Mediating Potent Anti-inflammatory and Insulin-Sensitizing Effects. *Cell* **142**, 687-698, doi:10.1016/j.cell.2010.07.041 (2010).
415 Zhang, M. *et al.* Modulation of the balance between cannabinoid CB1 and CB2 receptor activation during cerebral ischemic/reperfusion injury. *Neuroscience* **152**, 753-760, doi:10.1016/j.neuroscience.2008.01.022 (2008).
416 Phan, T. X., Ton, H. T., Chen, Y., Basha, M. E. & Ahern, G. P. Sex-dependent expression of TRPV1 in bladder arterioles. *Am J Physiol-Renal* **311**, F1063-F1073, doi:10.1152/ajprenal.00234.2016 (2016).

417 Yen, C. H. *et al.* Characterization of a new murine cell line of sarcomatoid hepatocellular carcinoma and its application for biomarker/therapy development. *Sci Rep* **7**, 3052, doi:10.1038/s41598-017-03164-3 (2017).
418 Lafite, P. *et al.* Role of Arginine 117 in Substrate Recognition by Human Cytochrome P450 2J2. *Int J Mol Sci* **19**, doi:10.3390/ijms19072066 (2018).
419 Xie, F. C., Li, B. B. X., Alkayed, N. J. & Xiao, X. S. Synthesis of 14,15-Eet from Arachidonic Acid Using Urea-Hydrogen Peroxide as the Oxidant. *Synthetic Commun* **45**, 105-110, doi:10.1080/00397911.2014.956369 (2015).
420 Corey, E. J., Niwa, H. & Falck, J. R. Selective Epoxidation of Eicosa-Cis-5,8,11,14-Tetraenoic (Arachidonic) Acid and Eicosa-Cis-8,11,14-Trienoic Acid. *J Am Chem Soc* **101**, 1586-1587, doi:Doi 10.1021/Ja00500a035 (1979).
421 GrahamLorence, S. *et al.* An active site substitution, F87V, converts cytochrome p450 BM-3 into a regio- and stereoselective (14S,15R)-arachidonic acid epoxygenase. *Journal of Biological Chemistry* **272**, 1127-1135, doi:DOI 10.1074/jbc.272.2.1127 (1997).
422 Kubo, T., Peters, M. W., Meinhold, P. & Arnold, F. H. Enantioselective epoxidation of terminal alkenes to (R)- and (S)-epoxides by engineered cytochromes P450 BM-3. *Chemistry* **12**, 1216-1220, doi:10.1002/chem.200500584 (2006).
423 Falck, J. R. *et al.* Practical, enantiospecific syntheses of 14,15-EET and leukotoxin B (vernolic acid). *Tetrahedron Lett* **42**, 4131-4133, doi:Doi 10.1016/S0040-4039(01)00694-3 (2001).
424 Mosset, P., Yadagiri, P., Lumin, S., Capdevila, J. & Falck, J. R. Arachidonate Epoxygenase - Total Synthesis of Both Enantiomers of 8,9-Epoxyeicosatrienoic and 11,12-Epoxyeicosatrienoic Acid. *Tetrahedron Lett* **27**, 6035-6038, doi:Doi 10.1016/S0040-4039(00)85391-5 (1986).
425 Moustakis, C. A., Viala, J., Capdevila, J. & Falck, J. R. Total Synthesis of the Cytochrome-P-450 Epoxygenase Metabolites 5(R),6(S)-Epoxyeicosatrienoic, 5(S),6(R)-Epoxyeicosatrienoic, and 14(R),15(S)-Epoxyeicosatrienoic Acid (Eet) and Hydration Products 5(R),6(R)-Dihydroxyeicosatrienoic and "14(R),15(R)-Dihydroxyeicosatrienoic Acid (Dhet). *J Am Chem Soc* **107**, 5283-5285, doi:Doi 10.1021/Ja00304a048 (1985).
426 Falck, J. R., Manna, S. & Capdevila, J. Enantiospecific Synthesis of Methyl 11,12-Epoxyeicosatrienoate and 14,15-Epoxyeicosatrienoate. *Tetrahedron Lett* **25**, 2443-2446, doi:Doi 10.1016/S0040-4039(01)81200-4 (1984).
427 Jat, J. L. *et al.* Regio- and enantioselective catalytic monoepoxidation of conjugated dienes: synthesis of chiral allylic cis-epoxides. *Organic letters* **17**, 1058-1061, doi:10.1021/acs.orglett.5b00281 (2015).
428 Lomsadze, K., Merlani, M., Barbakadze, V., Farkas, T. & Chankvetadze, B. Enantioseparation of Chiral Epoxides with Polysaccharide-Based Chiral Columns in HPLC. *Chromatographia* **75**, 839-845, doi:10.1007/s10337-012-2289-2 (2012).
429 Mesaros, C. & Blair, I. A. Targeted chiral analysis of bioactive arachidonic Acid metabolites using liquid-chromatography-mass spectrometry. *Metabolites* **2**, 337-365, doi:10.3390/metabo2020337 (2012).
430 Falck, J. R. *et al.* Absolute-Configuration of Epoxyeicosatrienoic Acids (Eets) Formed during Catalytic Oxygenation of Arachidonic-Acid by Purified Rat-Liver Microsomal Cytochrome-P-450. *J Am Chem Soc* **106**, 3334-3336, doi:Doi 10.1021/Ja00323a046 (1984).

431 Hammonds, T. D., Blair, I. A., Falck, J. R. & Capdevila, J. H. Resolution of Epoxyeicosatrienoate Enantiomers by Chiral Phase Chromatography. *Anal Biochem* **182**, 300-303, doi:Doi 10.1016/0003-2697(89)90598-8 (1989).
432 Mesaros, C., Lee, S. H. & Blair, I. A. Analysis of epoxyeicosatrienoic acids by chiral liquid chromatography/electron capture atmospheric pressure chemical ionization mass spectrometry using [13C]-analog internal standards. *Rapid communications in mass spectrometry : RCM* **24**, 3237-3247, doi:10.1002/rcm.4760 (2010).
433 Lucas, D. *et al.* Stereoselective epoxidation of the last double bond of polyunsaturated fatty acids by human cytochromes P450. *J Lipid Res* **51**, 1125-1133, doi:10.1194/jlr.M003061 (2010).
434 Zeldin, D. C., DuBois, R. N., Falck, J. R. & Capdevila, J. H. Molecular cloning, expression and characterization of an endogenous human cytochrome P450 arachidonic acid epoxygenase isoform. *Arch Biochem Biophys* **322**, 76-86, doi:10.1006/abbi.1995.1438 (1995).
435 Daikh, B. E., Lasker, J. M., Raucy, J. L. & Koop, D. R. Regio- and stereoselective epoxidation of arachidonic acid by human cytochromes P450 2C8 and 2C9. *J Pharmacol Exp Ther* **271**, 1427-1433 (1994).
436 Barbosa-Sicard, E. *et al.* Eicosapentaenoic acid metabolism by cytochrome P450 enzymes of the CYP2C subfamily. *Biochem Biophys Res Commun* **329**, 1275-1281, doi:10.1016/j.bbrc.2005.02.103 (2005).
437 Balazy, M. Metabolism of 5,6-epoxyeicosatrienoic acid by the human platelet. Formation of novel thromboxane analogs. *J Biol Chem* **266**, 23561-23567 (1991).
438 Herse, F. *et al.* Cytochrome P450 subfamily 2J polypeptide 2 expression and circulating epoxyeicosatrienoic metabolites in preeclampsia. *Circulation* **126**, 2990-2999, doi:10.1161/CIRCULATIONAHA.112.127340 (2012).
439 Carroll, M. A. *et al.* Adenosine(2A) receptor vasodilation of rat preglomerular microvessels is mediated by EETs that activate the cAMP/PKA pathway. *Am J Physiol-Renal* **291**, F155-F161, doi:10.1152/ajprenal.00231.2005 (2006).
440 Vriens, J. *et al.* Modulation of the Ca2 permeable cation channel TRPV4 by cytochrome P450 epoxygenases in vascular endothelium. *Circ Res* **97**, 908-915, doi:10.1161/01.RES.0000187474.47805.30 (2005).
441 Zeldin, D. C. *et al.* Regio- and enantiofacial selectivity of epoxyeicosatrienoic acid hydration by cytosolic epoxide hydrolase. *J Biol Chem* **268**, 6402-6407 (1993).
442 Zhang, Y. D. *et al.* EET homologs potently dilate coronary microvessels and activate BKCa channels. *Am J Physiol-Heart C* **280**, H2430-H2440 (2001).
443 Sun, P. *et al.* High Potassium Intake Enhances the Inhibitory Effect of 11,12-EET on ENaC. *J Am Soc Nephrol* **21**, 1667-1677, doi:10.1681/Asn.2009111110 (2010).
444 Zou, A. P. *et al.* Stereospecific effects of epoxyeicosatrienoic acids on renal vascular tone and K+-channel activity. *Am J Physiol-Renal* **270**, F822-F832 (1996).
445 Falck, J. R. *et al.* 17(R),18(S)-Epoxyeicosatetraenoic Acid, a Potent Eicosapentaenoic Acid (EPA) Derived Regulator of Cardiomyocyte Contraction: Structure-Activity Relationships and Stable Analogues. *Journal of Medicinal Chemistry* **54**, 4109-4118, doi:10.1021/jm200132q (2011).
446 VandenBrink, B. M., Foti, R. S., Rock, D. A., Wienkers, L. C. & Wahlstrom, J. L. Evaluation of CYP2C8 Inhibition In Vitro: Utility of Montelukast as a Selective CYP2C8

Probe Substrate. *Drug Metabolism and Disposition* **39**, 1546-1554, doi:10.1124/dmd.111.039065 (2011).

447 Bahadur, N. *et al.* CYP2C8 polymorphisms in Caucasians and their relationship with paclitaxel 6α-hydroxylase activity in human liver microsomes. *Biochemical Pharmacology* **64**, 1579-1589, doi:http://dx.doi.org/10.1016/S0006-2952(02)01354-0 (2002).

448 Lundblad, M. S., Stark, K., Eliasson, E., Oliw, E. & Rane, A. Biosynthesis of epoxyeicosatrienoic acids varies between polymorphic CYP2C enzymes. *Biochemical and Biophysical Research Communications* **327**, 1052-1057, doi:http://dx.doi.org/10.1016/j.bbrc.2004.12.116 (2005).

449 Marupudi, N. I. *et al.* Paclitaxel: a review of adverse toxicities and novel delivery strategies. *Expert opinion on drug safety* **6**, 609-621, doi:10.1517/14740338.6.5.609 (2007).

450 Klose, T. S., Blaisdell, J. A. & Goldstein, J. A. Gene structure of CYP2C8 and extrahepatic distribution of the human CYP2Cs. *Journal of biochemical and molecular toxicology* **13**, 289-295, doi:10.1002/(sici)1099-0461(1999)13:6<289::aid-jbt1>3.0.co;2-n (1999).

451 Enayetallah, A. E., French, R. A., Thibodeau, M. S. & Grant, D. F. Distribution of Soluble Epoxide Hydrolase and of Cytochrome P450 2C8, 2C9, and 2J2 in Human Tissues. *Journal of Histochemistry & Cytochemistry* **52**, 447-454, doi:10.1177/002215540405200403 (2004).

452 Node, K. *et al.* Anti-inflammatory Properties of Cytochrome P450 Epoxygenase-Derived Eicosanoids. *Science (New York, N.Y.)* **285**, 1276-1279 (1999).

453 Michaelis, U. R. *et al.* Cytochrome P450 2C9-derived epoxyeicosatrienoic acids induce angiogenesis via cross-talk with the epidermal growth factor receptor. *The FASEB Journal* (2003).

454 Sun, J. *et al.* Inhibition of Vascular Smooth Muscle Cell Migration by Cytochrome P450 Epoxygenase-Derived Eicosanoids. *Circ Res* **90**, 1020-1027, doi:10.1161/01.res.0000017727.35930.33 (2002).

455 Zhou, S. F. Polymorphism of human cytochrome P450 2D6 and its clinical significance: Part I. *Clinical pharmacokinetics* **48**, 689-723, doi:10.2165/11318030-000000000-00000 (2009).

456 Zhou, S. F. Polymorphism of human cytochrome P450 2D6 and its clinical significance: part II. *Clinical pharmacokinetics* **48**, 761-804, doi:10.2165/11318070-000000000-00000 (2009).

457 Dai, D. *et al.* Polymorphisms in human CYP2C8 decrease metabolism of the anticancer drug paclitaxel and arachidonic acid. *Pharmacogenetics and Genomics* **11**, 597-607 (2001).

458 Yu, L., Shi, D., Ma, L., Zhou, Q. & Zeng, S. Influence of CYP2C8 polymorphisms on the hydroxylation metabolism of paclitaxel, repaglinide and ibuprofen enantiomers in vitro. *Biopharmaceutics & Drug Disposition* **34**, 278-287, doi:10.1002/bdd.1842 (2013).

459 Hertz, D. *et al.* Genetic heterogeneity beyond CYP2C8*3 does not explain differential sensitivity to paclitaxel-induced neuropathy. *Breast Cancer Res Treat* **145**, 245-254, doi:10.1007/s10549-014-2910-1 (2014).

460 Hertz, D. L. *et al.* CYP2C8*3 increases risk of neuropathy in breast cancer patients treated with paclitaxel(). *Annals of Oncology* **24**, 1472-1478, doi:10.1093/annonc/mdt018 (2013).

461 Soyama, A. *et al.* Non-synonymous Single Nucleotide Alterations Found in the CYP2C8 Gene Result in Reduced in Vitro Paclitaxel Metabolism. *Biological and Pharmaceutical Bulletin* **24**, 1427-1430, doi:10.1248/bpb.24.1427 (2001).

462 Kaspera, R. *et al.* Drug metabolism by CYP2C8.3 is determined by substrate dependent interactions with cytochrome P450 reductase and cytochrome b5. *Biochemical Pharmacology* **82**, 681-691, doi: 2011).

463 Gao, Y., Liu, D., Wang, H., Zhu, J. & Chen, C. Functional characterization of five CYP2C8 variants and prediction of CYP2C8 genotype-dependent effects on in vitro and in vivo drug–drug interactions. *Xenobiotica* **40**, 467-475, doi:doi:10.3109/00498254.2010.487163 (2010).

464 Soyama, A. *et al.* Amiodarone N-deethylation by CYP2C8 and its variants, CYP2C8*3 and CYP2C8 P404A. *Pharmacology & toxicology* **91**, 174-178 (2002).

465 Denisov, I. G., Makris, T. M., Sligar, S. G. & Schlichting, I. Structure and chemistry of cytochrome P450. *Chemical reviews* **105**, 2253-2277, doi:10.1021/cr0307143 (2005).

466 Fleming, I. *et al.* Endothelium-Derived Hyperpolarizing Factor Synthase (Cytochrome P450 2C9) Is a Functionally Significant Source of Reactive Oxygen Species in Coronary Arteries. *Circ Res* **88**, 44-51, doi:10.1161/01.res.88.1.44 (2001).

467 Edin, M. L. *et al.* Endothelial expression of human cytochrome P450 epoxygenase CYP2C8 increases susceptibility to ischemia-reperfusion injury in isolated mouse heart. *The FASEB Journal* **25**, 3436-3447, doi:10.1096/fj.11-188300 (2011).

468 Nesnow, S. *et al.* Propiconazole increases reactive oxygen species levels in mouse hepatic cells in culture and in mouse liver by a cytochrome P450 enzyme mediated process. *Chemico-Biological Interactions* **194**, 79-89, doi:http://dx.doi.org/10.1016/j.cbi.2011.08.002 (2011).

469 Leung, T. *et al.* Cytochrome P450 2E1 (CYP2E1) regulates the response to oxidative stress and migration of breast cancer cells. *Breast Cancer Research* **15**, R107 (2013).

470 Hunter, A. L., Bai, N., Laher, I. & Granville, D. J. Cytochrome p450 2C inhibition reduces post-ischemic vascular dysfunction. *Vascular Pharmacology* **43**, 213-219, doi:http://dx.doi.org/10.1016/j.vph.2005.07.005 (2005).

471 Bayburt, T. H., Grinkova, Y. V. & Sligar, S. G. Self-assembly of discoidal phospholipid bilayer nanoparticles with membrane scaffold proteins. *Nano Lett* **2**, 853-856, doi:Doi 10.1021/Nl025623k (2002).

472 Orlando, B. J. *et al.* Cyclooxygenase-2 catalysis and inhibition in lipid bilayer nanodiscs. *Arch Biochem Biophys* **546**, 33-40, doi:10.1016/j.abb.2014.01.026 S0003-9861(14)00053-8 [pii] (2014).

473 Das, A., Varma, S. S., Mularczyk, C. & Meling, D. D. Functional investigations of thromboxane synthase (CYP5A1) in lipid bilayers of nanodiscs. *Chembiochem* **15**, 892-899, doi:10.1002/cbic.201300646 (2014).

474 Zelasko, S., Palaria, A. & Das, A. Optimizations to achieve high-level expression of cytochrome P450 proteins using Escherichia coli expression systems. *Protein Expr Purif* **92**, 77-87, doi:S1046-5928(13)00143-5 [pii] 10.1016/j.pep.2013.07.017 (2013).

475 Kim, H. K. *et al.* Reactive oxygen species (ROS) play an important role in a rat model of neuropathic pain. *Pain* **111**, 116-124, doi:10.1016/j.pain.2004.06.008 (2004).

476 Scripture, C. D., Figg, W. D. & Sparreboom, A. Peripheral neuropathy induced by paclitaxel: recent insights and future perspectives. *Curr Neuropharmacol* **4**, 165-172 (2006).
477 Reed, J. R. & Hollenberg, P. F. New perspectives on the conformational equilibrium regulating multi-phasic reduction of cytochrome P450 2B4 by cytochrome P450 reductase. *Journal of inorganic biochemistry* **97**, 276-286 (2003).
478 Das, A., Grinkova, Y. V. & Sligar, S. G. Redox potential control by drug binding to cytochrome P450 3A4. *J Am Chem Soc* **129**, 13778-13779, doi:10.1021/ja074864x (2007).
479 Sokalingam, S., Raghunathan, G., Soundrarajan, N. & Lee, S. G. A Study on the Effect of Surface Lysine to Arginine Mutagenesis on Protein Stability and Structure Using Green Fluorescent Protein. *Plos One* **7**, doi:ARTN e40410 10.1371/journal.pone.0040410 (2012).
480 Li, L. B., Vorobyov, I. & Allen, T. W. The Different Interactions of Lysine and Arginine Side Chains with Lipid Membranes. *Journal of Physical Chemistry B* **117**, 11906-11920, doi:10.1021/jp405418y (2013).
481 Li, H., Horiguchi, T., Croteau, R. & Williams, R. M. Studies on Taxol Biosynthesis: Preparation of Taxadiene-diol- and triol-Derivatives by Deoxygenation of Taxusin. *Tetrahedron* **64**, 6561-6567, doi:10.1016/j.tet.2008.04.008 (2008).
482 Lokeshwar, B. L., Ferrell, S. M. & Block, N. L. Enhancement of radiation response of prostatic carcinoma by taxol: therapeutic potential for late-stage malignancy. *Anticancer research* **15**, 93-98 (1995).
483 Xu, P., Bhan, N. & Koffas, M. A. G. Engineering plant metabolism into microbes: from systems biology to synthetic biology. *Current opinion in biotechnology* **24**, 291-299, doi:http://dx.doi.org/10.1016/j.copbio.2012.08.010 (2013).
484 Marienhagen, J. & Bott, M. Metabolic engineering of microorganisms for the synthesis of plant natural products. *Journal of Biotechnology* **163**, 166-178, doi:http://dx.doi.org/10.1016/j.jbiotec.2012.06.001 (2013).
485 Keasling, J. D., Mendoza, A. & Baran, P. S. Synthesis: A constructive debate. *Nature* **492**, 188-189 (2012).
486 Keasling, J. D. Manufacturing Molecules Through Metabolic Engineering. *Science* **330**, 1355-1358 (2010).
487 Pickens, L. B., Tang, Y. & Chooi, Y.-H. Metabolic Engineering for the Production of Natural Products. *Annual review of chemical and biomolecular engineering* **2**, 211-236, doi:10.1146/annurev-chembioeng-061010-114209 (2011).
488 Ajikumar, P. K. *et al.* Isoprenoid pathway optimization for Taxol precursor overproduction in Escherichia coli. *Science* **330**, 70-74, doi:10.1126/science.1191652 330/6000/70 [pii] (2010).
489 Biggs, B. W. *et al.* Overcoming heterologous protein interdependency to optimize P450-mediated Taxol precursor synthesis in Escherichia coli. *Proceedings of the National Academy of Sciences*, doi:10.1073/pnas.1515826113 (2016).
490 Hefner, J. *et al.* Cytochrome P450-catalyzed hydroxylation of taxa-4(5),11(12)-diene to taxa-4(20),11(12)-dien-5alpha-ol: the first oxygenation step in taxol biosynthesis. *Chemistry & biology* **3**, 479-489 (1996).
491 Jennewein, S., Long, R. M., Williams, R. M. & Croteau, R. Cytochrome p450 taxadiene 5alpha-hydroxylase, a mechanistically unusual monooxygenase catalyzing the first

oxygenation step of taxol biosynthesis. *Chemistry & biology* **11**, 379-387, doi:10.1016/j.chembiol.2004.02.022 (2004).

492 Rontein, D. *et al.* CYP725A4 from yew catalyzes complex structural rearrangement of taxa-4(5),11(12)-diene into the cyclic ether 5(12)-oxa-3(11)-cyclotaxane. *The Journal of biological chemistry* **283**, 6067-6075, doi:10.1074/jbc.M708950200 (2008).

493 Yadav, V. G. Unraveling the multispecificity and catalytic promiscuity of taxadiene monooxygenase. *Journal of Molecular Catalysis B: Enzymatic* **110**, 154-164, doi:http://dx.doi.org/10.1016/j.molcatb.2014.10.004 (2014).

494 Edgar, S. *et al.* Mechanistic Insights into Taxadiene Epoxidation by Taxadiene-5α-Hydroxylase. *ACS chemical biology* (2015).

495 Barton, N. A. *et al.* Accessing low-oxidation state taxanes: is taxadiene-4 (5)-epoxide on the taxol biosynthetic pathway? *Chemical Science* (2016).

496 Biggs, B. W. *et al.* Orthogonal assays clarify the oxidative biochemistry of Taxol P450 CYP725A4. *ACS Chemical Biology*, doi:10.1021/acschembio.5b00968 (2016).

497 McDougle, D. R., Palaria, A., Magnetta, E., Meling, D. D. & Das, A. Functional studies of N-terminally modified CYP2J2 epoxygenase in model lipid bilayers. *Protein Science* **22**, 964-979, doi:10.1002/pro.2280 (2013).

498 Hammarström, M., Woestenenk, E., Hellgren, N., Härd, T. & Berglund, H. Effect of N-terminal solubility enhancing fusion proteins on yield of purified target protein. *J Struct Funct Genomics* **7**, 1-14, doi:10.1007/s10969-005-9003-7 (2006).

499 Wang, M. *et al.* Three-dimensional structure of NADPH-cytochrome P450 reductase: prototype for FMN- and FAD-containing enzymes. *Proc Natl Acad Sci U S A* **94**, 8411-8416 (1997).

500 Denisov, I. G. & Sligar, S. G. Cytochromes P450 in nanodiscs. *Biochim Biophys Acta* **1814**, 223-229, doi:10.1016/j.bbapap.2010.05.017 S1570-9639(10)00142-1 [pii] (2011).

501 Bayburt, T. H. & Sligar, S. G. Membrane protein assembly into Nanodiscs. *FEBS Letters* **584**, 1721-1727, doi:http://dx.doi.org/10.1016/j.febslet.2009.10.024 (2010).

502 Leitz, A. J., Bayburt, T. H., Barnakov, A. N., Springer, B. A. & Sligar, S. G. Functional reconstitution of Beta2-adrenergic receptors utilizing self-assembling Nanodisc technology. *Biotechniques* **40**, 601-602, 604, 606, passim, doi:000112169 [pii] (2006).

503 Boldog, T., Grimme, S., Li, M., Sligar, S. G. & Hazelbauer, G. L. Nanodiscs separate chemoreceptor oligomeric states and reveal their signaling properties. *Proceedings of the National Academy of Sciences* **103**, 11509-11514 (2006).

504 Nath, A., Atkins, W. M. & Sligar, S. G. Applications of phospholipid bilayer nanodiscs in the study of membranes and membrane proteins. *Biochemistry* **46**, 2059-2069, doi:10.1021/bi602371n (2007).

505 Duan, H. & Schuler, M. Heterologous expression and strategies for encapsulation of membrane-localized plant P450s. *Phytochem Rev* **5**, 507-523, doi:10.1007/s11101-006-9009-1 (2006).

506 Das, A. & Sligar, S. G. Modulation of the Cytochrome P450 Reductase Redox Potential by the Phospholipid Bilayer. *Biochemistry* **48**, 12104-12112, doi:10.1021/bi9011435 (2009).

507 Bayburt, T. H. & Sligar, S. G. Self-assembly of single integral membrane proteins into soluble nanoscale phospholipid bilayers. *Protein Science : A Publication of the Protein Society* **12**, 2476-2481 (2003).

508 Bayburt, T. H. & Sligar, S. G. Single-molecule height measurements on microsomal cytochrome P450 in nanometer-scale phospholipid bilayer disks. *Proceedings of the National Academy of Sciences of the United States of America* **99**, 6725-6730, doi:10.1073/pnas.062565599 (2002).
509 Civjan, N. R., Bayburt, T. H., Schuler, M. A. & Sligar, S. G. Direct solubilization of heterologously expressed membrane proteins by incorporation into nanoscale lipid bilayers. *BioTechniques* **35**, 556-560, 562-553 (2003).
510 Duan, H., Civjan, N. R., Sligar, S. G. & Schuler, M. A. Co-incorporation of heterologously expressed Arabidopsis cytochrome P450 and P450 reductase into soluble nanoscale lipid bilayers. *Archives of biochemistry and biophysics* **424**, 141-153, doi:http://dx.doi.org/10.1016/j.abb.2004.02.010 (2004).
511 McDougle, D. R., Palaria, A., Magnetta, E., Meling, D. D. & Das, A. Functional studies of N-terminally modified CYP2J2 epoxygenase in model lipid bilayers. *Protein Science* **22**, 964-979 (2013).
512 Kelley, L. A., Mezulis, S., Yates, C. M., Wass, M. N. & Sternberg, M. J. E. The Phyre2 web portal for protein modeling, prediction and analysis. *Nat. Protocols* **10**, 845-858, doi:10.1038/nprot.2015.053 (2015).
513 Humphrey, W., Dalke, A. & Schulten, K. VMD: visual molecular dynamics. *Journal of molecular graphics* **14**, 33-38 (1996).
514 Gonzalez, F. J. & Korzekwa, K. R. Cytochromes P450 expression systems. *Annual review of pharmacology and toxicology* **35**, 369-390, doi:10.1146/annurev.pa.35.040195.002101 (1995).
515 Larson, J. R., Coon, M. J. & Porter, T. D. Purification and properties of a shortened form of cytochrome P-450 2E1: deletion of the NH2-terminal membrane-insertion signal peptide does not alter the catalytic activities. *Proceedings of the National Academy of Sciences of the United States of America* **88**, 9141-9145 (1991).
516 von Wachenfeldt, C., Richardson, T. H., Cosme, J. & Johnson, E. F. Microsomal P450 2C3 Is Expressed as a Soluble Dimer inEscherichia coliFollowing Modifications of Its N-terminus. *Archives of biochemistry and biophysics* **339**, 107-114, doi:http://dx.doi.org/10.1006/abbi.1996.9859 (1997).
517 Richardson, T. H. *et al.* A Universal Approach to the Expression of Human and Rabbit Cytochrome P450s of the 2C Subfamily inEscherichia coli. *Archives of biochemistry and biophysics* **323**, 87-96, doi:http://dx.doi.org/10.1006/abbi.1995.0013 (1995).
518 Barnes, H. J., Arlotto, M. P. & Waterman, M. R. Expression and enzymatic activity of recombinant cytochrome P450 17 alpha-hydroxylase in Escherichia coli. *Proc Natl Acad Sci U S A* **88**, 5597-5601 (1991).
519 Miki, Y. & Asano, Y. Biosynthetic Pathway for the Cyanide-Free Production of Phenylacetonitrile in Escherichia coli by Utilizing Plant Cytochrome P450 79A2 and Bacterial Aldoxime Dehydratase. *Applied and environmental microbiology* **80**, 6828-6836, doi:10.1128/AEM.01623-14 (2014).
520 Guo, Z. Y., Gillam, E. M. J., Ohmori, S., Tukey, R. H. & Guengerich, F. P. Expression of Modified Human Cytochrome P450 1A1 in Escherichia coli: Effects of 5′ Substitution, Stabilization, Purification, Spectral Characterization, and Catalytic Properties. *Archives of biochemistry and biophysics* **312**, 436-446, doi:http://dx.doi.org/10.1006/abbi.1994.1330 (1994).

521 C. Budriang, P. R. a. J. Y. An Expression of an Insect Membrane-bound Cytochrome P450 CYP6AA3 in the Escherichia coli in Relation to Insecticide Resistance in a Malarial Vector. *Pakistan Journal of Biological Sciences* **14**, 466-475, doi:10.3923/pjbs.2011.466.475 (2011).

522 Müller, P. *et al.* Field-Caught Permethrin-Resistant Anopheles gambiae Overexpress CYP6P3, a P450 That Metabolises Pyrethroids. *PLoS Genetics* **4**, e1000286, doi:10.1371/journal.pgen.1000286 (2008).

523 Larkin, M. A. *et al.* Clustal W and Clustal X version 2.0. *Bioinformatics* **23**, 2947-2948 (2007).

524 Al-Gailany, K. A. S., Houston, J. B. & Bridges, J. W. The role of substrate lipophilicity in determining type 1 microsomal P450 binding characteristics. *Biochemical Pharmacology* **27**, 783-788, doi:http://dx.doi.org/10.1016/0006-2952(78)90521-X (1978).

525 Baudry, J., Li, W., Pan, L., Berenbaum, M. R. & Schuler, M. A. Molecular docking of substrates and inhibitors in the catalytic site of CYP6B1, an insect cytochrome P450 monooxygenase. *Protein Engineering* **16**, 577-587 (2003).

Appendix A: Polymorphisms of CYP2C8 alter interactions with CPR

A.1 Introduction

Cytochrome P450 2C8 (CYP2C8) is a clinically important member of the cytochrome P450 (CYP) epoxygenase family that metabolizes over 60 drugs on the market [446-448]. For example, CYP2C8 is the primary enzyme involved in the metabolism of paclitaxel (PAC), a common chemotherapeutic that works by interfering with microtubule function [449]. CYP2C8 is primarily expressed hepatically, though it is also present in the vasculature and kidneys [199,450,451]. In the vasculature and kidneys, CYP2C8 metabolizes lipids, such as arachidonic acid (AA), to form biologically active epoxyeicosatrienoic acids (EETs). EETs are known to be anti-inflammatory [452], angiogenic [453], and inhibit vascular smooth muscle cell migration, and so CYP2C8 is important for the physiology of the vasculature and kidneys [454].

Polymorphic variations in CYPs have been of clinical interest due to individual differences in drug metabolism. For example, CYP2D6 is among the most highly polymorphic CYPs that greatly contributes to the poor, intermediate, extensive, and ultra-rapid metabolizer phenotypes [455,456]. Two common, naturally occurring polymorphic variants of CYP2C8—CYP2C8*2 and CYP2C8*3—display altered drug elimination rates and EET production [457,458]. For instance, the CYP2C8*3 polymorphism (R139K/K399R) is present in 2% of African-American and 13% of Caucasian populations [457]. It is interesting to note that these mutations do not change the charge of the residues but instead interchange the Lys or Arg residues. CYP2C8*3 is associated with an increase in peripheral neuropathy in patients treated with PAC, which is presumed to be due to a slower elimination of PAC by CYP2C8*3 [459,460]. *In vitro* studies corroborate that CYP2C8*3 has only 30% and 15% of the activity compared to wild-type (WT) for the turnover of AA and PAC, respectively [457]. However, others report that PAC metabolism is not significantly affected by this polymorphism [458,461], and one study observed greater PAC turnover compared to WT [462]. Therefore, the effects of CYP2C8*3 on PAC metabolism are convoluted. The CYP2C8*2 (I269F) polymorphism, present in 18% of African-American populations [457], shows lower, albeit not always statistically significant, *in vitro* PAC turnover compared to WT [457,458,463].

Importantly, the R139, K399, and I269 residues are not located within the enzyme active site of CYP2C8 but on the surface of the protein (Figure A.1) [447,457,461,462]. This suggests that these

mutations disrupt mechanisms of substrate metabolism not directly related to substrate binding. Indeed, CYP2C8*3 showed WT activity for the deethylation of amiodarone, and so it appears that this polymorphism does not affect substrate binding as a whole [464]. The CYP catalytic cycle is a complex series of redox reactions that require assistance from redox partners such as cytochrome P450 reductase (CPR) (Figure A.1) [465]. Therefore, these mutations may be affecting other steps in the CYP catalytic cycle, such as electron transfer from redox partners. Earlier work demonstrated that CYP2C8*3 has different binding affinities to its redox partners compared to WT. Particularly, CPR interacts with PAC-bound CYP2C8*3 better than WT as determined indirectly by PAC metabolism assays using varying CPR concentrations (K_{mapp} = 5.5 ± 1.5 nM for CYP2C8*3 versus 35 ± 10 nM for WT) [462]. The higher interaction with CPR ought to lead to a faster transfer of electrons and a greater substrate turnover. In the same study, the authors determined that PAC metabolism was increased with CYP2C8*3 compared to WT [462]. However, the consensus through other studies is that PAC metabolism is either lower or similar to WT [457,458,461]. Taken together, these data suggest that the CYP-CPR interaction may be disrupted in CYP2C8*3 and effects PAC metabolism.

CPR transfers two electrons to CYPs during the CYP catalytic cycle, with the first electron reducing the ferric heme to a ferrous heme and the second reducing the dioxygen-heme to a peroxy-heme (Figure A.1). Many reactive oxidized intermediates are involved in the CYP catalytic cycle *en route* to substrate oxidation [465]. These intermediates can sometimes decompose to form reactive oxygen species (ROS) instead of progressing towards substrate oxidation, a process known as uncoupling. Hydrogen peroxide (HOOH) and superoxide are formed in large quantities by CYP2C enzymes [466,467]. ROS can induce mitochondrial dysfunction in cardiomyocytes, coronary artery vasoconstriction, and promote carcinogenesis [466,468-470], and ROS specifically generated by endothelial CYP2C8 has been shown to impair functional recovery after ischemia/reperfusion injury [467]. Another potential effect of these polymorphisms may therefore be on the coupling efficiency of PAC metabolism.

Herein, we determined the effects of the CYP2C8*2 and CYP2C8*3 polymorphisms in regards to first-electron transfer (FET) kinetics and PAC metabolism uncoupling. We tested CYP2C8*1, CYP2C8*2, and CYP2C8*3, as well as the single mutations of the CYP2C8*3 polymorphism (R139K and K399R). To study these polymorphisms, we utilized the Nanodisc technology to

solubilize these CYP2C8 variants in a membrane mimic [471,472]. We find that CYP2C8*2 has a lower PAC turnover rate compared to WT. We further determined that CYP2C8*3 produces significantly more HOOH compared to WT, indicating a greater uncoupling of the catalytic cycle. Using stopped-flow measurements of the FET, we determined that the CYP2C8*2 and CYP2C8*3 have profoundly distinct and slower FET kinetics compared to WT. We determined that there is no change in the reduction potential of the polymorphisms compared to WT, which supports that the altered FET kinetics is due to an altered redox interaction with CPR. None of the single-mutant variants of CYP2C8*3 (R139K and K399R) reproduce the effects of the CYP2C8*3, indicating that the effects of this polymorphism are a synergism of both mutations. Taken together, these data demonstrate that these polymorphisms have altered FET kinetics, leading to an increase in HOOH production and greater PAC metabolism uncoupling.

A.2 Materials and Methods

Materials. The human CYP2C8 gene cloned into the Amp^R pAr5 (modified pCWOri+) plasmid was a gift from Dr. Eric Johnson. PCR reagents were purchased from New England Biolabs. Molecular biology enzymes and *E. coli* DH5α were purchased from Invitrogen. Plasmid DNA was purified using a Qiagen Gel Extraction kit. Ampicillin (Amp), arabinose, chloramphenicol (Chlr), isopropyl β-D-1-thiogalactopyranoside (IPTG), and Ni-NTA resin were purchased from Gold Biotechnology. δ-Aminolevulinic acid (δ-ALA) was purchased from Frontier Scientific. 1-palmitoyl-2-oleoyl-sn-glycero-3-phosphocholine (POPC) and 1-palmitoyl-2-oleoyl-sn-glycero-3-phospho-L-serine (POPS) were purchased from Avanti Polar Lipids. Carbamazepine and paclitaxel were purchased from Cayman Chemicals. NADPH was purchased from P212121.com.

*Protein Engineering of CYP2C8*1/*2/*3/R139K/K399R.* The CYP2C8 plasmid from Dr. Johnson was used directly for engineering the CYP2C8 variants. Plasmids were amplified and purified using a Qiagen Plasmid mini-prep kit (Valencia, CA). The R139K and K399R single nucleotide substitutions were made using forward and reverse primers containing each mutation and an inserted BspQI restriction enzyme site (New England Biolabs) (Supplementary Table A.1). BspQI is a class II restriction enzyme that will create a unique sticky-end cut one nucleotide removed from the restriction enzyme site. The resulting gene of the R139K amplification and the K399R primers were then used to construct the CYP2C8*3 gene. A single *2 mutation was made

similarly containing a single substitution at I269F. The PCR reaction consisted of 1 µM of forward and reverse primers in HF reaction buffer (New England Biolabs) containing 50 pg/µL CYP2C8-containg plasmid, 200 µM dNTPs, 5% DMSO, and Phusion DNA polymerase (10 U/mL). The PCR thermocycler was set to 95℃ for 3', 20 cycles (95℃ for 30", 65℃ for 30"), and then 72℃ for 4'. The mutated plasmids were then digested with BspQI and the resulting sticky ends were ligated to make complete plasmids. Chemically competent DH5α cells were transformed by heat shock at 42℃ for 45", and then set on ice. The addition of 1 mL of warm Super Optimal Broth (SOC) media was followed by shaking (250 rpm, 37℃) for 1 hr. Cells were plated on an LB Amp to screen for the desired mutant plasmid. Mutant dsDNA was confirmed by DNA sequencing. Cells were co-transformed with pTGro7 plasmid containing the GroES-GroEL chaperonin system.

*Protein Expression and Purification of CYP2C8*1/*2/*3/R139K/K399R.* All CYP2C8 proteins were expressed according to the protocol used in CYP2J2 expression, as previously described [247,311]. The protein concentrations were determined using a UV-Vis spectrophotometer (Agilent Technologies) (ε = 108 mM^{-1} cm^{-1}).

Expression of Cytochrome P450 Reductase. Expression of CPR from *Rattus norvegicus* was performed as previously described [247,311].

Assembly of CYP2C8-Nanodiscs. CYP2C8-ND were assembled as previously described [311,473,474] by mixing CYP2C8, membrane scaffold protein (MSP1E3D1), an 80:20 ratio of POPC:POPS lipids, and cholate, followed by detergent removal using Amberlite®, and purification by size exclusion chromatography [471,472].

Carbon Monoxide Binding Assay. The heme content of the purified CYP2C8 proteins was analyzed using UV-Vis spectroscopy (Agilent Technologies) as previously described [473].

Paclitaxel Metabolism. Samples containing 0.1 µM of CYP2C8-ND (*1/*2/*3/R139K/K399R) were incubated with CPR (0.3 µM), and PAC (70 µM) in 0.3 mL of 0.1 M potassium phosphate buffer (pH 7.4) for 5 min at 37° C. NADPH (200 µM) was added and the mixture was incubated for 5, 10, and 20 min at 37℃, then quenched with equivolume ethyl acetate. Samples were vortexed and thrice-extracted with ethyl acetate, dried under a stream of N_2 gas, and then resuspended in 180 proof ethanol for LC-MS/MS quantification.

Tandem LC-MS/MS for the Quantification of 6α-Hydroxypaclitaxel. Samples were analyzed with the 5500 QTRAP LC/MS/MS system (Sciex, Framingham, MA) in Metabolomics Lab of Roy J. Carver Biotechnology Center, University of Illinois at Urbana-Champaign. Software Analyst 1.6.2 was used for data acquisition and analysis. The 1200 series HPLC system (Agilent Technologies, Santa Clara, CA) includes a degasser, an autosampler, and a binary pump. The LC separation was performed on an Agilent Eclipse XDB-C18 (4.6 x 150mm, 5μm) with mobile phase A (0.1% formic acid in water) and mobile phase B (0.1% formic acid in acetontrile). The flow rate was 0.4 mL/min. The linear gradient was as follows: 0-2min, 95%A; 8-15min, 5%A; 15.5-22min, 95%A. The autosampler was set at 15°C. The injection volume was 5 μL. Mass spectra were acquired under positive electrospray ionization (ESI) with the ion spray voltage at +5000 V. The source temperature was 450 °C. The curtain gas, ion source gas 1, and ion source gas 2 were 32, 50, and 65, respectively. Multiple reaction monitoring (MRM) was used for quantitation: Paclitaxel m/z 854.4 → m/z 569.2; 6α-hydroxy-paclitaxel m/z 870.4 → m/z 286.2. Internal standard carbamazepine was monitored at m/z 237.1 → m/z 194.0.

HOOH Measurements. Hydrogen peroxide measurements were made using an Amplex Red Hydrogen Peroxide/Horseradish peroxidase (HRP) Kit (Life Technologies) according to the published protocol. Amplex Red combined with HRP reacts with HOOH in a 1:1 stoichiometry producing the red-fluorescent oxidation product, resorufin (A_{560nm}). Samples containing 0.1 μM of CYP2C8-ND (*1/*2/*3/R139K/ K399R) were incubated with CPR (0.3 μM) in 0.3 mL of 0.1 M potassium phosphate buffer (pH 7.4), ± paclitaxel (70 μM), for 5 min at 37°C. NADPH (200 μM) was added and the mixture was incubated for 10, 15, and 20 min at 37°C, then quenched with equivolume ethyl acetate, vortexed thoroughly, and centrifuged at 3000 rpm at 4°C for 5 min. The aqueous fraction containing H_2O_2 was extracted and centrifuged at 10,000 rpm at 4°C for 10 min to remove precipitated protein and lipids. Next, 50 μL of each sample was diluted eight-fold and sixteen-fold and combined with Amplex Red/HRP (10 mM Amplex Red, 10 U/mL HRP in 1X reaction buffer) in a clean, dry 96-well plate. Each sample was analyzed in triplicate. The reactions were incubated at room temperature for 30 min in the dark. The UV A_{560nm} was measured using a microplate reader. Baseline corrected absorbance values of each sample were compared to a standard curve ([HOOH] = 0 to 20 μM).

NADPH Assay. The rate of NADPH (ε= 6.2 $mM^{-1} \cdot cm^{-1}$ at A_{340nm}) consumption by each CYP2C8 variant (0.2 μM) incubated with CPR (0.6 μM) and PAC (70 μM) in 0.1 M KPi buffer and 200 μM NADPH was determined via UV-Vis spectroscopy using a Cary 300 UV-Vis spectrometer in kinetics mode (Agilent Technologies), as previously described [247,311].

Stopped-flow Kinetics of Electron Transfer. An Applied Photophysics SX-17 MV Spectrophotometer (Leatherhead UK) was used to monitor the reduction of CYP2C8*1/*2/*3/R139K/K399R, as previously described with the following modifications [247]. Reaction cell 1 containing CYP2C8 (2 μM) in 0.1% cholate, CPR (2 or 6 μM), paclitaxel (70 μM), glucose oxidase (1 U/mL), and glucose (10 mM) dissolved in 100 mM potassium phosphate buffer was kept anaerobic and CO-saturated. Reaction cell 2 containing excess NADPH (1 mM), paclitaxel (70 μM), glucose oxidase (1 U/mL), and glucose (10 mM) dissolved in 100 mM potassium phosphate buffer was also kept anaerobic until rapid mixing followed by absorbance readings.

Data analysis of stopped-flow experiments. The reduction of ferric CYP2C8 to a ferrous–CO complex was monitored near A_{450nm} upon mixing the two separate reaction cells in logarithmic mode and analyzed as described previously, with the following changes [247]. All data indicate the average of 3-6 individual reactions fitted using a monophasic or biphasic exponential equations using OriginLab software. The decrease in A_{450nm} corresponding to the rapid reduction of CPR were not included in these analyses due to spectroscopic noise. R^2 values for fits exceeded 0.99 in most cases. The errors reported are SEM.

Reduction potential. Reduction potential of the CYP2C8 proteins was determined using safranin T as a redox probe as previously described [473]. Samples containing 5 μM of CYP2C8 variant, 20 nM paraquat (methyl viologen), 0.5 μM safarinin T, 10 mM EDTA, 50 μM of a 20% lipid reconstituted system [404], with or without 70 μM paclitaxel were prepared in 0.1 M potassium phosphate buffer, pH 7.4, in glass vials capped with a septa. Samples were purged with $N_{2(g)}$ for 20 min and then loaded into a Coy anaerobic glove box. 0.5 mL of each samples was loaded into UV-invisible plastic cuvettes stopped with a septa. Reduction potential was determined spectroscopically using a Cary 300 UV-Vis spectrometer (Agilent Technologies). Cuvettes were equilibrated at 25° C for each reading. Safranin T was used as the redox indicator to measure the reduction potential of the solution. Oxidation of the protein was monitored at 417 nm (reduction

at 408 nm) and compared to the oxidation of safranin T at 535 nm. Reduction of the samples was initially achieved by irradiating samples on ice with time points up to 5 min with a 250 W tungsten lamp. Samples were further reduced by titrating anaerobic dithionite from x and y mM stocks. Re-oxidation was achieved by titrating anaerobic $K_3[Fe(CN)_6]$ from 10 mM stocks. Spectral data were then processed using a MATLAB subroutine and analyzed using the Nernst equation as previously described [473].

A.3 Results and Discussion

*P450 characterization of CYP2C8*1/*2/*3/R139/K399-ND.* In order to assess if these variants of CYP2C8 lead to unfolding of the protein and improper ligation of the heme group, we performed anaerobic CO-binding assays. All the variants showed a 90%-100% shift in the heme absorbance to 450 nm and resemble CYP2C8*1 characteristics (Figure A.2 and Supplementary Table A.2). Therefore, these mutations do not lead to aberrant folding of CYP2C8 and these samples contain high amounts of active protein.

Effect of polymorphisms on PAC metabolism. Next, we sought to examine the effect that these polymorphisms have on PAC turnover rates. Linearity was established for the hydroxylation of 70 µM PAC to 6α-hydroxypaclitaxel (PAC-OH) over a 20 min period. Based on the time linearity, we can estimate the catalytic efficiency of the PAC metabolism among the variants by fitting the data to Equation A.1

$$[S] = [S_0]e^{-kt} \quad \text{(Equation A.1)}$$

where $[S_0]$ is the initial concentration of the substrate and $k \equiv \frac{k_{cat}}{K_m}[E]$ (Supplementary Figure A.1) [272]. The catalytic efficiencies of these variants range from 0.207 to 1.02 $min^{-1} \cdot nM^{-1}$ (Supplementary Figure A.1, Table A.1). CYP2C8*2 showed a marked decrease in turnover rate (47.2% WT), consistent with earlier reports of its inefficient PAC metabolism [457,458]. Compared to WT, CYP2C8*3 had slightly, albeit not significantly, lower PAC turnover rates. These results for CYP2C8*3 agree with the findings of Yu, et al. [458] and Soyama, et al. [461], but contradict the findings of Dai, et al. [457], who were unable to measure PAC metabolism, and contradict the findings of Kaspera, et al., who reported higher PAC metabolism [462]. The CYP2C8-K399R variant also metabolized PAC with WT rates, but interestingly the CYP2C8-R139K variant showed a remarkable increase in PAC turnover (265% compared to WT). Therefore, the overall effect of

CYP2C8*3 on PAC metabolism cannot be explained by the additive contribution of each single mutation. Overall, we observed that the CYP2C8*3 polymorphism does not significantly affect PAC turnover, but CYP2C8*2 is half as efficient as WT.

Polymorphisms lead to greater HOOH uncoupling. To assess the uncoupling efficiency of PAC metabolism, we next measured the rate of HOOH production by each variant. We firstly did not observe a significant difference in the HOOH production rates upon the addition of 70 μM PAC with any of the variants, likely due to the high amounts of HOOH produced compared to PAC turnover (Supplementary Figure A.2). The overall amount of HOOH linearly decreased for all CYP2C8 variants over this time, indicating a burst of activity at the initiation of the reaction followed by decomposition of HOOH (Figure A.3). CYP2C8*3 displayed nearly 200% higher HOOH production compared to WT at all of the time points. There was an increase in HOOH production with the CYP2C8-K399R variant at the start of the reaction and a minor decrease in HOOH production over time with the CYP2C8-R139K variant. Therefore, likewise to the PAC metabolism experiments, the individual mutations of the CYP2C8*3 do not additively contribute to the CYP2C8*3 phenotype. Taken together, the CYP2C8*3 polymorphism does not affect PAC turnover but leads to a greater uncoupling of the reaction to produce ROS. PAC and ROS have both been implicated in the progression of neuropathic pain [475,476], and therefore it would be interesting to see if the increase in HOOH production contributes to the neuropathy observed with CYP2C8*3 [459,460]. CYP2C8*2 did not have a significant difference in the HOOH production compared to WT, but this polymorphism also displayed half the PAC turnover as WT. If we normalize the amount of HOOH produced to the activity of the enzyme by looking at the HOOH produced per PAC turnover, we see that both CYP2C8*2 and CYP2C8*3 produce almost 200% more HOOH per PAC turnover than WT (Table A.2). The CYP2C8*2 and CYP2C8*3 polymorphisms, therefore, are about twofold more uncoupled (i.e., produce twofold more ROS), with CYP2C8*3 producing significantly more HOOH than WT. To gain a better idea into how the CYP2C8 polymorphisms are utilizing electrons, we proceeded to measure the first-electron transfer (FET) kinetics.

Polymorphisms show altered first electron transfer (FET) kinetics as determined by CO stopped-flow. To further probe the effect of these polymorphisms on the CYP2C8 catalytic mechanism, we determined the kinetics of the FET from CPR to the CYP2C8 variants during the

metabolism of 70 μM PAC. We firstly determined that there is not a significant change in the NADPH oxidation rates among the variants (Supplementary Figure A.3), which supports previous findings [462]. As NADPH is the initial step in the reaction, we then proceeded to conduct stopped-flow measurements in order to determine how CPR transfers electrons to the CYP2C8 variants. CYPs display a characteristic shift in the heme absorbance to 450 nm upon CO binding to the heme. In order for CO to bind, the heme must be reduced to the ferrous state by CPR, which we determine by the appearance of the 450 nm absorbance band over time (Figure A.4A). Therefore, the rate at which CO binds to the heme is directly related to the FET rate.

The rate of CO binding was monophasic across all variants (Figure A.4B-F). Compared to WT, CYP2C8*2 and CYP2C8*3 showed higher rates of CO binding and the CYP2C8-R139K and CYP2C8-K399R variants showed lower rates (Table A.3). These data indicate that the FET rate is significantly higher in the CYP2C8*2 and CYP2C8*3 polymorphisms. In order to determine if the FET is dependent on the interactions of CYP2C8 with CPR, we repeated the experiments by lowering the CPR:CYP ratio from 3:1 to 1:1. Interestingly, CYP2C8*1, CYP2C8-R139K, and CYP2C8-K399R all showed biphasic CO binding at the 1:1 CPR:CYP ratio and had similar fast (k_1) and slow (k_2) kinetics compared to WT (Figure A.4B, E, and F, Table A.3). Altering the CPR:CYP ratio has previously been shown to change the phasicity of the FET in certain situations likely by forcing CPR to associate with CYPs in unproductive confirmations at higher CPR:CYP ratios [477]. Likewise, the 3:1 ratio with CYP2C8*1, CYP2C8-R139K, and CYP2C8-K399R may be promoting unproductive confirmations with CPR to produce these observations.

Contrariwise, CYP2C8*2 and CYP2C8*3 only show the slow phase of the CO binding (Figure A.4C and D, Table A.3). The values of k_2 for these polymorphisms are about half that compared to WT. If we look at the data as a whole, the CYP2C8*2 and CYP2C8*3 rates in the 3:1 CPR:CYP experiments resemble those of the WT slow phase in the 1:1 ratio. Therefore, it appears that more CPR is required for the CYP2C8*2 and CYP2C8*3 polymorphisms to rescue the WT activity of this slow phase. Furthermore, the fast phase of the WT likely indicates that there is a subpopulation of CYP2C8 that is optimally reduced by CPR that is absent in CYP2C8*2 and CYP2C8*3. Together, these data suggest that these polymorphisms reduce either the binding of CPR to CYP2C8 or the transfer of electrons from CPR to CYP2C8. We will refer to these two events as the CYP-CPR redox interaction. Kaspera, et al. had previously determined that the apparent

affinity of CPR for CYP2C8*3 is greater than WT; however, the study also used a different recombinant system with cytochrome b5 as an auxiliary redox partner [462]. Homology modeling (Supplementary Figure A.4) reveals that R139, K399, and I269 all lie on the putative CYP-CPR binding interface, which means these mutations may be directly interfering with the CYP-CPR interaction. Further, K399 is located near the N-terminus at the protein-membrane interface (Figure A.1A), and we showed previously that the N-terminus is essential for the CPR-mediated reduction of CYP2J2, which has a close homology to CYP2C8 [247]. Although the altered FET kinetics can be explained by an altered CYP-CPR redox interaction, the altered FET may also be the result of an intrinsic change to the reduction potential of the heme. In order to delineate the cause of the altered FET kinetics, we therefore proceeded to determine the reduction potential of the CYP2C8 polymorphisms.

Reduction potentials of CYP2C8 polymorphisms. We determined the reduction potential of the CYP2C8 variants using safranin T as a redox indicator as previously described [473]. Substrates binding to CYPs, such as CYP3A4, often perturbs water binding at the 6th coordinate position to produce a pentacoordinated high-spin heme (Figure A.1). This results in an increase in the reduction potential of the heme and helps facilitate electron transfer from CPR [478]. The high-spin content can be observed as a shift in the heme absorbance from ~417 to ~390 nm. We did not observe a significant high-spin shift upon PAC binding to CYP2C8 in any of the variants, as was similarly observed for PUFAs binding to CYP2J2 [289]. We also determined that there is not a significant change in the reduction potential of CYP2C8*1 upon PAC binding (Figure A.5A, Table A.4), which correlates to the poor high-spin content of the PAC-bound protein. The poor high-spin content and minimal change to the reduction potential together support the slow metabolism of PAC by CYP2C8 compared to other CYP-mediated drug metabolisms. Compared to the polymorphisms, CYP2C8*2 had a slightly albeit not significantly lower reduction potential, and the reduction potential of CYP2C8*3 was similar to WT (Figure A.5, Table A.4). Altogether, there is not a significant change to the intrinsic redox properties of the heme in these polymorphisms. Therefore, the observed changes to the FET kinetics in the polymorphisms must be occurring upstream from the heme supporting that the polymorphisms affect the CYP-CPR redox interaction.

A.4 Conclusions

CYP2C8*2 and CYP2C8*3 contain mutations that are on the periphery of CYP2C8. Therefore, these residues do not directly contribute to substrate binding and instead must affect CYP2C8 activity through other points in the CYP catalytic cycle. These mutations lie on the putative CYP-CPR interface and thus may be affecting the redox interactions between these proteins. We determined that CYP2C8*2 is 47% as active towards PAC turnover compared to WT and that CYP2C8*3 shows WT activity. The metabolism of PAC is 200% more uncoupled in the CYP2C8*2 and CYP2C8*3 polymorphisms and CYP2C8*3 produces significantly more HOOH compared to WT. Stopped-flow kinetics of the FET suggest that the polymorphisms reduce either the binding of CPR or the transfer of electrons by CPR to CYP2C8. In conclusion, the CYP2C8*2 and CYP2C8*3 polymorphisms reduce the CYP-CPR redox interaction and promote greater uncoupling of PAC metabolism. Therefore, not only is the FET disrupted in these polymorphisms, the electrons are being utilized towards ROS formation in lieu of PAC turnover. The mutations may be altering the architecture of CYP2C8 that disfavors redox interactions with CPR while also destabilizing the peroxy-heme intermediate to produce HOOH. CYP2C8*2 contains an I269F mutation, which is a significant change to the physical and chemical properties of the residue. It is likely that this mutation has a profound effect on the folding of CYP2C8 and the interaction with CPR. CYP2C8*3 contains a R139K/K399R double mutation, which interestingly does not change the charge of the residues but switches the amino acid position. While Lys and Arg are both positively charged residues, they differ significantly in their physical properties. For instance, Arg can form a greater number of electrostatic interactions and better maintains a positive charge compared to Lys. It has been shown that Arg can increase the stability of GFP, which was shown *in silico* to be facilitated by a greater number of salt bridge interactions [479]. Arg also interacts differently to phospholipids and increases interfacial binding and perturbations to membranes [480]. Therefore, this polymorphism may be affecting how CYP2C8 associates with lipids as well as interacting with CPR.

Another important finding is that the effects of the CYP2C8*3 polymorphism on CYP2C8 activity cannot be explained by the additive contribution of the individual mutations themselves. In all experiments, CYP2C8*3 had distinct activities compared to the linear combination of the R139K and K399R individual data. In fact, the single mutations either showed WT activity

(especially concerning FET kinetics) or were significantly different than either WT or CYP2C8*3 (e.g., the 265% increase in PAC metabolism by CYP2C8-R139K). These two residues therefore synergistically contribute to the CYP2C8*3 phenotype.

A.5 Figures and Tables

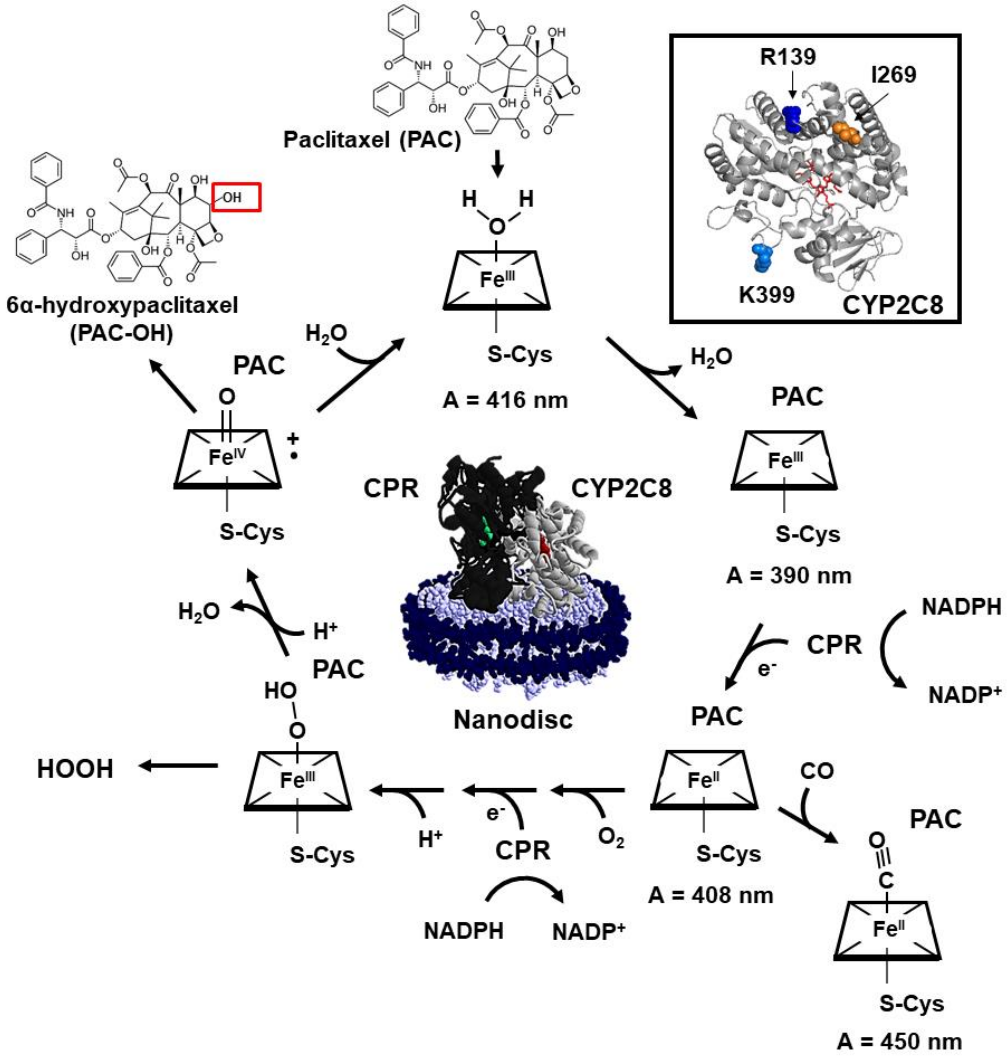

Figure A.1. *Schematic of the CYP catalytic cycle.* Inset shows the structure of CYP2C8 with residues R139 (blue), I269 (orange), and K399 (light blue) highlighted. Structure was generated in PyMol using the PDB entry 1PQ2. A schematic of CYP2C8 (grey) and CPR (black) incorporated into nanodiscs is shown in the center of the cycles. *Catalytic cycle*. Substrate (PAC) binds to the CYP active site, which perturbs the H_2O coordination to the iron heme. H_2O unbinds leaving a pentacoordinated high-spin iron heme. CPR reduces the iron heme using an electron obtained from NADPH. Under anaerobic conditions, CO ligates the heme to terminate the cycle. Under aerobic conditions, O_2 ligates the heme, followed by another one-electron reduction by CPR and the addition of a proton to produce a peroxy-heme. The peroxy-heme can decompose forming HOOH or eliminate an H_2O molecule to produce the catalytic ferryl iron heme radical (Compound I). Compound I can oxidize substrate (PAC) to product (PAC-OH), followed by the coordination of an H_2O molecule to begin the cycle again. Spectroscopically visible species are indicated with their characteristic absorbance wavelength. More details of the cycle can be found in such reviews as Denisov, et al. [465].

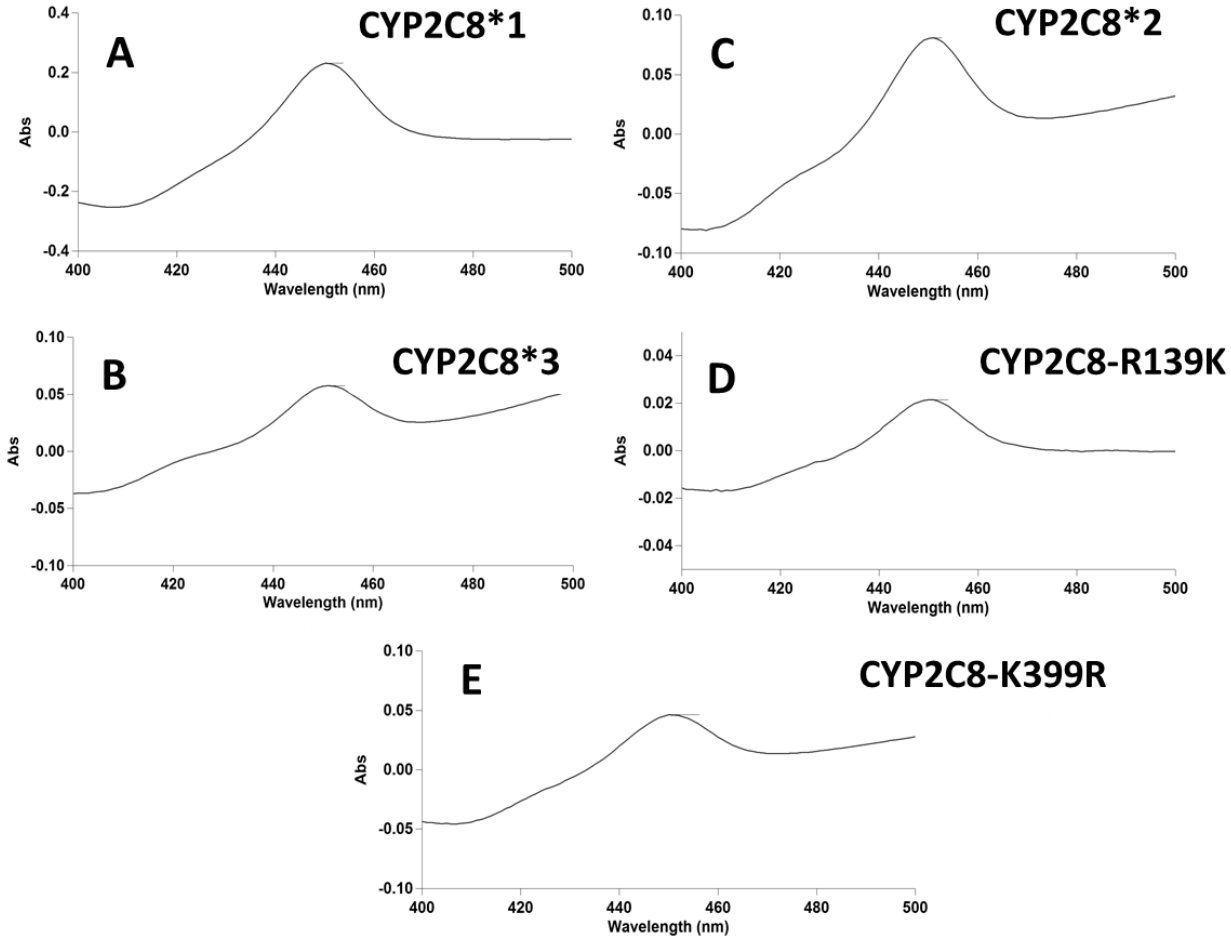

Figure A.2. *CO-binding difference spectra.* **(A)** CYP2C8*1, **(B)** CYP2C8*2, **(C)** CYP2C8*3, **(D)** CYP2C8-R139K, and **(E)** CYP2C8-K399R.

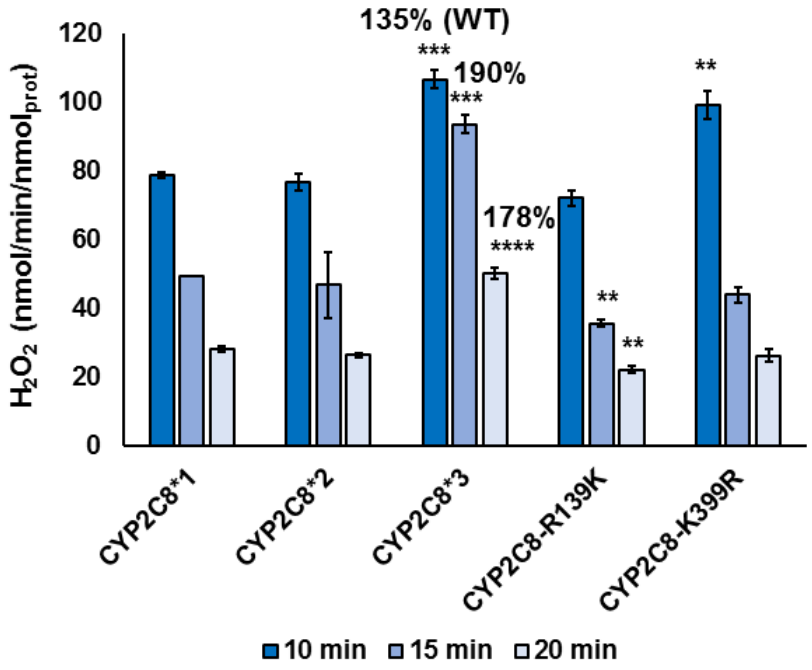

Figure A.3. *HOOH production rates*. The rate of HOOH production by each CYP2C8 variant was measured using an Amplex Red peroxidase kit at 10 min, 15 min, and 20 min reaction times, in the presence of 70 μM PAC. Error represents the SEM of 3-4 experiments. Statistical significance was determined by comparing experiments to their respective WT controls. **P < 0.01; ***P = 0.0001; ****P < 0.0001.

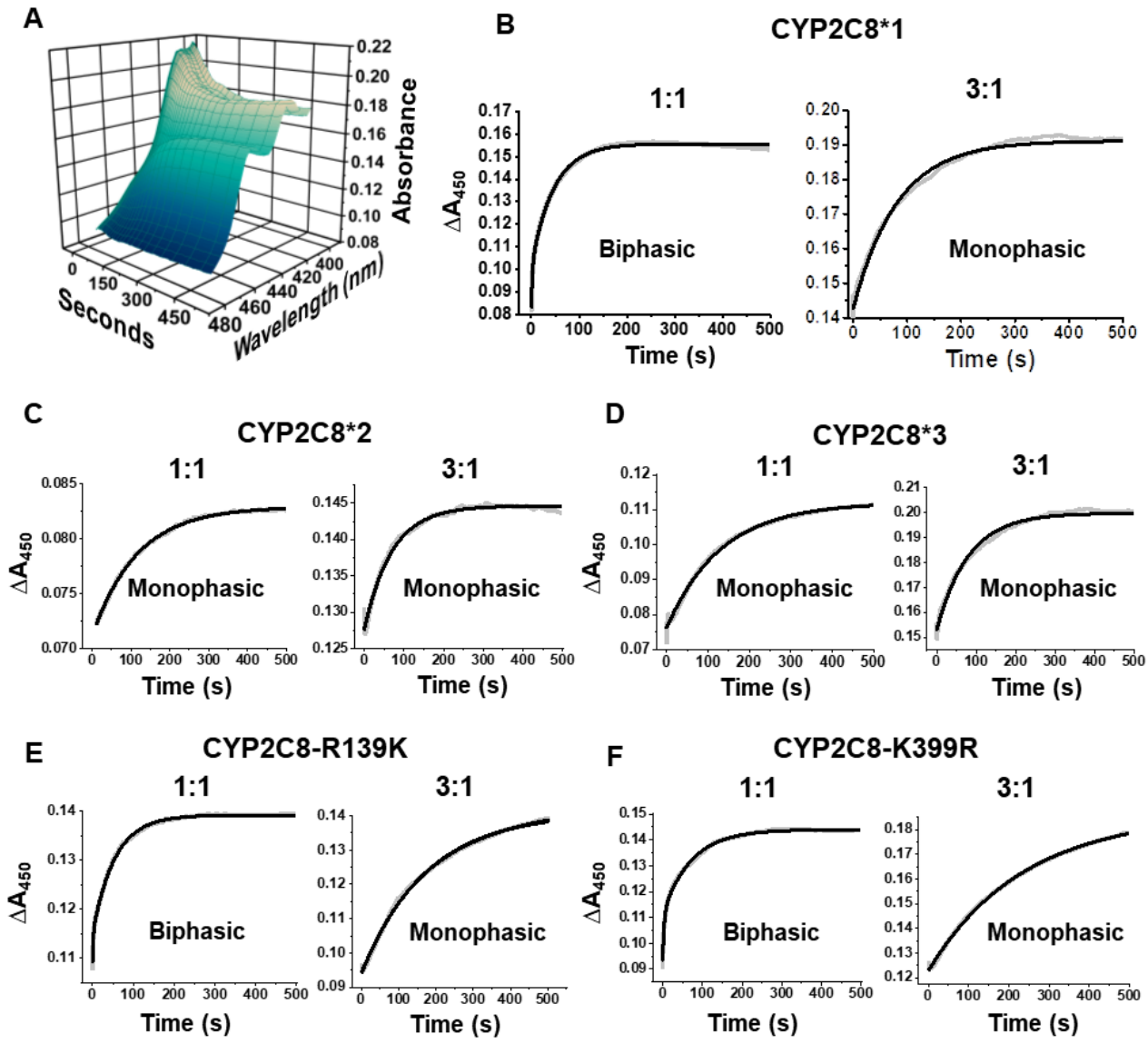

Figure A.4. *Stopped-flow electron transfer rate to CYP2C8 variants.* **(A)** Three-dimensional plot of representative absorbance spectra from 0 to 500 s showing the increase in absorbance near 450 nm following the mixing of NADPH with a pre-incubated complex of paclitaxel-bound CYP2C8 and CPR. **(B-F)** Representative plots of the change in peak absorbance at 450 nm from 0 s to 500 s. Experiments were conducted at either a 1:1 CPR:CYP or a 3:1 CPR:CYP ratio. Data points (grey squares) are overlaid with the line of best fit (solid black line) derived from a fit of the data to either monophasic (single exponential) or biphasic (two exponential) kinetic equations in OriginLab as indicated.

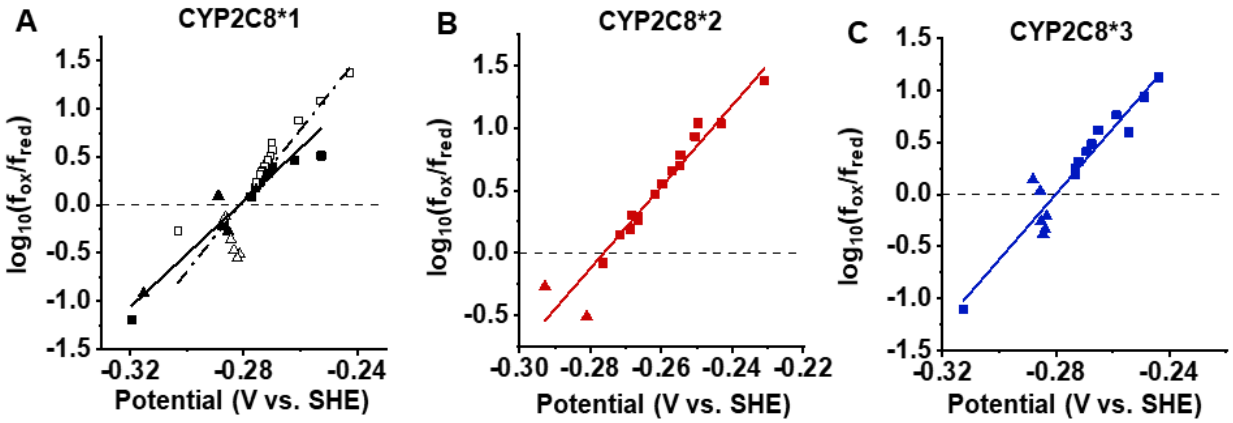

Figure A.5. *Reduction potential of CYP2C8 variants.* Redox titration of CYP2C8 variants was conducted in 0.1 M phosphate buffer (pH 7.4 at 25 °C) with or without 70 μM PAC. The potential was measured spectroscopically by using a safranin T as the redox indicator. Reduction was achieved using light and dithionite and oxidation was achieved using $K_3[Fe(CN)_6]$ as stated in the Methods section. Representative Nernst plots for **(A)** CYP2C8*1 without paclitaxel (open black) and with paclitaxel (solid black), **(B)** CYP2C8*2, and **(C)** CYP2C8*3 from two experiments are shown. Data obtained from reduction is given as squares and data from oxidation is given as triangles. The zero intercept gives $E°'$, the redox potential of the protein.

Variant	Rate ($pmol/min/nmol_{prot}$)	% WT	k_{cat}/K_m ($min^{-1} \cdot nM^{-1}$)	%WT
CYP2C8*1 (WT)	38.8 $\pm$ 0.2	100	0.381	100
CYP2C8*2	18.3 $\pm$ 3.5	47.2	0.207	54.4
CYP2C8*3	34.0 $\pm$ 3.0	88	0.321	84.4
CYP2C8-R139K	103 $\pm$ 2	265	1.02	269
CYP2C8-K399R	47.1 $\pm$ 4.3	121	0.441	116

Table A.1. *PAC metabolism by CYP2C8 variants*. Linear rates of 70 μM PAC metabolism by each CYP2C8 variant to PAC-OH was determined over a 20 minute period. Estimates of the catalytic efficiencies were determined using Equation 1 as stated in the text. Error represents the SEM of three experiments.

Variant	$nmol_{HOOH}/pmol_{PAC\text{-}OH}$ (at 20 min)	%WT
CYP2C8*1 (WT)	1.58	100
CYP2C8*2	2.96	187
CYP2C8*3	3.25	206
CYP2C8-R139K	0.46	29.6
CYP2C8-K399R	1.24	78.4

Table A.2. *HOOH production per PAC turnover*. The amount of HOOH formed at 20 min was divided by the amount of PAC-OH produced at 20 min. These values are compared to WT.

	1:1 CYP:CPR		1:3 CYP:CPR
Variant	**k_1 (ms^{-1})**	**k_2 (ms^{-1})**	**k_2 (ms^{-1})**
CYP2C8*1	468 ± 21	20.7 ± 0.4	9.70 ± 0.98
CYP2C8*2	---	8.67 ± 0.49 [****]	17.4 ± 1.6 [***]
CYP2C8*3	---	10.8 ± 1.84 [****]	13.7 ± 0.7 [****]
CYP2C8-R139K	406 ± 52	18.2 ± 0.65	6.02 ± 0.19 [**]
CYP2C8-K399R	445 ± 51	19.4 ± 0.99	3.90 ± 0.10 [***]

Table A.3. *Stopped-flow CO binding kinetics*. Fast (k_1) and slow (k_2) rates are in units of ms^{-1}. Experiments were conducted using a 1:1 and a 1:3 CYP:CPR ratios. Error represents the SEM of 3-6 experiments. Statistical significance compares to WT. **P < 0.01, ***P = 0.001, ****P < 0.0001.

Variant	Reduction potential (V)
CYP2C8*1 No PAC	-0.283 ± 0.002
CYP2C8*1	-0.279 ± 0.002
CYP2C8*2	-0.297 ± 0.021
CYP2C8*3	-0.281 ± 0.001

Table A.4. *Reduction potentials*. Reduction potentials of the CYP2C8 variants was determined as described in the text. Error represents the SEM of two experiments.

A.6 Supplementary information

Figures

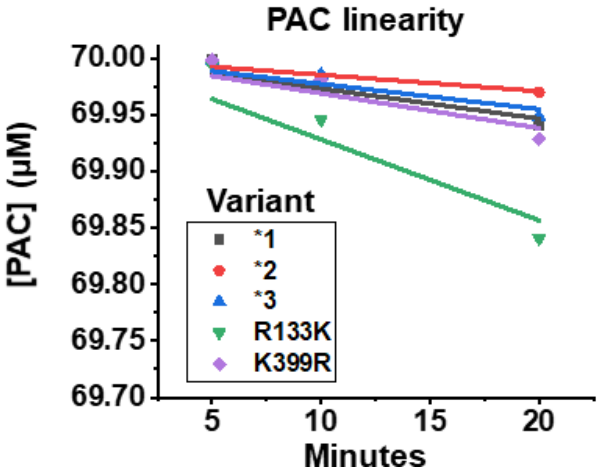

Supplementary Figure A.1. *PAC linearity and catalytic efficiency estimates*. Concentration of PAC was determined by subtracting the amount of PAC-OH measured from 70 µM of the starting PAC. Catalytic efficiency was estimated using Equation 1 as stated in the text. Data represents the mean of 3 replicates.

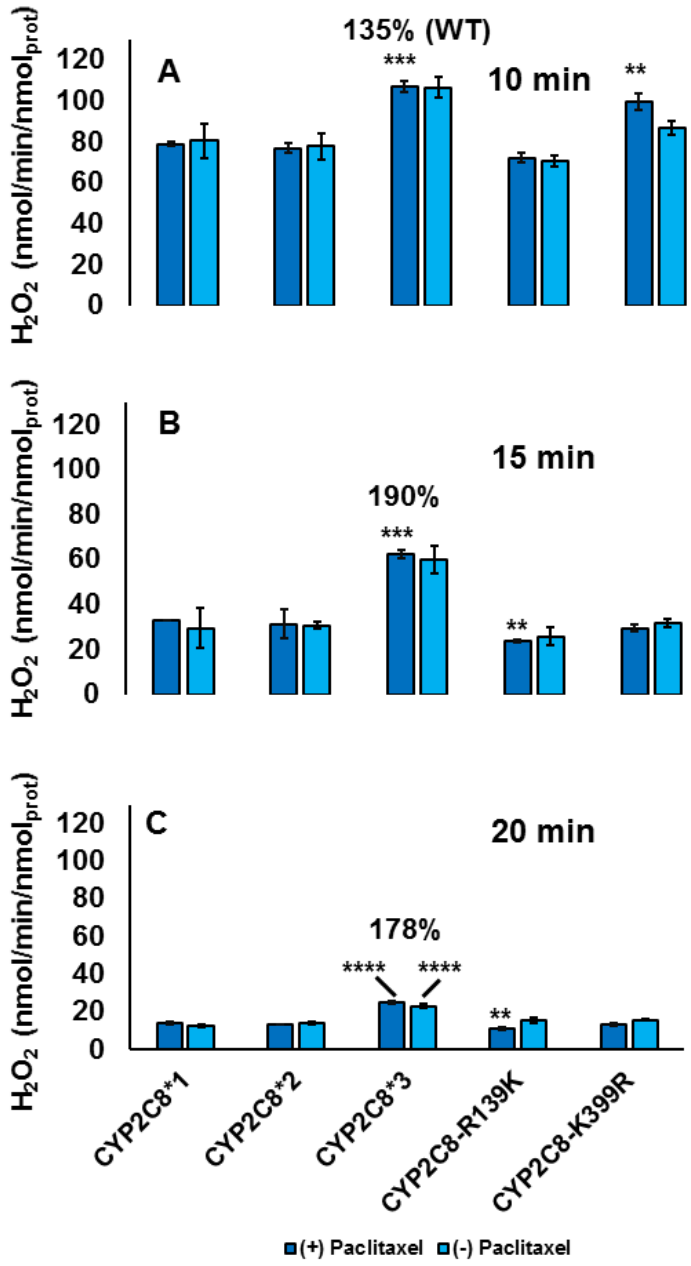

Supplementary Figure A.2. *HOOH production rates*. The rate of HOOH production by each CYP2C8 variant was measured using an Amplex Red peroxidase kit at **(A)** 10 min, **(B)** 15 min, and **(C)** 20 min reaction times, with and without 70 μM paclitaxel. Error represents the SEM of at least three experiments. Statistic significance was determined by comparing (+) and (-) paclitaxel experiments to their respective WT controls. **P < 0.01; ***P = 0.0001; ****P < 0.0001

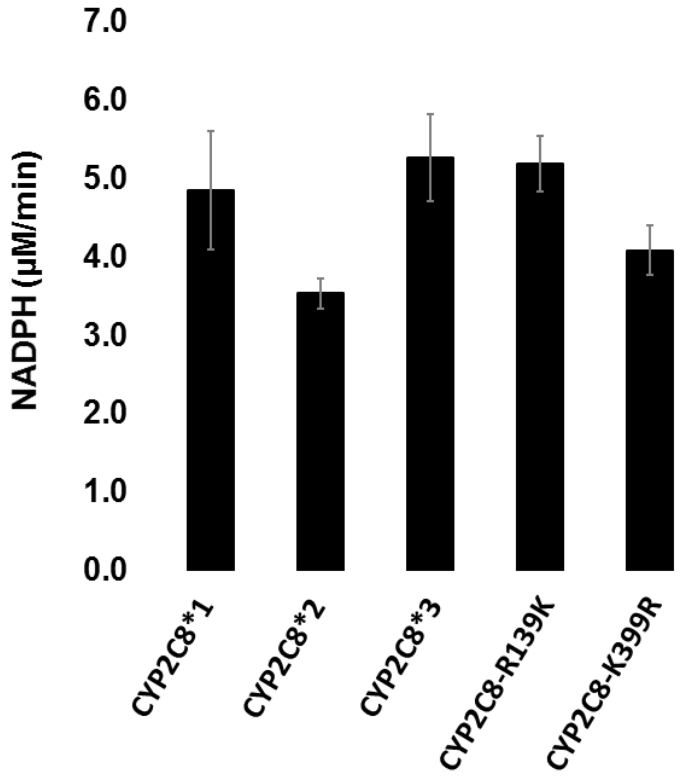

Supplementary Figure A.3. *NADPH consumption rates*. Rates of NADPH consumption were measured by monitoring the decrease in absorbance at λ = 340 nm as NADPH is converted to $NADP^+$ by CPR. NADPH consumption levels are close to WT (CYP2C8*1) in all variants, with slight, albeit statistically not significant decreases in CYP2C8*2 and CYP2C8-K399R. Error represents the SEM of at least three experiments

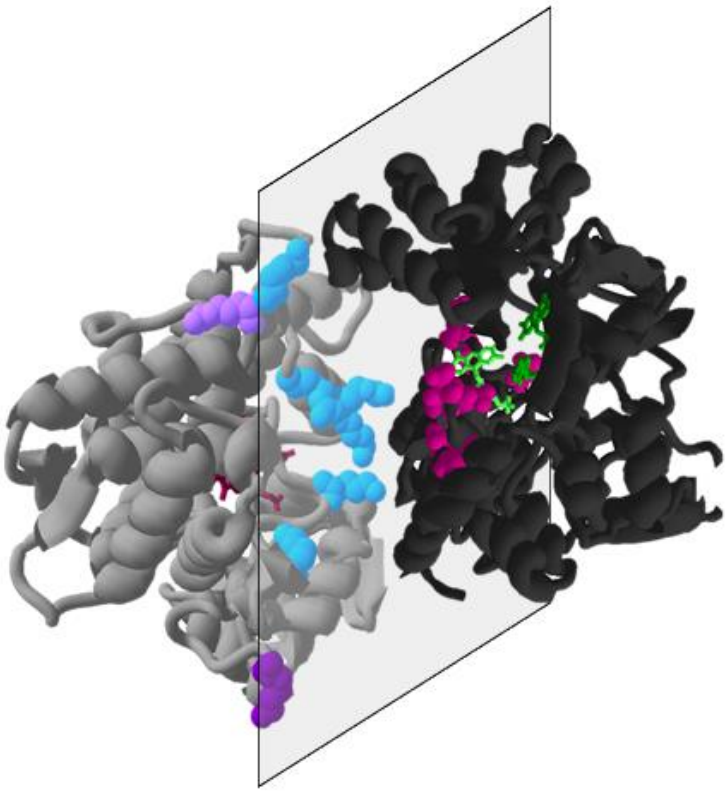

Supplementary Figure A.4. *Schematic of CPR-CYP2C8 complex highlighting interface residues and the location of CYP2C8*3 mutations.* The amino acid residues involved in CYP-CPR interaction are highlighted based on a previously published model of CYP2B4-CPR (Ref), as CYP2C8 and CYP2B4 share high homology. The backbone of CYP2C8 is displayed as grey ribbons and the heme is dark red. CYP2C8*3 polymorphic mutations R139 and K399 are highlighted as light and dark purple spheres, respectively. Positively-charged arginine and lysine residues identified in CYP2B4-CPR binding (K121, R125, R132, K138, K421, K432, R442, Bridges et al. 1998) are displayed on CYP2C8 in blue. The CPR backbone is displayed as black ribbons with its FAD and FMN domains in dark and light green, respectively. Negatively charged residues implicated in binding to CYPs (E142, D144, D147, D207, D208, D209, E213, E214, D215 by Zhao et al. 1999; Shen/Kasper et al. 1995) are displayed in magenta. Images were generated using PyMOL software.

Tables

Supplementary Table A.1. Mutagenesis primers.

Mutation	**Primer Sequence**
I269F	
Forward	TCAATTGCTCTTCGTTCAAAATGGAGCAGGAAAAGGACAACCAAA
Reverse	TCGAGCGCTCTTCTGAACAGGAAGCAATCGATAAAGTCCCG
R139K	
Forward	TTCGCATGCTCTTCAAGAGCATTGAGGACCGTGTTCAAGAGG
Reverse	AAGCTCGCTCTTCCTCTTCTTCCCCATCCCAAAATTCCG
K399R	
Forward	TAGTACGCTCTTCCAGAGAATTTCCTAATCCAAATATCTTTGACC
Reverse	GGTTTAGCTCTTCCTCTGTCATCATGTAGCACGGAAGTCAGT

Supplementary Table A.2. *Spectral Characterization of CYP2C8 and mutants*. Wavelength values were obtained from spectra of substrate-free, oxidized protein samples and Fe(II) CO-bound samples of CYP2C8, *3, R139K, and K399R protein.

Spectral Characteristics of CYP2C8					
	CYP2C8*1	**CYP2C8*2**	**CYP2C8*3**	**CYP2C8-R139K**	**CYP2C8-K399R**
Oxidized λ (nm)	416	416	416	420	420
CO-bound λ (nm)	450	451	450	450	450

Appendix B: Heterologous expression of plant Taxadiene-5α-Hydroxylase (CYP725A4) in Escherichia coli[4]

B.1 Introduction

Taxadiene-5α-hydroxylase (CYP725A4) is a membrane-bound cytochrome P450 (CYP) found in the Japanese yew tree, *Taxus cuspidata,* which catalyzes the oxidation of taxadiene to taxadiene-5α-ol. This is the first functionalization step in the biological synthesis of the valuable phytochemical cancer therapeutic, taxol[481,482]. Natural sources are incapable of fully satisfying the demand for taxol and current total chemical synthesis approaches are economically cost-prohibitive [483-485]. As a result, emphasis has been placed on developing alternative synthetic routes. One such method is to use easily cultivated organisms such as *Escherichia coli* or *Saccharomyces cerevisiae* to perform heterologous biological production, also known as metabolic engineering [486,487]. To date, this strategy was used for producing approximately g/L titers of taxadiene using *E. coli* culture [488]. The next step in native taxol synthesis is the CYP725A4-mediated hydroxylation of taxadiene to taxadiene-5α-ol. Initial studies have shown that the incorporation of CYP725A4 into a bacterial expression system leads to the generation of many other byproducts [488,489]. Therefore, it is apparent that further optimizations of the metabolic engineering of taxol will require a more complete understanding of the CYP725A4 enzyme mechanism. This necessitates the ability to express this protein in milligram quantities for biochemical studies.

CYP725A4 was initially identified in microsomes made from *Taxus brevifolia* saplings as well as suspended *Taxus cuspidata* cell cultures [490]. In 2004, Croteau and coworkers were able to isolate

[4] This work has been published as: Rouck, J. E.; Biggs, B. W.; Kambalyal, A.; Arnold, W. R.; De Mey, M.; Ajikumar, P. K.; and Das, A. "Heterologous expression and characterization of Plant Taxadiene-5α-Hydroxylase (CYP725A4) in Escherichia coli." Protein Expression & Purification, 2017, 132 60-67. The work is allowed to be republished under the Creative Commons Attribution license (https://creativecommons.org/licenses/by/4.0/)

the CYP725A4 cDNA, successfully express CYP725A4 in the fall armyworm *Spodoptera fugiperda*, create microsomes, and characterize CYP725A4-mediated taxadiene hydroxylation to taxadiene-5α-ol using kinetic and binding assays [491]. In 2008, Tissier and coworkers expressed CYP725A4 in the tobacco plant *N. sylvestris* along with taxadiene synthase and observed the product 5(12)-Oxa-3(11)-cyclotaxane (OCT) in the leaf exudate instead of the expected taxadiene-5α-ol [492]. As part of the same study, CYP725A4 was expressed in yeast, and microsomes were prepared that also converted taxadiene to OCT rather than taxadiene-5α-ol [492]. In 2014, Yadav studied a CYP725A4 construct and found that CYP725A4 acts on 4 substrates to form 12 products, and that taxadiene-5α-ol was only a very minor product [493]. Additionally, other groups have suggested the presence of an epoxide intermediate in the conversion of taxadiene to taxadiene-5α-ol [494,495]. In order to help resolve the ambiguity surrounding CYP725A4-mediated taxadiene hydroxylation, we conducted a study comparing the product distribution of different CYP725A4 constructs that are purified via *E. coli* fermentation [496]. The use of purified protein is important because it reduces the chances for non-specific protein-protein interactions and other contaminants in the microsomes that might influence the metabolism of taxadiene by CYP725A4.

In general, membrane proteins such as CYP725A4 are difficult to express recombinantly in bacterial systems and thereby lead to poor expression of functional protein [474]. One method of increasing expression of functional membrane proteins in *E. coli* is to modify the protein's hydrophobic N-terminal domain, which increases the protein solubility during expression [245,474,497,498]. In this work, we prepare several different constructs of CYP725A4 with N-terminus modifications in order to increase the expression of these constructs in bacterial systems.

The redox partner of CYP725A4 is cytochrome P450 reductase (CPR). CPR is the obligate redox partner of most CYPs [499]. We have shown that different constructs, i.e. CYP725A4 fused to

Taxus cuspidata CPR, CYP725A4 paired with mammalian CPR, and CYP725A4 paired with plant CPR, catalyzed the conversion of taxadiene to both taxadiene-5α-ol and OCT [496].

Further functional characterization was pursued with the CYP725A4 construct that yielded the highest amount of functional protein when expressed in *E. coli*. In order to provide a native-like lipid environment to the protein, purified CYP725A4 was reconstituted into nanodiscs to analyze the kinetics of CYP725A4 taxadiene metabolism. Nanodiscs are uniform-sized nanoscale lipid bilayers encompassed by membrane scaffold proteins (MSPs) and which mimic a native-like membrane environment for membrane protein stability (Figure B.1) [478,500-505]. In addition, it has been shown that membrane proteins in nanodiscs maintain their native-like functionality [501,503,506-510]. In 2004, Schuler and coworkers successfully inserted purified plant CYP73A5 into nanodiscs demonstrating the potential of this technology in studying plant CYPs [510]. Therefore, the nanodisc is an ideal system to stabilize purified membrane-bound CYP725A4 in order to evaluate the reaction kinetics of taxadiene metabolism.

We studied the taxadiene binding to CYP725A4 through UV-Vis spectral shifts of the heme Soret band at 417 nm to lower wavelengths upon substrate binding. Concentration-dependent shifts in the heme absorption from 417 nm to 393 nm were observed, indicative of a type-1 substrate binding pattern.

Molecular Operating Environment (MOE) software was used to dock taxadiene into the CYP725A4 active site in order to understand the origin of the substrate binding. Several residues close to the active site were identified that are highly likely to influence substrate docking. Altogether, the best-docked conformation demonstrated favorable binding of taxadiene to CYP725A4.

Taken together, herein we present a method of expression and purification of four new constructs and two previously reported constructs of CYP725A4. Binding of taxadiene to CYP725A4 is analyzed using UV-vis spectroscopy. CYP725A4 is incorporated into nanodiscs in order to evaluate taxadiene metabolism reaction kinetics. Additionally, we perform MOE modeling studies to gain insight to the protein's active site.

B.2 Materials and Methods

Materials: The reactants used were purchased from Fisher Scientific or Sigma-Aldrich unless stated otherwise. The yeast extract used in media was provided by Difco. Plasmid preparations were performed using Qiagen kits. Alfa Aesar provided the Ethylenediaminetetraacetic acid (EDTA) and Thiamine HCl. Gold Biotechnology was the source of the antibiotics (Spectinomycin and Ampicillin), arabinose, isopropyl β-D-1-thiogalactopyranoside (IPTG), PINKstain^{TM} Protein Ladder, and Ni-NTA resin. Lipids were acquired from Avanti Polar Lipids and cholate was obtained from Affymetrix. Delta-ALA was bought from Frontier Scientific. EMD Millipore provided the Pall Nanosep MF (0.2 μM) and Amicon Ultra (50,000 and 10,000 MWCO) centrifugal filters. P212121.com was the source of NADPH and NADP. SimplyBlue^{TM} SafeStain was purchased from Invitrogen. 7.5% Miniprotean® TGX^{TM} PAGE was obtained from Bio-Rad. The taxadiene used in this project was synthesized and purified as described previously and dissolved in DMSO to 15 mM concentration [488].

Construction of his-tagged gene constructs for protein expression: Constructs were created as described before [488]. The histidine tags to construct 17-α-L-CPR and 17-α-CYP725A4 were added as published [496]. The remaining histidine tags were added using standard molecular cloning protocols. The plasmids p5Trc-(MA)CYP-l-CPR-6His (Construct CYP725A4-MA-L-CPR)and p5Trc-(2b1)CYP-l-CPR-6His (Construct CYP725A4-2b1-L_CPR) were created by amplification

of the C-terminal part of CPR using primers Fw-CPRint-NcoI (5'-aagagcgcgagccatggttg) and Rv-CPR6His-SalI (5'-cggccgtcgac*tta*gtgatggtgatgatgatgccaaatatcccgtaagtagc). A 6-His tag was added and subsequently cloned with the use of restriction enzyme sites *Nco*I and *Sal*I. The plasmids p5Trc-(MA)CYP6His-o-(MA)CPR (Construct CYP725A4 MA) and p5Trc-(2b1)CYP6His-o-(2b1)CPR (Construct CYP725A4 2b1) were constructed by replacing the CYP fragment with an amplified CYP6His fragment with primers Fw-p5Trc (5'- atcatgccataccgcgaaag) and Rv-CYP6His-*Bam*HI (5'- cgtcggatcc*tta*gtgatggtgatgatgatgcggacgagggaacag) using restriction enzyme sites *Nde*I and *Bam*HI. An alignment of modifications made to the CYP is contained as Figure B.2.

Fully Optimized CYP725A4 Expression: Colonies containing the CYP725A4 gene plasmid were cultured in 30 mL Luria Bertani broth supplemented with 60 μg/mL Spectinomycin or 0.1 mg/mL ampicillin antibiotics at 30° C, 250 rpm overnight (100 μg/mL ampicillin for unlinked constructs and 60 μg/mL spectinomycin for linked constructs). 5 mL of the overnight culture were used to inoculate 500 mL of Terrific Broth supplemented with 125 μL trace minerals and 60 μg/mL spectinomycin or 0.1 mg/mL ampicillin and grown at for 2 hours at 30° C and 250 rpm for 2.5 hours. Trace mineral composition is 166 mM $FeCl_3$, 15 mM $ZnCl_2$, 8.3 mM $NaMoO_4$, 8.4 mM $CoCl_2$, 9mM $CaCl_2$, 7.3mM $CuCl_2$, and 8.1 mM H_3BO_3 in 1.6 M HCl. After 2.5 hours, 250 μL of 0.1 mM delta-ALA was added to facilitate formation of the heme prosthetic group. When the OD_{600} approached 0.9, the addition of 500 μg IPTG and 2 g arabinose per 0.5 liter of media induced protein expression. The cells were grown for 44 hours at 250 rpm and 22° C. The bacteria cells were harvested by centrifugation for 30 minutes at 8000 rpm (10,000g) in a Sorvall GSA rotor (Thermo Scientific, Waltham, MA) at 4° C.

Purification of CYP725A4: In order to create spheroplasts and to isolate the CPR from the bacterial proteases that are known to remove the N-terminus, the cell pellet was resuspended in

500 mL of Lysozyme buffer containing 75 mM Tris-HCl pH 8, 0.25 M Sucrose, 0.25 mM EDTA, and 0.02 mg/mL Lysozyme at 4° C for 30 minutes. Spheroplasts were pelleted using the same Sorvall rotor at 8000 rpm (10,000g) and 4° C for 30 minutes and resuspended in lysis buffer. Lysis buffer contains 0.1 M pH 7.4 potassium phosphate buffer, 20% glycerol, 6 mM $MgCl_2$, 0.1 mM DTT, 0.2 mM PMSF, and 5 mg of DNase. Spheroplasts were lysed by sonication at 40 seconds on, 40 seconds off intervals for 6 cycles. The lysate was centrifuged at 4° C for 45 minutes at 35,000 rpm (140,000g) using a Beckman Ti-45 rotor (Beckman, Coulter, Brea, CA). The pelleted *E. coli* membrane fraction was then suspended in extraction buffer for 5-6 hours at 4° C. Extraction buffer is 0.1 M pH 7.4 potassium phosphate buffer, 20% glycerol, 200 mM NaCl, 0.1mM DTT, and 1% Cholate. After 5 hours the mixture was centrifuged at 140,000g for 45 minutes at 4° C. The supernatant containing CYP725A4 was loaded onto a Ni-NTA column pre-incubated with column buffer. CYP725A4 column buffer is 0.1 M pH 7.4 potassium phosphate buffer, 20% glycerol, 0.1% cholate, 1 mM EDTA, and 1 mM DTT. The loaded column was washed with 50 mL of column buffer and 50 mL of column buffer containing 20 mM imidazole to remove weakly bound nonspecific proteins. CYP725A4 was eluted with 50-100 mL of column buffer spiked with 200 mM imidazole and 200 mM NaCl. A schematic of this protocol is shown as Supplementary Supplementary Figure B.1. Unlinked CYP725A4 (N-terminally modified CYP725A4 constructs not fused to CPR) was concentrated by centrifugation in Amicon Ultra 10,000 MWCO concentrators and chimera CYP725A4 was concentrated by centrifugation in Amicon Ultra 50,000 MWCO concentrators. Imidazole was removed by buffer exchanging the protein to 0.1 M pH 7.4 potassium phosphate buffer, 20% glycerol, 0.1% cholate, 1 mM DTT, and 200 mM NaCl. Concentration and quality were assessed by UV-VIS Spectroscopy using a 1-cm path length quartz cuvette. Concentration was calculated using ε_{417} = 116,000 M^{-1} cm^{-1}.

SDS-PAGE and native PAGE Gel: 10 μL (corresponding to 0.1-0.2 nmol) of CYP725A4 were mixed with 3 μL of 5X Laemmli Buffer (60 mM Tris-HCl pH 6.8, 10% glycerol, 5% β-mercaptoethanol, 0.01% bromophenol blue) with and without 2% SDS. Denaturing samples were boiled with 100^{o} C water for 10 min prior to being loaded into the gel. The samples were loaded into a 7.5% Miniprotean® TGX™ PAGE gel and ran at 85 mV for approximately 1-2 hours. Running buffer used was standard 1x PAGE Buffer consisting of 25 mM Tris, 192 mM glycine, with and without 0.1% SDS. PINKstain™ Protein Ladder was used to determine the protein molecular mass estimates. After being washed thrice with water, the gel was stained with SimplyBlue™ SafeStain for one hour. The gel was then washed with water to remove background dye.

Substrate Titration: CYP725A4-17α-L-CPR was pre-incubated at 32° C in a quartz cuvette. Taxadiene was then titrated into the solution using concentrations ranging from 0.06 μM to 91.7 μM and the Soret band shift at 417 nm was recorded by UV-Vis spectrometry. After addition of each aliquot of taxadiene, the titration mixture was incubated for 5 min to equilibrate before the spectra was taken. The difference in the Soret band shift from 417 to 393 nm was measured and fitted to the one-site binding model.

Nanodisc Assembly: The gene for MSP1E3D1 expression was generously provided by Dr. Stephen G. Sligar. Membrane scaffold protein (MSP) was expressed, purified, and subsequently optimized for the nanodisc assembly as previously described [478,500-505]. A nanodisc mixture was used to stabilize CYP725A4-17α-L-CPR for kinetic metabolism studies. Briefly, POPC lipids were dried under nitrogen overnight and subsequently solubilized in 200 mM cholate. MSP was added to this mixture in a 1:130 MSP:lipid ratio and incubated for 60 minutes at 4° C on a rocker. CYP725A4-17α-L-CPR was then added in a 10:1 MSP:CYP ratio and the mixture was allowed to

incubate as before for 1 hour. Detergent was removed with an equivolume amount of Amberlite Bio-Beads for four hours at 4° C. Finally the Bio-Beads were removed from the nanodisc mixture using a spin column.

High Performance Liquid Chromatography (HPLC) Analysis of Nanodiscs: Nanodisc HPLC was performed as described previously [511].

Taxadiene Metabolism Kinetics Assays: 0.2 μM of CYP725A4-17α-L-CPR mixed nanodiscs was incubated with 50 μM POPC Lipids, 400 μM NADPH, and a range of taxadiene concentrations dissolved in DMSO (20μM, 40 μM, 60 μM, 90 μM, 120 μM, 160 μM or 200 μM) in 0.1 M potassium phosphate buffer pH 7.4. The total reaction volume was 2 mL and the volume of DMSO remained constant throughout. The reaction mixtures incubated at 32° C for 1 hour and were quenched with 1x reaction volume of 4 M NaCl. The product was then extracted twice with 2x reaction volume of 4:1 hexane:ether and the organic extracts were combined and dried under nitrogen gas. The dried organic extract was shipped on dry ice for GC-MS analysis that was performed as previously described [496]. Products were identified by matching retention time to the retention times of previously verified structures [496]. Data were fit to the Michaelis-Menten equation.

Molecular Operating Environment Modeling: Molecular Operating Environment (MOE) modeling was used to observe the docking of taxadiene into a PDB structure of wild type CYP725A4 developed using PHYRE2 homology modeling [512]. The initial model created by PHYRE2 does not contain a heme; therefore, a heme was added using MOE and an open conformation of the protein model (not energy minimized) was used as a starting point. Docking utilized the MOE docking module. Before docking, cavities around the heme oxygen were chosen for the substrates to dock in. Each cavity found in the homology model was given a propensity of

ligand binding number (PLB) and MOE listed these cavities with their PLB score in order from greatest propensity for a ligand to bind to the least. The two cavities that were chosen were closest to the heme oxygen and were the first cavities listed. The taxadiene molecule was inserted into chosen cavities, and MOE generated a multitude of ligand conformations in these binding sites. Several residues were found within 4.5 Å of the substrate and were influential of positioning. The conformation selected for future modeling was the conformation with the shortest distance between the heme and the atom it hydroxylated, which is the fifth carbon on taxadiene. Once the conformation was chosen, MOE was used to conduct an energy minimization step causing the protein to clamp down on the substrate more tightly, illustrating induced fitting of a substrate to its enzyme.

After the substrate was docked and the energy minimization was performed the final distance between the heme oxygen and site of attack on the substrate was measured. The interaction energy number was also found using MOE, which shows if the binding state of the substrate in the protein is feasible and energetically favorable by indicating the change of free energy when the substrate is bound. The interaction energy number for the substrate bound was a negative number, indicating a negative free energy, which corresponds to favorable binding of the substrate with 5-α hydroxylase. All renderings were created using Virtual Molecular Dynamics (VMD) [513].

B.3 Results and Discussion

Construction of CYP725A4 N-terminal Mutants. The Kyte-Dolittle plot of wild-type CYP725A4 reveals that the N-terminus of the protein is highly hydrophobic (Supplementary Supplementary Figure B.2). Truncating and modifying the hydrophobic N-terminal regions of CYPs has been shown to increase expression without affecting protein activity [514-517]. Previously, several modified versions of CYP725A4 were created [488]. Herein we express only three of those

CYP725A4 constructs. These three N-terminal modifications are denoted as MA, 2b1, and 17α. MA features a 59-residue truncation and an insertion of a Met-Ala sequence at the start of the N-terminus, which has previously shown to increase CYP expression levels. [518-520]. 2b1 is the N-terminal addition of a 16-residue peptide MAKKTSSKGKLPPGPS, adopted from the N-terminus of rabbit CYP 2b1, to a 59-residue N-terminally truncated CYP725A4. Addition of the MAKKTSSKGKLPPGPS peptide has been shown to increase solubility of an insect CYP [521]. 17α is the addition of the N-terminal 8-residue peptide MALLLAVF, adopted from the N-terminus of bovine steroid hydroxylase, to a 24-residue N-terminal truncation of CYP725A4. The 17α modification was used in our previous study and has been shown to increase recombinant protein expression in *E. coli* [518,522]. An alignment of these N-terminal modifications was created using Clustal 2.1 Multiple Element Sequence Alignment on standard settings [523]. This alignment is shown in Figure B.2. Additionally, a six-residue histidine tag was added to each construct to make them amenable to purification using a Ni-NTA column. The modified gene constructs were inserted into plasmid p5Trc for expression.

Construction of CYP725A4-taxus CPR-linked constructs. For each N-terminal modification to CYP725A4, a chimera construct linking the modified CYP to a similarly modified *Taxus cuspidata* CPR was also created. The CPR modifications are as follows. The CPR linked to the MA CYP has the MA peptide added to a 74-residue N-terminally truncated CPR. The CPR linked to the 2b1 CYP has the MAKKTSSKGKLPPGPS peptide added to an 89-residue N-terminally truncated CPR. The CPR linked to the 17α CYP has the MALLLAVF peptide added to a 74-residue N-terminally truncated CPR. In all chimera constructs the linker peptide is GSTGS. These constructs feature the same six-residue histidine tag to enable Ni-NTA column purification. Complete sequences of linked chimera constructs are shown in Supplementary Figures B.7-9.

Expression and Purification. Each gene was transformed into BL21 (DE3) *E. coli* cells. Initial growth was performed with the unlinked MA strain in order to optimize growth volume and temperature. Purification yields of these initial expressions are shown in Figure B.2**.** Both 2b1 and 17α increased yields when compared to the MA construct. As the yield of the CYP725A4-17α-L-CPR was the highest, further studies were performed with this construct. In addition, separate membrane extractions were performed with 1% cholate for 5-6 hours, 1% cholate overnight, 1% Lubrol overnight, and 1% CHAPS overnight to determine the optimal detergent for further purifications. Purifications using all detergents but lubrol generated comparable amounts of CYP725A4 while the lubrol purification generated slightly less CYP725A4. Therefore, for further studies 1% cholate was used to extract the proteins from the membranes with an incubation time of 5-6 hours.

UV-Vis Spectroscopy Characterization. UV-Vis Spectroscopy was used to assess protein concentration and quality. The representative spectrum of purified CYP725A4-17α-L-CPR is shown in Figure B.3A. The protein had an absorbance peak at 417 nm. This peak indicates successful incorporation of the heme to the protein and suggests a properly folded CYP. Furthermore, the absorbance spectrum of CYP linked to CPR features a prominent shoulder at 456 nm. This shoulder corresponds to the flavin co-factors of CPR and indicates that holo-CPR has been properly expressed and purified in this linked construct.

PAGE analysis of protein: SDS-PAGE and native-PAGE were performed to assess CYP725A4-17α-L-CPR purity. Under native conditions a major band at ~175 kDa was obtained. Since estimations of molecular mass are inexact using native gels, it is likely that this chimeric construct, with two large proteins connected by a linker peptide, was hindered by the gel matrix and migrated much more slowly than the ladder. This makes it appear to have an artificially high

molecular mass. Using SDS-PAGE we obtain a better estimate of the molecular mass of the protein. A clear band corresponding to a closer estimate of the molecular mass was obtained (~132 kDa observed and ~128 kDa calculated for the construct).

Assembly of Nanodisc Mixture. The nanodiscs mixture was assembled and the quality of the nanodiscs was assessed using size exclusion chromatography (Figure B.3B). As seen by Figure B.3B, there is an absorbance peak found at approximately 16.5 mL. Based on previously run standards of cytochrome P450-CPR-nanodiscs, a peak at 16.5 mL signifies reconstituted CYP-CPR nanodiscs. The lipid bilayers of nanodisc provides a homogenous, stable environment for measuring the activity of CYP725A4, free of other interacting proteins as compared to microsomes [478,500-505].

Taxadiene Titration. Typically for drug-metabolizing and steroid-synthesizing CYPs, binding of substrate near the active site heme produces a spin-state shift. This subsequently produces a Soret (heme absorbance) band shift from 417 to ~390 nm, which can be utilized to measure substrate binding. This is also termed as a type-1 shift [524]. CYP725A4-17α-L-CPR was titrated with taxadiene to determine the spin state shift of the heme iron upon substrate binding. Upon substrate binding, the CYP725A4 Soret band absorbance shifted from 417 nm to 393 nm. The binding fit to a one-site binding model with a calculated spin-state equilibrium constant, K_S, of 2.1 $\pm$ 0.4 μM (Figure B.4A). K_S is taken to be approximately equal to K_D during these experiments. Our K_S (K_D) of 2.1 $\pm$ 0.4 μM compares favorably to the previously reported one-binding site behavior observed by both Croteau and coworkers (Ks varying between 5 and 8 μM) and Tissier and coworkers (K_D of 6.9 $\pm$ 0.4 μM) [491,492]. The work done by Croteau analyzed unmodified CYP725A4 in insect microsomes while Tissier analyzed CYP725A4 with a slight C-terminal modification in yeast microsomes. This suggests that the N-terminal modification and

fusion to CPR has not affected the ability of CYP725A4 to bind taxadiene. However, these modifications have shown to slightly increase binding affinity.

Taxadiene Metabolism Kinetics. To determine taxadiene metabolism kinetics, we measured the taxadiene hydroxylation activity of CYP725A4-17α-L-CPR in nanodiscs. In these experiments, CYP725A4-17α-L-CPR nanodiscs were incubated with 20-200 μM taxadiene concentrations and 400 μM NADPH for 1 hour. NADPH acts as an electron source by donating electrons to the linked CPR that then transfers them to CYP725A4. CYP725A4 subsequently uses these electrons to oxidize taxadiene into taxadiene-5α-ol or OCT [491,492]. After extraction, the products of these incubations were identified and quantified by GC-MS [496]. Data from one of the trials is shown as Figure B.4B. The metabolism of taxadiene by CYP725A4 followed Michaelis-Menten kinetics showing a V_{max} of 30 $\pm$ 8 pmol/min/nmol and a K_M of 123 $\pm$ 52 μM. Our K_M is greater than the K_M determined by Croteau's microsomal assays (16 $\pm$ 3.2 μM) [491], but nevertheless our kinetics display reliable conversion of taxadiene to taxadiene-5α-ol indicating the expression of a functional protein. Additionally, taxadiene-5α-ol formation was not observed until CYP725A4-17α-L-CPR was incubated with 90 μM taxadiene. This suggests that metabolism was below the detecting limit or that OCT is made first.

CYP725A4 homology modeling with taxadiene: Molecular Operating Environment (MOE, Chemical Computing Group, Montreal, QC, Canada) software was used to identify substrate binding characteristics within the active site of the protein. A hybrid structure model was constructed from the crystal Protein Data Bank coordinates of similar CYP isozymes (class-dependent sequence alignment strategy), as described in Materials and Methods. This approach takes advantage of the conserved sequences that maintain the secondary and tertiary CYP folds to generate the core structures surrounding the buried catalytic sites. An MOE modeling system was

used to dock taxadiene in the most preferred conformation (Figure B.5A). This conformation placed the heme 2.36 Å away from Carbon 5 of the substrate taxadiene (Figure B.5B). This distance is close enough for the hydroxylation to occur and closer than the 3.50 Å difference between the heme and carbon of attack of the best conformations of the furanocoumarins (plant toxins) xanthoxin and bergapten docked into the robustly investigated insect enzyme CYP6B1 [525]. Furthermore, the interaction potential energy number, a value calculated by MOE used to predict binding, was negative. Negative values for interaction potential energy correspond to favorable binding of the substrate to the protein active site. Several residues were influential in the docking of taxadiene to the active site. The hydrophobic residues Trp 125, Ala 129, Met 133, Ala 306, Pro 373, Val 374, Phe 375, Gly 376, Pro 482, and Leu 483 helped to stabilize and mediate the position of the highly hydrophobic taxadiene in the active site. These residues are displayed as Figure B.5C. The polar residues Ser 302, His 305, Asp 309, Thr 310, and Thr 377 also influenced positioning and could function to stabilize reaction intermediates (Figure B.5D). These residues would be part of future mutation studies or protein engineering of CYP725A4.

B.4 Conclusions

In this work we report the expression and purification of CYP725A4 from *E. coli* expression system. We then performed binding and kinetic studies of the highest yielding CYP725A4 construct (CYP725A4-17α-L-CPR) in nanodisc. To this end we titrated CYP725A4 with taxadiene and determined a binding affinity that agrees with previously published data. Furthermore, a kinetics analysis determined that the linked construct catalyzed the conversion of taxadiene to taxadiene-5α-ol and OCT following Michaelis-Menten kinetics. We therefore demonstrate that our expression and purification protocol produces functional CYP725A4. This expression and purification protocol will be useful for purifying other plant CYPs expressed in *E. coli.*

B.5 Figures

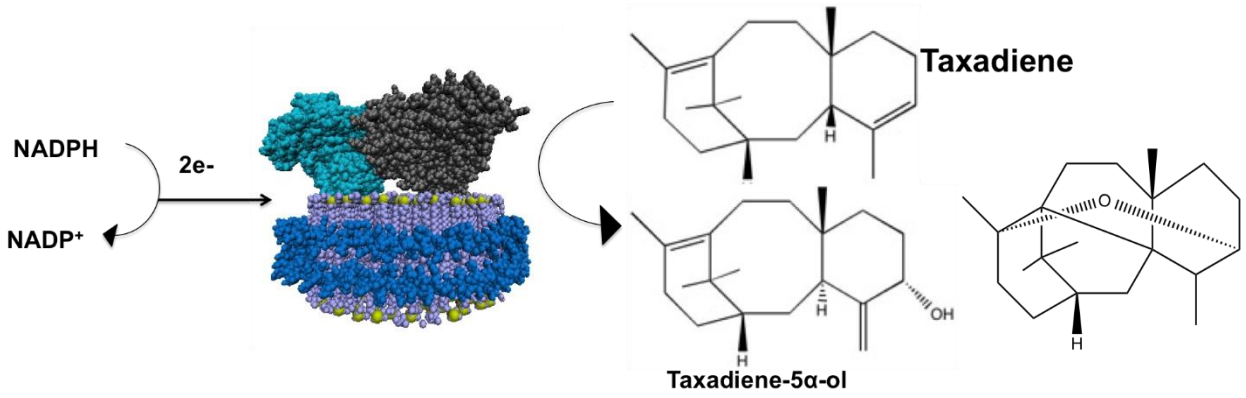

Figure B.1. Schematic of CYP725A4 (grey) and CPR (cyan) inserted into the nanodisc (lipids are purple, phosphate atoms are yellow, and membrane scaffold protein is shown in blue). When NADPH is given to the system, the electrons are used in conjunction with molecular oxygen to convert taxadiene to taxadiene-5α-ol or OCT.

CYP725A4 Construct	N-Terminal Alignment	Yield
CYP725A4 MA	----------	1.54 nmol/liter
CYP725A4 2b1	----------MAKKTSSKG 9	1.76 nmol/liter
CYP725A4 17 α	----------MALLLAVFFSIALSAIAGILLLLLLFRSKRHSSL 34	4.83 nmol/liter
CYP725A4	MDALYKSTVAKFNEVTQLDCSTESFSIALSAIAGILLLLLLFRSKRHSSL 50	Yield of Chimera
CYP725A4 MA	-----MA--PFIGESFIFLRALRSNSLEQFFDERVKKFGLVFKTSLIGHP 43	0.362 nmol/liter
CYP725A4 2b1	KLPPGPS--PFIGESFIFLRALRSNSLEQFFDERVKKFGLVFKTSLIGHP 57	1.61 nmol/liter
CYP725A4 17 α	KLPPGKLGIPFIGESFIFLRALRSNSLEQFFDERVKKFGLVFKTSLIGHP 84	7.21 nmol/liter
CYP725A4	KLPPGKLGIPFIGESFIFLRALRSNSLEQFFDERVKKFGLVFKTSLIGHP 100	

Figure B.2. *Sequence Alignment of CYP725A4 modifications in comparison to wild type CYP725A4*. Yellow residues are amino acids that are added during the modification procedure. Green residues are amino acids that are part of wild type CYP725A4 but are deleted in one or more truncations. The yields of the purified protein from each CYP725A4 construct is shown to the right.

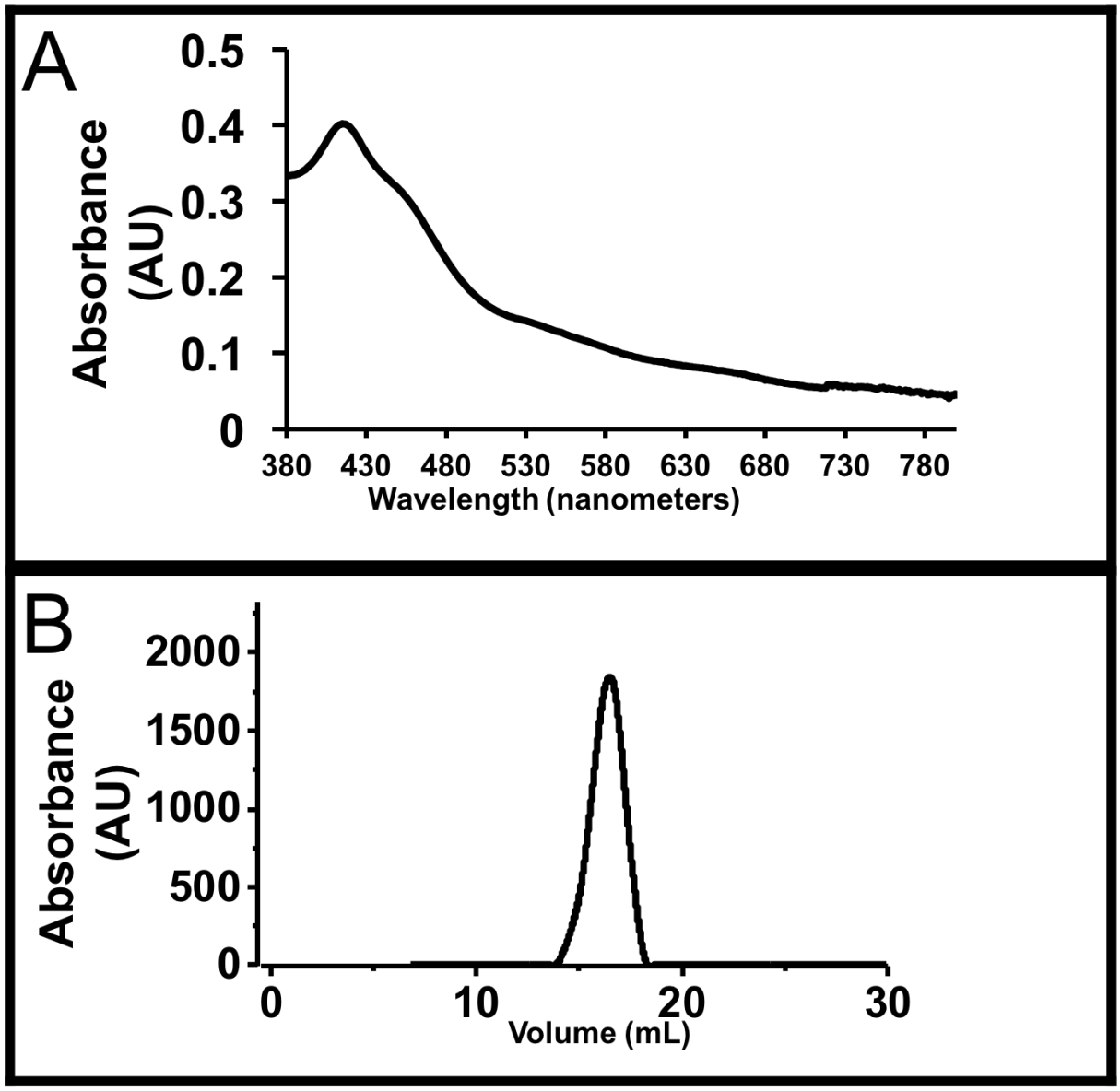

Figure B.3. *Characterization of CYP725A4*. (A) UV-Vis spectra of CYP725A4-17-α-L-CPR. The peak at 417 nm is characteristic of Soret band of heme proteins. The shoulder at 456nm is due to the flavin cofactors of CPR that is linked to the CYP. (B) Size exclusion chromatogram of CYP725A4-17α-L-CPR Nanodisc mixture. The peak at 16.5 mL is indicative of CYP725A4-17α-L-CPR-nanodisc.

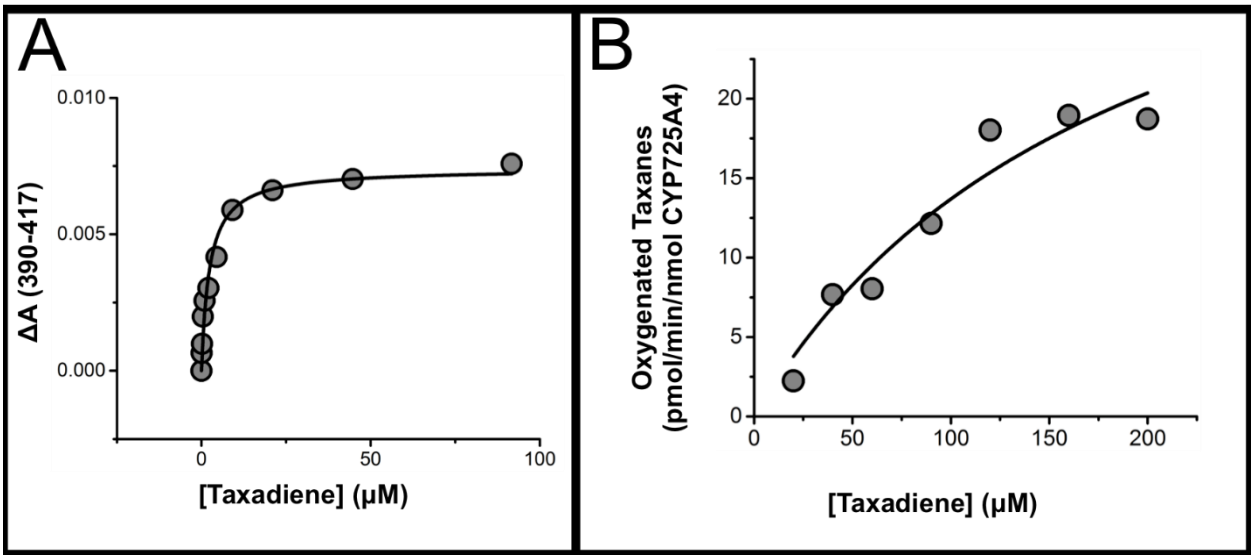

Figure B.4. *CYP725A4-17α-L- CPR taxadiene titration*. (A) Soret band at 417 nm wavelength shifts to lower wavelengths CYP725A4-17α-L-CPR upon taxadiene binding. The data was fit to the single binding isotherm and the average K_s was determined to be 2.1 $\pm$ 0.4. μM. Data shown is one trial. (B) Metabolism of taxadiene by CYP725A4-17-α-L-CPR follows Michaelis-Menten kinetics. The Vmax was 30 $\pm$ 8 pmol/min/nmol CYP725A4 and the Km was determined to be 123 $\pm$ 52 μM taxadiene. Data shown is one trial.

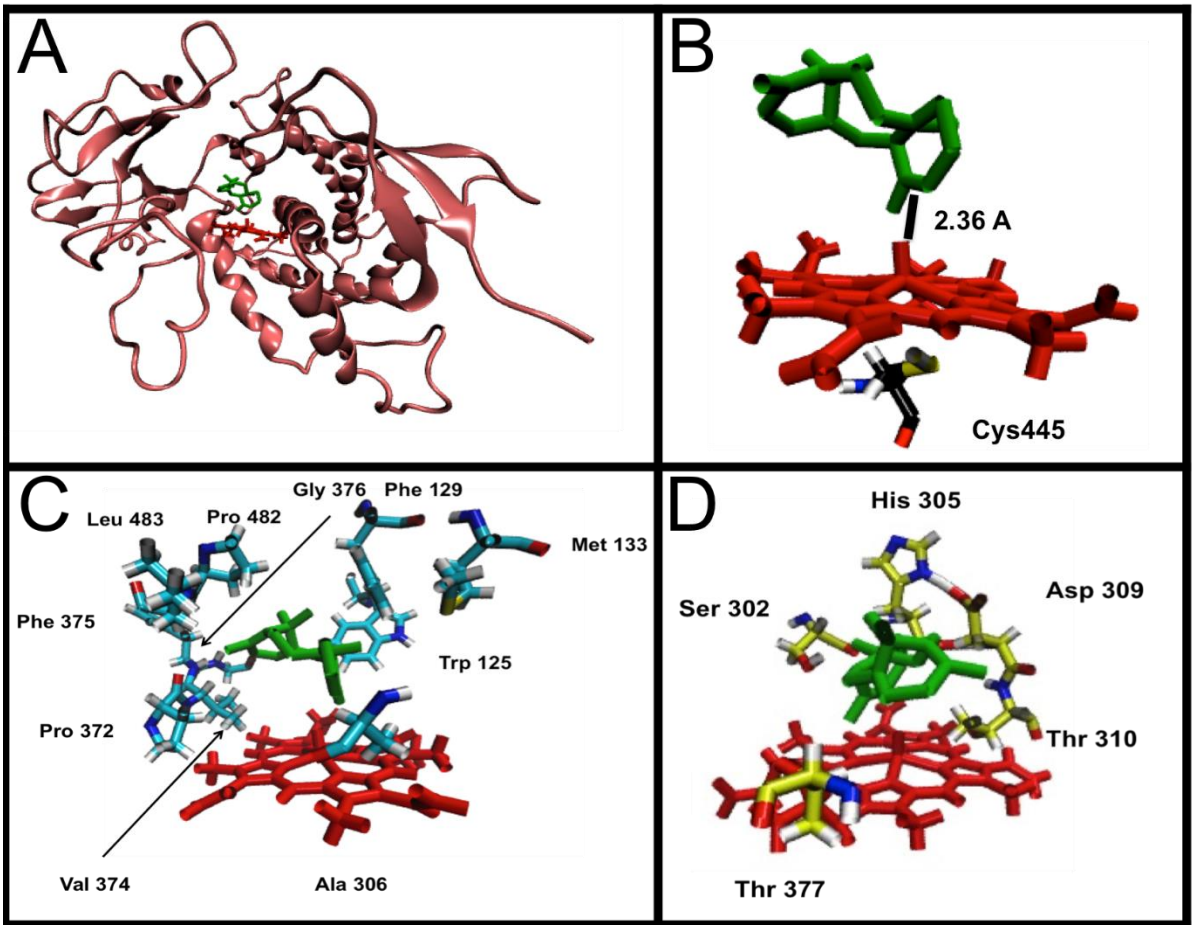

Figure B.5. *MOE docking of taxadiene to CYP725A4.* The images in this figure feature a molecule of taxadiene docked into the active site of CYP725A4 by the MOE Docking program. In all images the red structure is CYP725A4 Heme and the green structure is taxadiene. (A) CYP725A4 (champagne colored molecule) with taxadiene docked into the active site. (B) View of the CYP725A4 active site. From this view it is possible to see that the heme is 2.36 angstroms away from the carbon atom it hydroxylates. The catalytic cysteine is included as well with the following color scheme: Carbon-Black, Nitrogen-Blue, Oxygen-Red, Sulfur-Yellow, Hydrogen-Grey (C) The nonpolar residues used to position taxadiene in the active site. The residue color scheme is Carbon-Cyan, Nitrogen-Blue, Oxygen-Red, Sulfur-Yellow, Hydrogen-Grey. (D) Polar residues identified by MOE that could stabilize reaction intermediates. The residue color scheme is Carbon-Yellow, Nitrogen-Blue, Oxygen-Red, Hydrogen-Grey.